STUDY OF GAS ELECTRON MULTIPLIER DETECTORS FOR THE CMS EXPERIMENT AT THE LHC & ITS APPLICATION IN OTHER FIELDS

A THESIS

Submitted to the

PANJAB UNIVERSITY, CHANDIGARH

For the Award of

DOCTOR OF PHILOSOPHY

2024

in
FACULTY OF SCIENCE

BY
SUNIL KUMAR

GUIDE

Dr. SUSHIL SINGH CHAUHAN **Prof. VIPIN BHATNAGAR**

DEPARTMENT OF PHYSICS
PANJAB UNIVERSITY
CHANDIGARH, INDIA

November, 2024

Declaration

I declare that the thesis entitled **"STUDY OF GAS ELECTRON MULTIPLIER DETECTORS FOR THE CMS EXPERIMENT AT THE LHC & ITS APPLICATION IN OTHER FIELDS"** has been prepared by me under the guidance of Dr. Sushil Singh Chauhan, Assistant Professor, and Prof. Vipin Bhatnagar, Professor, Department of Physics, Panjab University, Chandigarh. No part of this thesis has formed the basis for the award of any degree or fellowship previously.

Sunil Kumar

Department of Physics
Panjab University, Chandigarh

Date:

Certificate

We certify that Sunil Kumar has prepared his thesis entitled **"STUDY OF GAS ELECTRON MULTIPLIER DETECTORS FOR THE CMS EXPERIMENT AT THE LHC & ITS APPLICATION IN OTHER FIELDS"**, for the award of PhD degree of the Panjab University, Chandigarh, under our guidance. He has carried out the work at the Department of Physics, Panjab University, Chandigarh.

Dr. Sushil Singh Chauhan

Assistant Professor
Department of Physics
Panjab University, Chandigarh

Prof. Vipin Bhatnagar

Professor
Department of Physics
Panjab University, Chandigarh

Date:

Dedicated to
My Parents,
Family,
&
Friends

Acknowledgements

I am immensely grateful to my parents for their unwavering support, enabling me to embark on a PhD journey after three years of employment. Their consistent encouragement has been a source of strength during challenging times.

I extend my heartfelt appreciation to my diligent supervisors, Dr. Sushil Singh Chauhan and Prof. Vipin Bhatnagar, for their invaluable guidance, expertise, and mentorship throughout the research process. Their insightful feedback, constructive criticism, and commitment to excellence have greatly influenced the quality of this thesis.

I also wish to express my gratitude to Prof. Manjit Kaur, Prof. Suman Bala Beri, Prof. Jasbir Singh, and Dr. Sunil Bansal for their unwavering support, dedication, and valuable suggestions as members of the Panjab University Experimental High Energy (PU-EHEP) Group. I am thankful to the India-CMS Collaboration for facilitating regular meetings to discuss research progress and provide valuable insights.

I sincerely thank Prof. Ghan Shyam Singh Saini, the Chairperson of the Department of Physics at Panjab University, for generously providing the necessary facilities for my research within the department. I also extend my gratitude to former Chairpersons, Prof. Rajeev Kumar Puri and Prof. Navdeep Goyal, who served during my PhD. I deeply appreciate the contributions of the technical, library, and purchase sections at Panjab University, which significantly contributed to the completion of this research work.

I am deeply grateful to the Department of Science and Technology (DST) and the Council of Scientific and Industrial Research (CSIR) for their invaluable financial support, which made this research possible.

I am profoundly grateful to CERN for providing computing resources and hosting services on multiple occasions. Additionally, I extend my heartfelt thanks to the CMS collaboration and the GEM community for providing essential resources for my research. I also want to express special appreciation to Prof. Othmane Bouhali from Texas A&M University, Qatar, for granting me access to the RAAD2 supercomputer for one of my analyses.

I want to thank my colleagues at the PU-EHEP lab for their assistance, camaraderie, and positive working environment. In particular, I want to thank Jyoti Babbar, Amandeep Kaur Virdi, Amandeep Kaur, Harjot Kaur, Geetanjali, Meena, Anureet Kaur, Prachi Sharma, Tanvi Sheokand, and Bhumika Mehta. I also want to thank the technical staff of PU-EHEP group, Ajit Singh, Subhash, Gian, Shiv, Navjot and Amarjeet for their assistance.

To my dear friends who have been with me through the ups and downs of this academic journey, I extend my heartfelt gratitude. Your support, encouragement, and shared moments of joy have provided a necessary balance to the rigours of research: Somnath Mardi, Munish Kumar, Anshul Bhatia, Rohit Bhota, Asar Ahmed, Navam Dhania, Abhishek, Nitin Kakria, Manish Kadwalia, Anuj Kaushik, Nikhila, and Amandeep.

Those whose names are not mentioned here deserve my personal and heartfelt gratitude.

This achievement is not solely attributed to me; it is a collaborative success made possible by the invaluable contributions of these exceptional individuals. I am deeply grateful for their unwavering support throughout my academic journey.

Date: ***(Sunil Kumar)***

Abstract

STUDY OF GAS ELECTRON MULTIPLIER DETECTORS FOR THE CMS EXPERIMENT AT THE LHC & ITS APPLICATION IN OTHER FIELDS

by **Sunil Kumar**

The muon system of Compact Muon Solenoid (CMS) is intended for prompt and accurate identification of muons generated from proton-proton (p-p) collisions. The forward region of the end-caps was under-equipped and relied solely on Cathode Strip Chambers (CSCs), thus resulting in a lack of redundancy during Large Hadron Collider (LHC) Run-2. This lack of redundancy was projected to pose challenges with the upcoming High Luminosity-LHC (HL-LHC) upgrades, as increasing background rates were predicted to impact Level-1 (L1) trigger performance and, as a result, the selection of crucial physics channels.

The integrity of the muon system will face additional challenges due to the ongoing upgrades to the LHC, especially in the high-rate environment, where there will be a 2.5-fold increase in instantaneous luminosity ($\mathcal{L}$) to 5×10^{34} cm^{-2}s^{-1}. Furthermore, prolonged operation in a high-rate environment is expected to have a detrimental impact on the performance of the CSCs, thereby presenting a challenge to the overall performance of the muon system in the forward region.

In response to increasing particle rates and the ageing of CSCs, the proposal to integrate Gas Electron Multiplier (GEM) detectors alongside existing CSCs was made. The CMS-GEM Collaboration proposed to strengthen the under-equipped high-η region with GEM detectors, referred as GEM End-cap Station 1 Ring 1 (GE1/1), GEM End-cap Station 2 Ring 1 (GE2/1), and Muon End-cap Station 0 (ME0)

specific to their location in the CMS end-cap. This integration aimed to increase the precision of muon bending angle measurements, thereby improving muon trigger capabilities. GEMs, renowned for their high-rate handling capabilities, are especially well-suited for deployment in the forward regions of the CMS muon system.

This doctoral thesis presents comprehensive research on GEM detector technology including four distinct studies. The initial study involves assembling the GE1/1 detectors and the execution of QC procedures on the assembled chambers at Panjab University, Chandigarh. Following this, the chambers were sent to Conseil Européen pour la Recherche Nucléaire (CERN) and integrated into the CMS experiment detector during Long Shutdown 2 (LS2). Currently, the installed GE1/1 detectors are actively collecting data during the ongoing Run-3, which started in July 2022.

The second study is dedicated to precisely estimating the sensitivity of the triple-GEM GE1/1 detector to the significant background radiation inherent to CMS. These background radiations are mainly composed of neutrons and photons that are produced as a result of interactions with CMS detectors. These predicted sensitivity metrics serve to gauge the background radiation hit-rate within the GE1/1 region, aiding in the development of a predictive model for background radiation in anticipation of the upcoming GEM-based detector upgrade in the forward region. The evaluation of background hit-rates was estimated using FLUktuierende KAskade (FLUKA) + GEometry ANd Tracking (GEANT) simulation and is further validated using background data obtained from the GE1/1 Slice Test. This technique is presently undergoing another validation through the analysis of background data collected for GE1/1 detectors from the ongoing LHC Run-3.

The third study in this thesis assesses the performance of blank and random-hole segmented GEM foils, specifically in the context of the ME0 detector upgrade. While blank segmentation was utilised in the photo-lithographic manufacturing technique of GE1/1 GEM-foils, the high-rate environment at the ME0 region necessitates the adoption of random-hole segmented foils for the ME0 detector. A beam

test was conducted using a muon beam, involving assembled triple-GEM chambers, one containing blank segmented foils and another containing random-hole segmented foils. The performance of both types of GEM foils is thoroughly evaluated using ANalysis SYStem (ANSYS) + Garfield simulation, enabling a comparative analysis with experimental data.

Finally, the fourth study discusses the expansion of GEM foil applications beyond the High-Energy Physics (HEP), specifically introducing a novel detection technique for Positron Emission Tomography (PET). This technique utilises the polarisation correlation inherent in the annihilation of positron and electron (in the case of para-positronium), producing two photons with orthogonal polarisation. A comprehensive research using a GEM-based detector prototype simulation has been conducted, with preliminary findings presented accordingly.

The anticipated outcomes of this doctoral research effort are expected to make substantial contributions to advancing the upcoming GEM upgrades within the CMS. Ongoing research efforts are rigorously directed towards further refining the proposed detection technique, aiming to not only augment but also ensure the better quality and precision of imaging data.

Contents

List of Figures

List of Tables

List of Abbreviations

ADC Analog to Digital Converter

ALICE A Large Ion Collider Experiment

ANSYS ANalysis SYStem

APDL ANSYS Parametric Design Language

APV25 Analog Pipeline Voltage 25

ATLAS A Toroidal LHC ApparatuS

ASIC Application-Specific Integrated Circuit

BARC Bhabha Atomic Research Centre

BCM1F Beam Condition Monitor 1 Fast

BCM1L Beam Condition Monitor for Losses

BPIX Barrel Pixel Detector

BRIL Beam Radiation, Instrumentation, and Luminosity

BSM Beyond Standard Model

BX Bunch-Crossing

CBM Compressed Baryonic Matter

CERN Conseil Européen pour la Recherche Nucléaire

CKF Combinatorial Kalman Filter

CMS Compact Muon Solenoid

CP Charge-Parity

COMPASS Common Muon and Proton Apparatus for Structure and Spectroscopy

COVID-19 Corona-virus Disease-2019

CSC Cathode Strip Chamber

CT Computed Tomography

DAC Digital to Analog Converter

DAQ Data Acquisition

DC-DC Direct Current-Direct Current

DESY Deutsches Elektronen-SYnchrotron

DT Drift Tube

EB ECAL Barrel

ECAL Electromagnetic Calorimeter

EE ECAL Endcap

EM Electro-Magnetic

ENC Equivalent Noise Charge

EW Electro-Weak

EYETS Extended Year-End Technical Stop

FAIR Facility for Antiproton and Ion Research

FEM Finite Element Method

FIT Fast Interaction Trigger

FLUKA FLUktuierende KAskade

FPIX Forward Pixel Detector

FPGA Field-Programmable Gate Array

FWHM Full Width at Half Maximum

GBT Gigabit Transceiver

GE1/1 GEM Endcap Station 1 Ring 1

GE2/1 GEM Endcap Station 2 Ring 1

GEM Gas Electron Multiplier

GEANT GEometry ANd Tracking

GeV Giga-electron Volt

GM Geiger-Muller

GUT Grand Unified Theory

GWP Global Warming Potential

HB Hadron Barrel

HCAL Hadron Calorimeter

HE Hadron Endcap

HEED High-Energy Electro-Dynamics

HF Hadron Forward

HGCAL High Granularity Calorimeter

HEP High-Energy Physics

HERA Hadron-Electron Ring Accelerator

HLT High-Level Trigger

HL-LHC High Luminosity-Large Hadron Collider

HO Hadron Outer

HPD Hybrid Photo-Diode

HV High Voltage

INC intra-nuclear cascades

IP Interaction Point

IR Insertion Regions

IT Inner Tracker

ITS Inner Tracking System

iRPC improved-Resistive Plate Chamber

IV Intravenous

L1 Level-1

LCT Local Charged Track

LEP Large Electron-Positron

LHC Large Hadron Collider

LHCb LHC beauty

LINAC2 Linear Accelerator 2

LINAC4 Linear Accelerator 4

LUT Look-Up Table

LS Long Shutdown

LSP Lightest Supersymmetric Particle

LV Low Voltage

MC Monte Carlo

ME0 Muon Endcap Station 0

MICROMEGAS MICRO MEsh GAseous Structure

MFT Muon Forward Tracker

MIP Minimum Ionising Particle

MPGD Micro-Pattern Gas Detector

MRI Magnetic Resonance Imaging

MSGC Micro-Strip Gaseous Chamber

MTD Minimum Ionising Particle Precision Timing Detector

MSSM Minimal Supersymmetric Standard Model

MWPC Multi-Wire Proportional Chamber

NMSSM Next-to-Minimal Super-Symmetric Standard Model

PANDA antiProton ANnihilation at DArmstadt

PCB Printed Circuit Board

PDG Particle Data Group

PDF Probability Density function

PET Positron Emission Tomography

PHENIX Pioneering High Energy Nuclear Interaction eXperiment

PLT Pixel Luminosity Telescope

PMT Photo-Multiplier Tube

PUGEM Panjab University GEM

PU Pile-Up

p-Pb proton-Lead

p-p proton-proton

Pb-Pb Lead-Lead

PS Proton Synchrotron

PSB Proton Synchrotron Booster

QA Quality Assurance

QC Quality Check

QCD Quantum Chromo-Dynamics

QE Quantum Entangled

QED Quantum Electro-Dynamics

QFT Quantum Field Theory

QGP Quark-Gluon Plasma

RC Resistance-Capacitance

R&D Research and Development

RHIC Relativistic Heavy Ion Collider

RICH Ring Imaging Cherenkov

RPC Resistive Plate Chamber

RU Response Uniformity

Sci-Fi Scintillating Fibre

SiPM Silicon Photo-Multiplier

SL Super-Layer

SM Standard Model

SPS Super Proton Synchrotron

SSC Superconducting Super Collider

STAR Solenoidal Tracker at RHIC

SuperFRS Super Fragment Separator

SUSY Super-Symmetry

TCA Tracker Control and Readout ASIC

TDR Technical Design Report

TD Timing Detector

TEC Tracker End Cap

TIB Tracker Inner Barrel

TID Tracker Inner Disks

TPC Time Projection Chamber

TOB Tracker Outer Barrel

TOTEM TOTal Elastic and diffractive Measurement

TPC Time Projection Chamber

UGent Ghent University

USG Ultrasonography

UNK Uskoritel' Nuklonov Kol'tsevogo

US United States

USC Underground Service Cavern

UV Ultra-Violet

VBF Vector Boson Fusion

VELO VErtex LOcator

VEV Vacuum Expectation Value

VFAT Very Forward ATLAS and TOTEM

VLQ Vector-Like Quarks

WLCG Worldwide LHC Computing Grid

WW-II World War-II

WWW World Wide Web

Xe-Xe Xenon-Xenon

YETS Year-End Technical Stop

List of Symbols

A atomic mass

N atomic density

Ar Argon

Ar/CO_2 Argon/Carbondioxide

Ar/CO_2/CF_4 Argon/Carbondioxide/Tetrafluoromethane

CF_4 Tetrafluoromethane

χ^2 chi-squared

cm centimetres

$\sqrt{s}$ center-of-mass energy

CO_2 Carbondioxide

ϵ_{coll} collection efficiency

ϵ_{ext} extraction efficiency

ΔE energy loss transmitted to a specified volume

E_C critical electric field

η pseudo-rapidity

eV electronvolt

$\delta(\beta\gamma)$ Fermi density effect correction

fC femtocoulomb

G_{eff} effective gas gain

GeV gigaelectronvolt

GJ gigajoules

G_{int} intrinsic gas gain

Gy Gray

Hz hertz

I characterstic average ionization and excitation potential of the medium

fb^{-1} inverse femtobarns

λ interaction length

$\mathcal{L}_{int}$ integrated luminosity

k Boltzmann constant

K Kelvin

kA kiloamperes

keV kiloelectronvolt

kHz kilohertz

km kilometres

kV kilovolts

$\mathcal{L}$ instantaneous luminosity

m metres

m_e rest mass of an electron

T_m maximum energy transfer

$M\Omega$ megaohms

E_T^{miss} Missing Transverse Energy

MeV megaelectronvolt

mrad milliradian

MHz megahertz

mm millimetres

Mrad megarad

ns nanoseconds

$PbWO_4$ lead tungstate

P Pressure

pF picofarads

p_T transverse momentum

f_p Penning transfer probability

Q electric charge

X_0 radiation length

R134a/iC_4H_{10}/SF_6 1,1,1,2-Tetrafluoroethane/Isobutane/Sulfur hexafluoride

R_M Molière radius

SF_6 Sulfur hexafluoride

T Tesla

T_e electron transparency

TeV teraelectronvolt

θ polar angle

T_3 isospin

μA microamperes

μm micrometres

μs microseconds

μrad microradian

μC microcoulomb

V volts

W_i effective average energy required for the formation of a single electron-ion pair

Z atomic number

R134a 1,1,1,2-Tetrafluoroethane

Preface

The journey from the initial spark of an idea to the completion of this thesis has been a journey filled with challenges and rewards. As I contemplate the pages that follow, I am reminded of the countless hours devoted to research, analysis, and deep reflection that have culminated in the creation of this work.

This thesis explores the *GEM detector*, aiming to *study its importance in the CMS experiment and explore its potential applications*. This research journey has been an enriching experience, giving me the chance to explore the complexities of *Experimental High-Energy Physics* and to make my own modest contribution to the body of knowledge within this field.

At the end-cap of the CMS experiment lies the GEM detector, a crucial component that provides an innovative and highly effective method of particle detection. This thesis thoroughly investigates the GEM detector, uncovering details about its design, assembly, quality control, functionality, and its sensitivity for particles in the context of the CMS experiment.

This academic exploration transcends mere technical details, aiming to connect theoretical frameworks with experimental realities in the realm of particle physics. The narrative unfolds against a backdrop of scientific curiosity, pushing the boundaries of understanding and innovation.

Reading this thesis takes you on a journey through important moments, difficulties, and successes in using the GEM detector in the CMS experiment. From its conceptualization to its integration into the LHC, the GEM detector exemplifies precision and ingenuity, capturing particles to study unknown physics processes.

Our research extends beyond HEP. The knowledge gained from studying the GEM detector applies to various fields, including medical imaging, shaping our understanding of the world and fostering real-world advancements with tangible impacts.

In conclusion, this thesis serves as a testament to the collaborative efforts of the scientific community, pushing the boundaries of knowledge and technology in the pursuit of truth. It is my earnest hope that the findings presented herein will not only enrich the corpus of scientific knowledge but also inspire future generations to continue unraveling the mysteries that lie at the core of the cosmos.

Sunil Kumar
Research Fellow
November 3, 2024

"I know quite clearly what I want out of my life. Life and my emotions are the only things I am conscious of. I love the consciousness of life and I want as much of it as I can get. But the span of one's life is limited. What comes after death no one knows. Nor do I care. Since, therefore, I cannot increase the content of life by increasing its duration, I will increase it by increasing its intensity. Art, music, poetry and everything else that consciousness I do have this one purpose - increasing the intensity of my consciousness of life. "

— **Bhabha Homi Jehangir**

General Introduction

Particle physics, a specialised field of physics, explores the fundamental building blocks of the universe and how they interact. It's like solving a cosmic puzzle, trying to understand the many ways things happen in space. At its heart is a big question: where do all the things around us come from? This question has puzzled philosophers, theologians, and scientists for centuries and forms the basis of our understanding of the world. It might seem like a simple question that kids ask, but the answer is pretty complex. It's not just an answer about things; it's like the starting point for everything we see and know.

In the early 1600s, Galileo Galilei's endorsement of the heliocentric hypothesis ignited debates but eventually garnered widespread acceptance. A few decades later, Isaac Newton achieved a significant "first great unification in physics" with his formulation of the laws of motion and the law of universal gravitation. Following Newton, James Clerk Maxwell introduced groundbreaking electromagnetic equations, often regarded as the "second great unification in physics". However, scientific hypotheses, including these, require evidence for acceptance. Galileo's pioneering use of a telescope marked a pivotal moment in the development of the Scientific Method. The importance of evidence is exemplified in Maxwell's equations, whose significance was underscored by Heinrich Hertz's later discovery of electromagnetic radiation. Scientific ideas since the Modern Age have profoundly influenced human interactions with information. Quantum Electro-Dynamics (QED) stands as one of the most rigorously tested and verified theories in physics. Thus, what distinguishes scientific investigation is its capacity to demonstrate the accuracy of a hypothesis through experiments that observe the processes the hypothesis predicts. This is particularly crucial in particle physics, where most theories deal with phenomena at incredibly small scales and processes that are not yet fully realised.

During the late 19^{th} and early 20^{th} centuries, scientists embarked on an exploration of atomic structure. J. J. Thomson's discovery of the electron and Ernest Rutherford's

revelation of the dense, positively charged nucleus at the atom's core were pivotal breakthroughs. These discoveries led to the formulation of sophisticated theories concerning electron orbital dynamics and the forces within the nucleus. Before these discoveries, the prevailing model of the atom was Thomson's plum pudding model, which depicted the atom as a positively charged "pudding" with embedded electrons. However, these discoveries introduced a new perspective on atomic structure, challenging traditional notions of matter.

Louis de Broglie's wave-particle duality concept and Werner Heisenberg's uncertainty principle played a crucial role in shaping the foundations of quantum mechanics. The emergence of quantum mechanics stemmed from the realisation that accurate descriptions of particle behaviour required a departure from classical physics. Quantum mechanics introduced a probabilistic interpretation of particle behaviour, blurring the distinction between particles and waves. Erwin Schrodinger's development of wave functions, became central to understanding particle behaviour, representing the probabilities of finding particles in specific states.

Scientists developed the Standard Model (SM) to unify fundamental forces and particles, achieving unprecedented precision and agreement with experiments. According to this model, cosmic matter consists of fermions (matter particles) and bosons (force carriers), with interactions governed by three fundamental forces: electromagnetic, weak, and strong. However, the SM lacks a comprehensive explanation, especially regarding gravity at the quantum level. Observations of galaxy rotations suggest the existence of Dark Matter, likely composed of yet-to-be-discovered particles.

The SM faces theoretical challenges, such as the gauge hierarchy problem associated with divergent terms in the Higgs boson theory. To tackle this issue, an extension of the SM has been proposed. This extension introduces a theoretical framework that predicts additional particles, including vector-like quarks with distinctive experimental signatures. These particles are potentially producible in high-energy particle collisions. Exploring the cosmos involves a variety of methods, including cosmological observations, nuclear experiments, and particle collisions. Ongoing efforts in advancements of accelerator and detector technologies are directed toward deepening our understanding of the SM and facilitating groundbreaking discoveries. Crucially, technologies developed through particle physics research play vital roles in improving healthcare, advancing technology, and driving innovation.

Technological advancements in research progressed with each iteration, yet expenses also escalated. Collaboration became crucial for funding large-scale experiments. Following World War-II (WW-II), the United States (US) experienced economic prosperity and assumed a leadership role in global scientific research. Meanwhile, war-torn Europe grappled with reconstruction challenges, underscoring the necessity for collaboration. As a result, in 1954, twelve European countries, including former adversaries, founded the CERN, marking a pivotal moment in international scientific cooperation.

In the late twentieth century, CERN and the US engaged in a competitive race to construct larger particle accelerators, leading to the development of technologies such as CERN's Super Proton Synchrotron (SPS) and the Tevatron in the US. Escalating costs prompted the US to terminate the construction of the proposed Superconducting Super Collider in the 1990s, effectively ending the competition. As a result, the LHC at CERN became the primary major particle collider. This shift in focus prompted the formation of a global partnership, leading to the renaming of CERN as the European Organisation for Nuclear Research, reflecting its role as a collaborative international scientific institution. Today, CERN exemplifies unparalleled international collaboration aimed at advancing our comprehension of the universe and associated technologies.

Scientific progress often involves incremental advances or pushing the boundaries of established technologies. Occasionally, groundbreaking solutions are necessary to create something truly unique and significantly improve performance. A notable example of such innovation is exemplified by Georges Charpak's contributions. In 1992, he was awarded the Nobel Prize in Physics for his work on particle detectors, including the Multi-Wire Proportional Chamber (MWPC) he invented in 1968. This invention transformed particle physics by offering superior spatial resolution and high trigger rates, overcoming the limitations of earlier bubble chambers. While silicon detectors are now faster, gas chambers based on Charpak's innovation maintain an additional advantage: high-rate capability. The four primary experiments at the LHC, the world's most powerful particle accelerator, integrate chambers inspired by Charpak's work. Without these advancements, much of the LHC program's implementation today would be nearly impossible.

Similarly, the Resistive Plate Chamber (RPC) was a groundbreaking invention pioneered by Italian physicist R. Santonico and Italian engineer G. P. P. Grillo in 1981. Initially intended for HEP experiments, RPCs have evolved into indispensable tools in particle physics research. Their fast response time, excellent timing resolution, and

ability to operate in high-rate environments make RPCs invaluable for a wide range of experiments.

While silicon detectors are now faster, gas chambers, based on Charpak's innovation, offer an additional advantage of high-rate capability. The four main experiments at the LHC, incorporate chambers inspired by Charpak's work. Without these advancements, implementing much of the LHC program today would be nearly impossible.

Fabio Sauli's GEM was invented in 1997 at CERN and is used to amplify electrons from gas when charged particles pass through. It consists of a thin metal-clad polymer foil with regularly spaced holes, acting as a proportional amplifier. Applying a potential difference between electrodes causes electrons generated by radiation to multiply and transfer, resulting in signal amplification. The GEM can operate independently or as a pre-amplifier, providing high gains even in environments with high radiation levels.

Key features of the GEM include compatibility with various gases, gains exceeding 10^5, 18% Full Width Half Maximum (FWHM) energy resolution at 5.9 keV, spatial resolution of 60 μm Root Mean Square (RMS) or greater, rate capability exceeding 10^5 counts/mm^2/s, active areas up to 1000 cm^2, a flexible shape, and versatile readout patterns.

In 2018, the LHC concluded a three-year data-collection cycle and underwent a three years of upgrades known as Long Shutdown 2 (LS2). The upgrades implemented during LS2 mark the initial phase of preparations for the HL-LHC phase. These upgrades, including the addition of a new layer of GEM detectors to the muon system at CMS, are pivotal for managing increased data rates and improving the efficiency of particle detection. With these improvements, the LHC is poised to achieve unprecedented levels of performance, paving the way for groundbreaking discoveries in particle physics.

Thesis Blueprint

This thesis can be viewed as a compilation of discussions centred on four main topics: the upgrade of the CMS muon system by integrating GEM detectors, estimating the background radiation hit-rate in GE1/1 region, the impact of electrode segmentation within GEM foils on detector performance, and the application of GEM detectors in

medical imaging. The following explanation will detail the organisational structure of the thesis.

Chapter 1 provides a brief description of SM and introduces five categories of physically manifested bosons and twelve types of fermions within the resultant SM. Additionally, it addresses certain limitations of the SM, including the gauge hierarchy problem, prompting discussions on theories Beyond Standard Model (BSM). After that, we will emphasise the importance of exploring BSM physics phenomena to validate theories that offer a comprehensive understanding of our universe.

Chapter 2 explores the operations of the LHC at CERN, where high-energy p-p collisions provide valuable insights into the fundamental components and mechanisms of the universe. This chapter discusses the LHC upgrade plan, crucial for exploring BSM physics. Subsequently, it offers a comprehensive overview of the CMS experiment in its second section. After providing a general presentation of the CMS upgrades, our focus will turn to the forward region of the CMS muon end-caps. We will illustrate how this area can be enhanced through the introduction of innovative detection technology.

Chapter 3 introduces the concept of a gaseous detector, the preferred choice for the CMS muon system. The first section focuses on particle interactions with matter, particularly within gaseous media, examining processes relevant to the CMS environment. It then offers a broad review of gaseous detector functioning, evolution since the early twentieth century, and contemporary applications. The chapter concludes with an exploration of GEM-based detector upgrades, the chosen technology for the CMS muon end-cap upgrade.

Chapter 4 outlines the GEM plan for upgrading the initial station of the CMS muon end-caps, with a specific emphasis on the GE1/1 project. It addresses the technical complexities of the large GEM-based detectors designed for CMS, detailing their characteristics and the requisite measures to guarantee their effective operation in the end-cap environment while adhering to CMS standards. Additionally, this chapter presents and discusses the GEM detector assembly and Quality Control (QC) procedures and results conducted at Panjab University.

Chapter 5 focuses on estimation of background flux in the region of GE1/1 and assessing the sensitivity of the GE1/1 gaseous detector to background particles, including neutrons, photons, electrons, and positrons. It utilises FLUKA simulation package for flux estimation and GEANT simulation package as the primary tool for

constructing the shape and components of detectors for the simulation. The results from the simulation are validated using the data from the literature.

Chapter 6 addresses the proposed ME0 GEM upgrade, a scheduled upgrade in the muon very-forward end-cap during Phase-II. The chapter offers a brief introduction to the station, explores technical solutions, and details prototypes for the ME0 station. The primary focus lies in ANSYS + Garfield studies, comparing conventional and newly proposed GEM foil electrode segmentation methods developed for the ME0 detector.

Chapter 7 looks into the potential applications of GEM detectors in Medical Imaging. The study, based on GEANT simulations, introduces a new method for polarisation-based event selection in PET. Unlike traditional methods relying on energy deposit and coincidence time details, this innovative approach incorporates Quantum Entanglement. It specifically investigates the unique connection between two photons formed during para-positronium decay, supplementing the conventional criteria. The study aims to evaluate how quantum entanglement might influence traditional imaging methods.

In the concluding chapter, we will provide a comprehensive summary of this thesis, encapsulating the key findings from the detailed studies conducted. Specifically, we will conclude the outcomes of the GEM assembly and QC procedures implemented for the GE1/1 detectors at Panjab University. Subsequently, a detailed summary of the GEM sensitivity study will be presented, emphasising its relevance to the background study in Run-2 and its confirmation for the Run-3 background study. Additionally, the chapter will elaborate on the results of the ME0 GEM foil electrode segmentation study and discuss its prospective contributions to various GEM projects in the near future. Finally, a thorough evaluation will be undertaken to confirm the suitability of GEM detectors for medical applications.

Chapter 1

The Standard Model Physics

"It is through science that we prove, but through intuition that we discover."
— J C Bose, 1858–1937

1.1 Introduction

In this chapter, we will provide an overview of fundamental particles and their interactions described by the SM. Following this, we will address significant limitations within the SM and discuss why it is important to explore new physics Beyond Standard Model (BSM). The discussion will highlight the importance of muon detection in the pursuit of physics discoveries, we advocate for the integration of improved muon systems in HEP experiments. This advocacy is substantiated through various instances, including applications in Higgs physics and non-standard phenomena.

1.2 The SM of Particle Physics

The goal of particle physics research is to discover the fundamental building blocks of matter, understand their characteristics, and disentangle their interactions across a broad spectrum, ranging from nuclear processes within stars to fundamental electron behaviours. The SM [1] is a successful framework that provides a clear understanding and makes sense of our current knowledge about particles.

Experimental research of many years, have led to the identification of natural symmetries in the universe, forming the basis for constructing physics models by incorporating these observed symmetries. To create these models, scientists use mathematical tools and different groups of measurements called gauge groups. Certain symmetries are exclusive to high-energy environments and exhibit distinct manifestations at lower energy levels, are referred to as "broken" symmetries. The SM is a theoretical framework in contemporary particle physics, based on the gauge invariance principle within the context of Quantum Field Theory (QFT) [2]. The SM incorporates both broken and unbroken symmetries [3] and is defined by the gauge group $SU(3)_C \otimes SU(2)_L \otimes U(1)_Y$[1]. A comprehensive understanding of particle physics and SM necessitates a profound comprehension of essential groups and concepts, as underscored in [4].

The theory that explains strong interactions, called Quantum Chromo-Dynamics (QCD) [5], is defined by an unbroken symmetry denoted as $SU(3)_C$. This symmetry represents the interactions among coloured quarks and gluons, which make up the strong force. The SU(3) theory precisely details how quarks interact and combine to create particles called hadrons, introducing three distinct "colour" charges to describe these interactions.

The combination $SU(2)_L \otimes U(1)_Y$ explains the Electro-Weak (EW) interaction in particle physics, where "L" represents weak isospin and "Y" represents hypercharge [6–8]. In contrast to QCD, this combination has a broken symmetry, which is integral to the SM. This broken symmetry is at the heart of the SM, explaining the EW force at high-energy levels and splitting into two distinct forces at lower energy levels that we experience in present universe. Infact, this theory breaks in a precise manner, accounting for all observed EW phenomena to date [9].

This thesis would not go into the detailed development of the SM because it is mainly focused on experiments. However, for a more comprehensive understanding and in-depth information, may be found at [1]. Many experiments, like CERN's Large Electron-Positron (LEP) Collider, Fermilab's Tevatron, Deutsches Elektronen-SYnchrotron (DESY), Hadron-Electron Ring Accelerator (HERA), and the more recent LHC at CERN, have confirmed the SM predictions with high accuracy. However, it's important to note that the SM doesn't fully explain certain experimental findings mentioned in Section 1.2.3.

[1] SU stands for Special Unitary group matrices and U stands for Unitary group matrices

1.2.1 Elementary Particles of Matter

In the SM, elementary particles are described as excitations of quantum fields. The theory categorises particles into two types: fermions and bosons as presented in Figure 1.1. The key difference lies in their spin-fermions have half-integer spin and govern by the Fermi-Dirac statistics, whereas bosons have integer spin and follows the Bose-Einstein statistics [10].

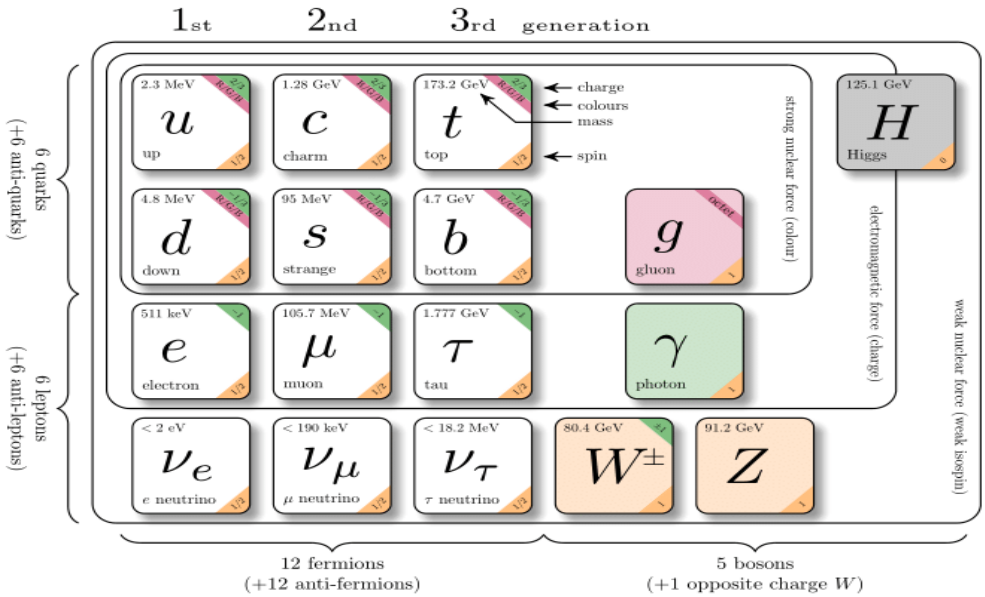

Figure 1.1: The SM particles, showcasing fermions and bosons [11].

1.2.1.1 Fermions

Fermions can be divided into two types based on their interactions or charges: quarks and leptons. Both types are involved in weak interactions, with a weak isospin (T_3) = $\pm$ 1/2, and only quarks are affected by the strong interaction. Quarks have a fractional electric charge (Q) equal to 2/3 or 1/3, as well as a colour charge. The latter is associated with the strong force and is represented by the colours red, green, and blue. Table 1.1 provides a summary of the fundamental fermions.

Quarks come in six types, called flavors, and they're grouped into three generations. The first generation has up (u) and down (d) quarks. The up quark has Q = +2/3 and $T_3 = +1/2$, while the down quark has Q = $-1/3$, $T_3 = -1/2$, and a different

Table 1.1: Table of the various quarks and leptons of the SM divided into families with their mass and electric charge according to the PDG [12]. The errors in the electron and muon masses are less than 10^{-10} and 10^{6} MeV, respectively. The anti-matter states are not depicted.

Generation	Name	Symbol	Charge	Mass [1/c^2]
		Quarks		
1st	Up	u	+2/3	$2.2^{+0.5}_{-0.3}$ MeV
	Down	d	-1/3	$4.7^{+0.5}_{-0.2}$ MeV
2nd	Charm	c	+2/3	$1.27^{+0.02}_{-0.02}$ GeV
	Strange	s	-1/3	$93.4^{+8.6}_{-3.4}$ MeV
3rd	Top	t	+2/3	$172.69^{+0.30}_{-0.30}$ GeV
	Bottom	b	-1/3	$4.18^{+0.03}_{-0.02}$ GeV
		Leptons		
1st	Electron	e^-	-1	0.511 MeV
	Electron neutrino	ν_e	0	$\leq$ 1.1 eV [90% CL]
2nd	Muon	μ^-	-1	0.106 GeV
	Muon neutrino	ν_μ	0	$\leq$ 0.19 MeV [90% CL]
3rd	Tau	τ^-	-1	$1776.86^{+0.12}_{-0.12}$ MeV
	Tau neutrino	ν_τ	0	$\leq$ 18.2 MeV [95% CL]

mass. The next two generations are identical copies of the first generation, each containing an up-type and a down-type quark. The second generation includes charm (c) and strange (s) quarks, and the third generation comprises top (t) and bottom (b) quarks. It's important to note that each of the six quark flavors has corresponding anti-matter states with the same mass but opposite quantum numbers. For instance, a red anti-up-type quark has Q $= -2/3$, $T_3 = -1/2$, and carries anti-red colour.

Leptons are also classified into six different types, grouped into three generations: electron (e), muon (μ), and tau (τ), each getting heavier in that order. In each generation, there's a lepton with Q = -1 and $T_3 = +1/2$, named after its generation. Also, in each generation, there's a neutral lepton called the neutrino (ν), which doesn't have an electric charge and has $T_3 = -1/2$. Initially, scientists believed that neutrinos were massless within the framework of the SM. However, experimental observations from neutrino oscillations present compelling evidence that these elusive particles indeed possess a minuscule, albeit non-zero, amount of mass.

The stable matter in the SM universe is composed of the heavier particles among the first types of quarks and leptons. The heavier versions of quarks and leptons undergo decay processes, transforming into lighter counterparts through their interactions. While free leptons can be observed independently, quarks, such as those found in neutrons and protons, exist only in collective formations known as hadrons. This phenomenon is attributed to a strong interaction property called confinement [13]. These observable groups of quarks are either colourless and consist of three quarks with a half-integer spin, referred to as baryons or are made up of two quarks with an integer spin referred to as mesons.

1.2.1.2 Bosons

Bosons are particles characterised by integer spins. In bosonic systems, the spin-1 gauge fields serve as carriers for forces. The photon (γ) is a massless particle having no electric charge, serving as the mediator of the Electro-Magnetic (EM) force. In contrast, the W^+, W^-, and Z bosons possess substantial mass. The Z boson is electrically neutral, while the $W^\pm$ bosons have electric charges $Q = \pm 1$ respectively. Gluons (g_i) lack mass and electric charge, playing a pivotal role in conveying the strong force and influencing quark interactions. Comprising eight distinct types, each gluon facilitates a unique manner in which quarks can exchange colour.

The Higgs boson, a particle with no electric charge and spin-0 or scalar, is part of the SM. The Higgs field imparts mass to all SM particles through the Higgs mechanism [14], as demonstrated by the Higgs mechanism generating mass terms for the $W^\pm$ and Z bosons due to spontaneous symmetry breaking in the EW sector [15–17]. A detailed list of the SM bosons can be found in Table 1.2.

1.2.2 Elementary Interactions

The SM introduces quantum particles called gauge bosons, each with a spin-1, to explain how fundamental forces work. These particles play a key role in different interactions: EM interactions (mediated by γ), strong interactions (mediated by eight gluons (g_i), and weak interactions (mediated by $W^\pm$ and Z). The strength of these interactions is measured using coupling constants shown in Table 1.2.

Table 1.2: The three interactions represented by the SM and their accompanying gauge bosons [1, 12]. The strength is relative to the strong interaction.

Interaction	Influenced Particles	Relative Strength	Gauge Bosons	Charge	Mass [1/c^2]
Strong	Quarks, Gluons	1	gluons g_i	0	0
EM	Charged Particles	1/137	photons γ	0	0
Weak	Quarks, Leptons	$10^{-5} - 10^{-7}$	$W^{\pm}$	± 1	$80.377^{+0.012}_{-0.012}$ GeV
			Z	0	$91.188^{+0.0021}_{-0.0021}$ GeV

- **Strong Interactions**: The strong interaction exclusively influences quarks and gluons, with eight gluons serving as carriers of this force, capable of interacting among themselves. The QCD model provides a precise description of the strong interaction processes. Because of the confinement principle [13], only colour-neutral particles called hadrons exist freely in nature. At the same time, quarks always stick together, forming baryons like protons and neutrons. They also combine in bound states like mesons, which consist of quark and anti-quark pairs, or anti-baryons, formed from three anti-quarks [1].

- **EM Interactions**: All charged particles, encountered in various contexts, experience the EM force. Maxwell's equations, originating from classical physics, provided an initial framework for understanding of the Electromagnetism. However, it was Richard Feynman who later improved and explained these interactions within the Quantum Electro-Dynamics (QED) theory [18], bridging the gap between classical and quantum perspectives. The EM interaction plays a pivotal role in particle detection through gaseous detectors. This technique allows scientists to identify and study particles with greater precision, illustrating the seamless connection between theoretical foundations and practical applications in the realm of EM interactions.

- **Weak Interactions**: The weak force interacts with all fundamental particles, allowing heavier fermions to decay into lighter fermions. Scientists Glashow, Salam, and Weinberg developed the EW theory, which brings together two forces, EM and weak. This theory predicted the existence of specific gauge bosons

known as $W^{\pm}$ and Z. These particles were confirmed through experiments at CERN in 1983 [19]. In simpler terms, the EW theory helps us understand how particles transform, and experimental evidence supports its predictions.

Gravitation, the fourth elementary interaction, is a not included in the SM, highlighting a primary limitation in the model. The SM currently lacks a quantum description of gravitational interactions, presenting a key challenge in theoretical physics. Integrating gravity into the model is a crucial area of ongoing research for a more comprehensive understanding of fundamental forces.

1.2.3 Limitations of SM

In recent decades, the SM has been measured precisely across a wide energy range. However, various aspects indicate that the SM is not the ultimate theory but a specific instance or approximation of a more extensive unified theory. These factors include, but are not restricted to, the presence of Dark Matter, the challenge of integrating gravity into the framework, the hierarchy problem linked to the mass of the Higgs boson, and the lack of a clear candidate for dark energy.

- **Energy Scale Divergence**: The SM does not provide any explanation for the significant disparity in the coupling constants of elementary forces or why these constants fail to converge at higher energies. This discrepancy raises questions about the fundamental nature of these forces and hints at the existence of physics beyond the scope of the SM.
- **Gravity**: The SM does not incorporate the fourth basic force known as gravity. Gravity is the force that pulls things with mass towards each other, like what keeps us on the ground. The SM mainly deals with other forces that act on fundamental particles at the most basic level.
- **Dark Matter**: Cosmic studies reveal that only 4.9% of the Universe is made up of visible matter [20]. The term "Dark Matter" was coined following the emergence of the concept of an imbalance in 1933, when astronomers observed a significant anomaly [21]. Dark matter's gravity helps explain why galaxies spin faster than expected and why light from objects behind it bends. On the flip side, dark energy makes up about 70% of the Universe and is connected to the empty space between objects. Its widespread existence everywhere creates an expulsive force,

speeding up the Universe's expansion. This means that the SM can only account for a small portion of the entire cosmic picture.

- **Neutrino Oscillations**: In the SM, neutrinos were thought to have no mass and no charge. Yet, recent experiments [22] on neutrino oscillation, where neutrinos transform from one type to another, revealed that they do have a non-zero mass difference.

- **Matter-Antimatter Asymmetry**: The SM suggests the existence of antimatter, but in our observable universe, antimatter is not widely observed. The difference between what the SM predicts and what we observe, with matter being more common than antimatter, is called matter-antimatter asymmetry [23].

- **Gauge Hierarchy Problem**: While the SM successfully aligns with experimental observations, the theoretical foundation for the specific choice of SM gauge groups and the existence of three generations of fermions remains unclear. Moreover, the SM is characterised by 19 free parameters, including fermion masses and interaction coupling constants, which are determined solely through experimental measurements, but these parameters could potentially increase to 62, offering a detailed specification of the model [24]. The challenge lies in the inability to predict these parameters within the SM.

  Additionally, higher-order corrections to these parameters are infinite and require the process of renormalization. The Higgs potential's structure is more complex than the SM suggests. To tackle issues like quadratic divergences in the renormalized μ^2 parameter, the introduction of new particles with masses around several TeV is expected. This challenge is termed the "gauge hierarchy problem" and often motivates the exploration of new physics [25].

1.3 BSM Physics

Given the constraints discussed earlier, it is considered that an additional theory, unifying the SM while addressing its limitations, needs to be formulated and proved through experimental verification. We, briefly discuss some of the auspicious alternatives in this section.

1.3.1 GUT

Grand Unified Theory (GUT)s propose combining EW and strong interactions, similar to how the SM unifies EM and weak interactions. Originated by Howard Georgi and Sheldon Glashow, GUTs rely on a simple group, like SU(5), SO(10)[2], or E_6[3]. Two vital conditions must be met for GUTs to work: the proposed unified group should include the SM group as a subgroup, ensuring the inclusion of EM, weak, and strong interactions. Secondly, the unified group must exhibit complex representations replicating the chiral structure in the SM. These conditions are crucial for GUTs to provide a comprehensive explanation of fundamental particle interactions [26].

1.3.1.1 SU(5) Model

The gauge group SU(5), proposed in particle physics [27, 28], is the smallest group that effectively encompasses all particles in the SM. According to this theory, SU(5) begins as a unified group and then, at an exceptionally high-energy scale known as the grand unification scale (10^{16} GeV), it spontaneously undergoes a breakdown into the familiar SM subgroup. SU(5) is composed of 24 traceless, Hermitian matrices with dimensions $(n^2 - 1)$, where n is the order of the gauge matrix. It constitutes a group of unitary 5×5 - dimensional matrices with a unit determinant. In the context of GUTs, analogous to the Higgs field, when a scalar field acquires a Vacuum Expectation Value (VEV), it results in the spontaneous breaking of symmetry within SU(5).

$$SU(5) \mapsto SU(3) \otimes SU(2) \otimes U(1) \tag{1.1}$$

The 24 symmetry generators within SU(5) break down into the $8 \oplus 3 \oplus 1$ generators of the SM. This results in 12 new massive gauge bosons interacting with quarks and leptons in a manner similar to familiar particles in SM. These newly introduced bosons play a role in various novel interactions, including their involvement in proton decay.

1.3.1.2 E_6 Model

The E_6 gauge group is a prominent unification group that encompasses the SM as a subgroup [29, 30]. It transitions from spontaneous symmetry to either $SO(10) \otimes U(1)$ or

[2] SO(10) represents the Special Orthogonal group in 10 dimensions.
[3] E_6 represents the Exceptional Lie group of rank 6

$SU(3)_C \otimes SU(3)_L \otimes SU(3)_R$. Each fermion family is represented by a 27-dimensional set, containing SM fermions and exotic fields denoted as $27 \sim \bar{5} \oplus 10 \oplus 1 \oplus \bar{5} \oplus 5 \oplus 1$.

The E_6 breaking at a higher scale is expressed as:

$$E_6 \mapsto SU(5) \otimes U(1) \otimes U(1) \tag{1.2}$$

The associated particles with the U(1) include new, heavy gauge bosons, gaining mass through additional Higgs fields and potentially pairing with SM matter fields.

1.3.2 The Minimal Supersymmetric Standard Model

To address the limitations of the SM, achieve the unification of coupling constants, and incorporate potential dark matter candidates, SUSY introduces a new gauge invariance that connects bosons and fermions. Consequently, each SM particle has a corresponding Ş partner with identical quantum numbers, differing only in spin by 1/2. This allows us to associate SUSY bosons, referred to as "sfermions" with SM fermions. For instance, the superpartner of the top quark is known as the "stop" ($\tilde{t}$). Conversely, SUSY fermions are associated with SM bosons and are termed "bosinos". Table 1.3 provides an overview of the new particles introduced by the SUSY model.

Table 1.3: SUSY particles and their equivalent SM particles [31]

SM Particle	SUSY Particle	Physical State
lepton	slepton	$\tilde{e}, \tilde{\mu}, \tilde{\tau}$
quarks	squarks	$\tilde{u}, \tilde{d}, \tilde{c}, \tilde{s}, \tilde{t}, \tilde{b}$
gluons	gluinos	$\tilde{g}$
boson $W^{\pm}$	winos	Mix into charginos $\tilde{\chi}^{\pm}_{1,2}$
boson $h^{\pm}$	charged Higgsinos	
boson Z	zino	Mix into neutralinos $\tilde{\chi}^{0}_{1,2,3,4}$
boson γ	photino	
boson h^0	neutral Higgsinos	

The Minimal Supersymmetric Standard Model (MSSM) stands out for having the fewest independent parameters compared to other extensions of the SM. This model

anticipates an expanded Higgs sector featuring five new bosons: the lightest Higgs (h_0), identical to the SM Higgs, two neutral heavy Higgs bosons (H and A), and two charged Higgs bosons ($H^{\pm}$). Crucial parameters in the MSSM include the mass of the pseudo-scalar A (denoted as m_A) and the parameter $\tan\beta$, derived from the ratio of the VEVs of the Higgs fields ($\tan\beta = v_u/v_d$). The MSSM's credibility relies on discovering projected particles: sfermions, bosinos, and the heavy Higgs, accompanied by accurate measurements of its independent parameters.

The SUSY particles may manifest during collider experiments, undergoing decay into a series of SM particles and the LSPs in the final state. LSPs exhibit weak interactions with matter and may escape the detection system without emitting any signal, necessitating the incorporation of considerations for missing energy in the identification of SUSY particles. Despite the fact that no evidence of SUSY particles has yet been discovered, ongoing research on the formation of gluino pairs and the search for dark matter candidates at the LHC has imposed limitations on the mass of SUSY particles [32].

1.4 Search for New Physics

The validation of theoretical physics models designed to address the missing pieces of the SM involves more than just Higgs physics. It encompasses identifying unconventional decay modes and observing new particles in order to comprehensively refine our understanding of fundamental physical phenomena.

1.4.1 Search for SUSY Particles

SUSY-based theories postulate the existence of supersymmetric analogues to particles in the SM, anticipated to be detectable at the LHC within the TeV mass range. There are different theories within the idea of SUSY, each with various possibilities. The emergence of gluinos, third-generation squarks, and chargino-neutralinos stands out as significant deviations from conventional expectations. These phenomena are particularly prominent within the framework of the next-to-leading order of the SUSY QCD model, as discussed in [33]. The production cross-section of SUSY particles, plotted as a function of mass, is depicted in Figure 1.2. Then, one can find numerous decay processes are under investigation at the LHC, as detailed in the reference [34].

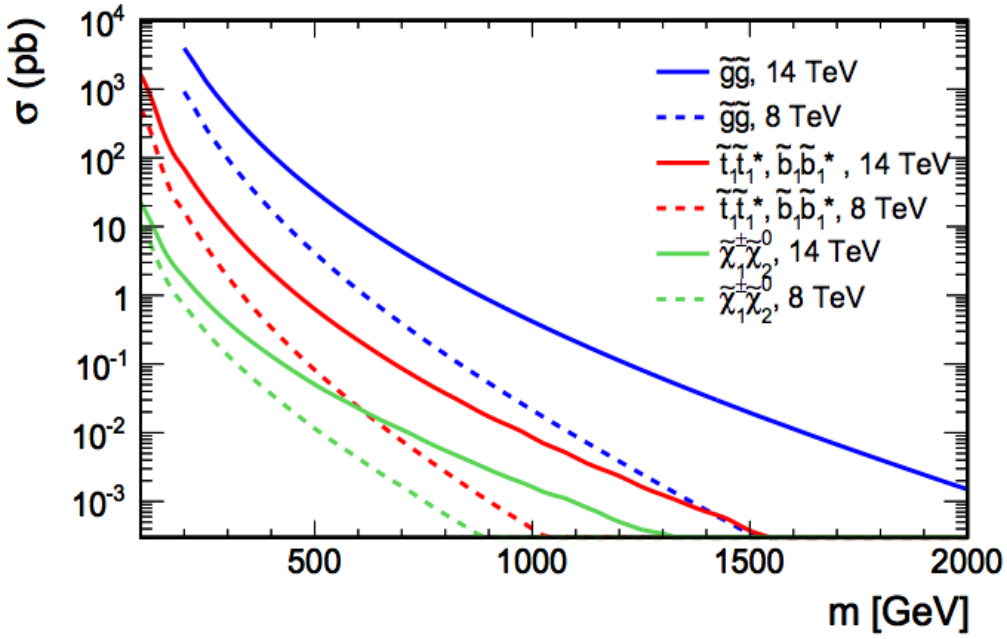

Figure 1.2: Next-to-leading order production cross-section as a function of the mass of the SUSY pair particles [34].

This thesis focuses on the GEM detector upgrade in the muon endcap of the CMS experiment. Consequently, we will specifically address certain decays leading to a final state involving a lepton. The GEM upgrade is expected to enhance muon reconstruction, thereby increasing the likelihood of detecting these decays. The primary decay modes of superpartners generated by coloured SUSY particles, along with their signatures at the detector level, are outlined in Table 1.4.

- **Gluino Pair Production and Decay** $\tilde{g} \rightarrow t\bar{t}\tilde{\chi}_1^0$: The process involves the splitting of a pair of gluinos into four top quarks. These top quarks subsequently undergo decay, producing W bosons that leave behind a distinct signature involving leptons and have a high branching ratio. The detection of the LSP, denoted as SUSY particle $\tilde{\chi}_1^0$, is identified by measuring the the missing energy. Figure 1.3 illustrates the Feynman diagram representing this process.
- **Stop Squark Production and Decay** $\tilde{t} \rightarrow t\tilde{\chi}_1^0$ and $\tilde{t} \rightarrow b\tilde{\chi}^+$: The decay process of stop squarks involves their transformation into top quarks paired with neutralinos or bottom quarks coupled with charginos. The chargino ($\tilde{\chi}^+$) is an unstable particle, and its decay yields neutralinos and a W boson. Enhancing the search for leptons in the final state proves advantageous for detecting these SUSY scenarios,

Table 1.4: Production of superparticles and their main decay modes

Production	Main Decay Mode	Signature
$\tilde{g}\tilde{g}, \tilde{q}\tilde{q}, \tilde{g}\tilde{q}$	$\left.\begin{array}{l}\tilde{g} \to q\bar{q}\tilde{\chi}_1^0 \\ \quad q\bar{q}'\tilde{\chi}_1^\pm \\ \quad g\tilde{\chi}_1^0\end{array}\right\} m_{\tilde{q}} > m_{\tilde{g}}$	$\not{E}_T$ + Multijets (+ leptons)
	$\left.\begin{array}{l}\tilde{q} \to q\tilde{\chi}_i^0 \\ \tilde{q} \to q'\tilde{\chi}_i^\pm\end{array}\right\} m_{\tilde{g}} > m_{\tilde{q}}$	
$\tilde{\chi}_1^\pm\tilde{\chi}_2^0$	$\tilde{\chi}_1^\pm \to \tilde{\chi}_1^0 l^\pm \nu, \tilde{\chi}_{12}^0 \to \tilde{\chi}_1^0 ll$	Trilepton + $\not{E}_T$
	$\tilde{\chi}_1^\pm \to \tilde{\chi}_1^0 q\bar{q}', \tilde{\chi}_{12}^0 \to \tilde{\chi}_1^0 ll$	Dilepton + jet + $\not{E}_T$
$\tilde{\chi}_1^+\tilde{\chi}_1^-$	$\tilde{\chi}_1^+ \to l\tilde{\chi}_1^0 l^\pm \nu$	Dilepton + $\not{E}_T$
$\tilde{\chi}_i^0\tilde{\chi}_i^0$	$\tilde{\chi}_i^0 \to \tilde{\chi}_1^0 X, \tilde{\chi}_i^0 \to \tilde{\chi}_1^0 X'$	Dilepton + jet + $\not{E}_T$
	$\tilde{t}_1 \to c\tilde{\chi}_1^0$	Two noncollinear jets + $\not{E}_T$
$\tilde{t}_1\tilde{t}_1$	$\tilde{t}_1 \to b\tilde{\chi}_1^\pm, \tilde{\chi}_1^\pm \to \tilde{\chi}_1^0 q\bar{q}'$	Single lepton + $\not{E}_T$ + b's
	$\tilde{t}_1 \to b\tilde{\chi}_1^\pm, \tilde{\chi}_1^\pm \to \tilde{\chi}_1^0 l^\pm \nu$	Dilepton + $\not{E}_T$ + b's
$\tilde{l}\tilde{l}, \tilde{l}\tilde{\nu}, \tilde{\nu}\tilde{\nu}$	$\tilde{l}^\pm \to l^\pm \tilde{\chi}_i^0, \tilde{l}^\pm \to \nu_l \tilde{\chi}_i^\pm$	Dilepton + $\not{E}_T$
	$\tilde{\nu} \to \nu\tilde{\chi}_1^0$	Single lepton + $\not{E}_T$

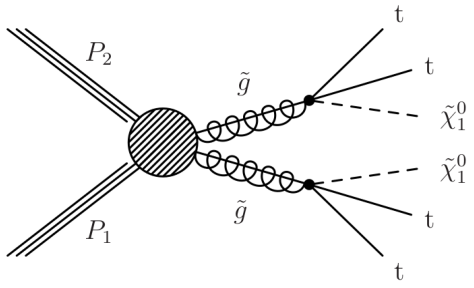

Figure 1.3: Feynman diagrams of the gluino pair production and decay into top quarks and neutralinos [34].

primarily due to the involvement of W bosons. Figure 1.4 represents the Feynman diagrams depicting the production of stop squarks and their subsequent decays into heavy quarks.

- **Sbottom Squark Production and Decay** $\tilde{b} \to tW\tilde{\chi}_1^0$: The decay of the sbottom squark results in the production of top quarks and charginos. These charginos subsequently undergo decay, leading to the formation of W bosons and neutrali-

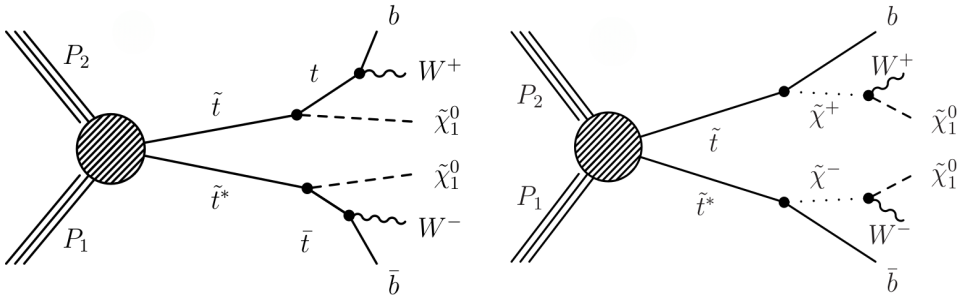

Figure 1.4: Feynman diagrams of the stop squark pair production and decay into neutralinos, heavy quarks and bosons W [35].

nos. Simultaneously, the top quark decays into W bosons and bottom quarks. Figure 1.5 (left) illustrates this process through an equivalent Feynman diagram.

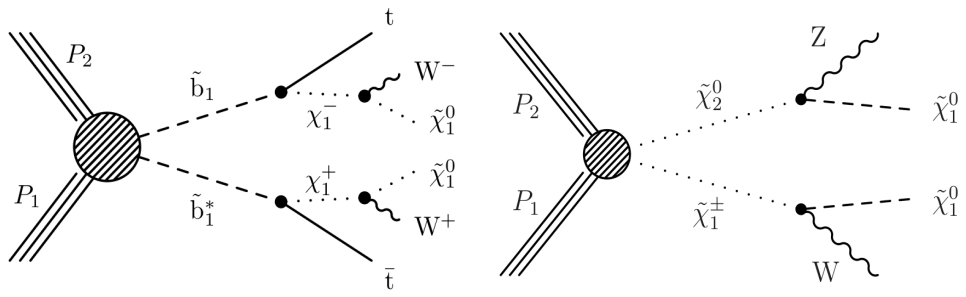

Figure 1.5: Left: Feynman diagram of the sbottom squark pair production and decay into top quarks and charginos [34]. Right: Feynman diagram of the chargino-neutralino pair production and decay into gauge bosons and lightest neutralinos [34].

- **Chargino-Neutralino Pair Production and Decay** $\tilde{\chi}_2^0 \rightarrow Z\tilde{\chi}_1^0$, $\tilde{\chi}_1^\pm \rightarrow W\tilde{\chi}_1^0$: The decay of chargino-neutralino pairs results in the creation of bosons Z and W along with the lightest neutralinos. The presence of numerous leptons in the final state from the decay of W and Z serves as a clear signature of the process, characterised by high branching ratios. Figure 1.5 (right) presents a Feynman representation of this phenomenon.
- **Chargino-Neutralino Pair Production and Higgs Decay** $\tilde{\chi}_2^0 \rightarrow H\tilde{\chi}_1^0$, $\tilde{\chi}_1^\pm \rightarrow W\tilde{\chi}_1^0$: The decay of chargino-neutralino pairs leads to the formation of a W boson, the lightest neutralinos, and a Higgs boson, resulting in a distinct multi-lepton end state. Figure 1.6 illustrates the relevant Feynman process.

As an illustration, Figure 1.7 presents a simplified SUSY spectrum showcasing SUSY partners that could be within reach of the LHC. In this scenario, the decay of heavy

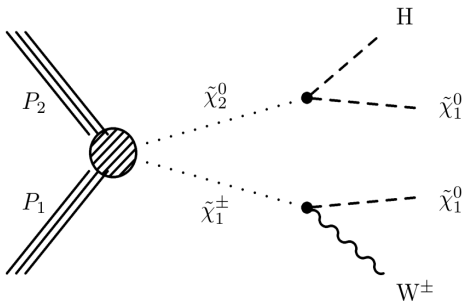

Figure 1.6: Feynman diagram of the chargino-neutralino pair production and decay into a Higgs boson, W boson and lightest neutralinos [34].

squarks and gluinos commonly gives rise to charginos and neutralinos. Charginos, in turn, undergo decay into gauge bosons, and their detection can be accomplished through leptonic decays. Particularly interesting final states involve muons, and distinguishing them from background contributions relies on accurately measuring their momentum.

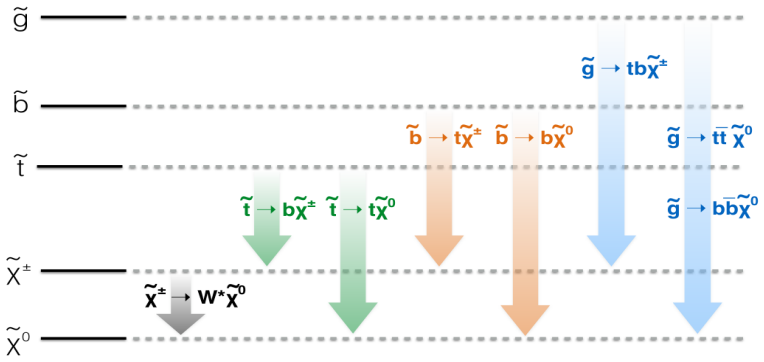

Figure 1.7: A simplified SUSY "natural" spectrum illustrating the SUSY partners and common decay modes accessible at the LHC. The neutralino $\tilde{\chi}^0$ is thought to be the LSP [36].

1.4.2 Search for Other Exotic New Particles and Processes

Several recent physics scenarios predict the existence of particular heavy "exotic" particles that can be explored at the LHC. The likelihood of detecting them is expected to increase with the upcoming upgrades of the LHC.

The Z′ bosons are heavier version of the familiar SM Z bosons. The mechanism of production suggests that this novel particle would specifically be neutral, colourless, and self-adjoint. There are several possible interpretations for this unique state [37].

One of the decay mechanisms suggests the particle decaying into a pair of charged leptons through a narrow resonance, denoted as $Z' \rightarrow ll$. The identification of this particle could significantly advance our understanding of mass mechanisms, quantum gravity, extra dimensions, and dark matter [38].

Similarly, certain theories predict the existence of heavy charged gauge bosons W', which, if present, could decay into an isolated lepton with a significant transverse momentum p_T[4] and a neutrino, resulting in missing transverse energy [39].

In the quest for searching unknown new particles, scientists are exploring dark matter candidates and heavy stable charged particles. The final configurations that involve leptons stand out significantly across various scenarios due to their high sensitivity, a good branching ratio, and a distinct signal-to-noise ratio [34].

The LHC will explore diverse BSM processes, especially with the increased energy in proton-proton (p-p) collisions. These investigations encompass multi-boson production, top quark physics, and the exploration of Vector-Like Quarks (VLQ). Specialised runs involving heavy ions at the LHC are dedicated to the examination of nuclear matter, with a specific emphasis on the Quark-Gluon Plasma (QGP) state [34]. The quest for new physics demands robust detection systems proficient in the efficient reconstruction of heavy quarks, missing energy, and leptons (electrons and muons).

1.5 Conclusion

The SM has proven quite effective in understanding the fundamental particles and their fundamental interactions over the last few decades. The recent discovery of a new boson, the SM Higgs boson, poses a significant challenge to the SM. Despite its successes, there are still some unanswered questions and experimental findings that don't quite fit into the SM framework. Scientists suggest that the SM might be a rough approximation of a more complete theory that unifies the four fundamental forces and thoroughly explains physical phenomena. One intriguing possibility is SUSY, which proposes the existence of partner particles for those in the SM and introduces five Higgs bosons. This theoretical framework holds promise for deepening our understanding of fundamental forces and particle interactions.

[4] a measure of particle momentum perpendicular to the beamline

In this chapter, we examined distinct decay modes exhibited by SUSY particles. Typically, completely hadronic decays show elevated branching ratios, but their investigation poses challenges due to background particle contamination from SM processes. Nonetheless, studies have shown that the inclusion of leptons in the final state acts as a unique indicator of interesting decay modes, especially in the presence of $W^{\pm}$, Z, or Higgs bosons. A good signal-to-noise ratio, coupled with exceptional resolution, offsets the commonly observed low branching percentage in lepton decay. Muons possess the advantage of being less impacted by radiation losses compared to electrons, which can degrade the detection resolution. Consequently, advancements in physics discoveries necessitate the development of effective muon detection systems that integrate efficient muon reconstruction with excellent muon momentum resolution.

Bibliography

[1] F. Halzen and Alan D. Martin. *Quarks and Leptons: An introductory course in modern particle physics*. 1984. ISBN: 978-0-471-88741-6.

[2] Matthew D. Schwartz. *Quantum Field Theory and the Standard Model*. Cambridge University Press, Mar. 2014. ISBN: 978-1-107-03473-0, 978-1-107-03473-0.

[3] Paul Langacker. *The standard model and beyond*. Vol. 150. CRC Press, Dec. 2009. DOI: 10.1201/B22175.

[4] Nadir Jeevanjee. *An introduction to tensors and group theory for physicists; 1st ed.* New York, NY: Birkhäuser, 2011. DOI: 10.1007/978-0-8176-4715-5. URL: https://cds.cern.ch/record/1494077.

[5] H. Fritzsch, Murray Gell-Mann, and H. Leutwyler. "Advantages of the Color Octet Gluon Picture". In: *Phys. Lett. B* 47 (1973), pp. 365–368. DOI: 10.1016/0370-2693(73)90625-4.

[6] Steven Weinberg. "A Model of Leptons". In: *Phys. Rev. Lett.* 19 (1967), pp. 1264–1266. DOI: 10.1103/PhysRevLett.19.1264.

[7] S. L. Glashow. "Partial Symmetries of Weak Interactions". In: *Nucl. Phys.* 22 (1961), pp. 579–588. DOI: 10.1016/0029-5582(61)90469-2.

[8] Abdus Salam. "Weak and Electromagnetic Interactions". In: *Conf. Proc. C* 680519 (1968), pp. 367–377. DOI: 10.1142/9789812795915_0034.

[9] David Griffiths. *Introduction to elementary particles*. 2008. ISBN: 978-3-527-40601-2.

[10] W. Pauli. "The Connection Between Spin and Statistics". In: *Phys. Rev.* 58 (1940), pp. 716–722. DOI: 10.1103/PhysRev.58.716.

[11] Shane Davy Breeze. "Precision measurement of the Z invisible width with the CMS experiment". Presented 13 Dec 2019. PhD thesis. Imperial Coll., London, 2019. URL: https://cds.cern.ch/record/2723370.

[12] Particle Data Group. "Review of Particle Physics, 2020-2021. RPP". In: *PTEP* 2020.8 (2020), p. 083C01. DOI: 10.1093/ptep/ptaa104. URL: https://cds.cern.ch/record/2729066.

[13] Walter Greiner, Stefan Schramm, and Eckart Stein. *Quantenchromodynamik*. 2007.

[14] Peter W. Higgs. "Broken Symmetries and the Masses of Gauge Bosons". In: *Phys. Rev. Lett.* 13 (16 Oct. 1964), pp. 508–509. DOI: 10.1103/PhysRevLett.13.508. URL: https://link.aps.org/doi/10.1103/PhysRevLett.13.508.

[15] F. Englert and R. Brout. "Broken Symmetry and the Mass of Gauge Vector Mesons". In: *Phys. Rev. Lett.* 13 (1964). Ed. by J. C. Taylor, pp. 321–323. DOI: 10.1103/PhysRevLett.13.321.

[16] Peter W. Higgs. "Broken Symmetries and the Masses of Gauge Bosons". In: *Phys. Rev. Lett.* 13 (1964). Ed. by J. C. Taylor, pp. 508–509. DOI: 10.1103/PhysRevLett.13.508.

[17] G. S. Guralnik, C. R. Hagen, and T. W. B. Kibble. "Global Conservation Laws and Massless Particles". In: *Phys. Rev. Lett.* 13 (1964). Ed. by J. C. Taylor, pp. 585–587. DOI: 10.1103/PhysRevLett.13.585.

[18] A. Rouge. *Introduction to subatomic physics*. Introduction a la physique subatomique. France: Ellipses edition marketing, 1997. ISBN: 2-7298-5713-3. URL: http://inis.iaea.org/search/search.aspx?orig_q=RN:29015997.

[19] P. M. Watkins. "DISCOVERY OF THE W AND Z BOSONS". In: *Contemp. Phys.* 27 (1986), pp. 291–324. DOI: 10.1080/00107518608211015.

[20] R. Adam et al. "Planck 2015 results. I. Overview of products and scientific results". In: *Astron. Astrophys.* 594 (2016), A1. DOI: 10.1051/0004-6361/201527101. arXiv: 1502.01582 [astro-ph.CO].

[21] F. Zwicky. "Die Rotverschiebung von extragalaktischen Nebeln". In: *Helv. Phys. Acta* 6 (1933), pp. 110–127. DOI: 10.1007/s10714-008-0707-4.

[22] K. Abe et al. "Precise Measurement of the Neutrino Mixing Parameter θ_{23} from Muon Neutrino Disappearance in an Off-Axis Beam". In: *Phys. Rev. Lett.* 112.18 (2014), p. 181801. DOI: 10.1103/PhysRevLett.112.181801. arXiv: 1403.1532 [hep-ex].

[23] Michael Dine and Alexander Kusenko. "The Origin of the matter - antimatter asymmetry". In: *Rev. Mod. Phys.* 76 (2003), p. 1. DOI: 10.1103/RevModPhys.76.1. arXiv: hep-ph/0303065.

[24] Michael E. Peskin. "On the Trail of the Higgs Boson". In: *Annalen Phys.* 528.1-2 (2016), pp. 20–34. DOI: 10.1002/andp.201500225. arXiv: 1506.08185 [hep-ph].

[25] Michael Dine. "Naturalness Under Stress". In: *Ann. Rev. Nucl. Part. Sci.* 65 (2015), pp. 43–62. DOI: 10.1146/annurev-nucl-102014-022053. arXiv: 1501.01035 [hep-ph].

[26] John C. Baez and John Huerta. "The Algebra of Grand Unified Theories". In: *Bull. Am. Math. Soc.* 47 (2010), pp. 483–552. DOI: 10.1090/S0273-0979-10-01294-2. arXiv: 0904.1556 [hep-th].

[27] G.G. Ross. *Grand Unified Theories*. Frontiers in physics. Westview Press, 1985. ISBN: 9780805379020. URL: https://books.google.co.in/books?id=iRpOPgAACAAJ.

[28] R. N. Mohapatra. *Unification and Supersymmetry. The Frontiers of Quark-Lepton Physics: The Frontiers of Quark-Lepton Physics*. Berlin: Springer, 1986. ISBN: 978-1-4757-1930-7, 978-1-4757-1928-4. DOI: 10.1007/978-1-4757-1928-4.

[29] F. Gursey, Pierre Ramond, and P. Sikivie. "A Universal Gauge Theory Model Based on E6". In: *Phys. Lett. B* 60 (1976), pp. 177–180. DOI: 10.1016/0370-2693(76)90417-2.

[30] David London and Jonathan L. Rosner. "Extra Gauge Bosons in E(6)". In: *Phys. Rev. D* 34 (1986), p. 1530. DOI: 10.1103/PhysRevD.34.1530.

[31] F Gianotti. "Collider physics: LHC". In: (2000). DOI: 10.5170/CERN-2000-007.219. URL: https://cds.cern.ch/record/458489.

[32] Aram Hayrapetyan et al. "Search for supersymmetry in final states with disappearing tracks in proton-proton collisions at $\sqrt{s}$ = 13 TeV". In: (Sept. 2023). arXiv: 2309.16823 [hep-ex].

[33] W. Beenakker et al. "Squark and gluino production at hadron colliders". In: *Nucl. Phys. B* 492 (1997), pp. 51–103. DOI: 10.1016/S0550-3213(97)80027-2. arXiv: hep-ph/9610490.

[34] "Projected Performance of an Upgraded CMS Detector at the LHC and HL-LHC: Contribution to the Snowmass Process". In: *Snowmass 2013: Snowmass on the Mississippi*. July 2013. arXiv: 1307.7135 [hep-ex].

[35] Serguei Chatrchyan et al. "Search for Top-Squark Pair Production in the Single-Lepton Final State in pp Collisions at $\sqrt{s}$ = 8 TeV". In: *Eur. Phys. J. C* 73.12 (2013), p. 2677. DOI: 10.1140/epjc/s10052-013-2677-2. arXiv: 1308.1586 [hep-ex].

[36] "Exclusion limits on gluino and top-squark pair production in natural SUSY scenarios with inclusive razor and exclusive single-lepton searches at 8 TeV." In: (2014).

[37] Thomas G. Rizzo. "Z' phenomenology and the LHC". In: *Theoretical Advanced Study Institute in Elementary Particle Physics: Exploring New Frontiers Using Colliders and Neutrinos*. Oct. 2006, pp. 537–575. arXiv: hep-ph/0610104.

[38] Vladlen Timciuc. "Search for High-Mass Resonances in the Dilepton Final State with the CMS Detector". In: *31st International Symposium on Physics In Collision*. Nov. 2011. arXiv: 1111.4528 [hep-ex].

[39] D. L. Evans. "Search for di-lepton resonances and Wprimes with CMS". In: *PoS* 2008LHC (2008). Ed. by Karl Jacobs, Daniel Denegri, and Ivica Puljak, p. 105. DOI: 10.22323/1.055.0105.

Chapter 2

The LHC, CMS and Upgrades

"The true wealth of a nation consists not in the stored-up gold but in the intellectual and physical strength of its people."

— C V Raman, 1888–1970

2.1 Introduction

In this chapter, we will discuss the experimental setup used to collect and analyse data for the research work described in this thesis. We will explore the LHC, where high-energy p-p collisions can reveal fascinating physics phenomena within the SM and potentially the extended models discussed in the preceding chapter. Additionally, we will explore the CMS experiment, with an emphasis on the Muon System. The CMS experiment is the main tool we use throughout this thesis. After presenting a brief overview of the general upgrades to the LHC and CMS, we will concentrate on the CMS Muon System upgrade and the detection environment that will be experienced at the HL-LHC operation. Finally, we will emphasise on the need of implementing a novel detecting technique in the forward region of the muon spectrometer.

2.2 The CERN and The LHC

2.2.1 Motivations and Principles

The CERN received approval on September 29, 1954, from 12 European nations. Its objective was to combine technological, financial, and human resources for the advancement of particle physics research by developing a state-of-the-art particle accelerator complex. The scientific objectives include precise measurements of the SM, the study of the mass of fundamental particles, and the exploration of BSM physics.

CERN is currently governed by 23 member nations and has a workforce exceeding 10,000 individuals, including scientists, engineers, technicians, and administrative personnel from over 100 countries. In addition to numerous confirmed discoveries and validated hypotheses within the SM, CERN's fundamental research holds extensive implications for business, medical sciences, and daily life.

Some noteworthy milestones in CERN's history include the identification of weak neutral currents within the Gargamelle bubble chamber in 1973, the discovery of W and Z bosons in 1983 through proton-antiproton collisions [1], the production of anti-matter in a laboratory in 1995 [2], and the observation of Charge-Parity (CP) violation in 1999 [3]. These achievements predate the era of the LHC. An iconic example is Tim Berners-Lee's invention of the World Wide Web (WWW) in 1989 [4]. Originally conceived to facilitate the exchange of scientific knowledge among research institutions, the "web" has evolved into the predominant medium for modern communication. In 2012, the discovery of the Higgs boson underscored the success of this unique multinational collaboration.

CERN's contributions extend to various applications, including the utilisation of particle detectors for medical imaging, hadron therapy [5], and diverse computer and electronics technologies. Additionally, CERN plays a significant role in knowledge transfer and annually trains hundreds of students in both basic research and engineering disciplines.

2.2.2 The LHC

The identification of $W^{\pm}$ and Z bosons at substantial masses marked the establishment of EW unification. However, it required a more comprehensive theory to explain the

existence of these massive particles. The dominant explanation emerged with the Higgs process-induced symmetry breaking, prompting the search for the Higgs boson.

In 1983, a three-way competition unfolded as the United States (US), Europe, and the Soviet Union sought to discover the Higgs boson. The US proposed the Superconducting Super Collider (SSC) with ring circumference 87 kilometres (km) in Texas, Europe suggested the LHC with ring circumference 27 km at CERN, and the Soviet Union proposed the Uskoritel' Nuklonov Kol'tsevogo (UNK) proton accelerator with ring circumference 21 km near Moscow. The UNK accelerator was terminated in 1990 due to financial constraints in the Soviet Union, while the SSC faced a similar fate in 1993, driven by financial limitations in the US. Consequently, the LHC at CERN stood as the sole operational particle accelerator.

CERN emerged as a result of international collaboration in the aftermath of World War-II (WW-II). This spirit of collaboration continued with the LHC, bringing together scientists from the US and the former Soviet Union. The significant financial investment in the LHC was made possible by this joint endeavour, turning the collider into a representation of global peace through scientific collaboration.

The LHC at CERN currently holds the distinction of being the world's most powerful circular hadron accelerator. It is situated within the pre-existing tunnel of the LEP collider, which ceased its operations in 2000 [6]. This colossal particle accelerator spans 27 km and is positioned 45 to 100 metres (m) underground on the border of France and Switzerland.

Designed for proton collisions occurring every 25 nanoseconds (ns), the LHC achieves a center-of-mass energy ($\sqrt{s}$) of 14 teraelectronvolt (TeV). Additionally, it facilitates Lead-Lead (Pb-Pb), proton-Lead (p-Pb), and Xenon-Xenon (Xe-Xe) [7] heavy-ion collisions, each with a $\sqrt{s}$ = 5.02 TeV, 8.16 TeV and 5.44 TeV per nucleon pair respectively.

The large-scale experiments at the LHC take place at four distinct Interaction Point (IP)s around the collider. These experiments include the A Toroidal LHC ApparatuS (ATLAS) experiment[8], the CMS experiment, the A Large Ion Collider Experiment (ALICE) [9], and the LHC beauty (LHCb) experiment [10]. Each of these experiments contributes valuable data and insights into the fundamental properties of particles and the nature of the universe.

2.2.3 Proton Odyssey

The LHC complex comprises a sequence of smaller accelerators that systematically increase the energy of particles before injecting them into the main LHC ring. These particles reach specific energy thresholds at each stage before advancing to the subsequent accelerator.

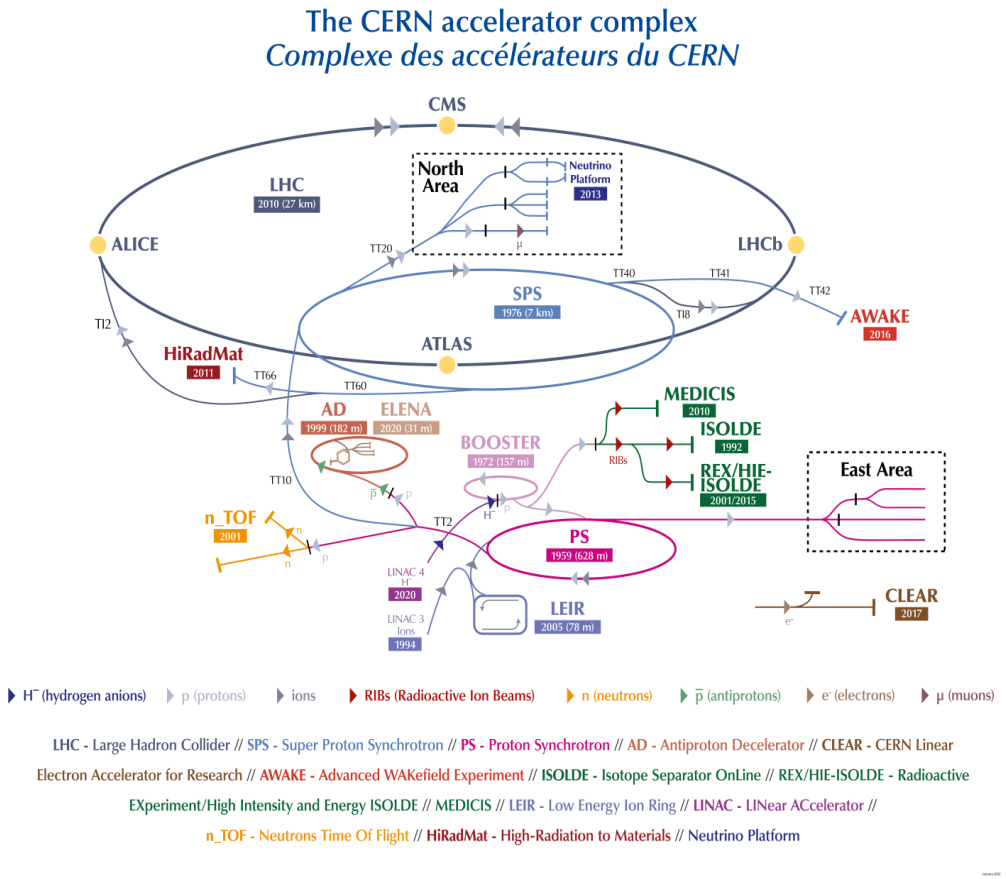

Figure 2.1: The CERN accelerator complex, including the LHC injection chain.

In the case of protons, the acceleration process initiates with a simple bottle of hydrogen at Linear Accelerator 4 (LINAC4) which was Linear Accelerator 2 (LINAC2) before 2020. Hydrogen atoms, carrying an additional electron (H^-), are pulsed into bunches lasting 100 microseconds (μs) and subsequently accelerated to 160 MeV using radio frequency quadrupoles. Once a sufficient energy level is achieved, the negative hydrogen ions undergo electron stripping, resulting in the pumping of protons into the Proton Synchrotron Booster (PSB). At this juncture, dipole magnets curve the protons into a circular path and boost their energy to 2 gigaelectronvolt (GeV) before

introducing them into the Proton Synchrotron (PS). This intermediary stage allows for a greater number of protons to be injected into the PS than would be feasible if the LINAC were to inject protons directly [11, 12].

In 1959, the PS stood as CERN's primary accelerator, currently playing a crucial role in boosting protons to 26 GeV before their insertion into the Super Proton Synchrotron (SPS). The SPS, initiated operation in 1972, now functions as the final stage in the LHC injection chain. Here, protons undergo acceleration to 450 GeV before being injected into the LHC at two distinct points. This process splits the proton beam into two, propelling them in opposing directions around the LHC [11, 12]. Figure 2.1 illustrates the complete CERN accelerator complex, encompassing the LHC injection chain.

The injector accelerators utilise normal (room-temperature) electromagnets, whereas the LHC utilises superconducting magnets crafted from Niobium-Tin. These magnets, operating at 8.3 T, are maintained at a low temperature of 1.9 Kelvin (K) by liquid Helium. The 27 km ring incorporates dipole magnets to bend protons in a circular trajectory, quadrupole and sextupole magnets for compressing protons into tightly packed bunches, and radio-frequency cavities to accelerate protons while maintaining bunches at a frequency of 40 megahertz (MHz). The LHC has the capability to accelerate 2808 bunches, each containing 10^{11} protons, resulting in collisions with a design $\mathcal{L}$ of $10^{34}\,\mathrm{cm}^{-1}\mathrm{s}^{-2}$ at $\sqrt{s} = 14$ TeV [11, 12].

2.2.4 Proton Collisions

Probabilistic QFT computations are utilised to analyse physical processes arising from p-p interactions. The cross-section (σ), representing the likelihood of a process occurring, is determined through QFT. When the LHC generates a proton beam, the protons are densely packed into tight bunches, leading to a probability of interaction known as $\mathcal{L}$. The $\mathcal{L}_{int}$, expressed mathematically in Equation 2.1, is closely related to the amount of collected data. Consequently, the anticipated number of events for a specific process is calculated as follows:

$$\mathcal{L}_{\mathrm{int}} = \int \mathcal{L}\mathrm{d}t \tag{2.1}$$

$$\mathrm{N}_{\mathrm{events}} = \sigma \cdot \mathcal{L}_{\mathrm{int}} \tag{2.2}$$

The p-p collision interactions can be categorised into two types: soft scattering and hard scattering. In a soft scatter, protons interact over long distances, leading to the transfer of minimal amount of energy. This typically happens when two proton bunches collide at an interaction location. On the other hand, in a hard scatter, protons interact at short distances, leading to the sharing of a substantial amount of momentum. The $\sqrt{s}$ represents the maximum potential for momentum exchange [11, 12].

2.2.5 Important Characteristics of the LHC

Protons are grouped into bunches, each containing 10^{11} in number, with a length of 8 cm and transverse dimensions of 20 µm $\times$ 20 µm in the LHC. Two beams travel simultaneously in opposing directions before merging at four distinct locations, leading to p-p collisions every 25 ns. The LHC's performance is characterised by two parameters: $\mathcal{L}$ and $\sqrt{s}$:

- The $\mathcal{L}$ is dependent on several factors, including the number of particles per bunch for the two beams, denoted as n_1 and n_2, as well as the transverse beam profiles represented by σ_x and σ_y. Additionally, the $\mathcal{L}$ depends on the frequency of particle crossings, denoted as f:

$$\mathcal{L} = f\frac{n_1 n_2}{4\pi\sigma_x\sigma_y} \tag{2.3}$$

  The $\mathcal{L}_{int}$ over a specific time period is indicative of the number of bunch crossings within that duration, and consequently, it reflects the amount of data collected. This quantity is commonly measured in inverse femtobarns (fb^{-1}). The total number of events generated during a given time frame is obtained by multiplying the $\mathcal{L}_{int}$ by the interaction cross-section as described in Equation 2.2.

- The total energy available in the collisions is defined by the $\sqrt{s}$. This value is determined by the energies E_1 and E_2 of the protons in the two beams, along with their momenta $\vec{p_1}$ and $\vec{p_2}$. In the LHC, being a collider, the momenta of particles in one beam ($\vec{p_1}$) are precisely opposite in direction but equal in magnitude to the momenta of particles in the other beam ($\vec{p_2}$), resulting in $\vec{p_1} = -\vec{p_2}$. Therefore, the energy at the centre of mass is provided by:

$$\sqrt{s} = \sqrt{(E_1 + E_2)^2 - (\vec{p_1} + \vec{p_2})^2} = \sqrt{(E_1 + E_2)^2} \tag{2.4}$$

Therefore, the $\sqrt{s}$ of the LHC equals the sum of the energies of the two opposing beams.

The LHC initially operated for a year at $\sqrt{s} = 7$ TeV, providing a total integrated luminosity of 5.1 fb^{-1}. Subsequently, the energy was increased to 8 TeV, resulting in a delivered total integrated luminosity of 19.7 fb^{-1}.

High-energy collisions with a large $\sqrt{s}$ facilitate the creation of massive particles, offering opportunities for significant physics discoveries such as heavy MSSM Higgs, top-squarks, bottom-squarks, or gluinos. The increased luminosity, leading to an increased event rate, allow access to the research of rare phenomena, such as the production of the SM Higgs boson.

2.2.6 LHC Experiments

The LHC comprises eight Insertion Regions (IR), where additional equipment can be inserted into the beamline, interconnected by eight arc sections where the beam is bent using superconducting magnets as illustrated in Figure 2.2. These magnets regulate the size of the particle bunches and control their trajectory as they circulate in the accelerator ring. The LHC is designed to accommodate multiple collision points for proton beams. Specifically, there are four primary IPs where four large detector systems, known as experiments, are strategically positioned to capture and record the debris resulting from the collisions.

- **ATLAS**: It's a general-purpose particle detector located at IP1, designed for a wide range of precise measurements of various physics processes, including EW and strong physics. The detector is specifically crafted to provide best possible sensitivity to phenomena such as the Higgs boson and New Physics, covering concepts like SUSY, dark matter, extra dimensions, and more.

- **ALICE**: It's is a particle detector situated at IP2, designed for measuring the properties of nuclear matter at high-energy densities. Its primary purpose is to explore the confinement of quarks through the study of QGP generated in heavy-ion collisions [14], specifically in p-Pb and Pb-Pb collisions. ALICE's detection capabilities extend to various particles, with the identification of muons playing a crucial role in identifying particles that potentially contain heavy quarks, contributing to the study of heavy quark physics.

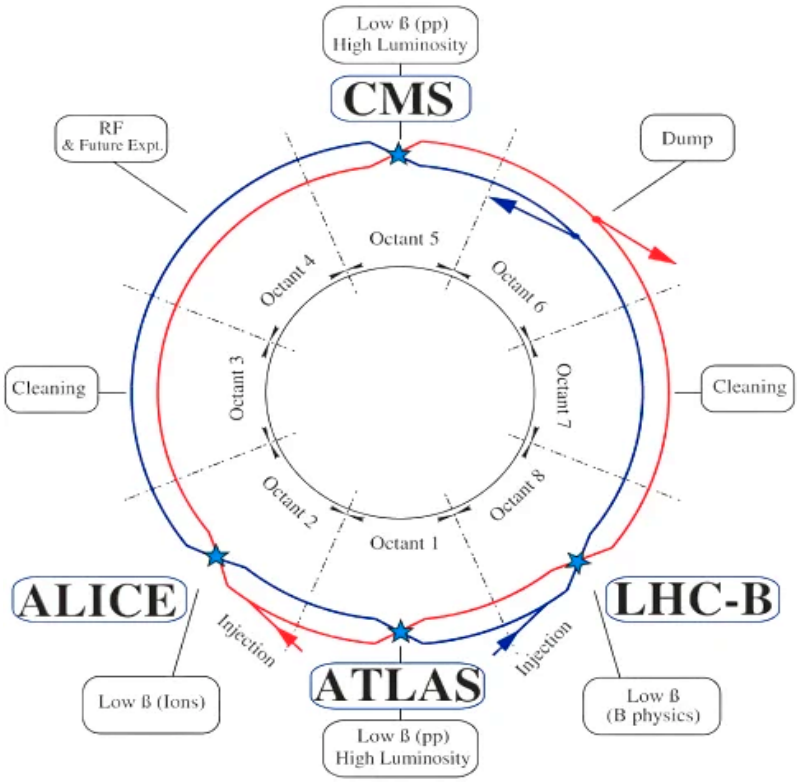

Figure 2.2: The diagram outlines the LHC, including its 8 sectors, paths of 2 particle beams. Superconducting magnets control particle bunch size and trajectory. Arrangement of the LHC, featuring the layout encompassing the four primary experiments [13].

- **CMS**: The CMS is a multi-purpose detector located at IP5, capable of precisely measuring various aspects of particle physics phenomena. It is designed to detect elementary particles, reconstruct hadron jets, and identify missing energy corresponding to weakly interacting particles, such as neutrinos and potential neutralinos. CMS shares common objectives with ATLAS, including the search for new particles and precision measurements of known particles. Its components include an inner tracker for measuring the charge and momentum of charged particles, an ECAL for measuring the energy of electrons and photons, a HCAL for measuring the energy of hadrons and jets, and a muon spectrometer for reconstructing muon tracks. These detectors are housed within a superconducting solenoid magnet, except the muon spectrometer, which facilitates the bending of charged particles to determine their momentum.

- **LHCb**: LHCb is a unique single-sided spectrometer located at IP8, specifically designed to study the cosmic imbalance between matter and antimatter. The primary objective of LHCb is to identify unusual processes involving b-quarks

and their corresponding antiparticles. Notably, the LHCb Collaboration at CERN achieved a significant milestone with the observation of CP violation in the decays of the D^0 meson, marking the first-time detection of this matter-antimatter asymmetry phenomenon [15, 16]. CP violation refers to the violation of the combined symmetry of charge conjugation (C) and parity (P) in particle physics processes.

2.2.7 The LHC Timeline

The LHC commenced its collision data collection at $\sqrt{s}$ = 7 TeV in 2010 and progressed to $\sqrt{s}$ = 8 TeV in 2012. This initial data collection phase is referred to as "LHC Run-1". Following its conclusion, the LHC underwent a two-year shutdown for upgrades known as "LS1". These upgrades increased luminosity, enabling the LHC to resume

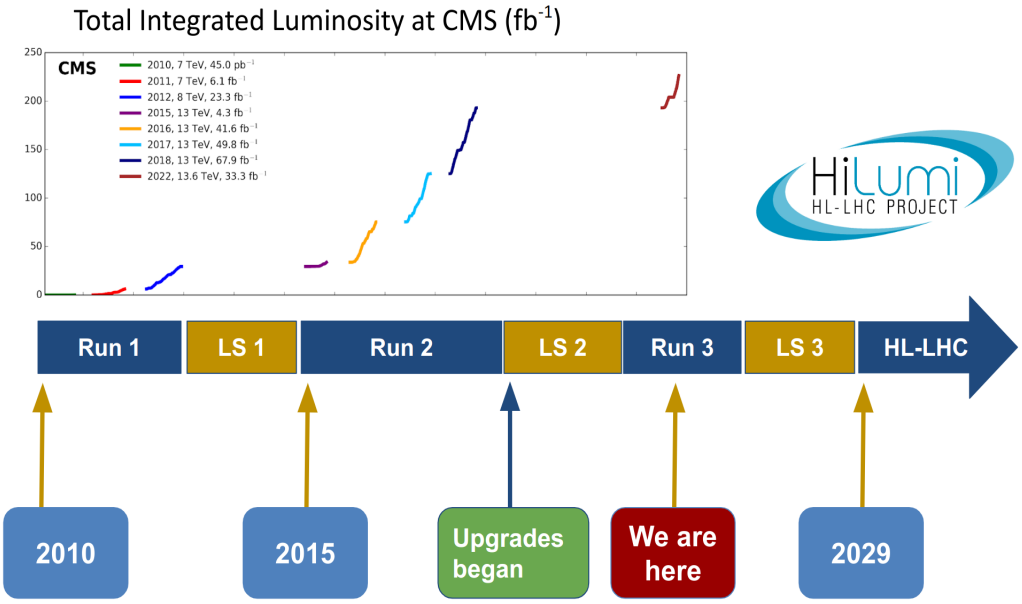

Figure 2.3: A chronology of the LHC with the $\mathcal{L}_{int}$ reported by CMS [17].

operations at a $\sqrt{s}$ = 13 TeV. The subsequent data collection phase, "LHC Run-2", spanned from 2015 to 2018. Data collected from CMS during Run-2 was actively utilised in the exploration for VLQ and the New physics. Subsequent to Run-2, the LHC initiated the first series of upgrades (Phase-I upgrades) aimed at a substantial luminosity increase, known as the HL-LHC program.

The LHC began operations for "LHC Run-3" in July 2022, initiating p-p collisions at an energy of $\sqrt{s}$ = 13.6 TeV. Figure 2.3 illustrates a brief time-frame with the

$\mathcal{L}_{int}$ observed by CMS during this period. The HL-LHC will be operational in

Figure 2.4: The diagram above illustrates the various stages involved in bringing the HL-LHC project to completion [18].

"LHC Run-4", with significant adjustments initiated during "LS2". LS2 involved an update to the CMS Muon System, introducing the first GEM muon detectors. Following the completion of LS2, the LHC successfully completed the first year of data collection for LHC Run-3 in July 2023, featuring collisions at $\sqrt{s}$ = 13.6 TeV and an $\mathcal{L}$ of 2×10^{34} cm^{-2}s^{-1}. Figure 2.4 depicts the current LHC improvement timeline, including multiple shutdowns and predicted beam performance.

2.3 The CMS Experiment

The CMS experiment, one of the primary experiments conducted at the LHC, collaborates in close cooperation with ATLAS to collectively advance scientific understanding. The combined efforts of CMS and ATLAS make significant contributions to the LHC program by providing dual, independent measurements, accelerating the validation of emerging scientific discoveries such as the confirmation of the Higgs boson and the exploration of processes BSM.

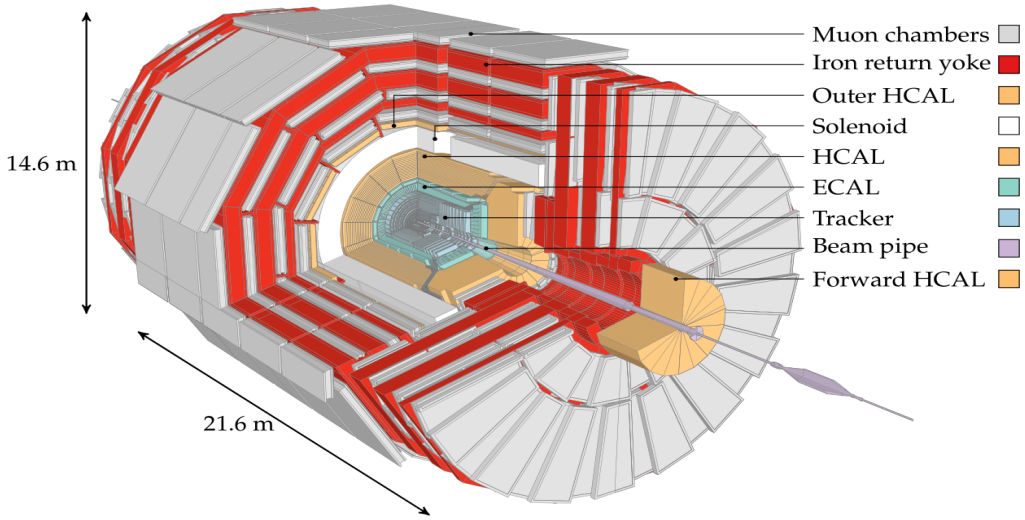

Figure 2.5: The CMS Experiment at the LHC [19].

The CMS detection system is a 14,000 ton cylinder that measures 21.6 m in length and 15 m in width. The CMS experiment takes the form of a cylindrical onion, comprising layers of distinct particle detectors, each serving a specific purpose.

The silicon tracking device precisely determines the locations of charged particles following collisions, while calorimeters measure the energy of known particles, excluding muons and neutrinos. A 3.8 T superconducting solenoid magnet that surrounds the tracking and calorimetry subdetectors, causing charged particles in the detector to travel in a curved path. An Iron return yoke is integrated to maintain a 2 T magnetic field outside the solenoid, with a particular focus on the muon subdetectors positioned outside. These subdetectors are equipped with gaseous detectors and are positioned outside the solenoid. Figure 2.5 provides a comprehensive overview of the CMS experiment, functioning like a large camera capturing images of particle collisions [20, 21].

2.3.1 Coordinates

A coordinate system is essential for the CMS experiment to accurately describe and analyse particle collision events, facilitating precise reconstruction of particle paths, positional accuracy, and standardised comparisons for a comprehensive understanding of particle physics. A singular coordinate system characterises collisions detected in the CMS experiment, where the Z-axis aligns with the beamline, the X-axis extends

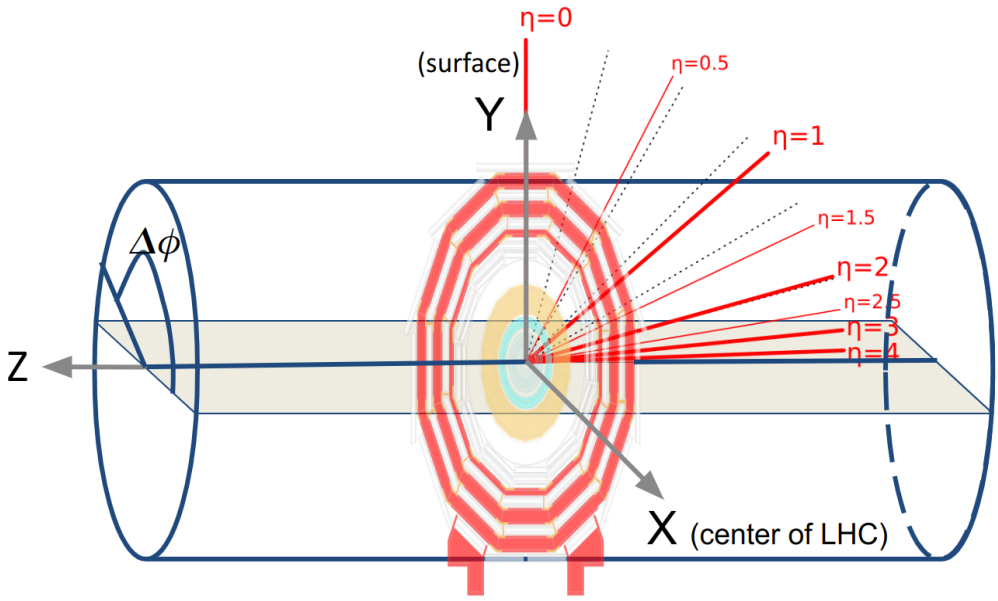

Figure 2.6: The CMS detector's coordinate system [17].

toward the centre of the LHC ring, and the Y-axis points upward in Cartesian coordinates. The radial distance (r), azimuthal angle (ϕ) in the XY-plane, and polar angle (θ) from the Z-axis in spherical coordinates are used to describe collisions, incorporating adjustments as specified by the η, defined as

$$\eta = -\ln\left(\tan\frac{\theta}{2}\right) \tag{2.5}$$

Variations in η are Lorentz invariant along the Z-axis (beamline). Figure 2.6 provides an illustration of the coordinate system diagram in CMS. The CMS detector subsystems are divided into central barrel regions for $|\eta| < 1.5$, endcap regions for $1.5 < |\eta| < 3.0$, with slight overlap and forward regions extends from $|\eta| \approx 3.0$ to the maximum η that the detector can cover, which is around $|\eta| \approx 5.0$. [12, 21, 22]. Additional subdivisions within the barrel, endcap, and forward regions are explained in detail in the respective subsections.

2.3.2 Silicon Tracking System

Silicon semiconductors serve as highly effective tracking device, generating an electron-hole pair when a charged particle passes through. The application of a potential difference across the silicon sensor, creating an electric field that propels the separated

electrons and holes towards opposite ends of the sensor. This movement of charge car-

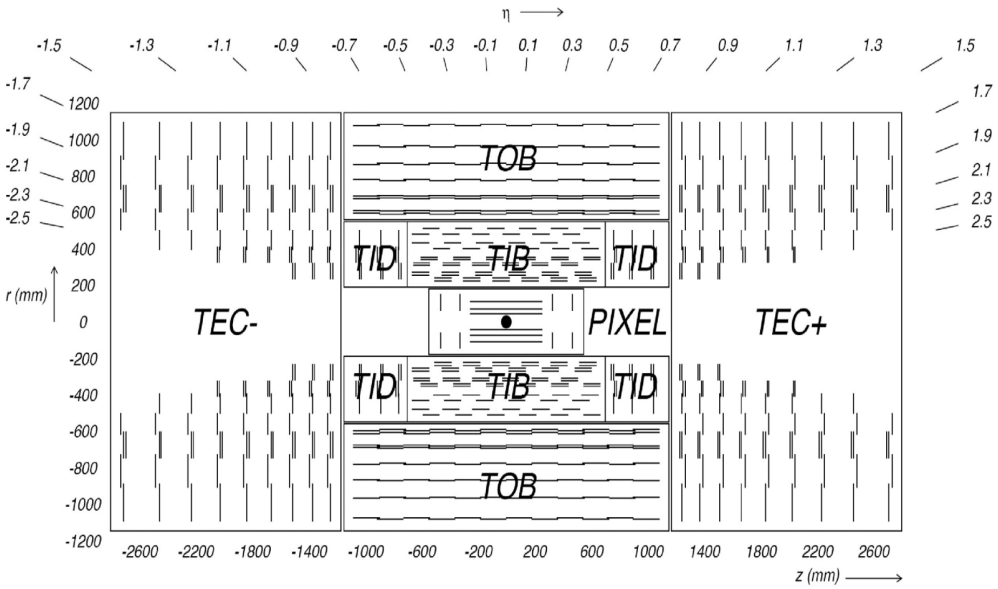

Figure 2.7: A representation of the CMS inner tracker in the (Y-Z) plane consisting of silicon pixels and microstrips [20].

riers through the silicon generates an electric current, producing measurable electrical signals that indicate the passage of charged particles. Silicon can be crafted into small sensors connected to thin readout wires, delivering significantly enhanced position resolution to the innermost tracking detectors of the CMS experiment when compared to other technologies [21]. The information derived from these signals allows for the reconstruction of particle paths and the determination of their energies.

The CMS tracking system comprises silicon pixels and microstrips, with microstrips surrounding the highly precise pixels situated closest to the IP. The system, illustrated comprehensively in Figure 2.7, spans a total length of 5.8 m and has a diameter of 2.6 m. Due to the presence of the magnetic solenoid, charged particles experience bending as they traverse the tracker, enabling precise reconstruction of their momentum. The CMS tracker achieves a momentum resolution of 1% for particles with p_T less than 20 GeV and exhibits decrement as p_T increases [11, 12, 22].

The inner tracking system utilises an iterative-tracking algorithm with four essential steps to reconstruct charged-particle tracks. The process commences with seed generation, identifying potential track seeds from reconstructed hits based on specific criteria. Subsequently, a pattern-recognition algorithm using the Combinatorial Kalman Filter (CKF) method [23] to extrapolate these seeds, updating track parameters

as compatible hits are identified in each layer. Ambiguities arising from multiple tracks associated with the same seed are resolved in the ambiguity removal step, prioritising tracks with the most hits and the highest chi-squared (χ^2) of the fit. The final step involves a comprehensive track fit, refining parameters with the CKF method and considering all hits from the pattern-recognition step. Unambiguously associated hits are removed, and the procedure iterates with slightly relaxed criteria to enhance track-finding efficiency. This approach achieves a high efficiency of over 98% for muons and between 75% and 95% for charged hadrons, with efficiency varying in the very high η region. The p_T resolution for muons is 1-2% up to $|\eta| < 1.6$ and up to 7% at the tracker boundary for p_T = 100 GeV, ensuring accurate track reconstruction across a range of momenta [21].

2.3.2.1 Silicon Pixels

During the Year-End Technical Stop (YETS) at the end of 2017, improvements were made to the CMS pixel detector. Consequently, the initial year of LHC Run-2 utilised an older detector featuring three layers of pixel rings in the barrel (located at r = 44, 73, 103 mm) and two layers of pixel disks in the endcaps (positioned at z = 345 and 465 mm). In order to improve the identification of primary and secondary

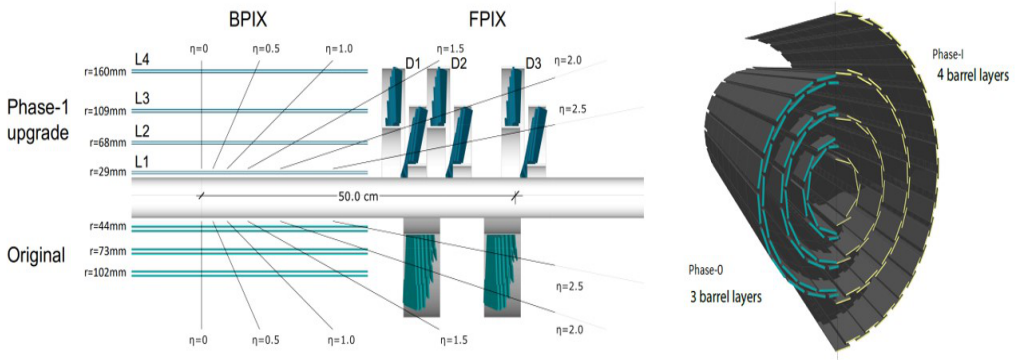

Figure 2.8: Left: The panel illustrates the conceptual layout of the various layers and disks in both Phase-0 (original) and Phase-I configurations. Right: A comparison of the pixel barrel layers in a transverse-oblique view [24].

vertices, the upgrade involved increasing the number of pixel layers and shifting the innermost layer closer to the beamline. The barrel region now comprises four rings (r = 29, 68, 109, 160 mm), while the endcaps consist of three disks with inner and outer components (z = 300, 400, 500 mm). Figure 2.8 illustrates a comparison

between the Phase-I (improved) and Phase-0 (original) pixel detectors in Forward Pixel Detector (FPIX) and Barrel Pixel Detector (BPIX). The spatial resolution of the pixels is 10 µm in the (r-ϕ) plane and 20 µm along the Z-axis [11, 12, 22, 25].

2.3.2.2 Silicon Microstrips

Silicon microstrips utilise the same physical principles as pixels but cover a significantly larger area with lower spatial resolution. The CMS microstrips comprise four

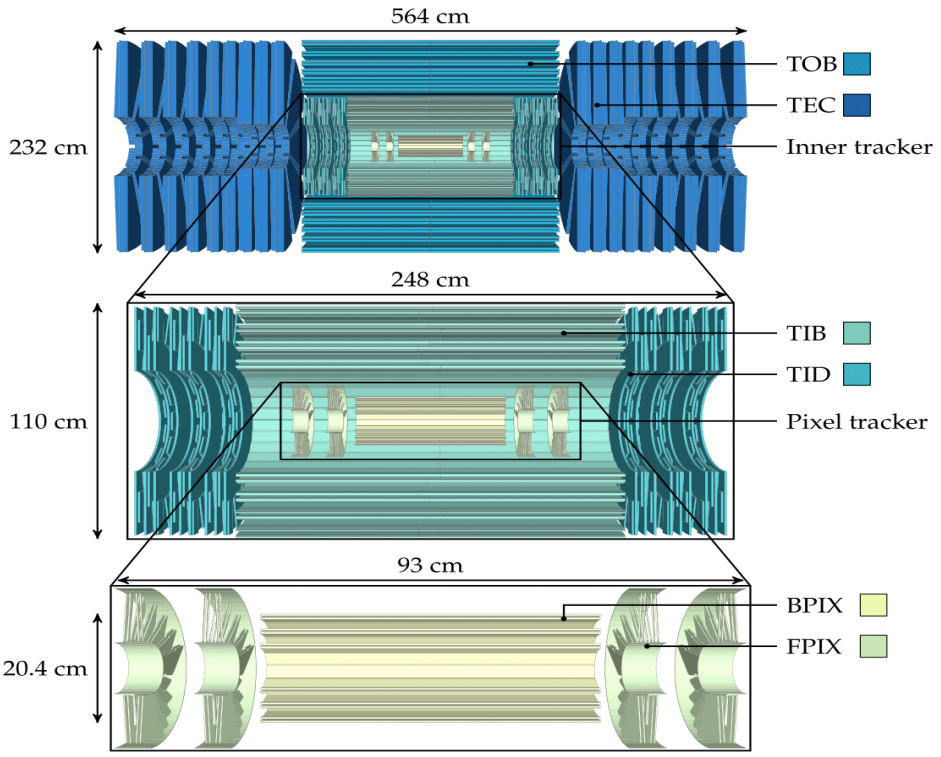

Figure 2.9: Cross-sectional view (Y-Z plane) of the silicon tracker, featuring the full tracker, an inset of the inner tracker, and a further zoomed inset of the pixel tracker. Acronyms for sub-components are defined in the text [19].

distinct subsystems: Tracker Inner Barrel (TIB), Tracker Outer Barrel (TOB), Tracker Inner Disks (TID), and Tracker End Cap (TEC) as shown in Figure 2.9. Each of these components exhibits a spatial resolution ranging from 35 µm to 52 µm [12, 21].

2.3.3 Calorimeters

Calorimeters are detectors designed to produce showers of lower-energy particles for the purpose of measuring the energy of incident particles. These showers are typically generated through Strong and EM interactions. ECAL is constructed with materials that emit photon and electron showers, while HCAL consist of dense nuclei that produce showers through the Strong force. Two types of calorimeters are used for these measurements: homogeneous and sampling calorimeters.

In a sampling calorimeter, the substance causing the shower differs from the material where the energy is deposited. As a result, some energy remains undetectable, requiring approximation. On the other hand, in a homogeneous calorimeter, the substance causing the shower is sensitive, allowing for more accurate measurement of the deposited energy.

Within the CMS, there is a sampling HCAL and a homogeneous ECAL. These components play crucial roles in accurately measuring and understanding particle energies [26].

2.3.3.1 ECAL

The CMS ECAL is constructed from lead tungstate ($PbWO_4$) crystals known for their short radiation length (X_0)[1] equals to 0.89 cm, a small Molière radius (R_M)[2] equals to 2.2 cm, and high radiation hardness[3] equals to 10 megarad (Mrad). These crystals can be utilised to construct a hermetic, homogeneous calorimeter, well-suited for the space constraints imposed by the magnetic solenoid. Emitting 80% of the light in a shower within 25 ns, these crystals enable rapid signal detection. The emitted light is captured using silicon avalanche diodes in the barrel and vacuum phototriodes in the endcaps. These technologies were carefully chosen to operate efficiently in robust magnetic fields [20, 21].

The ECAL Barrel (EB) section ($|\eta| < 1.479$) is equipped with 61200 crystals for fine granularity. Each crystal is 230 mm long (25.8 X_0) with a cross-sectional face of 22×22 mm^2. The each ECAL Endcap (EE) section ($1.479 < |\eta| < 3.0$) have 7324

[1] a mean length a high-energy electron loses 63.2% of its energy through bremsstrahlung.
[2] radius of lateral spread of an electromagnetic shower, encapsulating around 90% of its energy
[3] a material's resilience to ionizing radiation, ensuring stable performance under exposure.

crystals with a cross-sectional face of 28.6×28.6 mm^2 and a length of 220 mm (24.7 X_0). To improve granularity in the forward regions, each endcap features a preshower at $1.653 < |\eta| < 2.6$. This preshower consists of two silicon sensor planes, distinguishing a π^0 that generates two photon showers from an individual γ that generates just one shower. Figure 2.10 illustrates an overall diagram and an individual ECAL crystal [12, 21, 27].

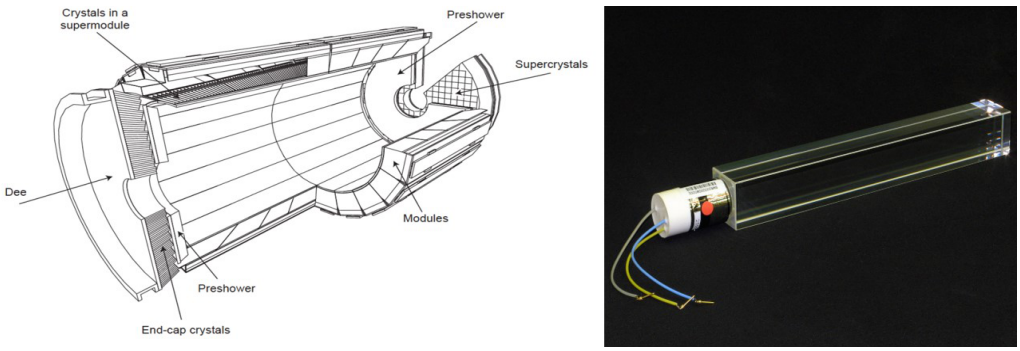

Figure 2.10: Left: A schematic of the CMS ECAL. Right: An individual ECAL crystal utilised in the endcap [20].

The energy resolution for the ECAL [28] is given by

$$\frac{\sigma_E}{E} = \frac{2.8}{\sqrt{E[GeV]}}\% + \frac{12}{\sqrt{E[GeV]}}\% + 0.3\% \tag{2.6}$$

In this context, the first term represents stochastic influences during the showering process, the second term describes electrical noise, and the last term accounts for calibration errors and non-uniformity in energy measurement. This results in an energy resolution ranging from 0.5% to 1.5% for energies ranging 10 to 250 GeV [12, 20–22, 27].

2.3.3.2 HCAL

The CMS HCAL is designed specifically to measure the energy of hadronic decays and, after reconstruction, to estimate the amount of missing p_T. The HCAL sampling calorimeter consists of the Hadron Barrel (HB), Hadron Outer (HO), Hadron Endcap (HE), and Hadron Forward (HF) subsystems, as illustrated in Figure 2.11 (left). Stringent requirements were imposed on the HCAL due to the presence of the magnetic solenoid, necessitating construction from non-magnetic materials. Consequently, high-purity Brass (70% Cu, 30% Zn) was chosen for HB, HO, and HE.

Remarkably, HE was constructed from over one million Russian navy artillery bullet casings dating back to WW-II. These casings, made of high-purity Brass, were repurposed (combined with copper from the US) to produce the 600 ton of Brass required for HE. This transformation became a symbolic representation of peace within the CMS experiment. Figure 2.11 (right) illustrates several of these historic bullet casings [20, 21, 29]. HB, HO, and HE consist of alternating layers of brass

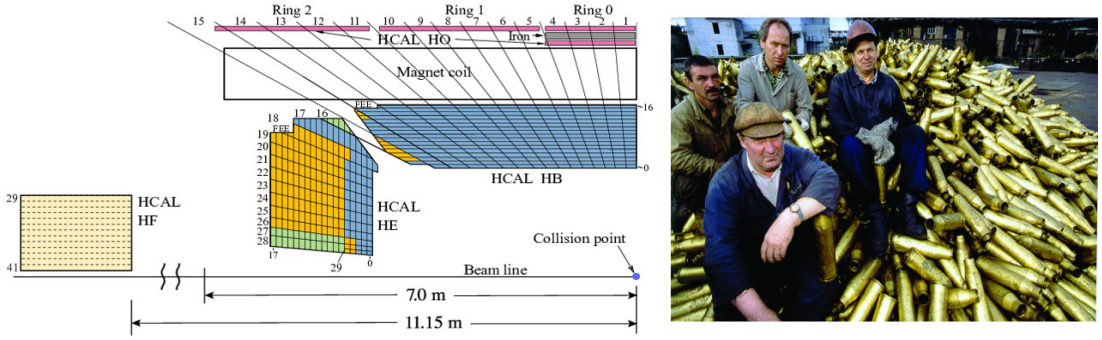

Figure 2.11: Left: An illustration of HCAL in the (r-Z) plane. Right: Russian navy shells melted down and mixed with US copper to create HE [30].

and active plastic scintillator. The plastic scintillator is read out using hybrid Photo-Multiplier Tube (PMT) (replaced by Silicon Photo-Multiplier (SiPM)s for LHC Run-3). The HB extends within the magnetic solenoid to provide comprehensive coverage up to $|\eta| < 1.3$. In the endcaps, HE provides coverage for $1.3 < |\eta| < 3.0$. HO is integrated with HCAL outside of the magnetic solenoid, covering $|\eta| < 1.26$ to ensure that the calorimeter system captures 11.8 interaction length (λ)[4] to ensure the proper hermeticity of the HCAL.

The HF calorimeter is positioned 11.2 m from the IP and covers the $|\eta|$ range from 3.0 to 5.2. This region experiences high particle fluxes, necessitating the use of radiation-hard technology. The HF utilises a Cherenkov light detector made of Quartz fibers, which, in addition to ensuring the HCAL's hermeticity, is utilised for measuring the $\mathcal{L}$. Constructed with alternating layers of Steel absorbers and Quartz scintillators, the HF is designed to withstand the high-energy and high-radiation environment of the very forward region of the CMS detector [20, 29].

[4] mean distance traveled by a particle before it undergoes an inelastic collision, typically losing a significant fraction of its energy.

The comprehensive energy resolution of the HCAL is defined by the equation:

$$\frac{\sigma_E}{E} = \frac{115.3}{\sqrt{E[GeV]}}\% + 5.5\% \tag{2.7}$$

Here, the initial term is attributed to the stochastic nature of a shower, while the subsequent term is a result of calibration inefficiency [20, 29].

2.3.4 Magnetic Solenoid

At the time of its development, the CMS superconducting magnetic solenoid stood as the most powerful solenoid globally, capable of storing 2.6 gigajoules (GJ) of energy. The 220 ton magnet comprises a 4 layer winding of stabilised, strengthened Nb-Ti, with a total length of 12.5 m and a diameter of 6 m. The superconducting volume is cooled to an operational temperature of 4.5 K using liquid Helium. During operation, the magnet carries a current of 19.14 kiloamperes (kA) through 2168 turns, resulting in a 3.8 T operating magnetic field [20, 29]. Figure 2.12 illustrates the resultant magnetic field.

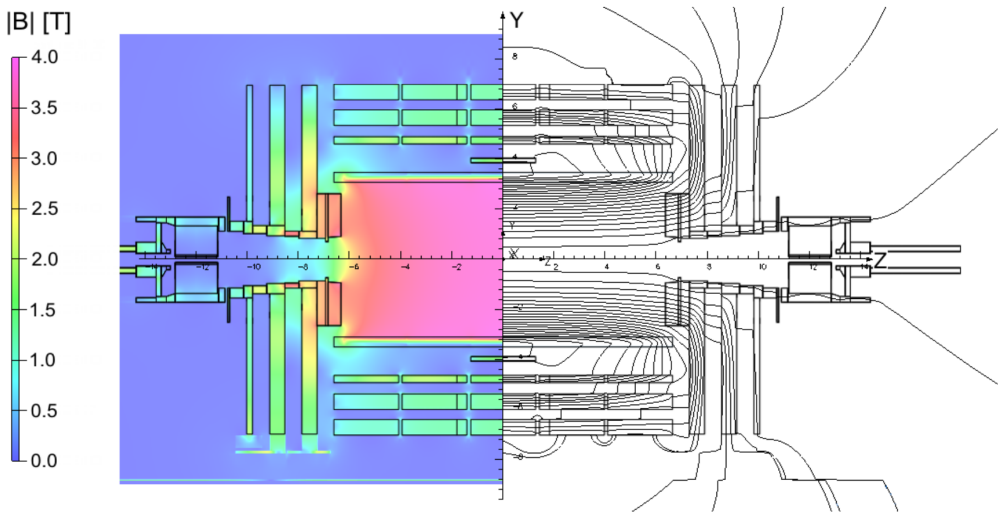

Figure 2.12: The magnetic field visualisation in the (r-Z) plane at the CMS experiment.

As charged particles traverse the magnetic field, they undergo bending within the CMS tracker. This bending curvature allows for the identification of charge as well as the reconstruction of p_T. The CMS exhibits a charge misidentification rate of less than 5% for muons with $p_T < 200$ GeV and less than 10% for muons with $p_T <$

1 TeV. Following the reconstruction of tracks, the p_T is recovered and follows a specific equation.

$$p_T = 0.3zB\rho \tag{2.8}$$

where z denotes the particle charge (in terms of electronic charge e), B is the magnetic field, and ρ is the radius of curvature of the charged particle track, the resolution of p_T is expressed as:

$$\frac{\sigma_{p_T}}{p_T} = \frac{\sigma_s p_T}{0.3BL^2}\sqrt{\frac{720}{N+4}} \tag{2.9}$$

Here, s represents the spatial resolution, L is the solenoid length, and N is the number of tracker hits utilised in the reconstruction process [31]. For charged particles with p_T = 100 GeV, this results in a momentum resolution of 1% [12, 20].

The magnetic flux from the solenoid is directed back through a 10000 ton Iron yoke featuring five wheels and two endcaps. The Muon System is interleaved within the return yoke, ensuring a consistent magnetic field for the operation of the muon detectors [20].

2.3.5 Muon System

The outermost detectors in CMS collectively form the robust and redundant Muon System. This system, crucial for muon identification, triggering, and momentum measurement, is mounted on the Iron yoke.

In the barrel region ($|\eta| < 1.2$), the system comprises five distinct wheels, each with four concentric layers of detectors. On the other hand, both the positive and negative endcaps ($0.8 < |\eta| < 2.4$) are equipped with four separate disks. This configuration allows the system to detect ionizing particles passing through the entire HCAL and ECAL, including muons with p_T greater than 3 GeV or hypothetical long-lived particles decaying outside the calorimeters. The Muon System is equipped with three types of gaseous detectors, with a fourth type recently installed during LS2. The operational principles of these gaseous detectors are elaborated in Chapter 3.

In the barrel region, characterised by low occupancy and a stable magnetic field, DTs are utilised. In the endcap region, CSCs are utilised, as this technology is effective

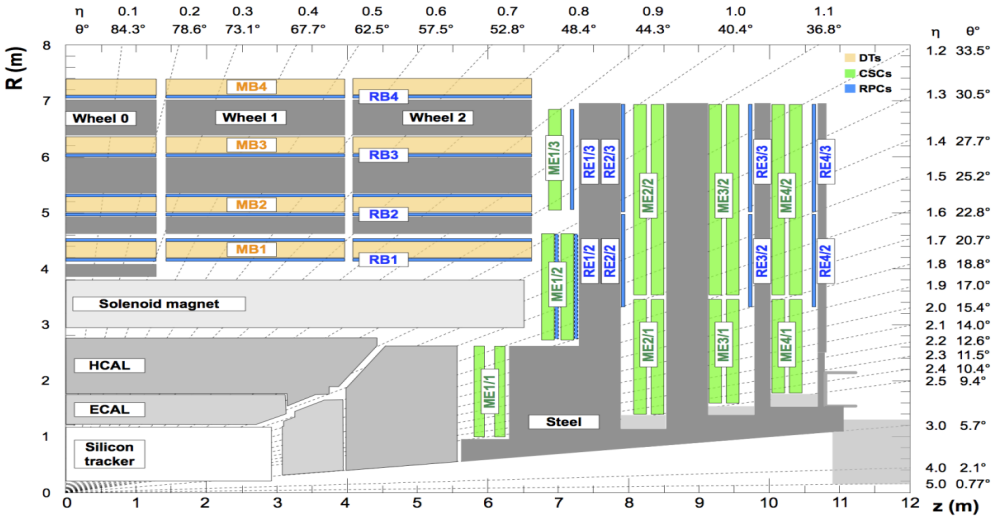

Figure 2.13: Representation of the (r-Z) quadrant of CMS during LHC Run-2 (before LS2 upgrade). In the figure, DTs are denoted as MB, CSCs as ME, and RPCs as RE/RB [32].

in coping with high particle rates and the non-uniform magnetic field in this region. RPCs are strategically placed throughout the Muon System to complement DTs and CSCs, providing a fast response and good time resolution. Initially designed to cover $|\eta| < 2.4$, RPCs are limited to $|\eta| < 2.1$ due to technological constraints in high-radiation environments.

After LHC Run-2, GEMs were introduced to the high-η zones to improve the measurement of the muon bending angle, a critical factor in reducing L1 Trigger rates. Chapters 3 and 5 provide further insights into GEM technology and updates on CMS GEM. Overall, the Muon System serves to identify muons and enhance the tracker p_T resolution [20, 29].

2.3.5.1 DTs

The barrel region's DTs are organised into 5 wheels, each containing 12 azimuthal sectors. Each wheel is equipped with four rings of DT chambers, each 2.5 m long and varying in breadth from 1.9 m to 4.1 m, depending on the position. These chambers consist of rectangular prism drift cells measuring 42×13 mm^2, running the length of the chamber, and featuring 50 m of Gold-plated Steel wire per cell. The gas volume comprises an Argon/Carbondioxide (Ar/CO_2) (in percentage ratio 85/15) combination. A Super-Layer (SL) consists of four staggered layers of drift cells. Figure 2.14

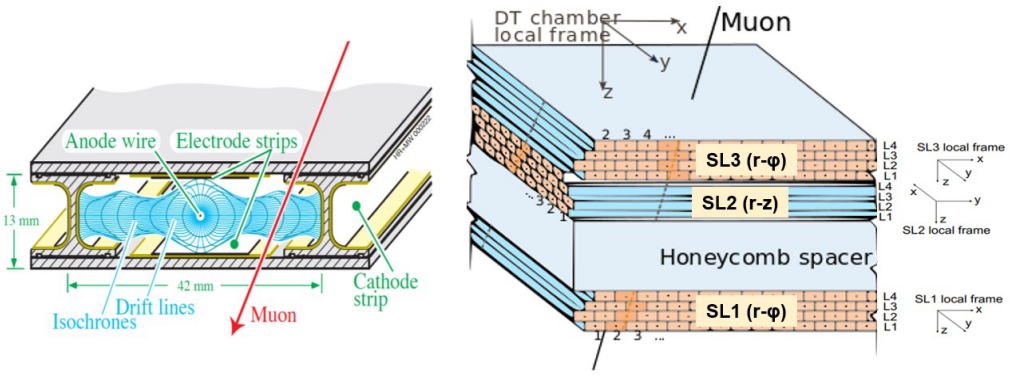

Figure 2.14: Left: Diagram depicting the layout of a DT cell, illustrating the electric field lines within the gas volume. Right: The DT Chamber comprises three superlayers, each consisting of four layers of DT cells [33].

illustrates a schematic of a drift cell and DT chamber. Two SLs are wire-oriented along the Z-axis for measuring the (r, ϕ) coordinate, while one SL is orthogonally oriented for measuring the (r, Z) coordinate. The DT chambers exhibit a detection effectiveness of over 98% and spatial resolutions ranging from 200 μm in central wheel to 600 μm in external wheels, resulting in an offline reconstruction resolution of 100 μm [20, 29].

2.3.5.2 CSCs

The CSCs are MWPC with short drift lengths to facilitate rapid signal collection, making them well-suited for the high-rate region in the endcaps. Each endcap houses four disks of CSCs, with the first innermost disk divided into three rings and the outer disks divided into two rings. All rings, except for the outermost one on the first disk, are staggered to achieve a 10° overlap configuration. Except for the innermost ring, closest to the IP designated ME1/1, all chambers feature wires perpendicular to radial strips. To address the Lorentz angle effect on electrons in the strong magnetic field, the wires in ME1/1 are slanted at 29°. Radial strips are positioned horizontally to measure the θ, while wires operate at 3.6 kilovolts (kV), and the ϕ is measured. The gas volume consists of a combination of Argon/Carbondioxide/Tetrafluoromethane ($Ar/CO_2/CF_4$) (in percentage ratio 40/50/10). The θ track position is determined with an accuracy of 0.5 cm and has a resolution ranging from 70 to 150 μm. Figure 2.15 illustrates a CSC chamber and a CSC signal generation [20, 29].

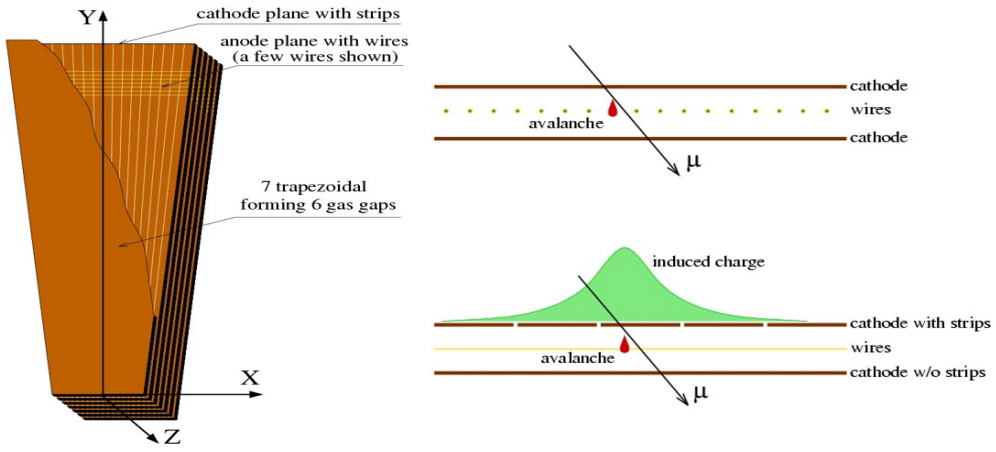

Figure 2.15: Left: A schematic of a CMS CSC revealing fan-shaped cathode strips and anode wires. The cutout showcases the arrangement with some wires visible. Right: An illustration demonstrates the operational principle of CSC: when a muon traverses a gas gap, it triggers an electron avalanche, generating a signal on anode wires and inducing a distributed charge on cathode strips [34].

2.3.5.3 RPCs

The RPCs integrated into the Muon System deliver robust redundancy and exceptional time resolution across six layers in the barrel and corresponding layers in all four endcap disks. The CMS utilizes double-gap RPCs, comprising four Bakelite plates separated by two gaps of 2 mm each [35]. These bakelite planes undergo a graphite coating to form electrodes, while insulated Aluminum strips serve to collect and read induced signals. The gas volume is a mixture of 1,1,1,2-Tetrafluoroethane/Isobutane/Sulfur hexafluoride ($R134a/iC_4H_{10}/SF_6$) (in percentage ratio 95.2/4.5/0.3). Figure 2.16 illustrate the CMS RPCs. The time resolution achieved by the resultant detector is about 1.5 ns [20, 29].

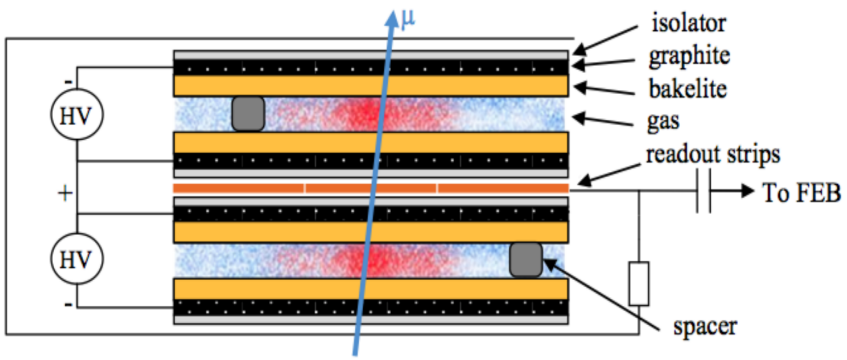

Figure 2.16: An illustration of a CMS RPC. Figure taken from [36].

2.3.5.4 Muon Reconstruction

Muons are reconstructed by incorporating hits data from the muon chambers, the tracker, and in certain circumstances, calorimeter events. The reconstruction process involves four main methods [37]:

- **Local Muon Reconstruction**: This involves the consolidation of hits collected by individual muon chambers to create muon segments or track stubs. This process is essential for accurately determining the trajectory and properties of muons within the detector system. By combining the information from various muon chambers, a more comprehensive understanding of the muon's track and characteristics is achieved, contributing to the precision and reliability of the overall reconstruction process.
- **Standalone Muon Reconstruction**: This involves utilizing different segments to reconstruct tracks within the Muon System using the initial estimation of the muon's p_T. By incorporating information from various segments, the reconstruction algorithm refines the estimation of the muon's trajectory and p_T, enhancing the overall accuracy of the reconstructed tracks in the Muon System. This step is crucial for precisely determining the muon's track and momentum, contributing to the reliability of the final analysis in high-energy physics experiments.
- **Global muon reconstruction ("outside-in")**: This is a technique where standalone muon tracks are aligned and matched with tracks originating from the inner tracker, commonly referred to as "tracker tracks". This integration process leads to a significantly enhanced p_T resolution. This method has demonstrated its superior accuracy in reconstructing muon tracks, particularly for muons traversing multiple stations, due to effective coordination between standalone muon tracks and inner tracker tracks.
- **Tracker muon reconstruction ("inside-out")**: This involves extending tracker tracks from potential muon candidates to the muon station and then matching them with at least one muon segment. The inside-out technique is not necessarily more efficient for low-momentum muons, as its effectiveness depends on various factors. Instead, it is utilized because it offers advantages in terms of track resolution and accuracy across the entire momentum spectrum, making it a versatile method for muon reconstruction.

Depending on the physics objectives, various reconstruction techniques with different selection criteria (such as the number of stubs, position, isolation of objects, etc.) may be utilized to achieve diverse levels of reconstruction efficiency and purity.

2.4 CMS Trigger and Data Acquisition (DAQ)

In the CMS experiment, protons collide every 25 ns, resulting in a collision rate of 40 MHz. Recognizing the impracticality and non-essential nature of recording each individual collision, only events of interest are preserved. This preservation is accomplished through a two-step triggering procedure involving the L1 Trigger [38] and the High-Level Trigger (HLT). After selecting the most interesting events, the collected data is shared within the physics community and transmitted to Worldwide LHC Computing Grid (WLCG) [12, 20], allowing for the calibration of datasets and the extraction of key signatures associated with specific decay channels or physical phenomena. This collaborative process contributes to a deeper understanding of the observed events and facilitates advancements in scientific knowledge. Figure 2.17 illustrate the steps involved in CMS Data Acquisition (DAQ).

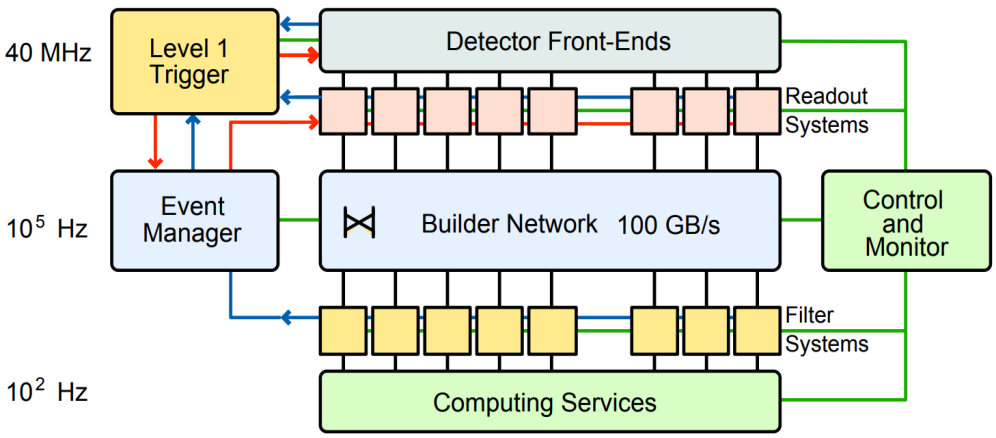

Figure 2.17: A schematic illustrating the CMS data acquisition system. [20].

2.4.1 L1 Trigger

At the detector level, the L1 Trigger incorporates preliminary reconstruction from the Muon System and the calorimeters. The calorimeters enable the trigger to make decisions based on the event's Missing Transverse Energy (E_T^{miss}). The muon p_T can be easily determined and used in decision-making through the Muon System. The best candidates are evaluated against p_T and E_T^{miss} thresholds before being either approved or rejected and sent to the next trigger level, as depicted in Figure 2.18. The tracker is excluded from the L1 Trigger due to its numerous channels, which could slow down the triggering process. The L1 Trigger mechanism has only 3.2 μs to make decisions. After L1 selection, the event rate is reduced from 400 MHz to a maximum of 100 kilohertz (kHz). The L1 Trigger is implemented using programmable electronics, utilizing Field-Programmable Gate Array (FPGA)s for flexibility and adaptability, and Application-Specific Integrated Circuit (ASIC)s with memory Look-Up Table (LUT)s when needed [12, 20].

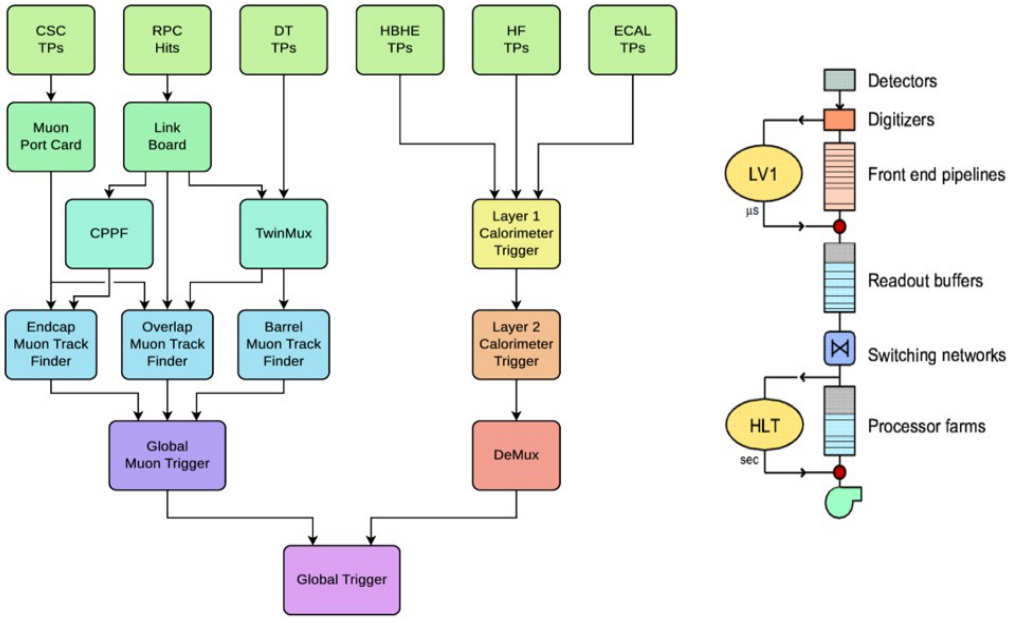

Figure 2.18: Left: An illustration of the components of the CMS L1 Trigger that lead to an L1 acceptance [39]. Right: A diagram illustrating the CMS trigger system [20].

2.4.1.1 Calorimeter Trigger

ECAL signals from EB and EE, as well as HCAL signals from HB, HE, and HF, are grouped into trigger towers. In EB and EE, these are 5×5 arrays of crystals, while for HE and HB up to $|\eta| = 1.74$, a single physical tower is used, and twice the number of physical towers in ϕ is used beyond this point. The energy of the physical tower is evenly distributed among the trigger towers. In the case of HF, physical towers are arranged in pairs in ϕ and threes in η. The transverse energy of each trigger tower is determined by on-detector electronics and sent, along with flexible pass-fail information, to the L1 Trigger electronics to encode depth structure. This information undergoes further processing with each Bunch-Crossing (BX) sent to one of ten processing nodes, scanning the full (η-ϕ) plane to identify physics objects such as jets, taus, electrons, and photons. Additionally, it calculates the transverse energy sum and E_T^{miss}. The processing nodes run concurrently, with a new BX occupying the first node upon completion of the previous crossing. This system, known as time-multiplexed, requires reassembly of the output into the original BX order (de-multiplexed) for the global trigger.

2.4.1.2 Muon Trigger

The muon trigger system primarily functions by identifying tracks through successive chamber hits caused by a muon. This process is divided into regional track finders utilizing a combination of DTs and RPCs in the barrel, CSCs and DTs in the endcaps, and all three chambers in the overlap region between the barrel and endcaps. Apart from track identification, the system is responsible for associating hits with the correct BX, achieved through the high timing precision of the RPCs and the anode wire response of the CSCs. Timing is also utilized with the DTs, although with lower resolution due to extended drift times of 400 ns. The tracks identified by these regional triggers are then forwarded to the global muon trigger, where they are merged and duplicate muon candidates are removed. Additionally, isolation information from the calorimeter trigger is combined, and the muons are sorted for the global trigger. This comprehensive process ensures accurate muon identification and precise timing information for effective event selection in the CMS experiment.

2.4.1.3 Global Trigger

The global trigger synchronizes and correlates trigger objects and variables from calorimeter and muon triggers. The L1 Trigger decision is based on a set of requirements on these trigger objects. To manage evolving conditions and events from high cross-sectional processes, the global trigger uses prescaling, reducing trigger efficiency by a specified factor (a prescale factor of 10 accepts 1 out of 10 events, resulting in a rate reduction and a drop efficiency of 90%). After prescaling, the L1 Trigger decision is communicated to data buffers, deciding whether to discard or transmit the bunch crossing to the software trigger.

2.4.2 HLT

The HLT is a sophisticated software program managed by a computer farm. This technique utilizes all CMS subsystems to identify compelling candidates with a specific event topology determined by the physics of interest. To make decisions on more complex calculations, the HLT leverages the full granularity of the event. The entire process takes only a few moments and reduces the event rate to approximately 100 hertz (Hz). Finally, the selected events are recorded on magnetic tape for offline analysis.

2.4.3 Significance of Muon System in CMS Trigger

The L1 Trigger decision relies on reconstructing various objects, including photons, electrons, muons, jets, the sum of transverse energy, and E_T^{miss}. Muon identification is essential for both the muon trigger system and, ultimately, the L1 Trigger system. Its significance lies in efficiently identifying and selecting events of interest for further analysis. Muons, being fundamental particles, are essential in various physics processes, and the Muon System is specifically designed for accurate identification and measurement of muon properties generated in high-energy p-p collisions. Additionally, the Muon System aids in reducing background noise by distinguishing muons from other particles that traverse multiple layers of the CMS detector. This background reduction is vital for isolating events relevant to the experiment's physics goals [40]. The Muon System contributes to the trigger decision-making process, providing prompt information about high-energy muons to determine which colli-

sion events to record. Events featuring high-energy muons often indicate interesting physics phenomena, guiding the trigger system's decision on event retention. Moreover, the Muon System is instrumental in identifying events associated with rare or novel phenomena, enhancing the CMS experiment's discovery potential. Finally, the precise measurements of muon momentum, charge, and trajectory enabled by the Muon System, in conjunction with other CMS subsystems, contribute to the overall precision of reconstructing particle properties produced in collisions.

2.5 The LHC Upgrades

To maximize its discovery potential, the LHC's accelerator infrastructure and experiments must undergo gradual updates. Two crucial components of the upgrade include the increase of the $\sqrt{s}$ to provide more energy during collisions, thereby revealing massive particles, and the increase of the $\mathcal{L}$ to access very rare physics events.

The first successful LHC physics beams were generated on November 20, 2009, initiating a continuous production of collisions with a gradual increase in energy until 2013. This period, referred to as LHC Run-1, included the generation of p-p collisions with $\sqrt{s}$ reaching up to 8 TeV. Throughout LHC Run-1, the LHC delivered about 30 fb^{-1} of $\mathcal{L}_{int}$ to the experiments, attaining a maximum $\mathcal{L}$ of 7×10^{33} $cm^{-2}s^{-1}$.

Following a successful run, the LHC underwent a two-year shutdown LS1 (2013-2015), to facilitate essential upgrades and replacements. Enhancements to magnet interconnections allowed for an increase in the $\sqrt{s}$ from 7-8 TeV to 13 TeV and ultimately to 13.6 TeV. The primary objective of LS1 was to prepare the accelerator for high-energy collisions at 14 TeV by improving experiment detection capabilities and repairing components and cabling damaged in the Run-1.

The accelerator recommenced its physics program in 2015 for Run-2 (2015-2018), featuring an energy level nearly double that of the Run-1. Proton beams collided at a $\sqrt{s}$ of up to 13 TeV. By the end of Run-2, the initially targeted instantaneous luminosity of 1×10^{34} $cm^{-2}s^{-1}$ was not only achieved but surpassed by a factor of two. The LHC completed the extended LS2 in 2022, originally scheduled for 2019-2020 but extended to 2021. During LS2, detector systems underwent significant upgrades, including improvements in trigger and data collection, front-end electronics, and overall enhancements. Integrating new features and replacing machine components will

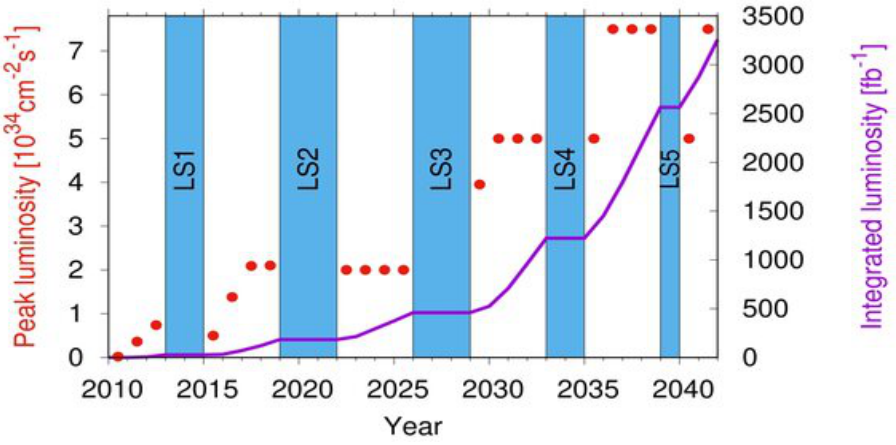

Figure 2.19: Schedule and designed values of $\mathcal{L}$ and $\mathcal{L}_{int}$ of the LHC as a function of the year, along with preliminary dates for LS. [41].

form the foundation for future collider performance, as highlighted by experiments emphasizing the necessity for comprehensive renewal and reinforcement. The main purpose of this extended shutdown was to strengthen the accelerator for both the near and long-term future, involving initial upgrades leading to the HL-LHC. The HL-LHC phase, anticipated to begin in 2026, is expected to result in a fivefold increase in luminosity compared to the LHC's original nominal value. Figure 2.19 provides an accurate representation of the projected $\mathcal{L}$ and $\mathcal{L}_{int}$ of the LHC throughout the years, taking into account the shutdown periods of the accelerator.

The LHC Run-3 is scheduled to conclude by the end of 2025, including an Extended Year-End Technical Stop (EYETS) at the close of 2024. Following this, during LS3, scheduled for 2026, a significant improvement is expected to further enhance the luminosity. Subsequently, the LHC will undergo the LHC Phase-II upgrade program for the HL-LHC and is projected to operate until 2040. This upgrade will involve an increase in $\sqrt{s}$ to 14 TeV and a substantially high $\mathcal{L}$ about $5-7\times10^{34}$ cm^{-2}s^{-1}. The goal is to collect 3000 fb^{-1} of data, which is ten times the current volume, by the end of the HL-LHC data collecting phase. Figure 2.19 represents the projected $\mathcal{L}$ and $\mathcal{L}_{int}$ as a function of years.

The upgrades for the HL-LHC are motivated by the necessity to address the approaching end of the useful life of several critical LHC components. As part of these upgrades, the electrical insulation of the dipole diodes bus-bars has been improved to ensure safe operation at higher energies, leading to the need for additional training for more magnets [18]. Additionally, maintenance interventions on the LHC cryomag-

nets were strategically planned based on a statistical analysis of electrical defects. A substantial enhancement effort was undertaken in the LHC injector chain, including the replacement of LINAC2 with LINAC4 and essential modifications to the PSB, PS, and SPS. These adjustments are designed to enable the production of beams that meet the stringent characteristics required for the HL-LHC. In order to fulfill the HL-LHC criterion for $\mathcal{L}_{int}$, the proton injectors are projected to generate proton beams with nearly double the intensity and 2.4 times the nominal luminosity [42].

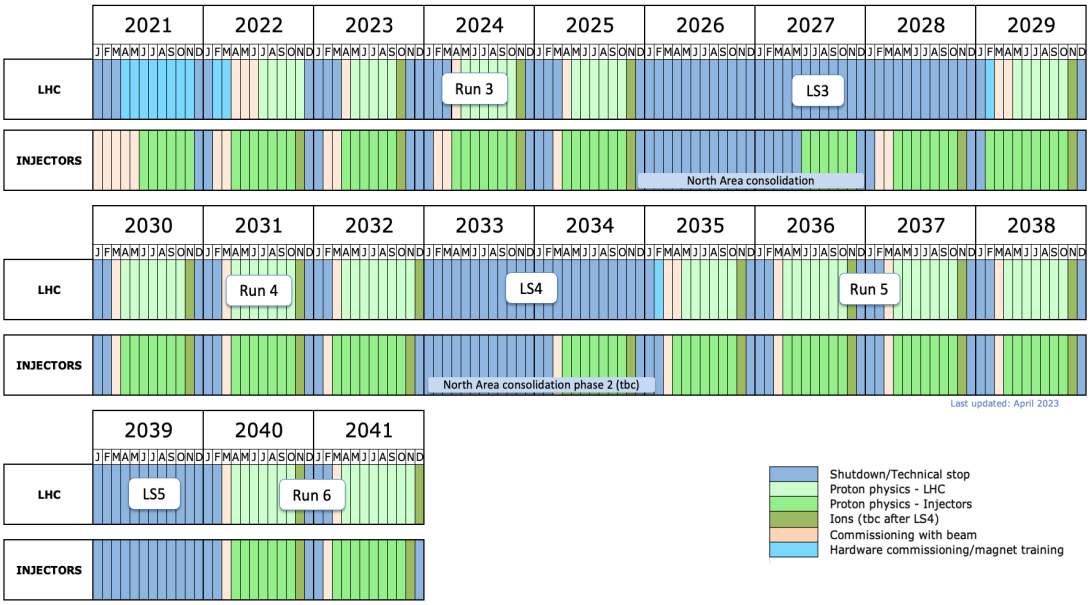

Figure 2.20: LHC long term schedule [43]

Figure 2.20 illustrates the most recent long-term LHC timetable, indicating the start of Run-3 in early spring 2022. Despite the LS2 upgrades, the expected increase in luminosity during Run-3 is likely to pose significant technical challenges for the experiments. This increment is anticipated to lead to higher average pileup, increased background radiations, larger average event size, and extended time requirements for event reconstruction. To effectively exploit the physics of Run-3, it is crucial to integrate faster detectors, advanced readout circuits, and more sophisticated trigger systems. These technologies must adeptly recognize event signatures while preserving the existing p_T resolutions. Additionally, detectors will need to withstand significantly higher radiation doses.

The ALICE experiment features a new Inner Tracking System (ITS) around the small-diameter beam-pipe, and the Muon Forward Tracker (MFT) uses its readout chips. The three previous trigger detectors are replaced by the Fast Interaction Trigger

(FIT) detector to eliminate unwanted input. To accommodate a higher interaction rate, the Time Projection Chamber (TPC) readout moved to four-layer GEM chambers [44].

The ATLAS experiment upgraded its trigger and DAQ for a 10 kHz HLT output [45]. The Liquid Ar and Tile calorimeters have enhanced electronics granularity, and a comprehensive Inner Tracker (IT) upgrade ensures efficiency for the next decade [46]. The Muon System is incorporating the New Small Wheel [47], with plans for a high-granularity Timing Detector (TD) to increase ATLAS performance in the forward region [48].

The LHCb Experiment concluded Run-2 and is now undergoing extensive improvements for efficient operation under new luminosity settings. Electronics and data capture systems have been revamped to manage expanded data collection. A section of the MWPC muon station is being replaced to complete the MWPC detector system replacement started during LS1 [49]. The installation of the Scintillating Fibre (Sci-Fi) tracker is ongoing for fine granularity and spatial resolution behind the dipole magnet [50]. To ensure its physics performance in new operating conditions, the VErtex LOcator (VELO), a silicon vertex detector, underwent enhancements involving hybrid pixel sensors [51].

Significant improvements to CMS eperiment have been done for the HL-LHC phase, including enhancemnt in Tracker, ECAL, HCAL and Muon System [52]. In the upcoming Section 2.6, we will provide a detailed discussion on these upgrades.

2.6 CMS Experiment Upgrades

As the operation of the LHC improves, the CMS experiment must evolve by implementing detector upgrades to keep pace with the LHC advancements. These upgrades are crucial for effectively utilizing the improved performance of the LHC, sustaining the accurate recording of collision data at increasing energy and luminosity levels anticipated in the coming years.

The primary goal of the CMS upgrade is to preserve the physics performance of the detector subsystems while optimizing particle reconstruction for LHC luminosities ranging from $5 - 7 \times 10^{34}$ cm^{-2}s^{-1}. Key concerns arising from the LHC upgrade include the high multiplicity of p-p collisions in each BX, commonly known as Pile-Up (PU), which is anticipated to reach approximately 140 at the HL-LHC. Other

challenges involve the rise in background rate and the potential for radiation damage to the detectors and their electronics.

The upgrade is divided into two phases: Phase-I, encompassing LS1, LS2, and other technical halts until 2023, and Phase-II, designed to prepare the detectors for HL-LHC operation after LS3 in 2024.

2.6.1 Phase-I Upgrades

The majority of Phase-I upgrades have already been completed during LS1 (2013-2014) and LS2 (2019-2022)

2.6.1.1 LS1

- **Tracker**: During the YETS in 2016, an improved pixel detector with four layers in the barrel and three endcap disks was installed, replacing the old detector. This upgrade enabled an additional fourth space-point measurement across the tracking η range. In the barrel, the inner layer is positioned close to the beam axis, while the outer layer is adjacent to the tracker's inner barrel. The introduction of a new Carbondioxide (CO_2) cooling system and lightweight mechanics, along with a revised cabling scheme for optical readout and powering using Direct Current-Direct Current (DC-DC) converters, led to a reduction in the material budget within the tracking acceptance. The integration of new readout electronics ensured that the pixels could operate at the highest anticipated luminosity without experiencing data loss.

- **Calorimeters**: The PMTs in the HF calorimeter were replaced with multi-anode PMTs, and SiPMs replaced the Hybrid Photo-Diode (HPD)s in the HB and HE calorimeters. These SiPMs are immune to magnetic fields, reducing spurious signals and enabling depth segmentation in the HE and HB for improved calibration and assessment of shower development. Additionally, new time digitizing capabilities were implemented in the front-end readout circuits to improve background rejection. The introduction of new optical connections Gigabit Transceiver (GBT) and back-end circuits based on Tracker Control and Readout ASIC (TCA) technology backplanes increased data output bandwidth. The installation of the back-end electronics had been completed by the end of 2015, allowing

the trigger improvement to be commissioned concurrently with operations. The front-end was implemented during the HF's YETS in 2016.

- **Muon System**: All defective DT chambers or circuits were rectified to ensure future performance. A total of 120 Trigger Boards were replaced with new technology. Additionally, some DT electronics were relocated from the experimental cavern to the servicing cavern. Custom Copper-to-optical converter modules were incorporated to facilitate the retransmission of signals over extended distances. These initiatives laid the foundation for the DT improvement program, empowering the subdetector's readout circuits to withstand higher LHC luminosities. Simultaneously, this enhanced flexibility was introduced to facilitate trigger enhancements as needed.

  The RPC's fourth disk (RE4) was installed in the endcap region, aligning with the specifications outlined in the CMS TDR. The chambers were fabricated and tested at CERN, along with laboratories in Belgium and India. The electronics for the front-end, read-out, and power system were produced in Pakistan, Italy, and Finland. During that period, the RPC system, comprising 912 chambers and over 110,000 electronic channels, underwent extensive maintenance and repair. Several planned technical interventions were implemented to restore the functionality of the 15 unconnected chambers and rectify issues affecting 2% of electronic channels that were not operational.

  An additional set of 72 CERN-produced chambers were installed to enhance the forward η coverage of muon station 4 (ME4/2), within the region $1.2 < |\eta| < 1.8$. This expansion was undertaken with the objective of improving the identification of muons in higher-energy and higher-rate collisions. Furthermore, the innermost sets of CSC were outfitted with significantly improved electronics, reinforcing its capacity to efficiently manage the exceedingly high collision rates.

2.6.1.2 LS2

- **Beam-Pipe**: The outdated beam-pipe has been replaced with a new 36 m long beam-pipe. The new beam-pipe is made of an aluminum alloy, which significantly reduces induced radioactivity by a factor of five when compared to Stainless Steel. In order to facilitate maintenance, a new vacuum pumping group has

been relocated 16 m away from the IP5. Furthermore, eight additional vacuum chambers, comprising four different types, have been successfully installed.

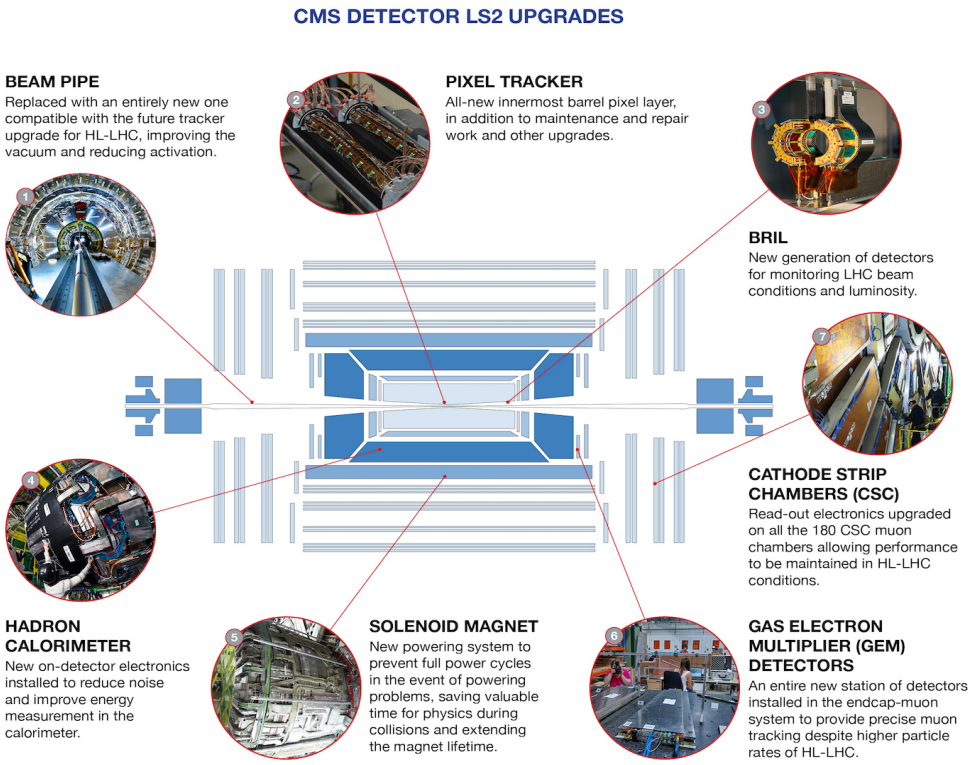

Figure 2.21: Comprehensive overview of the recent CMS upgrades during LS2 [53].

- **BRIL**: Three Beam Radiation, Instrumentation, and Luminosity (BRIL) instruments have been strategically positioned to evaluate luminosity and beam conditions: the Beam Condition Monitor 1 Fast (BCM1F), the Beam Condition Monitor for Losses (BCM1L), and the Pixel Luminosity Telescope (PLT). All three BRIL subsystems represent a new generation of design. The BRIL devices at CMS continuously measure the real-time collision rate, thereby improving both trigger rates and the quality of the LHC beams. They provide real-time monitoring of beam conditions, ensuring the protection of the LHC equipments and sensitive CMS sub-detectors. Moreover, their combined luminosity measurements contribute to determining the frequency of each type of interaction, including production cross-sections.
- **Solenoid Magnet**: The CMS magnet underwent several interventions and repairs to ensure its long-term efficiency. Control and safety systems were restored,

and specific electronics were completely replaced. A new powering mechanism was devised to manage the current flow inside the magnet. Historically, after a power outage, the magnet would take hours to restore to full field, resulting in a significant loss of time that impacted the efficient detection of particles. Due to these improvements, the restoration time has been substantially reduced to just a few minutes, resulting in considerable time savings for physics research.

- **Tracker**: The Pixel Tracker is exposed to significant radiation damage from particle collisions due to its location within the detector. Despite being stored at -20°C for protection, damage still occurs. To address this challenge, the subdetector underwent substantial repairs and enhancements in a cleanroom environment. Its design has been refined, and modifications to the innermost layer have been implemented to effectively mitigate the effects of radiation damage.

- **Calorimeter**: The CMS upgraded its detector system by replacing aging HPDs with advanced SiPMs. The new SiPMs indeed exhibit a significant threefold increase in photon detection efficiency and an impressive 200-fold gain compared to the original HPDs. SiPMs, with their excellent time resolution and insensitivity to magnetic fields, may offer superior radiation hardness in specific scenarios, making them suitable for prolonged operation in such environments. Their compact size renders them suitable for extended operational periods over HPDs.

- **Muon System**: The CMS experiment has recently integrated new GEM detectors into its outermost layer to identify muons scattering at an angle of approximately 10° relative to the LHC beam-axis. Detecting muons at such slight angles poses a challenge due to the release of a large number of background particles. The GEM chambers are constructed using a thin, metal-clad polymer foil chemically punctured with millions of holes, typically ranging from 50 to 100 per mm^2. This perforated foil is immersed in gas. Electrons generated by the gas drift into the holes, undergo rapid multiplication in a strong electric field, and are directed to a collection zone as muons pass through. Notably, the CMS experiment has incorporated 72 modules, each comprising two GEM detectors.

In addition to the detectors and their associated readout electronics, the upgrade includes improvements to the DAQ system, with the goal of enhancing bandwidth for data collection and transfer. The beam monitoring system is also being upgraded to improve the measurement of beam background and luminosity. A detailed information and technical specifications of the CMS Phase-I upgrade can be found in [54].

2.6.2 Phase-II Upgrades

Scheduled to begin operations in 2029, the HL-LHC is projected to generate approximately ten times the data collected in previous LHC runs. To fully leverage the physics potential of the HL-LHC, the CMS Collaboration is developing an optimized detector that pushes technological boundaries. Almost all CMS subsystems will be engaged, incorporating additional detector stations to enhance the detector's performance in terms of detection efficiency, resolution, and background rejection. Modifications will be made to the CMS tracker and calorimeter endcaps, a new Minimum Ionising Particle Precision Timing Detector (MTD) and luminosity detector will be integrated, the majority of old electronics will be replaced, and additional muon forward stations will be installed. The key upgrades planned for the LHC's Phase-II operation include:

- **Tracker**: The plan involves a comprehensive upgrade of the current tracking technology to mitigate radiation degradation and boost granularity by a factor of four. Additional detection layers will be integrated into the endcaps, expanding the entire system to $|\eta| = 4$. During Phase-II, the tracking data will be synergistically utilized with the L1 Trigger to optimize rate reduction and selection efficiency.

- **Calorimeters**: The High Granularity Calorimeter (HGCAL) upgrade is scheduled to replace the existing endcap system, integrating both EM and hadronic components. These components will possess total 110.9 X_0 and 10.7 λ [55]. The system will utilize metallic absorbers-Tungsten/Copper in the EM segment and Brass/Copper in the hadronic segment-in conjunction with silicon sensors. Both the EM and hadronic sections will undergo longitudinal and transversal partitioning. With remarkable granularity, featuring approximately 6 million readout channels, this upgrade aims to provide a comprehensive 3D energy deposition profile of the showers, complemented by rapid timing capabilities. This upgrade is expected to improve particle identification, enhance energy resolution, and increase PU rejection efficiency in the high particle rate and increased radiation dose endcap area.

- **Trigger**: To leverage statistical benefits from the increased LHC luminosity, it is essential to achieve a necessary reduction in the rate while avoiding excessive efficiency loss for the studied physics channels. To fulfill this objective, a tracking mechanism will be implemented at the L1 Trigger level. To facilitate this, improvements will be made to the L1 electronics, enabling the execution of more complex algorithms. Additionally, the L1 Trigger latency will be increased

from 4 μs to 12.5 μs. Adapting to these new operational conditions will require updates in the front-end electronics and an adjustment in the permissible trigger rate. This is particularly crucial for controlling algorithms using photons and hadrons, as they are more adversely affected by the pileup increase compared to other types of algorithms.

- **Muon System**: To maximize its discovery potential at the HL-LHC, the muon spectrometer will undergo a comprehensive modernization process. This will encompass the improvement of existing muon detectors and the incorporation of new ones utilizing diverse technologies. Critical attributes of the Muon System that require preservation include muon identification and reconstruction skills, as well as the momentum resolution achieved in previous runs. It is imperative to maintain and potentially enhance these capabilities for the successful integration of a new Track Trigger. This trigger will align candidate tracks in the tracker with L1 Trigger muons, leveraging their p_T information, and is integral to the overall efficiency of the system.

  To address these aspects, the installation of additional muon stations will be installed, to improve redundancy, facilitating the resolution of tracking ambiguities at the trigger level. This enhancement is pivotal for maintaining control over the trigger rate without the need for an increase in the p_T threshold. An elevation in the threshold could potentially result in the exclusion of novel physics events, particularly those involving low p_T muons. Furthermore, the construction of extra muon stations plays a critical role in independently triggering on long-lived BSM particles that undergo decay outside the CMS inner tracker.

  At the end of Run-2, the muon detector technologies comprised CSCs, DTs, and RPCs. To adapt to the increased L1 Trigger latency set for HL-LHC, CSCs are scheduled for upgrades primarily in their electronics, with the aim of improving performance. This will lead to higher power consumption, requiring a corresponding upgrade of the Low Voltage (LV) system. Conversely, the HV power system will be improved to handle increased background rates and enable better monitoring of detector currents.

  The second system, represented by DTs, will undergo enhancements in their front-end electronics components. These improvements are designed to extend their lifespan in the heightened radiation environment and boost trigger rate capability. Achieving this involves relocating the Minicrates to the Underground Service

Cavern (USC) counting room, housing logics dedicated to time digitization and L1 Trigger primitive generation. This upgrade also aims to provide more refined objects at the L1 Trigger level. Before LS3, the RPC system is set to implement

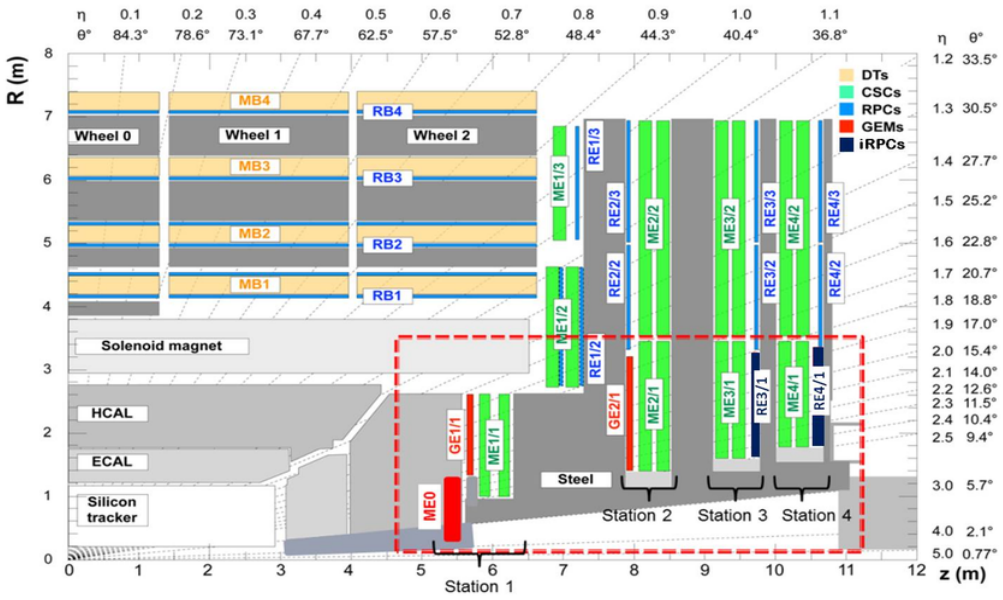

Figure 2.22: A quadrant of the CMS Muon Spectrometer is highlighted, featuring DT chambers (yellow), RPCs (light blue), and CSCs (green). The dashed box encloses the positions of the newly installed forward muon detectors for the HL-LHC project. These detectors are marked in red for GEM stations (ME0, GE1/1, and GE2/1) and in violet for upgraded iRPC stations (RE3/1 and RE4/1) [56].

new and iRPCs detectors in the region where $|\eta| > 1.6$, at stations RE3/1 and RE4/1, as depicted in Figure 2.22, with the aim of boosting endcap redundancy. To manage the higher rates prevalent in this area, the new RPCs will be designed to include smaller electrodes and gaps. The iRPC geometric setup boosts the detector's rate capability and enhances its ability to withstand the demanding background conditions of the HL-LHC. Furthermore, planned modifications to the RPC system's back-end electronics will be implemented to improve the timing resolution [56].

In the region $|\eta| > 1.6$, redundancy will be strengthened not only with RPC detectors but also by incorporating two additional stations near the existing CSC station: GE2/1 and ME0, as depicted in Figure 2.20. These stations will utilize GEM technology. The installation of stations GE2/1 and ME0 is planned during the Run-3 YETS and LS3.

Further detailed technical information about the CMS Phase-II update can be found in [57].

2.7 Motivation for Upgrading CMS Forward Muon System

The upgrade of the CMS muon spectrometer is essential to ensure an appropriate L1 Trigger rate while maintaining high selection efficiency. The initial station of the forward Muon System plays a crucial role in ensuring the quality of muon reconstruction. This is attributed to the stronger magnetic field at this station compared to others, leading to the highest muon bending angle and resulting in excellent p_T resolution and sensitivity to low p_T. Additionally, the presence of reconstructed stubs in the first station further aids in distinguishing significant tracks and background tracks.

However, the first station is vulnerable to the highest background levels. Various types of backgrounds may contribute to this vulnerability:

- The muon background originates from heavy flavor prompt muons, primarily from b and c decays, non-prompt muons resulting from π and K decays, and cosmic muons. In this context, detector hits demonstrate correlation, delineating muon tracks and regions characterized by low p_T.
- The predominant uncorrelated background within the overall environmental background is mainly attributed to neutrons and their interactions with matter. The upcoming section will conduct a more thorough exploration of the neutron background at the HL-LHC, providing a comprehensive understanding of the subject.
- Additional background contributions arise from hadron punch-through, beam halo particles, or high-energy particles generated during the de-excitation of detector materials.

The increased background hit rate at the LHC will complicate segment reconstruction, giving rise to spurious segments and degrading momentum resolution. Consequently, in the high-η zone, the misidentification of interesting muons will rise, resulting in an increase in the L1 muon trigger rate. Figure 2.23 depicts the simulated L1 Trigger rate as a function of η for p_T thresholds greater than 15 GeV. This effect is notably

more pronounced in the region $|\eta| > 1.6$, exclusively instrumented by CSC chambers. Integrating a new detection technique into the first station of the forward endcap

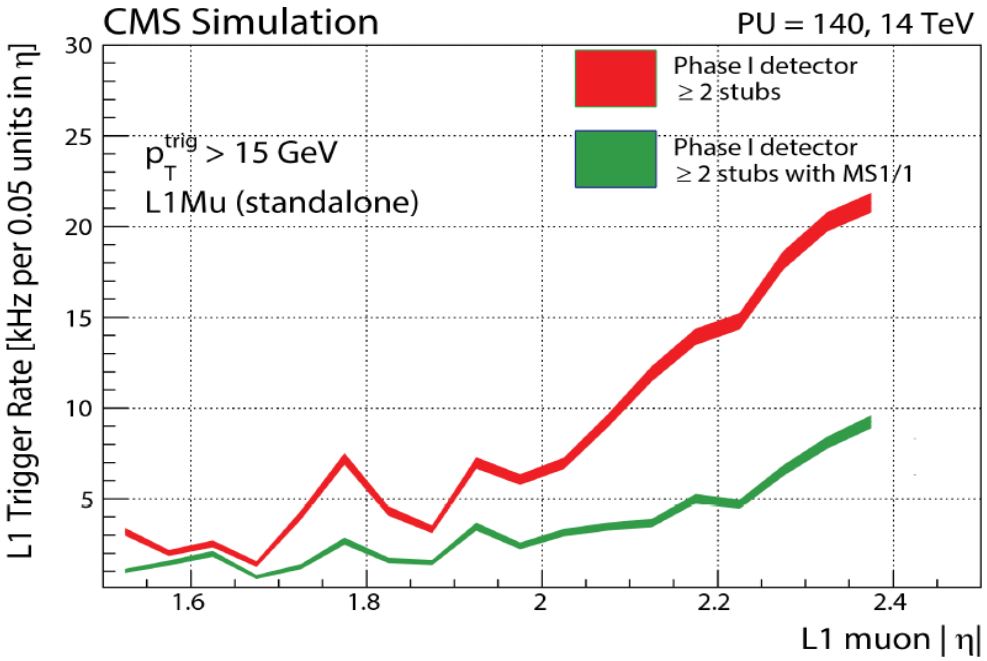

Figure 2.23: The L1 Trigger rate plotted against muons with more than two reconstructed stubs (shown in red) and the presence of hits in the first station MS1/1 (depicted in green). The mismeasurement of muon momentum, influenced by the substantial background contribution, dominates the rate at high-η region [58].

would, therefore, generate additional hits that could be utilized to resolve tracking ambiguities, improve momentum resolution, and decrease the L1 Trigger rate, without compromising optimal selection efficiency.

The current Muon System improvement plan was implemented under the framework of the GE1/1 project, which will be detailed in Chapter 3. It is crucial to clarify that the designation "GE1/1" specifically refers to the GEM-based detectors intended for installation in the first station of the CMS endcap during LS2.

2.7.1 Background Rate Evaluation

The high-η zone is prone to significant challenges posed by intense background radiations, a situation expected to worsen with the HL-LHC upgrade. Comprehensive understanding of these background radiations is vital, as they can lead to inaccuracies

in track reconstruction and muon momentum measurements. Furthermore, the increased radiations might accelerate the aging process of muon detectors, contributing to a gradual decline in their performance over an extended period. In conclusion, the determination of the background rate plays a pivotal role in shaping the detection environment and, consequently, influencing the choice of appropriate detection technology for the endcaps.

The estimated background rate and its diverse components were calculated using the CMS version of the FLUKA [59] simulation program with an instantaneous luminosity of $\mathcal{L} = 5 \times 10^{34}$ cm^{-2}s^{-1}. Additional information about the study is available in [58]. The expected maximum hit rate in the initial muon station at the HL-LHC

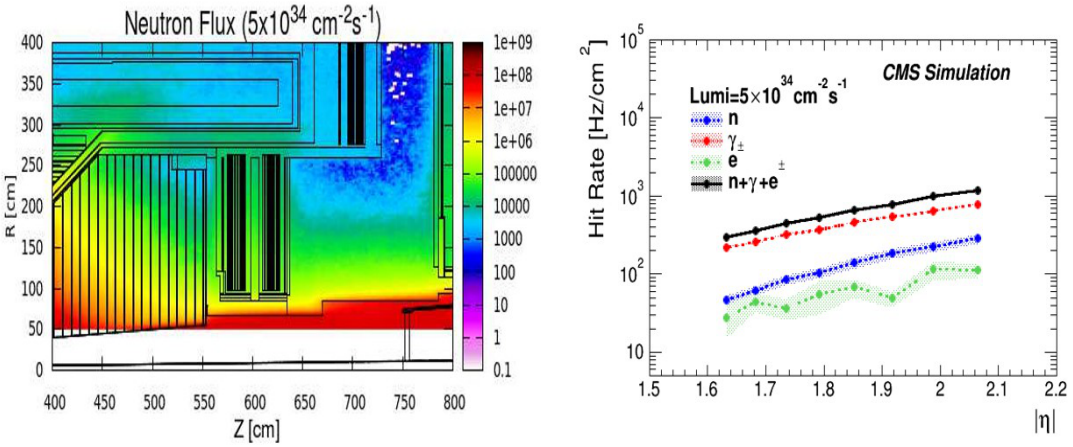

Figure 2.24: Left: A normalized 2D neutron flux map to an $\mathcal{L}$ of 5×10^{34} cm^{-2}s^{-1} and superimposed onto the diagram, illustrating the detector elements. Right: The per-chamber hit rate for the GE1/1 detector, influenced by long-lived neutron backgrounds, is depicted as a function of η at an $\mathcal{L}$ of 5×10^{34} cm^{-2}s^{-1} [58].

is forecasted to be up to 1 kHz/cm^2 as shown in Figure 2.24. Consequently, the improved forward Muon System needs to showcase resilience to radiation, extending up to 500 Gray (Gy), exhibit a high-rate capability, and demonstrate proficiency in discerning genuine muon tracks from false tracks. A detailed examination of the background radiations in the GE1/1 region will be presented in Chapter 5.

2.7.2 Influence on the Phase-I Trigger System

The six layers of CSC chambers in the first muon station cover a muon path length of 11.7 cm. Consequently, the bending angle is unsuitable for p_T measurement, and

the momentum resolution is inadequate for distinguishing interesting muon tracks from mismeasured tracks in the presence of noise. Specifically, for L1, p_T threshold below 20 GeV, the rate of mismeasured muon tracks surpasses the rate of muon tracks originating from $W^{\pm}$ and Z bosons by more than one order of magnitude. The contribution of mismeasurements to the L1 Trigger rate is expected to rise with the increasing luminosity of the LHC unless the p_T threshold is increased, leading to reduced efficiency. The integration of a second detection technology would extend the detection

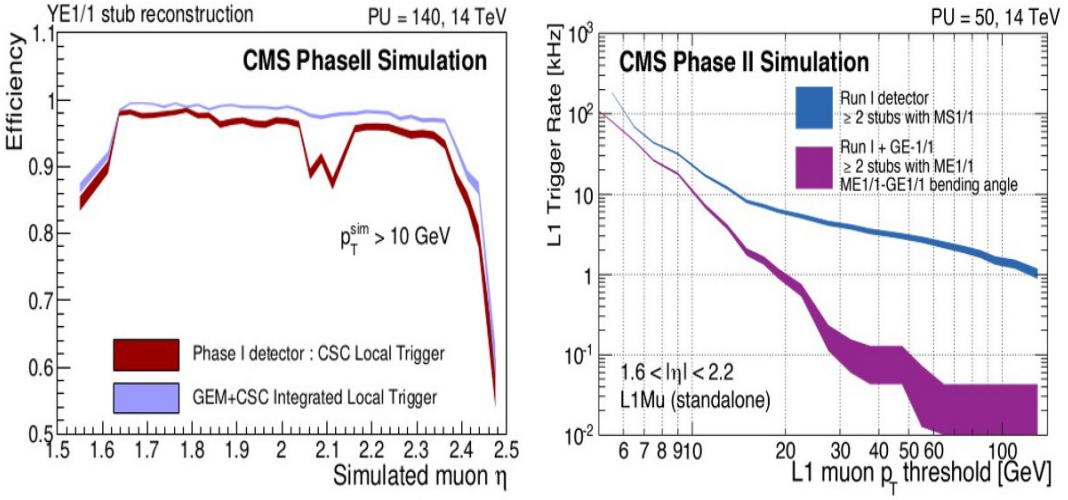

Figure 2.25: Left: The efficiency of the integrated GEM-CSC trigger's muon track segment a LCT reconstruction varies with the simulated muon $|\eta|$, in comparison to the Phase-I CSC-only algorithm [58]. Right: Muon L1 Trigger rates are compared before and after the GE1/1 upgrade at a luminosity of 2×10^{34} cm^{-2}s^{-1}, with a constant efficiency of 94%. MS1/1, the L1 Trigger for the first endcap muon station, exhibits a significant reduction in trigger rate with the introduction of GE1/1 and the utilization of the bending angle between the two stations [58].

path, resulting in the generation of additional hits. This enhancement facilitates the improvement of stub reconstruction and momentum resolution. Consequently, there is a reduction in both the rates of misidentified muon tracks and L1 Triggers. Figure 2.25 on the left, illustrates the efficiency of segment reconstruction for simulated muon for different η values, comparing the current CSC system with the integrated CSC+GE1/1 upgrade. On the right, the plot demonstrates the decrease in the L1 Trigger rate while maintaining a constant efficiency of 94% at the LHC luminosity $\mathcal{L} = 2 \times 10^{34}$ cm^{-2}s^{-1}.

Reducing the trigger rate proves advantageous by allowing the maintenance of a low p_T threshold, thereby improving the acceptability and efficiency of soft muon reconstruction. This improvement is particularly crucial for physics investigations

in the SM, extended Higgs sectors, and SUSY candidates. Figure 2.26 on the left, illustrates the muon p_T distribution for three interesting physics channels: the SM Higgs decay to τ-leptons, a heavy Higgs decay into τ-leptons and quarks, and the SUSY "stop" squarks generation. The right plot demonstrates how decreasing the p_T threshold leads to an increase in selection efficiency.

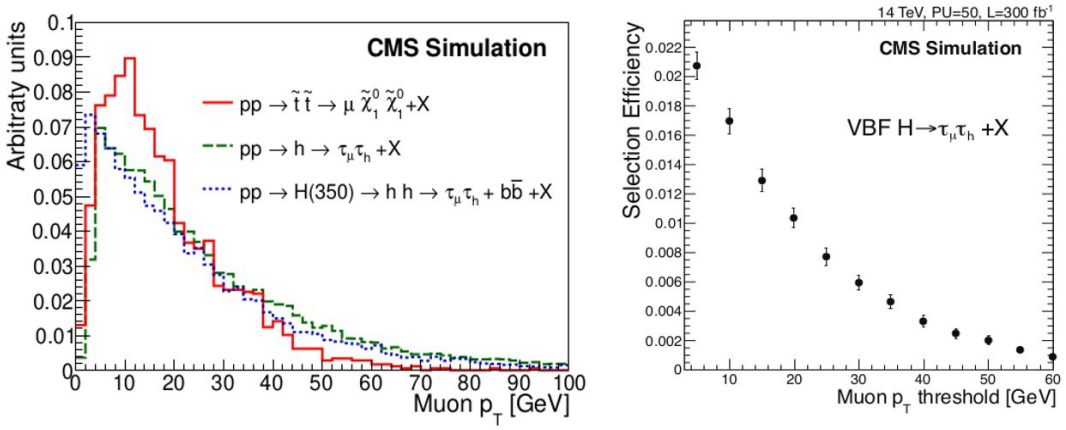

Figure 2.26: Left: Muon p_T distributions for the SM Higgs coupling to τ leptons, $h \to \tau\tau + X$; heavy Higgs decay into τ leptons, $H \to hh \to \tau\tau bb$; and the production of SUSY "stop" particles, $p \to \tilde{t}\tilde{t} \to \mu\tilde{\chi}_1^0\tilde{\chi}_1^0 + X$ [58]. Right: The complete analysis selection efficiency for the $h \to \tau\tau$ channel in the $\mu\tau_h$ VBF category is presented as a function of the selected offline muon p_T threshold [58].

2.7.3 Influence on the Phase-II Trigger System

The upgraded CMS L1 Trigger system following LS3 will markedly enhance muon reconstruction efficiency and quality by aligning standalone muons ("L1Mu") with tracker data ("track-trigger tracks"). This collaboration gives rise to the composite object "L1TkMu", ensuring a high-purity, low-rate trigger at low p_T thresholds.

Preserving the high quality of the standalone muon trigger is imperative for the HL-LHC. Several physics scenarios anticipate the presence of heavy, long-lived exotic particles that may undergo decay at a substantial distance from the IP, resulting in the production of a pair of muons. In such cases, only a few muon hits may be recorded in the tracker, leading to a significant inefficiency in the tracking trigger. Consequently, the standalone muon trigger emerges as the most practical option for detecting these events. These potential scenarios arise from SUSY extensions like the Next-to-Minimal Super-Symmetric Standard Model (NMSSM) [60], "hidden valleys"

(Dark SUSY) [61], and heavy resonance models [62]. In Dark SUSY scenarios, new bosons are expected following the decay of a 125 GeV SM-like Higgs boson H into pairs neutralinos (n_1). Subsequently, these neutralinos decay into dark neutralinos n_D and low-mass dark photons γ_D or dark neutralinos and heavy dark bosons Z_D. The dark bosons can then decay into a pair of muons. Figure 2.27 illustrates the trigger reconstruction efficiency for the two Dark SUSY decays as a function of the transverse distance between the decay vertex and the beamline. With increasing distance, the combined L1TkMu efficiency decreases rapidly, while the standalone L1Mu efficiency remains constant. Therefore, upgrading the first muon station will contribute to

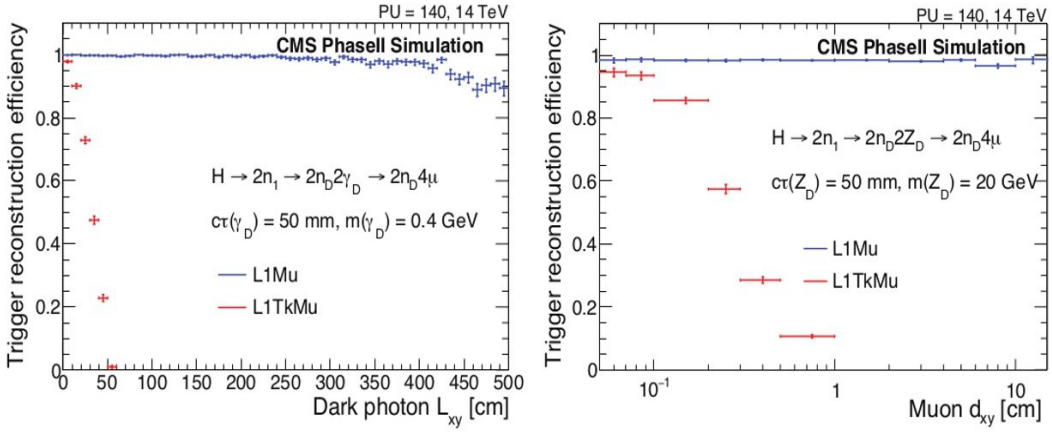

Figure 2.27: Left: Comparison of the efficiencies between the combined L1TkMu trigger and the standalone L1Mu trigger for Dark SUSY decays, $H(125) \rightarrow 2n_1 \rightarrow 2n_D 2\gamma_D \rightarrow 2n_D 4\mu$ [58]. Right: For $H(125) \rightarrow 2n_1 \rightarrow 2n_D 2Z_D \rightarrow 2n_D 4\mu$ [58].

maintaining the effectiveness of the L1 standalone muon trigger at the HL-LHC and improving the detection of displaced muons.

2.7.4 Effects of Aging on the CSC System

The CSC chambers, similar to other detectors functioning in high-radiation environments, are prone to aging, which means a decline in detection capability over time. Positioned as the sole system in the front endcaps, any decrease in performance or loss of detection regions would have a significant impact on the entire muon spectrometer, affecting both the L1 Trigger (Phase-I and Phase-II) and offline muon reconstruction. This aging concern becomes particularly critical at the HL-LHC, where the background rate is expected to reach approximately 1 kHz/cm^2 in the first station.

There are four acknowledged forms of aging: typical electronics deterioration, leading to around 1% losses per year; problematic low voltage and signal connections, estimated to result in 10% losses; challenges related to data transfer and potential data loss; and the traditional aging of gaseous detectors, especially wire chambers. The third factor is notably challenging to estimate due to its dependence on the operational environment. The CMS muon group has examined various scenarios, and in all instances, the projected proportion of non-operational CSCs at the HL-LHC is approximately 15% [63]. The introduction of a second detection layer will help

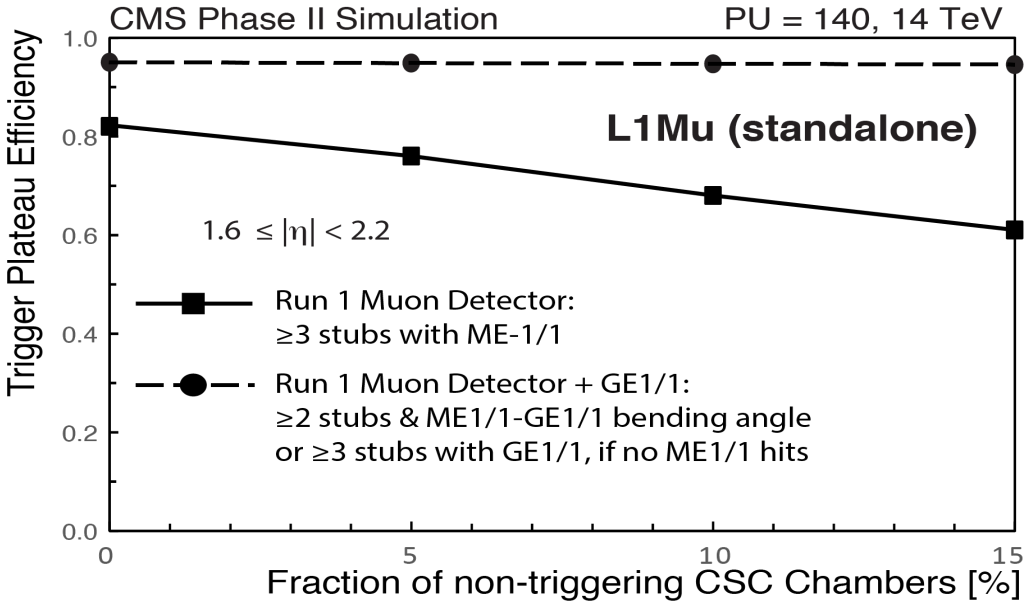

Figure 2.28: The efficiency of the single-muon trigger at the p_T plateau is illustrated based on the proportion of non-triggering CSC chambers in both Phase-I and Phase-II [58].

counteract any losses in the CSC system, ensuring the highest reconstruction and selection efficiency. The trigger efficiency at the p_T plateau is depicted in Figure 2.28 as a function of the proportion of non-triggering CSCs for the exclusive CSC system, associated with GE1/1 detectors.

2.8 Conclusions

The LHC upgrade aims to increase the $\sqrt{s} = 14$ TeV and steadily raise luminosity to $5 - 7 \times 10^{34}$ cm^{-2}s^{-1}. Consequently, the HL-LHC will grant access to higher energy ranges and explore rare decays that could either support or challenge hypotheses BSM.

However, the enhanced collision rate will impact the CMS detection environment. Specifically, an increase in the background rate in the forward area of the CMS muon endcaps will result in a higher L1 muon trigger rate and reduced selection efficiency within specified bandwidth constraints. Additionally, the increased radiation background may accelerate the aging of the existing CSC system, potentially causing performance degradation and the appearance of dead zones.

To tackle these challenges, the CMS GEM Collaboration proposes integrating additional gaseous detectors into the front endcaps to complement the existing CSC system. These new chambers, utilizing GEM technology, can operate at very high-rates while supplying valuable trigger information to optimize CMS operation.

Bibliography

[1] P. M. Watkins. "DISCOVERY OF THE W AND Z BOSONS". In: *Contemp. Phys.* 27 (1986), pp. 291–324. DOI: 10.1080/00107518608211015.

[2] Yu-Gang Ma, Jin-Hui Chen, and Liang Xue. "A brief review of antimatter production". In: *Front. Phys. (Beijing)* 7 (2012), pp. 637–646. DOI: 10.1007/s11467-012-0273-9. arXiv: 1301.4902 [nucl-ex].

[3] Bohdan Grzadkowski and Zenro Hioki. "Signals of CP violation in distributions of top-quark decay products at linear colliders". In: *7th International Symposium on Particles, Strings and Cosmology*. Mar. 2000, pp. 189–193. DOI: 10.1142/9789812792433_0028. arXiv: hep-ph/0003294.

[4] D M Sendall. "The World-Wide Web past present and future, and its application to medicine". In: (1997). URL: https://cds.cern.ch/record/321530.

[5] Navrit Johan Singh Bal et al. "Medipix3 proton and carbon ion measurements across full energy ranges and at clinical flux rates in MedAustron IR1". In: *JINST* 16.12 (2021), p. C12002. DOI: 10.1088/1748-0221/16/12/C12002. arXiv: 2108.01908 [physics.ins-det].

[6] "The Large Electron-Positron Collider". In: (2012). URL: https://cds.cern.ch/record/1997351.

[7] Michaela Schaumann et al. "First Xenon-Xenon Collisions in the LHC". In: *9th International Particle Accelerator Conference*. June 2018. DOI: 10.18429/JACoW-IPAC2018-MOPMF039.

[8] G. Aad et al. "The ATLAS Experiment at the CERN Large Hadron Collider". In: *JINST* 3 (2008), S08003. DOI: 10.1088/1748-0221/3/08/S08003.

[9] K. Aamodt et al. "The ALICE experiment at the CERN LHC". In: *JINST* 3 (2008), S08002. DOI: 10.1088/1748-0221/3/08/S08002.

[10] A. Augusto Alves Jr. et al. "The LHCb Detector at the LHC". In: *JINST* 3 (2008), S08005. DOI: 10.1088/1748-0221/3/08/S08005.

[11] Johan Sebastian Bonilla Castro. "Reconstructing the Top Quark in a Search for a Pair-Produced Supersymmetric Partner in the All-Hadronic plus Missing Energy Final State Using 139 fb^{-1} of $\sqrt{s} = 13$ TeV Proton-Proton Collisions Delivered by the Large Hadron Collider and Collected by the ATLAS Detector". Presented 25 Nov 2019. PhD thesis. 2019. URL: https://cds.cern.ch/record/2707010.

[12] Deborah Pinna. "Search for Dark Matter in Association with Top Quarks with the CMS Detector". PhD thesis. 2017. URL: https://cds.cern.ch/record/2291377.

[13] "LHC Machine". In: *JINST* 3 (2008). Ed. by Lyndon Evans and Philip Bryant, S08001. DOI: 10.1088/1748-0221/3/08/S08001.

[14] Tapan Nayak and Bikash Sinha. "Search and study of Quark Gluon Plasma at the CERN-LHC". In: *Physics at the Large Hadron Collider*. Ed. by Amitava Datta et al. 2009, pp. 131–144. DOI: 10.1007/978-81-8489-295-6_9. arXiv: 0904.3428 [nucl-ex].

[15] Roel Aaij et al. "Observation of CP Violation in Charm Decays". In: *Phys. Rev. Lett.* 122.21 (2019), p. 211803. DOI: 10.1103/PhysRevLett.122.211803. arXiv: 1903.08726 [hep-ex].

[16] Roel Aaij et al. "Measurement of the time-integrated CP asymmetry in $D^0 \to K^0_S K^0_S$ decays". In: *JHEP* 11 (2018), p. 048. DOI: 10.1007/JHEP11(2018)048. arXiv: 1806.01642 [hep-ex].

[17] Brendan James Regnery. "The BEST Thesis: The Boosted Event Shape Tagger, A Search for Vector-like Quarks, and A Real GEM in CMS". PhD thesis. UC Davis (main), UC Davis, Feb. 2023.

[18] I. Zurbano Fernandez et al. "High-Luminosity Large Hadron Collider (HL-LHC): Technical design report". In: 10/2020 (Dec. 2020). Ed. by I. Béjar Alonso et al. DOI: 10.23731/CYRM-2020-0010.

[19] Shane Davy Breeze. "Precision measurement of the Z invisible width with the CMS experiment". PhD thesis. Imperial Coll., London, 2019. DOI: 10.25560/80981.

[20] S. Chatrchyan et al. "The CMS Experiment at the CERN LHC". In: *JINST* 3 (2008), S08004. DOI: 10.1088/1748-0221/3/08/S08004.

[21] G. L. Bayatian et al. "CMS Physics: Technical Design Report Volume 1: Detector Performance and Software". In: (2006).

[22] Anna Benecke. "Searches for new heavy bosons and vector-like quarks with the CMS experiment at $\sqrt{s}$ = 13 TeV and novel pileup mitigation techniques". PhD thesis. Hamburg U., 2020.

[23] R. Fruhwirth. "Application of Kalman filtering to track and vertex fitting". In: *Nucl. Instrum. Meth. A* 262 (1987), pp. 444–450. DOI: 10.1016/0168-9002(87)90887-4.

[24] "CMS Technical Design Report for the Pixel Detector Upgrade". In: (Sept. 2012). Ed. by David Aaron Matzner Dominguez et al. DOI: 10.2172/1151650.

[25] W. Adam et al. "The CMS Phase-1 Pixel Detector Upgrade". In: *JINST* 16.02 (2021), P02027. DOI: 10.1088/1748-0221/16/02/P02027. arXiv: 2012.14304 [physics.ins-det].

[26] Francesca Cavallari. "Performance of calorimeters at the LHC". In: *J. Phys. Conf. Ser.* 293 (2011). Ed. by Yifang Wang, p. 012001. DOI: 10.1088/1742-6596/293/1/012001.

[27] Giovanni Mocellin. "Performance of the GE1/1 detectors for the upgrade of the CMS muon forward system". PhD thesis. RWTH Aachen University, Rheinisch-Westfälischen Technischen Hochschule (RWTH) Aachen, RWTH Aachen U., 2022. DOI: 10.18154/rwth-2021-07066.

[28] Serguei Chatrchyan et al. "Energy Calibration and Resolution of the CMS Electromagnetic Calorimeter in pp Collisions at $\sqrt{s} = 7$ TeV". In: *JINST* 8 (2013), P09009. DOI: 10.1088/1748-0221/8/09/P09009. arXiv: 1306.2016 [hep-ex].

[29] Giovanni Mocellin. "Performance of the GE1/1 detectors for the upgrade of the CMS muon forward system". Presented 19 Jul 2021. PhD thesis. 2021. URL: https://cds.cern.ch/record/2809098.

[30] Albert M Sirunyan et al. "Calibration of the CMS hadron calorimeters using proton-proton collision data at $\sqrt{s} = 13$ TeV". In: *JINST* 15.05 (2020), P05002. DOI: 10.1088/1748-0221/15/05/P05002. arXiv: 1910.00079 [physics.ins-det].

[31] R. L. Workman et al. "Review of Particle Physics". In: *PTEP* 2022 (2022), p. 083C01. DOI: 10.1093/ptep/ptac097.

[32] A. M. Sirunyan et al. "Performance of the CMS muon detector and muon reconstruction with proton-proton collisions at $\sqrt{s} = 13$ TeV". In: *JINST* 13.06 (2018), P06015. DOI: 10.1088/1748-0221/13/06/P06015. arXiv: 1804.04528 [physics.ins-det].

[33] Barbara Alvarez Gonzalez. "CMS Muon Drift Tubes HL-LHC Slice Test". In: (Oct. 2021). arXiv: 2110.15052 [physics.ins-det].

[34] V. Barashko et al. "Fast algorithm for track segment and hit reconstruction in the CMS cathode strip chambers". In: *Nucl. Instrum. Meth. A* 589 (2008), pp. 383–397. DOI: 10.1016/j.nima.2008.02.096.

[35] L. H. Baekeland. "The Synthesis, Constitution, and Uses of Bakelite." In: *Journal of Industrial & Engineering Chemistry* 1.3 (1909), pp. 149–161. DOI: 10.1021/ie50003a004. eprint: https://doi.org/10.1021/ie50003a004. URL: https://doi.org/10.1021/ie50003a004.

[36] Thomas Hebbeker and Andrey Korytov. "The Phase-2 Upgrade of the CMS Muon Detectors". In: (Sept. 2017).

[37] Serguei Chatrchyan et al. "Performance of CMS Muon Reconstruction in pp Collision Events at $\sqrt{s} = 7$ TeV". In: *JINST* 7 (2012), P10002. DOI: 10.1088/1748-0221/7/10/P10002. arXiv: 1206.4071 [physics.ins-det].

[38] "CMS Technical Design Report for the Level-1 Trigger Upgrade". In: (June 2013). Ed. by A. Tapper and Darin Acosta.

[39] Albert M Sirunyan et al. "Performance of the CMS Level-1 trigger in proton-proton collisions at $\sqrt{s} = 13$ TeV". In: *JINST* 15.10 (2020), P10017. DOI: 10.1088/1748-0221/15/10/P10017. arXiv: 2006.10165 [hep-ex].

[40] Carlos Vico Villalba. "Performance of the CMS muon trigger system in proton-proton collisions at 13 TeV". In: *PoS* EPS-HEP2021 (2022), p. 762. DOI: 10.22323/1.398.0762.

[41] Cecilia Tosciri. "The Large Hadron Collider and the ATLAS Detector". In: *Higgs Boson Decays into a Pair of Bottom Quarks: Observation with the ATLAS Detector and Machine Learning Applications*. Cham: Springer International Publishing, 2021, pp. 35–48. ISBN: 978-3-030-87938-9. DOI: 10.1007/978-3-030-87938-9_4. URL: https://doi.org/10.1007/978-3-030-87938-9_4.

[42] Hannes Bartosik et al. "The LHC Injectors Upgrade (LIU) Project at CERN: Ion Injector Chain". In: *8th International Particle Accelerator Conference*. May 2017. DOI: 10.18429/JACoW-IPAC2017-TUPVA020.

[43] M. Borsato et al. "Unleashing the full power of LHCb to probe stealth new physics". In: *Rept. Prog. Phys.* 85.2 (2022), p. 024201. DOI: 10.1088/1361-6633/ac4649. arXiv: 2105.12668 [hep-ph].

[44] "Addendum to the Technical Design Report for the Upgrade of the ALICE Time Projection Chamber". In: (Feb. 2015).

[45] Marco Valente. *The ATLAS Trigger and Data Acquisition Upgrades for the High-Luminosity LHC (HL-LHC)*. Tech. rep. Geneva: CERN, 2020. DOI: 10.22323/1.364.0184. URL: https://cds.cern.ch/record/2692161.

[46] Djamel Eddine Boumediene. "ATLAS Calorimeters: Run-2 performance and Phase-II upgrade". In: (2017). URL: https://cds.cern.ch/record/2274535.

[47] T Kawamoto et al. *New Small Wheel Technical Design Report*. Tech. rep. ATLAS New Small Wheel Technical Design Report. 2013. URL: https://cds.cern.ch/record/1552862.

[48] *Technical Design Report: A High-Granularity Timing Detector for the ATLAS Phase-II Upgrade*. Tech. rep. Geneva: CERN, 2020. URL: https://cds.cern.ch/record/2719855.

[49] F.P. Albicocco et al. "Long-term Operation of the Multi-Wire-Proportional-Chambers of the LHCb Muon System". In: *JINST* 14 (2019), P11031. DOI: 10.1088/1748-0221/14/11/P11031. arXiv: 1908.02178. URL: https://cds.cern.ch/record/2687705.

[50] Lukas Gruber. "LHCb SciFi — Upgrading LHCb with a scintillating fibre tracker". In: *Nucl. Instrum. Methods Phys. Res., A* 958 (2020), p. 162025. DOI: 10.1016/j.nima.2019.03.080. URL: https://cds.cern.ch/record/2712243.

[51] LHCb Collaboration. *LHCb VELO Upgrade Technical Design Report*. Tech. rep. 2013. URL: https://cds.cern.ch/record/1624070.

[52] *The Phase-2 Upgrade of the CMS Barrel Calorimeters*. Tech. rep. This is the final version, approved by the LHCC. Geneva: CERN, 2017. URL: https://cds.cern.ch/record/2283187.

[53] Fabienne Landua. "CMS detector LS2 upgrade in four languages". In: (2022). General Photo. URL: https://cds.cern.ch/record/2809003.

[54] CMS Collaboration. *Technical proposal for the upgrade of the CMS detector through 2020*. Tech. rep. 2011. URL: https://cds.cern.ch/record/1355706.

[55] *The Phase-2 Upgrade of the CMS Endcap Calorimeter*. Tech. rep. Geneva: CERN, 2017. DOI: 10.17181/CERN.IV8M.1JY2. URL: https://cds.cern.ch/record/2293646.

[56] M. Tytgat et al. *Improved RPC for CMS muon system upgrade for HL-LHC*. Tech. rep. 11. Geneva: CERN, 2020. DOI: 10.1088/1748-0221/15/11/C11012. arXiv: 2005.11396. URL: https://cds.cern.ch/record/2792678.

[57] "Technical Proposal for the Phase-II Upgrade of the CMS Detector". In: (June 2015). Ed. by D. Contardo et al. DOI: 10.17181/CERN.VU8I.D59J.

[58] A Colaleo et al. *CMS Technical Design Report for the Muon Endcap GEM Upgrade*. Tech. rep. 2015. URL: https://cds.cern.ch/record/2021453.

[59] C. Ahdida et al. "New Capabilities of the FLUKA Multi-Purpose Code". In: *Front. Phys.* 9 (2022), p. 788253. DOI: 10.3389/fphy.2021.788253. URL: https://cds.cern.ch/record/2806210.

[60] A. Djouadi, U. Ellwanger, and A. M. Teixeira. "Phenomenology of the constrained NMSSM". In: *JHEP* 04 (2009), p. 031. DOI: 10.1088/1126-6708/2009/04/031. arXiv: 0811.2699 [hep-ph].

[61] Tao Han et al. "Phenomenology of hidden valleys at hadron colliders". In: *JHEP* 07 (2008), p. 008. DOI: 10.1088/1126-6708/2008/07/008. arXiv: 0712.2041 [hep-ph].

[62] L. Basso et al. "Phenomenology of the minimal B-L extension of the Standard Model". In: *PoS* EPS-HEP2009 (2009), p. 242. DOI: 10.22323/1.084.0242. arXiv: 0909.3113 [hep-ph].

[63] J Butler et al. *CMS Phase II Upgrade Scope Document*. Tech. rep. Geneva: CERN, 2015. URL: https://cds.cern.ch/record/2055167.

Chapter 3

Gaseous Detectors and CMS GEM Upgrades

"No knowledge comes from the outer world to the mind. It has to be acquired by the mind in the outer world."

— S N Bose, 1894–1974

3.1 Introduction

In this chapter, we will explore the theoretical principles related to particle detection, with a specific emphasis on gaseous detectors. Our focus will be on understanding the underlying physics processes that may occur in the CMS endcaps or during Research and Development (R&D) activities in the laboratory. Additionally, we will present concrete examples to illustrate the detection capabilities using common gas molecules used in CMS muon systems, such as Ar, CO_2, and Tetrafluoromethane (CF_4). Furthermore, we will outline the fundamental operation of gaseous detectors and provide a concise historical overview of their evolution. Following this, we will closely examine GEM detectors and their role in the CMS upgrades.

3.2 Principles of Operation for Gaseous Detectors

The twentieth century experienced a notable increase in the development of detector technologies, with the gaseous detector standing out for its lasting impact. Contrary to the initial perception of theoretical simplicity, gaseous detectors underwent significant evolution during the twentieth century, driven by advances in electronic capabilities. This evolution coincided with the introduction of personal computers and the associated technology for microchip printing. This led to the development of Micro-Pattern Gas Detector (MPGD)s, which are currently utilised in various major High-Energy Physics (HEP) experiments and are consistently integrated as crucial components for planned experiments at future colliders.

In its most basic form, a gaseous detector consists of a gas volume enclosed between two metal electrodes. An electric field is applied across these electrodes, automatically designating them as the anode and cathode. As a particle, whether charged or neutral, moves through the gas, it locally interacts with the gas atoms, leading to the formation of electron-ion pairs. The generation of these pairs relies on various parameters, such as the particle's charge and mass, which are extensively discussed in Section 3.3 covering the physics of particle interaction. Under the influence of the electric field, electrons and ions both migrate towards the anode and cathode, respectively. If the electric field strength is sufficient, electrons can gain enough energy to further ionize the gas atoms, initiating an avalanche effect. This triggers an exponential increase in the number of free electrons and ions. Section 3.4 provides detailed discussions on drift, avalanche processes, and signal formation, illustrating how the specifics of the avalanche process are dependent upon the gas detector's mode of operation. The various operational modes for gas detectors will be examined in Section 3.5.

The electrons and ions continue to drift towards the anode and cathode, generating current on both electrodes. The readout electronics utilise this current to produce the final signal. The pulse form of this signal is subject to analysis, allowing for the determination of time resolution.

3.3 Particle-Matter Interactions

The initial phase of particle detection involves the interaction between particles and the detector's sensitive material. Among the particles generated in LHC collisions, those

that persist and traverse sufficiently to reach the sensitive layers of the experiments are most relevant for detection and called as stable particles. These particles do not decay within the timescale of the experiment, rendering them suitable for in-depth analysis. Unstable particles, prone to rapid decay, are usually excluded from detection considerations due to potential limitations in reaching the experiment's sensitive layers. Categorising particles based on their charge, as shown in Table 3.1, is useful for organising subsequent discussions.

Charged Particles (characteristics length[1] $\cong 10^{-5}\ m$)	**Uncharged Particles** (characteristics length $\cong 10^{-1}\ m$)
Heavy Charged Particles	Neutrons
Fast Electrons	X-Rays and Gamma rays

Table 3.1: Categorisation of particle on the basis of their charge [1].

3.3.1 Charged Particle-Matter Interaction

3.3.1.1 Heavy Charged Particles

As heavy charged particles (those with a mass significantly higher than that of an electron) traverse a medium, they undergo collisions mediated by EM, weak, or strong forces. While the weak interaction is typically only significant for particles like neutrinos, the strong interaction, responsible for binding nucleons within atomic nuclei, has a limited range, confined to the nuclear cross-section. This range is orders of magnitude lower (approximately 10^8 to 10^{10} times) than that of the EM interaction. As a result, the EM interaction becomes the predominant method for detecting charged particles.

3.3.1.1.1 Coulomb Interaction-Induced Energy Loss

The Coulomb interaction between the EM fields of the particle and the medium serves as the prevailing mechanism in EM interactions. This interaction excites and/or

[1] characteristic length refers to the typical distance scale associated with particle interactions or the spatial extent over which certain phenomena occur.

ionizes the medium, resulting in the release of free charges that can be utilised to generate electrical signals.

When a heavy charged particle passes through a layer of matter, it engages with atomic electrons, transferring a portion of its energy. This interaction leads to ionisation and/or excitation of the medium. In ionisation, atomic electrons acquire sufficient energy to be ejected from the atom, forming electron-ion pairs within the medium. In cases where atoms remain unionised, they become excited by the incoming particle, releasing electrons through de-excitation mechanisms.

The Bethe-Bloch formula computes the average energy dissipated by a particle as it traverses a material:

$$-\left\langle \frac{dE}{dx} \right\rangle = \frac{2\pi e^4 z^2}{m_e c^2 \beta^2} NZ \left[\ln\left(\frac{2m_e c^2 \beta^2 \gamma^2 T_m}{I^2} \right) - 2\beta^2 - \delta(\beta\gamma) \right] \tag{3.1}$$

where the charge of the incoming particle (ze), rest mass of an electron (m_e), atomic density (N), Z, Fermi density effect correction ($\delta(\beta\gamma)$) and characterstic average ionization and excitation potential of the medium (I) are represented by their respective symbols. The maximum energy transfer (T_m) for a single interaction is given by:

$$T_m = \frac{2m_e c^2 \beta^2 \gamma^2}{1 + 2\gamma \frac{m_e}{M} + \left(\frac{m_e}{M}\right)^2} \tag{3.2}$$

For heavy charged particle $M \gg m_e$

$$T_m = \frac{2m_e c^2 \beta^2}{1 - \beta^2} \tag{3.3}$$

In this form, the Bethe-Bloch formula is applicable within the range $0.1 \lesssim \beta\gamma \lesssim 1000$. When $\beta\gamma \gtrsim 4$, there is a relativistic increase in stopping power due to the heightened transverse electric field of the particle, resulting in increased distant interaction contributions. Simultaneously, the polarisation of the medium restricts field extension, serving as a shield for the electric field distant from the particle's path and diminishing long-range effects. To address this phenomenon, Equation 3.1 introduces the $\delta(\beta\gamma)$. The assumption that the electron is at rest becomes inaccurate at very low energies ($\beta\gamma \lesssim 0.1$), where the particle velocity aligns with the orbital velocity of atomic electrons, permitting electron capture activities.

To thoroughly explain the low-energy range, it becomes necessary to make additional corrections, including shell corrections, Bloch corrections, and Barkas corrections [2]. At higher energies ($\beta\gamma \gtrapprox 10^4$ for muons), radiative reactions surpass ionisation. The average energy loss $\langle \frac{dE}{dx} \rangle$ is no longer a continuous function solely based on Coulomb interactions. Instead, it transforms into a complex combination of various effects such as electron-positron pair formation, Bremsstrahlung, and photonuclear interactions [3]. In the realm of HEP experiments, specifically within the CMS

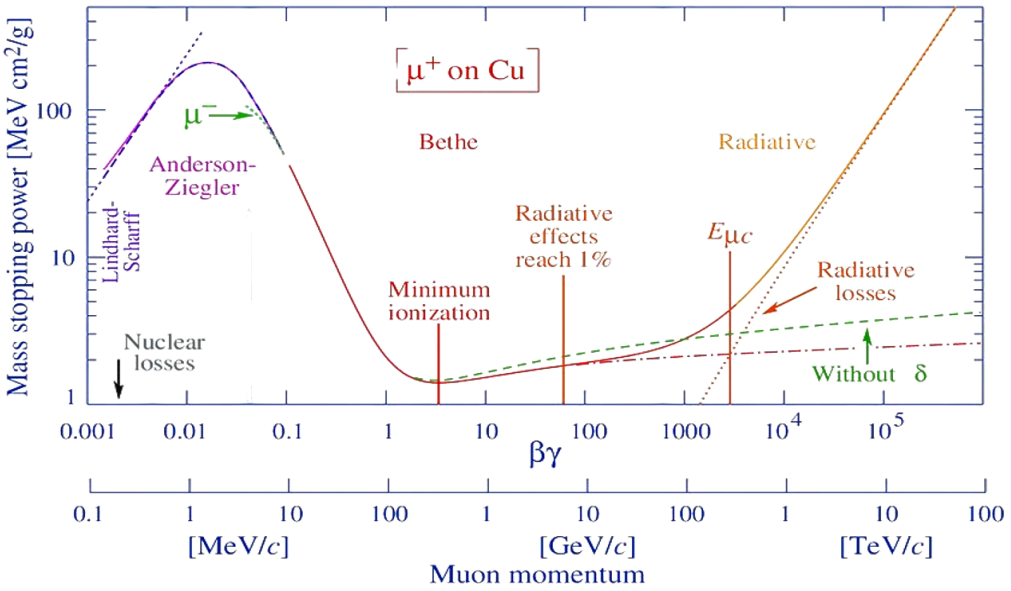

Figure 3.1: The stopping power of positive muons in copper is depicted as a function of $\beta\gamma$. The solid curves illustrate the complete stopping power [4].

muon system, most relativistic particles demonstrate a mean energy loss close to the minimum ionizing value. These particles are commonly denoted as MIP, and their mean energy loss is typically around 2 MeV/cm in the material of the CMS muon system. Figure 3.1 presents a depiction of the average energy loss of a positive muon in copper.

CMS muon detectors primarily operate using Ar-based mixtures. The average energy loss of MIPs in Ar is approximately 1.53 $\mathrm{MeV g^{-1} cm^2}$, as illustrated in Figure 3.2. With the density of Ar represented as $\rho = 1.78 \times 10^{-3}\,\mathrm{g \cdot\ cm^{-3}}$, the total energy loss per unit length in pure Ar is expressed as follows:

$$\Delta E_{argon} = -\left\langle \frac{dE}{dx} \right\rangle \times \rho \times d = 1.53 \times 1.78 \times 10^{-3} \times 1 = 2.72 \text{ keV/cm} \qquad (3.4)$$

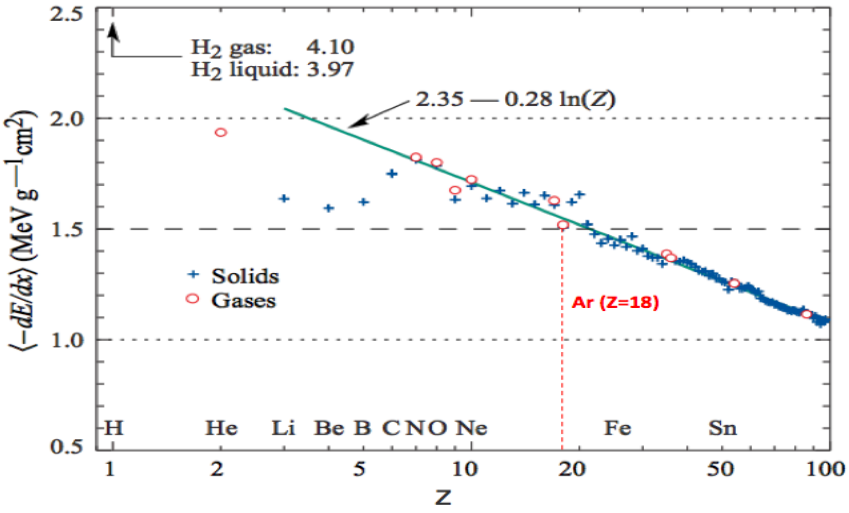

Figure 3.2: The energy loss of a MIP relative to the Z of the medium, with the red line specifically denoting Ar (Z = 18) [5].

3.3.1.1.2 Ionisation Processes

In the case of energy loss via ionisation, the incoming particle discharges a distinct number of electron-ion pairs in the surrounding medium. This process is referred to as primary ionisation. The released electrons may have enough kinetic energy to trigger secondary ionisation within the medium. These electrons are generally labelled as δ-rays and their quantity (n) per unit length (dx), with a kinetic energy in the range of T to T + dT, can be computed using the following method:

$$\frac{d^2n}{dTdx} = \frac{2\pi e^4 z^2}{m_e \beta^2 c^2} NZ \frac{1}{T^2} \left[1 - \beta^2 \frac{T}{T_m} \right] \tag{3.5}$$

The maximum energy that a heavy particle can transfer to an electron is described as follows [6]:

$$T_m = 2m_e \beta^2 c^2 \gamma^2 \tag{3.6}$$

The total number of electron-ion pairs generated within a specified volume due to both primary and secondary ionisation is formulable as follows:

$$n_T = \frac{\Delta E}{W_i} \tag{3.7}$$

where the overall energy loss transmitted to a specified volume (ΔE), while effective average energy required for the formation of a single electron-ion pair (W_i) are their respective symbols. Due to the absorption of some deposited energy by excitation processes, not always resulting in the liberation of electrons in the medium, the parameter W_i frequently exceeds the average ionisation and excitation potential I (see Equation 3.1).

If the target medium is composed of various elements, the average energy W_i of the medium is determined using a basic composition law. For example, in the scenario of a muon detector containing an Ar/CO_2 mixture (in percentage ratio 70/30) , the total count of primary electrons generated by MIPs can be determined. By applying the same method as described in Equation 3.4, the complete energy loss transmitted through the medium over a distance of 3 mm is ΔE = 861 eV. Consequently:

$$n_T = \Delta E \left[\frac{0.7}{W_i(Ar)} + \frac{0.3}{W_i(CO_2)} \right] \tag{3.8}$$

3.3.1.1.3 The Penning Effect

The earlier discussion specifically addressed direct ionisation, represented as $A \rightarrow A^+ e^-$. Additional ionisation processes may take place through the excited states of gas atoms, contingent on the gas composition. An example of this is when a charged particle excites an atom A, transferring its excitation energy to atom B. Atom B may undergo ionisation if the excitation energy of A exceeds the lowest ionisation potential of B. The Penning effect encapsulates this process, expressed as $A^* B \rightarrow AB^+ e^-$.

As more primary electrons are produced, the Penning effect decreases the W_i-value. It is crucial to integrate this phenomenon into simulation methods, as it can impact the detector's gain. The Penning transfer probability (f_p) acts as a measure for the Penning effect, depending on the gas mixture and the respective densities of the atoms. Determining f_p proves to be a challenging process, requiring alignment with experimental data and lacking a straightforward formula or theory. Consider the gas combination of Ar/CO_2 commonly used in gaseous detectors. CO_2 possesses a lowest ionisation potential of 13 eV, which is lower than the excitation levels of Ar. With a gas composition of 75-25%, the Penning transfer probability is indicated as f_p = 0.57.

3.3.1.2 Fast Electrons

Equation 3.1, initially devised to explain Rutherford scattering involving heavy particles, surprisingly finds application in describing low-energy incoming electrons. The complexity of electron scattering in matter increases due to their low mass, requires the inclusion of relativistic corrections even at kinetic energies as modest as several hundred keV. Importantly, the mass of an electron, comparable to that of the orbital electrons it interacts with, leads to substantial deviations in its trajectories. This phenomenon results in a significantly greater portion of the electron's energy being dissipated in a single interaction, setting electron interactions apart from those involving heavier particles.

Occasional electron-nuclear interactions can abruptly alter the electron's direction, further contributing to the overall complexity of its behaviour within matter. The computation of energy loss attributed to ionization and excitation entails complex calculations-resembling the physical quantity defined in Equation 3.1 as follows:

$$-\left\langle \frac{dE}{dx} \right\rangle_c = \frac{2\pi e^4 NZ}{m_0 v^2}\left(\ln \frac{m_0 v^2 E \gamma^2}{2I} - (\ln 2)(\frac{2}{\gamma} - \frac{1}{\gamma^2}) + \frac{1}{\gamma^2} + \frac{1}{8}(1 - \frac{1}{\gamma}) \right) \tag{3.9}$$

where $m_0 = m_e$ denotes the particle's mass and $\gamma = 1/(\sqrt{1-\beta^2})$, and the remaining symbols maintain the same significance as in Equation 3.1.

Another distinction between electrons and heavy charged particles is the capacity for energy dissipation through radiative processes, like Bremsstrahlung, which can occur at any location along the electron's track [1]. This radiative mechanism results in the following linear energy loss:

$$-\left\langle \frac{dE}{dx} \right\rangle_r = \frac{NEZ(Z+1)e^4}{137 m_0^2 c^4}\left(4 \ln \frac{2E}{m_0 c^2} - \frac{4}{3} \right) \tag{3.10}$$

The inclusion of the m_0^2 term in the multiplicative factor suggests that radiative losses have a negligible impact on heavy charged particles. However, these losses become more significant at higher electron energies and in materials with a higher Z. The determination of the ratio of specific energy losses is approximately determined by:

$$\frac{(dE/dx)_r}{(dE/dx)_c} \approx \frac{EZ}{700} \tag{3.11}$$

where E is expressed in MeV [1].

3.3.2 Neutral Particle-Matter Interactions

3.3.2.1 Photons

The CMS muon detectors will encounter high-energy photons, along with muons and high-energy electrons, exhibiting photon energy spanning from a few hundred keV to several tens of MeV. Moreover, a majority of calibration experiments and the characterization of gaseous detectors involve the utilization of X-ray sources with energies in the several keV range. It is imperative to revisit the fundamental mechanisms governing the interaction of photons with matter.

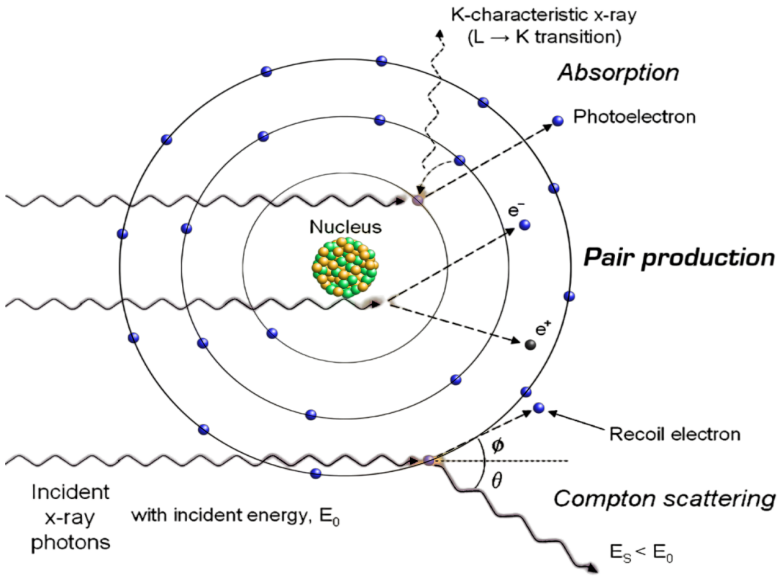

Figure 3.3: The primary absorption processes in photon interactions [5]

Three primary interaction mechanisms contribute to radiation measurements: photoelectric absorption, Compton scattering, and pair production. These mechanisms lead to the either absorption or scattering at a significant angle of the incident photon. Photons engage in EM interactions with matter. In contrast to charged particles that experience continuous energy loss in the medium, the process of photon absorption is a singular and isolated event. The formula for the intensity loss of a photon beam, characterized by energy E and intensity I, as it traverses a material with thickness x, is

expressed as follows:

$$dI = -N\sigma(E, Z)Idx \tag{3.12}$$

where σ denotes the overall cross-section of the interaction associated with a particular material characterised by an Z and N. When the initial intensity of the beam is denoted as I_0, the overall attenuation is determined by:

$$\frac{I}{I_0} = e^{-N\sigma(E,Z)x} = e^{-(\mu/\rho)X} \tag{3.13}$$

where $(\mu/\rho) = N(\sigma/\rho)$ denotes the mass attenuation coefficient, $X = \rho x$ indicates the reduced thickness of the medium, and ρ represents the density of the medium.

As shown in Figure 3.3, various absorption processes exhibit different relative significance depending on the energy of the photons. For energies below a few tens of keV, photoelectric absorption takes precedence, followed by Compton scattering (or incoherent scattering) up to several tens of MeV. At higher energies, the primary process shifts to electron-positron pair production. The total attenuation coefficient is the aggregate sum of all individual coefficients.

$$\frac{\mu}{\rho}_{\text{total}} = \frac{\mu}{\rho}_{\text{photoelectric}} + \frac{\mu}{\rho}_{\text{Compton}} + \frac{\mu}{\rho}_{\text{pair}} \tag{3.14}$$

Figure 3.4 (left) presents a plot of photon attenuation concerning photon energy in the Ar gas. Each of these processes is complex and is accompanied by secondary effects such as fluorescence radiations, Auger electron emission, recoil electrons, or positron annihilation.

3.3.2.1.1 The Photoelectric Absorption

In the case of photoelectric absorption, the entire energy of the incident photon is utilised to remove an electron from an atom's inner shell. This process is feasible only when the photon's energy E_γ exceeds the electron's binding energy E_{bind}. All energy levels with $E_{bind} \leq E_\gamma$ contribute to the phenomenon of photoelectric absorption. The impact is most pronounced near the energy threshold and gradually diminishes with increasing energy, resulting in a distinctive sequence of jumps in the absorption coefficient, as depicted in Figure 3.4 (left). The ejected electron carries an energy

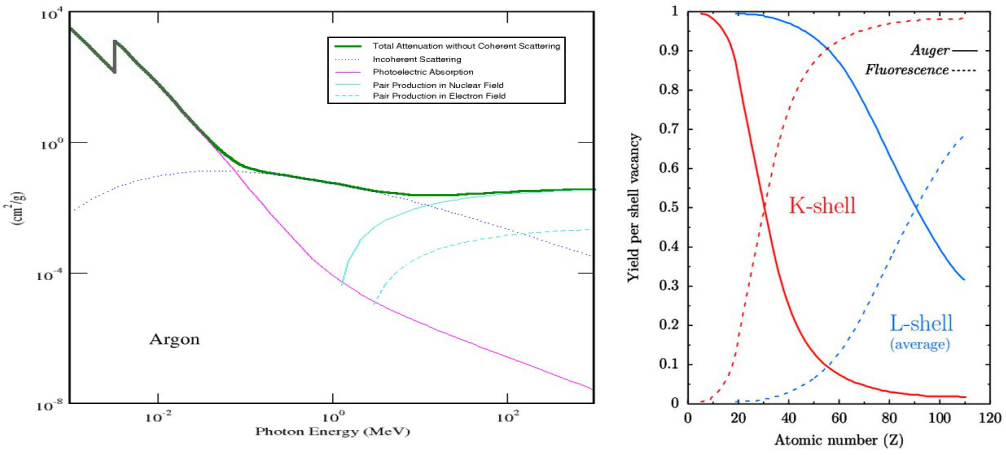

Figure 3.4: Left: Total and partial mass attenuation coefficients Ar gas [7]. Right: The fluorescence yields for K and L shells exhibit variation with the Z. The curve depicting the L-shell is an average of the effective yields for L1, L2, and L3 subshells [8].

$E_e = E_\gamma - E_{bind}$ and exits the medium with increased energy. The medium then returns to its initial state through two opposing mechanisms.

- The Auger process, the primary option under consideration, is characterised by the internal rearrangement of electrons accompanied by the emission of a specific electron. To provide a detailed example, if there is a vacancy in the K-shell, it can be occupied by an electron from the L-shell. During this transition, energy is transferred to an M-shell electron, causing its ejection. The electron emitted in this process is referred to as the Auger electron, and the magnitude of its kinetic energy is established by:

$$E_{Auger} = E_K - E_L - E_M \tag{3.15}$$

- In the following process, termed fluorescence, an electron from an outer i^{th}-shell occupies a vacancy on a j^{th}-shell, releasing an X-ray photon with energy $E_{Xray} = E_j - E_i$, where E_j and E_i represent the binding energies of the j^{th}-shell and i^{th}-shell, respectively. Figure 3.4 (right) illustrates the fraction of de-excitation through fluorescence, known as the fluorescence yield, for the K and L shells.

3.3.2.1.2 The Compton Scattering

In Figure 3.4 (left), the photoelectric absorption cross-section sharply declines after the K-edge. At energies beyond the highest atomic level, the predominant mechanism

causing the intensity loss of a photon beam is the elastic incoherent scattering on nearly free electrons in the medium, commonly known as Compton scattering. When a photon scatters at angle θ, the electron recoils at angle ϕ, as shown in Figure 3.3, the energies of the scattered photon (E_γ) and recoil electron (E_e) are determined by:

$$E_{\gamma}{}' = \frac{E_\gamma}{1 + \xi(1 - \cos\theta)} \tag{3.16}$$

$$E_e = \frac{E_\gamma \xi(1 - \cos\theta)}{1 + \xi(1 - \cos\theta)} \tag{3.17}$$

with $\xi = E_\gamma / m_e c^2$. In the case of back-scattering (i.e., $\theta = \pi$), the electron attains the maximum energy:

$$E_e^{max} = \frac{E_\gamma}{1 + \frac{1}{2\xi}} \tag{3.18}$$

The emission angle of the rebound electron is determined by:

$$\cot\phi = (1 + \xi)\tan\theta/2 \tag{3.19}$$

3.3.2.1.3 The Electron-Positron Pair Production

Pair production, also known as materialisation, involves the absorption of a photon, resulting in the generation of an electron-positron pair within the medium. At higher energies, this process emerges as a dominant mode of interaction, necessitating the presence of either a nucleus or an electron to maintain momentum conservation during the transition.

When a particle is at rest, its minimum energy is described by $E^2 = m_0^2 c^4$, encompassing both negative and positive solutions. The region between these solutions in Figure 3.5 denotes the forbidden energies. The materialisation energy is utilised to transition a particle from the negative energy state, known as the Dirac sea, to the positive realm, leaving the Dirac sea with a "hole" equivalent to an antimatter particle. The threshold energy for the creation of an electron-positron pair by a photon interacting with the electric field of a nucleus is $2m_e c^2 = 1.022$ MeV. The positron is highly likely to undergo annihilation in the medium, producing one or more high-energy photons.

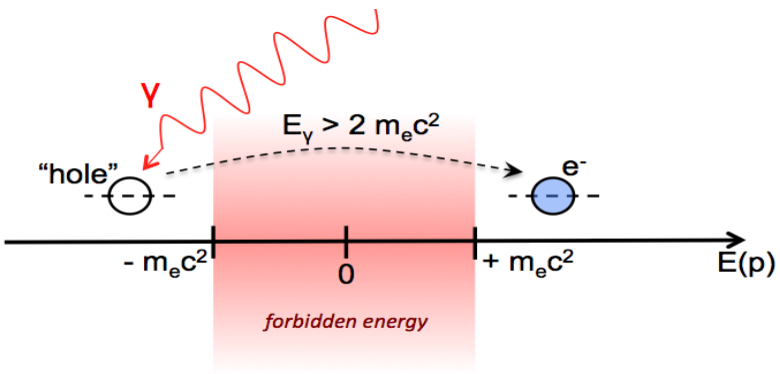

Figure 3.5: Schematic representation of the Dirac sea in the context of electron-positron pair production.

If these secondary photons exceed the threshold energy, they can initiate additional materialisation and annihilation events, leading to an EM cascade within the medium.

3.3.2.2 Neutrons

3.3.2.2.1 Interactions of Neutrons

Neutrons, similar to photons, lack any electric charge and therefore do not interact via the Coulomb interaction. Normally, a neutron interacts with the nucleus of the absorbing substance, although it can traverse matter for several centimetres without interaction. Upon interaction, the neutron might completely disappear, leading to the emergence of one or more secondary radiations, or it may undergo a substantial alteration in energy or direction. Unlike photons, these secondary radiations typically involve heavy charged particles. They stem from either a neutron-induced nuclear reaction or the nuclei of the absorbing material itself, acquiring energy through collisions with neutrons. When a neutron traverses a detector, it has the potential to interact with the surrounding material near the gas volume, resulting in the secondary emission of charged particles or photons. These emitted particles or photons may ionize or excite the gas.

The probability of diverse neutron interactions is notably impacted by the energy of neutrons. Neutrons are typically categorised into categories depending on their energy range as shown in Figure 3.6 and as described below:

- Thermal neutrons are in a state of thermal equilibrium with their surrounding environment, indicating that they have an energy below 0.5 electronvolt (eV)

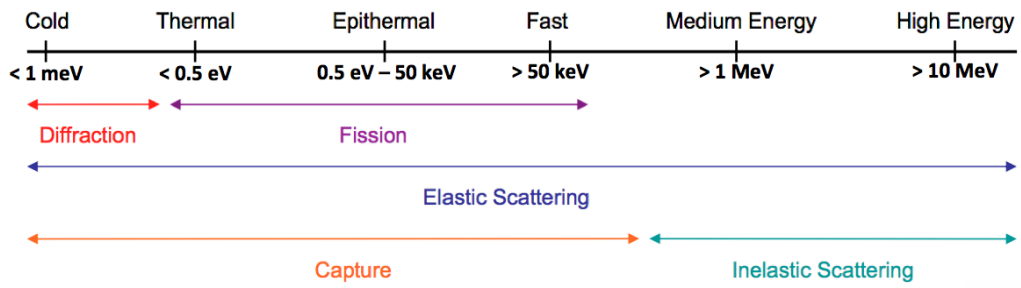

Figure 3.6: Classification of free neutrons based on the most likely sort of interaction with materials.

(where the "Cadmium cut-off" occurs). Their most probable energy is kT = 0.025 eV using Boltzmann constant (k) and they possess a mean energy of $\frac{3}{2}$kT = 0.038 eV.

- Epithermal neutrons possess an energy ranging from 0.5 eVto 50 keV.
- Fast neutrons exhibit an energy range spanning from 50 keV to 1 MeV.
- Medium energy neutrons with an energy range spanning from 1 MeV to 10 MeV.
- High-energy neutrons are characterised by an energy level ranging from 10 MeV to 1 GeV.
- Relativistic neutrons possess an energy greater than 1 GeV, aligning with the mass energy of a nucleon (940 MeV) at which relativistic effects become negligible.

Neutrons undergo various processes influenced by both their energy and the properties of the target material. Elastic collisions among neutrons, characterised by significant kinetic energy transfer, are limited to materials with low atomic mass (A) and hydrogenous properties, such as water, concrete, and polyethylene. Specifically, when the target nucleus consists of a single proton (^{1}H) having mass m_p, the relationship $M = m_p \approx m_n$ is valid. This leads to a maximum energy transfer of $\Delta T_m \approx T$ and a mean energy transfer of $\Delta T_m \approx T/2$ as an outcome of Equation 3.20.

$$\Delta T_m = T\frac{4Mm}{(M+m)^2}\cos^2\phi \tag{3.20}$$

where, T represents the initial kinetic energy, M signifies the mass of the stationary colliding nucleus, m denotes the mass of the incident particle, and ϕ stands for the

angle of the recoil nucleus following the collision, defined in relation to the incident direction of the projectile. The maximum energy transfer is observed when $\phi = 0$.

In the case of neutrons, inelastic scattering primarily involves a neutron capture followed by the emission of a neutron with lower energy in a direction different from the original neutron. The absorber nucleus may be left in an excited state and subsequently decay through photon channels. Conversely, if the nucleus remains in its ground state, the interaction is termed elastic scattering.

The process of capture shares fundamental similarities with inelastic scattering, differing in that it results in more particles in the end state than just a single neutron. This can encompass the emission of various particles, such as an electron, positron, proton, photon, deuteron, triton, α particle, or multiple neutrons. The incoming neutron's energy must surpass a specific threshold for the capture process to occur.

In materials with high Z, the renowned fission process takes place when neutron capture induces the nucleus to split, generating heavy fragments and nucleons with substantial kinetic energy.

Spallation reactions manifest when the neutron attains sufficient energy to interact with individual nucleons within the absorber nucleus. This interaction may lead to an intra-nuclear cascade, giving rise to various types of high-energy particles.

3.3.2.2.2 Neutron Cross-Sections

Experimental discoveries are integrated with theoretical or empirical simulations to formulate precise databases for neutron cross-sections. This collaborative process involves the collaborative efforts of researchers. The main neutron cross-section databases names can be found in Appendix A. These databases cover neutron cross-sections from thermal to 20 MeV and few recent libraries extend upto 150 MeV for certain isotopes.

Figure 3.7 illustrates the elastic and inelastic cross-sections of materials with low-Z, medium-Z, and high-Z. Elastic scattering tends to dominate the overall cross-section. Thermal neutrons have the potential for capture by atomic nuclei, leading to either a capture reaction (for low-Z materials) or nuclear fission (for high-Z materials). Capture processes in the thermal and epithermal regions display a decreasing cross-section following a $1/v$ law, where v represents the neutron velocity. Quantum properties of the nucleus result in discrete peaks, termed resonance peaks, at neutron energies

specific to a particular nuclide in non-elastic processes such as inelastic scattering, capture, and fission.

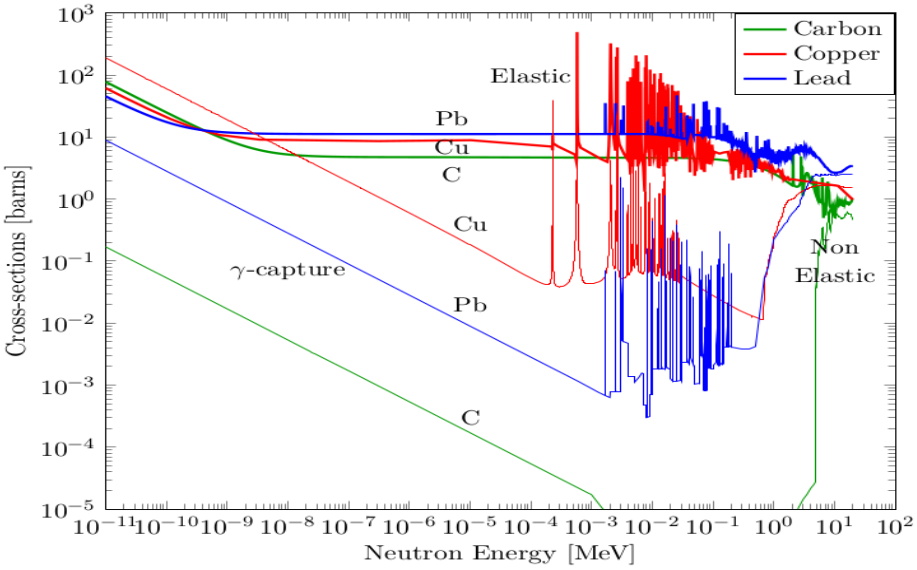

Figure 3.7: Neutron cross-sections for Carbon (Z = 6) are depicted in green, Copper (Z = 28) in red, and Lead (Z = 82) in blue. These data are sourced from neutron cross-section libraries [7]

Radiative capture constitutes the exclusive component of the non-elastic cross-section for non-fissionable nuclei in the thermal and epithermal ranges. Other capture processes occur solely above energy thresholds in the fast-neutron energy range.

3.3.2.2.3 Intra-Nuclear Cascade Models

High-energy heavy particle nuclear reactions involve complex processes, with de Broglie wavelengths at 450 MeV indicating nucleon-nucleon collisions [9]. Experimental nucleon-nucleon cross-sections are used, considering potential interference [10]. If transmitted energy exceeds 150 MeV, the nucleon may escape; otherwise, intra-nuclear cascades (INC) occur. Bertini's 1968 Monte Carlo (MC) simulation for INC [11] leads to non-equilibrium energy distribution across the nucleus. The exciton model [10] explains a pre-equilibrium phase where collisions create excitons, resulting in an equilibrated yet excited nucleus [12]. The excited nucleus emits particles through evaporation, following Weisskopf's model [13], ensuring an isotropic angular distribution. Particle emission continues until the excitation energy falls below a threshold. Breakup models may apply in extreme cases, such as light nuclei or when excitation

energy significantly exceeds binding energy, causing the nucleus to burst into neutrons and protons. Spallation reactions typically involve INC, pre-equilibrium, evaporation, fission, and decay stages. Over the past five decades, significant advancements in nuclear characteristics and particle physics have facilitated precise models for cascade stages, encompassing nucleon distribution, quantum effects, dynamics, exciton and evaporation models, transition models, and more.

3.4 Charge Transport in Gas

In previous sections, it was discussed that particle interaction with a gaseous medium leads to ionisation, known as the primary charge. This signature is exploited for generating electrical signals transmitted to a data acquisition system. The free electrons and ions produced during primary ionisation exist for a short duration, experiencing processes like diffusion, recombination, and others. Their trajectories are influenced by the electromagnetic field and collisions with gas atoms. A thorough understanding of these interactions is crucial when choosing the right gas mixture for particle detectors.

3.4.1 Drift

The primary electrons and ions experience a gradual energy loss during collisions with gas molecules. They also undergo diffusion through multiple scattering, following a Maxwell distribution for their energy ϵ [14]:

$$\frac{dn}{d\epsilon} = F(\epsilon) = \sqrt{\frac{\epsilon}{\pi kT}} e^{\left(-\frac{\epsilon}{kT}\right)} \tag{3.21}$$

n represents the number of charges, T is the absolute temperature. These charges are associated with the thermal energy of the gas, having an average value of $\epsilon_T = \frac{3}{2}kT$. Electrons released during ionisation processes cannot be considered completely free (only for a very short time period), but are influenced by collisions with gas atoms and the electric field within the detector. Due to the small mass of the gas atoms, electrons disperse isotropic ally. The average time interval between two collisions is denoted as τ, and the average electron energy can be expressed as the sum of the thermal energy

ϵ_0 and the contribution ϵ_E gained through electric field acceleration:

$$\epsilon = \epsilon_E + \epsilon_0 = \epsilon_E + \frac{3}{2}kT \tag{3.22}$$

The mean free path, denoted as λ, can be expressed in terms of the collision cross section $\sigma(\epsilon)$, as indicated below:

$$\lambda = \frac{1}{N\sigma(\epsilon)} \tag{3.23}$$

When the mean velocity v and the mean free path λ are combined, the average time between two collisions can be expressed as $\tau = \lambda/v$, or:

$$\tau = \tau(\epsilon) = \frac{1}{N\sigma(\epsilon)v(\epsilon)} \tag{3.24}$$

The collision rate is also known as the reciprocal of τ. An electron undergoes acceleration in an electric field with a component:

$$a = -\frac{eE}{m_e} \tag{3.25}$$

The drift velocity is defined as the average additional velocity acquired due to the electric field or the average acceleration multiplied by the time between two collisions:

$$v_d = \langle at \rangle = -\frac{e\tau}{m_e}E = -\frac{e}{m_e}\frac{1}{N\sigma(\epsilon)v(\epsilon)}E \tag{3.26}$$

This equation illustrates the dependence of v_d on the average energy ϵ of electrons (and consequently on E), as well as its dependence on the cross-section of the processes and environmental factors such as temperature and pressure.

3.4.2 Diffusion

The diffusion is the natural process involves the dispersion of a concentrated electron cloud in space. This effect is significant in particle detectors due to its impact on the movement of electrons. When a particle cloud is initially compressed at t = 0, converging at a singular point r = 0, it subsequently diffuses in space, adhering to a

Gaussian profile.

$$\frac{dn}{n} = \frac{1}{(4\pi Dt)^{3/2}} e^{-\frac{r^2}{4Dt}} dr \tag{3.27}$$

with a standard deviation represented as $\sigma = \sqrt{2Dt}$, where D is identified as the diffusion constant, influenced by the energy of electrons or ions.

In the presence of a uniform electric field E throughout the medium, free charges move in the direction of the field, accelerating until they reach their drift velocity v_d. The electrical mobility μ for these charges can be further explained as the measure of their ability to move in response to the applied electric field. The electrical mobility μ for these charges can be defined as follows:

$$\mu = \frac{v_d}{E} \tag{3.28}$$

The Nernst-Townsend or Einstein's formula demonstrates that mobility is related to the coefficient of diffusion:

$$\mu = \frac{e}{kT} D \tag{3.29}$$

The drift velocity as shown in Figure 3.8 and, consequently, the mobility of elec-

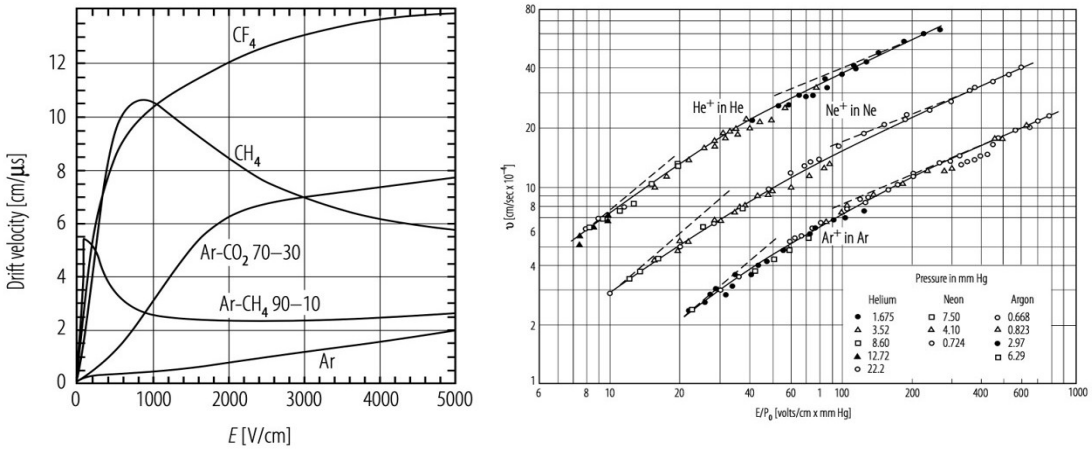

Figure 3.8: Left: Electrons drift velocity for typical gases. Right: For ions.

trons travelling in a gaseous medium under the influence of an electric field exhibit variability. This is due to electrons potentially gaining energy between collisions, a phenomenon attributed to their minuscule mass. Townsend's equation for electron

velocity is expressed as:

$$v_d^e = \frac{e}{2m_e} E\tau \tag{3.30}$$

In the ideal gas approximation, the drift velocity is proportional to the reduced electric field (E/P) and the medium temperature (T), where (P) represents gas pressure:

$$v_d^e = \frac{ET}{P} \tag{3.31}$$

The wavelength of these electrons, comparable to the size of gas molecules, results in significant variations in the interaction cross-section and hence the time, varies significantly with the energy of the electrons. These variations are described by the Ramsauer-Townsend effect, illustrated in Figure 3.9 (left). This relationship is

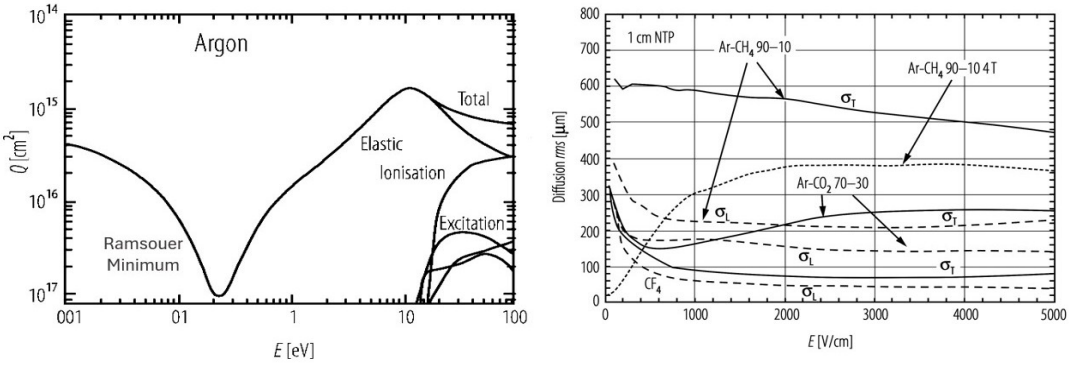

Figure 3.9: Left: Electron interaction cross-section in Ar [15]. Right: Electron cloud diameters after 1 cm drift with applied electric field. Graphs depict typical detector gases at normal conditions, without and with 4 T for Ar/CH_4 [16].

particularly crucial for the operation of gaseous detectors. In these detectors, charges released by an incoming particle migrate within the gas volume to reach a readout electrode.

3.4.3 Recombination

When a positively charged ion encounters a negatively charged electron, there is a possibility of recombination, resulting in the creation of a neutral atom that emits a

low-energy photon. The recombination rate equation is formulated as follows:

$$R_c = \frac{dn^+}{dt} = \frac{dn^-}{dt} = \alpha n^+ n^- \tag{3.32}$$

Here, n^+ and n^- represent the concentrations of ions and electrons, respectively, with α indicating the recombination coefficient. The significance of recombination lies in its potential to cause the loss of primary electrons, thereby reducing detector efficiency. However, it is noted that recombination has a diminished impact in the presence of high electric fields, as the charges are effectively separated by the field.

3.4.4 Attachment

Attachment plays a pivotal role in electron loss, particularly influenced by electronegative atoms such as Fluorine (F), Chlorine (Cl), and Oxygen (O), which possess high electron affinities. These atoms can attach electrons, resulting in the formation of stable negative ions and the emission of low-energy photons. Achieving an optimal electron collection process requires the careful selection of a gas combination. In scenarios where attachment is predominant, the movement of slow-moving negative ions towards the anode has the potential to introduce noise to the signal.

The reduction in electrons (dn) due to attachment per unit length (ds) is expressed as:

$$dn = -n\eta_a ds \tag{3.33}$$

Here, η_a represents the attachment coefficient in cm^{-1}, indicating the number of electrons attached per unit distance in the gas medium. This coefficient, influenced by gas composition and electric field, needs to be measured for each gas mixture.

At low electric fields, η_a is typically zero because the mean energy (ϵ) of electrons is insufficient for attachment, and cross-sections are extremely small. The attachment coefficient is primarily proportional to the electronegativity of gas atoms, with electronegative atoms like halogens (F, Cl, O) having the highest coefficients, while noble gases have an attachment coefficient of 0.

3.4.5 Amplification and Avalanches

In electric fields above a few kV/cm, electrons gain energy, inducing gas excitation/ionization, leading to an avalanche effect that amplifies the initial charge in gaseous detectors. The ionization mean free path, the reciprocal of which is the first Townsend coefficient α, is determined using Korff's approximation.

$$\frac{\alpha}{P} = Ae^{-\frac{BP}{E}} \tag{3.34}$$

Here, P is gas pressure, while A and B are parameters depending on the gas type and electric field. For a given location with n electrons, the amplified electron count at a distance dx is:

$$dn = n\alpha dx \tag{3.35}$$

By integrating Equation 3.35, you can obtain the amplification factor M:

$$M = \frac{n}{n_0} = e^{\alpha x} \tag{3.36}$$

In a non-uniform electric field, the Townsend coefficient varies with x. The amplification factor between x_1 and x_2 is expressed as:

$$M = e^{\int_{x_1}^{x_2} \alpha(x)dx} \tag{3.37}$$

The amplification factor M grows exponentially with electric field intensity but reaches a limit ($M = 10^8$) due to space charge impact and avalanche spreading, known as the Raether limit [2] is the minimum energy required by an incident charged particle to create an electron-ion pair in the gas medium of a detector. corresponding to $\alpha x \sim 20$.

The avalanche typically spans $10 - 100$ μm, primarily due to electron diffusion and electrostatic repulsion. Additionally, Ultra-Violet (UV) photons are generated during ionization, their energy dependent on atom excitation and energy transfer. These UV photons, produced in the amplification process, may extend the avalanche laterally. It is possible for a UV photon to trigger a second avalanche, causing a split.

[2] The Raether limit, also known as the Raether-Meitner limit, is the minimum energy required by an incident charged particle to create an electron-ion pair in the gas medium of a detector. Below this limit, the number of secondary electrons produced is insufficient to sustain the electron avalanche necessary for signal amplification.

Quench gases, like CO_2, alkanes (C_iH_{2i+2})[3], and ethylene, are commonly used to limit UV photon propagation due to their strong absorption cross sections.

3.5 Operational Parameters of Gaseous Detectors

The amount of induced signals is predominantly influenced by the strength of the applied field and the selection of a gas or gas mixture. In this section, we will provide a concise overview of both these factors.

3.5.1 Operational Modes

The fundamental operation of gaseous detectors can be demonstrated using the parallel plate detector. The signal generated in such detectors is formed when free charges, released by a particle, traverse the detecting medium influenced by the electric field established by two electrodes. The definition of four basic operating regimes depends on the magnitude of the electric field within the amplification zone. Figure 3.10 visually represents the correlation between collected charge and the amplification field across different operating zones.

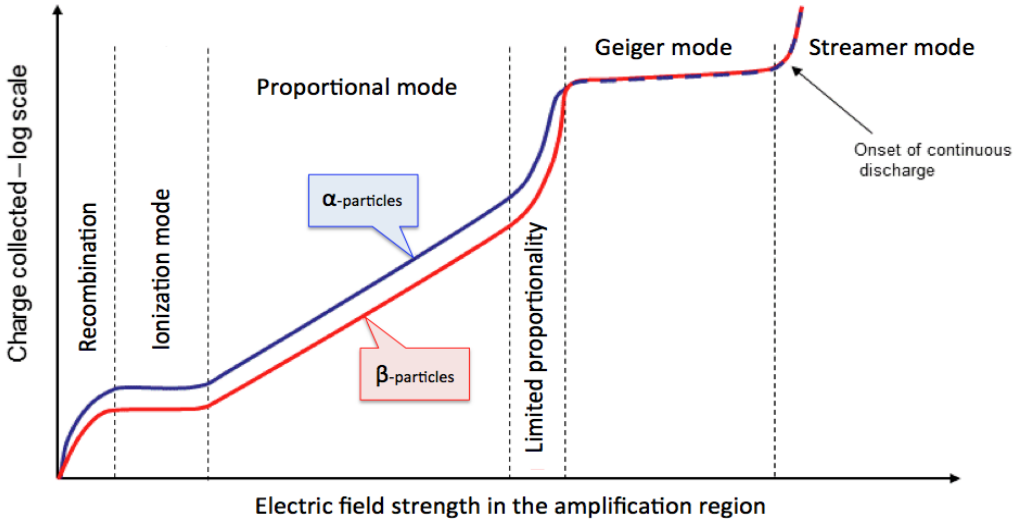

Figure 3.10: Gaseous detectors' gain-voltage characteristics depicting various modes, with the y-axis showing total charge in logarithmic scale [17].

[3]Here i is an integer with i > 0.

3.5.1.1 Ionization Mode

The number of primary charges remaining in a detector post-particle interaction depend on particle type, energy, and detecting medium parameters. Strongly ionizing events release a substantial charge in the gas, flowing along electric field lines and producing a significant signal on the electrodes, illustrated in Figure 3.11 (left). In this ionization regime, amplifying the primary charge before collection is unnecessary. A relatively modest electric field (typically < 10 kV/cm) suffices for signals above electronic noise. However, at extremely low electric fields, a significant portion of the original charge may be lost due to electron-ion recombination or attachment to neutral molecules. The ionization chamber, a precursor to many gaseous detectors, is still used, particularly in certain industrial smoke detectors, where smoke in the amplification zone can reduce current from a steady α-particle source, typically ^{241}Am.

3.5.1.2 Proportional mode

Gaseous chambers, used for detecting charged particles or high-energy photons, require signal amplification due to the initial charge deposition being insufficient for signals above readout system noise. A critical electric field (E_C) is established between electrodes at a threshold voltage (V_T) specific to the detector's shape. This field induces additional gas ionization, initiating avalanches as detailed in Section 3.4.5, influenced by electric field magnitude and gas mixture parameters. Post-amplification, the number of electrons is proportional to the initial charge (see Equation 3.35), making signals from proportional detectors representative of deposited particle energy. Figure 3.11 (right) schematically illustrates the amplification process in a proportional chamber. As the electric field strength increases, the amplification factor increases, leading to more secondary charges and significant avalanches. Eventually, space charge distorts the electric field around the avalanche, causing a progressive loss of proportionality.

This operational approach is commonly utilized in gaseous detection systems, including proportional counters, MWPCs, and, more recently, MPGDs. Proportional mode is employed in the operation of DTs, CSCs, and RPCs at CMS.

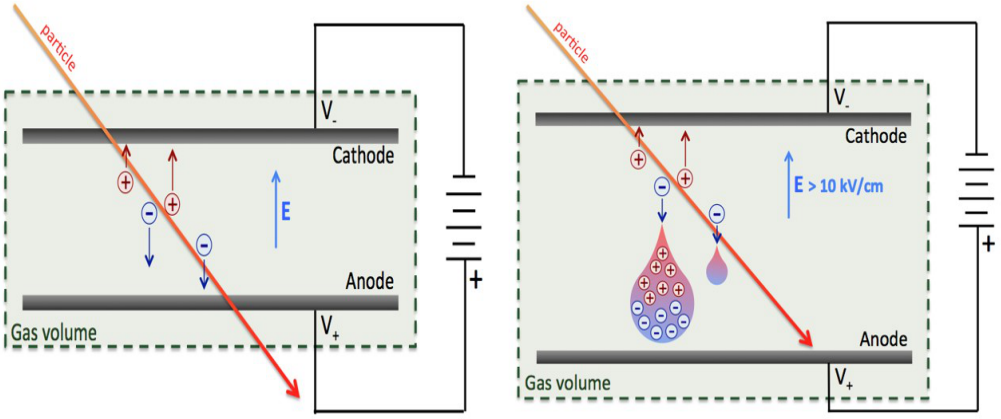

Figure 3.11: Left: A Schematic representation of ionization chambers. Right: For proportional chambers [5].

3.5.1.3 Geiger Mode

At higher electric fields, the initial avalanche triggers multiple secondary avalanches, primarily via UV photon emission or avalanche ion recombination on the cathode surface. This chain reaction extends throughout the sensor volume until terminated by a voltage drop on the electrodes or, in "self-quenching" detectors, by ion space charge. The accumulated charge post-amplification remains unaffected by the initial deposition. This phase, termed saturation or Geiger mode, is illustrated in Figure 3.12 (left).

Geiger detectors, mainly used for particle counting due to the loss of key charge information during amplification, can be optimized for specific particles in radio-protection applications. CMS muon detectors avoid Geiger mode due to challenges in reconstructing precise muon strike positions, and the extra time required to evacuate charges post-amplification conflicts with the minimum rate capability of CMS endcaps.

3.5.1.4 Streamer Mode

At more higher fields, the space charge density of the avalanche approaches the surface charge density of the electrodes, causing field lines to focus toward the avalanche zone. In Geiger mode, visible secondary photoelectrons migrate, contributing to the initial avalanche and forming a thin plasma filament (streamer) in the detecting medium.

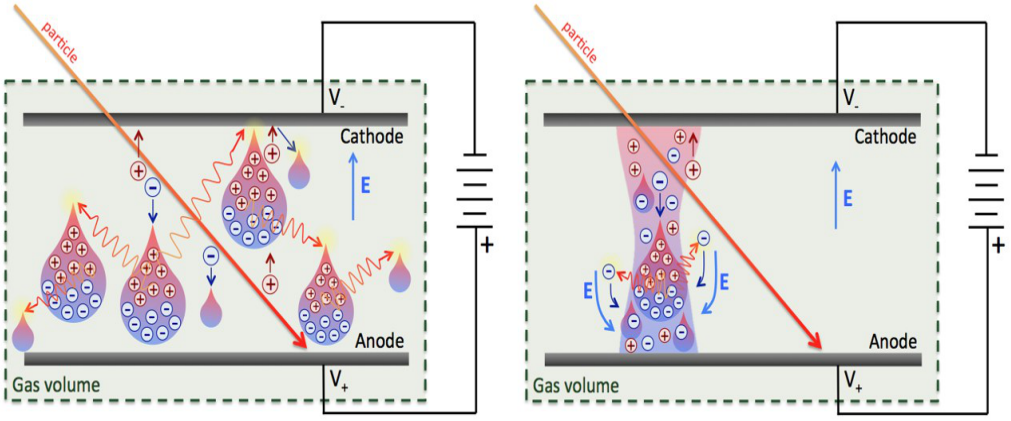

Figure 3.12: Left: A Schematic representation of GM chambers. Right: For streamer [5].

Illustrated in Figure 3.12 (right), the streamer may extend toward the electrodes, leading to a chamber discharge - common when detectors exceed the Raether limit as discussed in Section 3.4.5.

The streamer mode produces significant signals with a simple and cost-effective design but carries a risk of violent breakdowns, releasing most collected electrostatic charge in the electrodes. To mitigate this, electrodes are often shielded with highly resistant layers, limiting discharge energy and propagation, thus safeguarding detection and readout electronics. Originally designed for this purpose, RPCs are now widely employed in high-energy physics studies.

3.5.2 Gas Mixture Selection

Selecting the right gas is crucial for particle detectors. In the CMS endcap upgrade, two gas mixtures are considered: Ar/CO_2 (in percentage ratio 70/30) and $Ar/CO_2/CF_4$ (in percentage ratio 45/15/40). The choice depends on optimizing properties like ionization density, transport characteristics, and quenching abilities for effective detector performance. Noble gases, especially Ar, are favored for detecting MIPs at low electric fields due to their non-ionizing de-excitation processes. Ar is chosen for its cost-effectiveness and sufficient electron-ion pair production compared to xenon or krypton. However, the emission of high-energy photons by excited Ar atoms, with energies exceeding 11.6 eV, can potentially trigger secondary avalanches. To address this, a "quenching" gas like CO_2 is introduced, effectively absorbing photons within the energy range of Ar emission.

The introduction of "cold[4]" gases, like CF_4, enhances the detector's spatial and temporal performance by efficiently lowering the energy of electrons, decreasing the total scattering cross-section within Ar, and increasing the electron drift velocity. In thin gap detectors, the introduction of molecules with high total ionization per unit length, such as CF_4, improves the uniformity of primary cluster distribution, enhancing detector performance in terms of localization accuracy and time resolution. However, at electric fields surpassing 8 kV/cm, certain molecules like CF_4 can significantly impact signal amplitude by increasing the electron capture cross-section, resulting in a reduced signal along the drift path.

RPC detectors at the LHC use greenhouse gases 1,1,1,2-Tetrafluoroethane (R134a) and Sulfur hexafluoride (SF_6) for performance but face constraints due to their high Global Warming Potential (GWP). Immediate actions include system upgrades and leak fixes during LS2. Development of a R134a gas recuperation plant is underway, while R&D for "green" alternatives continues, though finding suitable replacements for current experiments is challenging [18].

3.6 Gaseous Detector Evolution

In 1906, H. Geiger and E. Rutherford introduced the first gaseous detector - a cylindrical single wire chamber. Over the subsequent decades, this concept evolved with W. Muller's Geiger-Muller detector in 1928. A significant development occurred in 1968 when G. Charpak and collaborators introduced the MWPC, a milestone in modern electronically readable detectors [19]. This innovation introduced pattern recognition, enabling extensive detection volumes and precise particle impact localization. This section offers a concise overview of the progression in particle detectors, encompassing the evolution from MWPCs to MSGCs, and culminating in the development of MPGDs. The discussion emphasizes their standard performance characteristics and inherent limitations.

[4] Refers to gases that have lower kinetic temperatures or energies and efficiently lower the energy of electrons within the detecting medium.

3.6.1 MWPCs

The MWPC, as depicted in Figure 3.13 (left), features parallel anode wires positioned between cathode plates, with a wire spacing of 2 mm and the distance to the cathode plates being three to four times larger. The application of a positive voltage to the wires generates a focused electric field E onto the wires [14].

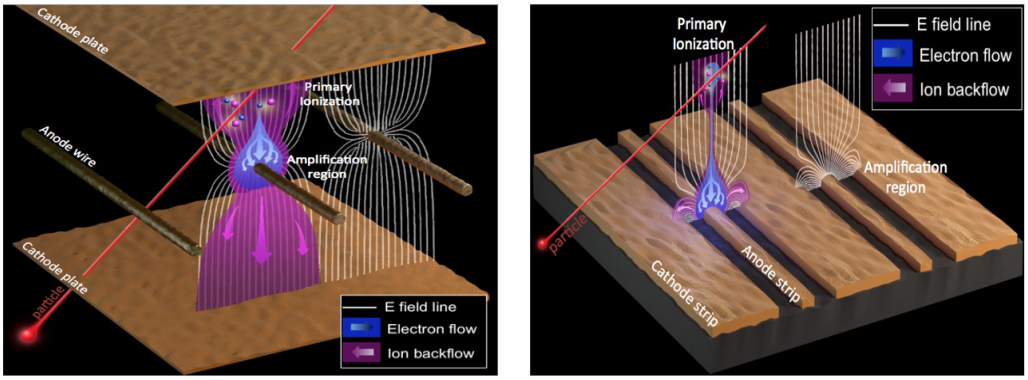

Figure 3.13: Left: A Schematic representation of a MWPC with parallel anode wires and cathode plates. Right: A Schematic representation of a MSGC with anode and cathode strips [5].

When filled with an appropriate gas mixture, a particle within the detector emits primary electrons that drift towards the nearest anode wire. In proximity to the wire, the electric field attains a critical intensity, initiating avalanche multiplication.

Due to the structured wire plane, spatial resolution is determined as $\sigma = \text{pitch}/\sqrt{12}$. A typical 2 mm pitch MWPC achieves spatial resolution of $\sim$ 0.5 - 1 mm. Combining MWPC layers with different orientations and segmented cathode plates improves resolution. The time resolution is approximately 10 ns in Ar/CO_2 (in percentage ratio 70/30). MWPCs serve in CMS for beam profile analysis, slow triggering, and, selectively, as spectrometers for low-energy particles. In the CMS, a modified version of the MWPC, referred to as CSCs, is utilized for the L1 trigger and muon reconstruction in the forward endcaps.

While large MWPCs offer cost-effectiveness, they demand precise geometry for maintaining uniform wire tension. Electrostatic forces can displace wires, affecting the electric field and gain uniformity. Wire aging necessitates specific operational conditions. A crucial limitation is gain reduction under high particle fluxes due to a extended transit time $\sim$ 100 μs for positive ions reaching the cathode. Positive space

charge accumulation modifies the electric field, disrupting charge amplification. The effective gain decreases rapidly at particle fluxes exceeding 10^4 Hz/mm^2 [14].

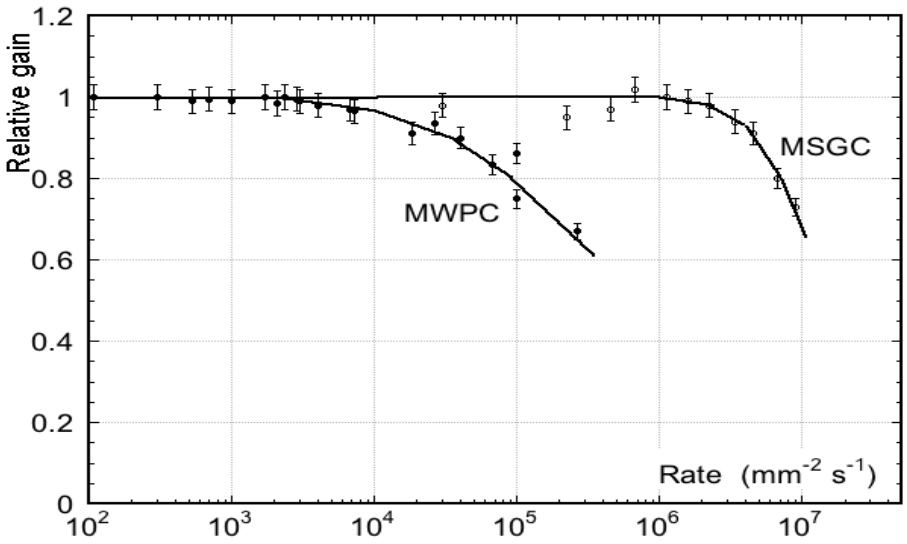

Figure 3.14: Normalized gas gain as a function of particle rate for MWPC and MSGC [20].

3.6.2 MSGCs

Recent semiconductor advancements in photolithography allow the creation of complex electrodes as small as 100 μm, reducing positive ion transit time to the sub-microsecond scale and improving rate capability compared to MWPCs as shown in Figure 3.14.

The MSGC, introduced by A. Oed in 1988 as the first MPGD, offers a cost-effective alternative to solid-state detectors. Suited for high-rate applications requiring fine spatial resolution in particle tracking [21], the MSGC features small parallel metal strips as anodes and cathodes on a thin resistive layer. Avalanche multiplication initiates with sufficient voltage, creating an intense electric field near the anode strips as depicted in Figure 3.13 (right).

In the 90's, systematic investigations yielded promising MSGC results, with gas gain exceeding 10^4, spatial resolution under 30 μm, and rate capability surpassing 10^6 Hz/mm^2[22, 23]. Challenges with high resistivity substrates led to gain instability at high-rates. Short-term issues included substrate charging and ion migration causing significant gain variations[23]. Long-term problems involved classical aging due

to small electrode size and materials used [24]. To address these, lower resistivity substances like diamond-like coated glass were utilized [25].

Despite superior performance, MSGCs face operational limitations in high-rate scenarios due to discharge risks. Excessive energy in the drift gap can surpass the Raether limit, causing streamer formation between electrodes. Dust on the readout board may create an electrical bridge, triggering harmful streamers that can permanently damage the small-sized detector. Research on gas mixtures and operating conditions has reduced discharge probability [26]. Nevertheless, uncertainties about MSGC's long-term integrity in severe environments led to exploring alternative solutions. However, MSGCs persist in various HEP studies, notably in the HERA-B inner detector at DESY [27].

3.6.3 MPGDs

Inspired by MSGCs, MPGD represent the most recent advancement in gaseous detector technology and have found application in various HEP experiments. The GEM and MICROMEGAS emerge as the predominant MPGD technologies.

In 1996, F. Sauli pioneered the GEM technique for signal pre-amplification within MSGCs. This method involves a thin insulating polymer layer (typically 50 μm polyimide) coated on both sides with 5 μm of copper, chemically perforated with closely spaced, small holes (average diameter of 70 μm, pitch of 140 μm). Applying a potential difference between the copper layers creates a substantial electric field (more than 10 kV/cm) within the holes. When primary electrons from particle crossings reach the GEM holes, they undergo avalanche multiplication due to the intense electric field, generating an electrical signal as the charge moves toward a readout board as shown in Figure 3.15 (left).

In 1992, G. Charpak and I. Giomataris introduced the MICROMEGAS structure, employing a mechanism similar to a parallel plate detector but with a sub-millimeter scale amplification gap (typically 100 μm). Adding a conversion gap measuring several millimeters is positioned atop the parallel plate design ensures high conversion efficiency and accommodates a large number of primary charges. By substituting the top plate with a small mesh as depicted in Figure 3.15 (right), primary electrons can move toward the anode, entering the amplification field and triggering avalanches. Subsequent versions include a resistive layer on the anode strips to limit energy

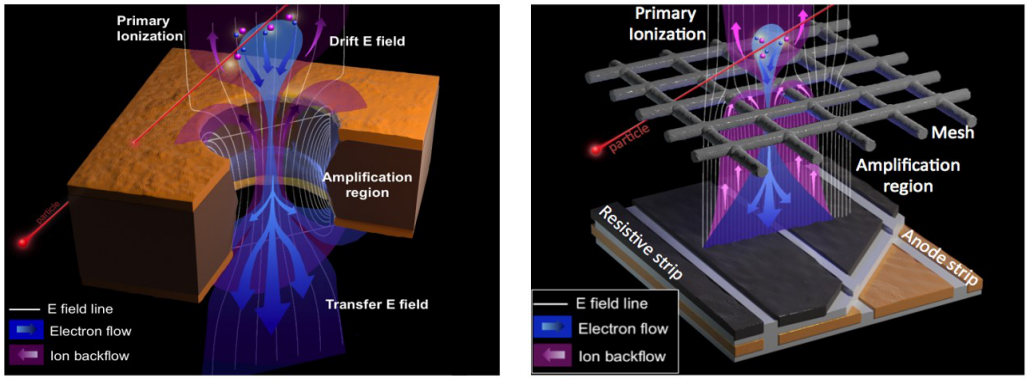

Figure 3.15: Left: Visual representation showcasing the operation of a GEM hole. Right: Diagram depicting the functionality of a MICROMEGAS detector [5].

emitted during spark creation and protect the readout electronics. MICROMEGAS technology was under consideration for the ATLAS small wheel update in 2018 due to its robust rate capabilities, spatial resolution exceeding 100 μm, and temporal resolution in the order of nanoseconds.

Various HEP experiments utilize detectors based on GEM and MICROMEGAS technologies, such as Common Muon and Proton Apparatus for Structure and Spectroscopy (COMPASS) and TOTal Elastic and diffractive Measurement (TOTEM) at CERN, Solenoidal Tracker at RHIC (STAR) and Pioneering High Energy Nuclear Interaction eXperiment (PHENIX) at Relativistic Heavy Ion Collider (RHIC), ALICE TPC and LHCb at CERN, Super Fragment Separator (SuperFRS), antiProton ANnihilation at DArmstadt (PANDA), Compressed Baryonic Matter (CBM) at FAIR, among others.

3.6.3.1 Triple-GEM Technology

A single GEM layer can achieve a maximum amplification of approximately 5×10^3, with a discharge probability of several percent due to the foil's proximity to electrical breakdown [28]. Significantly, the distinctiveness of GEM technology lies in its ability to transmit particle-induced signals for additional amplification beyond the initial GEM layer. This facilitates the integration of multiple GEM layers, yielding substantial amplification factors (up to 10^5) without approaching the electrical breakdown threshold for each layer. This strategy simplifies and lowers the cost of readout electronics while offering optimal protection against destructive events.

The widely adopted GEM-based detector comprises a triple-GEM structure positioned between a drift plane (cathode) and a readout board (anode). This configuration delineates specific regions within the detector: the drift region for primary charge deposition between the drift electrode and the initial GEM foil; transfer gaps between GEM1 and GEM2, and GEM2 and GEM3; and the induction gap between the GEM3 and the readout board, where the amplified charge induces the final readout signal. The overall arrangement of triple-GEM detectors utilized in the CMS GE1/1 upgrade (discussed in the following Section 3.7) is illustrated in Figure 3.16.

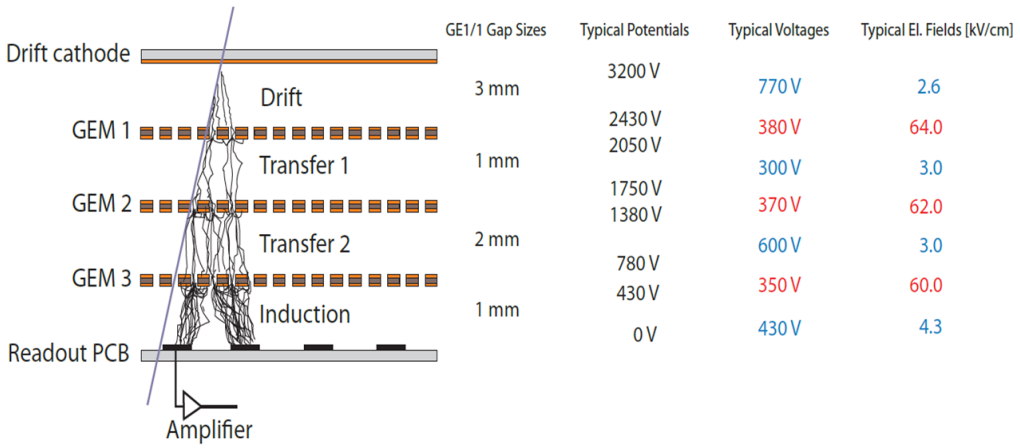

Figure 3.16: The triple-GEM detector operates in distinct areas: the drift region and transfer gaps between GEM1 and GEM2, GEM2 and GEM3, along with the induction gap (shown on the left). The GE1/1 detector's gap configuration provides details on electric potentials, voltages, and electric fields, utilizing a nominal potential of 3200 V for operation in Ar/CO_2 (in percentage ratio 70/30) on the drift electrode.

Gap dimensions between GEMs exhibit variability, typically in the order of millimeters, in order to balance mechanical constraints and the necessary electric fields for charge transfer. The drift gap, where conversion occurs, is typically larger to maximize sensitivity to incoming particles and ensure a sufficient number of primary electrons for compensation before amplification.

3.7 CMS GEM Upgrade

The CMS Collaboration had formulated plans to integrate GEM detectors, utilizing GEM technology, to address the challenging conditions and high luminosity rates anticipated at the LHC and its forthcoming upgrades. GEMs, serving as gas-based

detectors, demonstrated a detection efficiency exceeding 98% even at rates surpassing a few MHz/cm^2. They featured noteworthy spatial resolution of approximately 100 μm and commendable time resolution of about 8 ns and 5 ns at the efficiency plateau for Ar/CO_2 (in percentage ratio 70/30) and $Ar/CO_2/CF_4$ (in percentage ratio 45/15/40) gas mixtures, respectively. Additionally, the gas gain remained consistently stable up to several MHz/cm^2 of incident particle rate, highlighting a notable rate capability suitable for operations in the forward muon region of the CMS experiment, where an expected maximum rate is on the order of 150 kHz/cm^2.

CMS is in the process of upgrading its muon system with the incorporation of three new GEM technology-based stations - GE1/1, GE2/1, and ME0. These additions are intended to augment redundancy, regulate trigger rates, and enhance precision in muon measurements. This thesis will thoroughly explore the specifics of the GE1/1 upgrade, given its pivotal role in the upgrade work, and briefly touch upon the ME0 upgrade with some detail in Chapter 6.

3.7.1 GE1/1 Upgrade at CMS

3.7.1.1 Project Description

The CMS GEM collaboration, initiated in 2009, with a goal to develop and deploy triple-GEM detectors in the forward region of the CMS muon endcaps during the LS2 upgrade in 2018. The project, denoted as GE1/1, deciphers "G" for GEM, "E" for endcap, with the first "1" indicating the first muon station and the second "1" representing the first ring of the station.

In the GE1/1 Muon System, pairs of GE1/1 detectors are amalgamated to create "super-chambers", boosting detection efficiency by providing two measurement planes in the muon endcap. Each super-chamber covers an approximately 10° sector. To achieve complete azimuthal coverage, 72 super-chambers (36 per endcap) were required, forming a ring of superchambers. These superchambers alternate in ϕ between long ($1.55 < |\eta| < 2.18$) and short ($1.61 < |\eta| < 2.18$) versions (with η coverage shown in Figure 3.17). Each endcap accommodates 18 long and 18 short super-chambers, totaling 144 single chambers in the CMS Muon System. The comprehensive installation process of the GE1/1 station was successfully concluded in the year 2022. To acquire operational experience and demonstrate integration into the trigger, a demonstrator

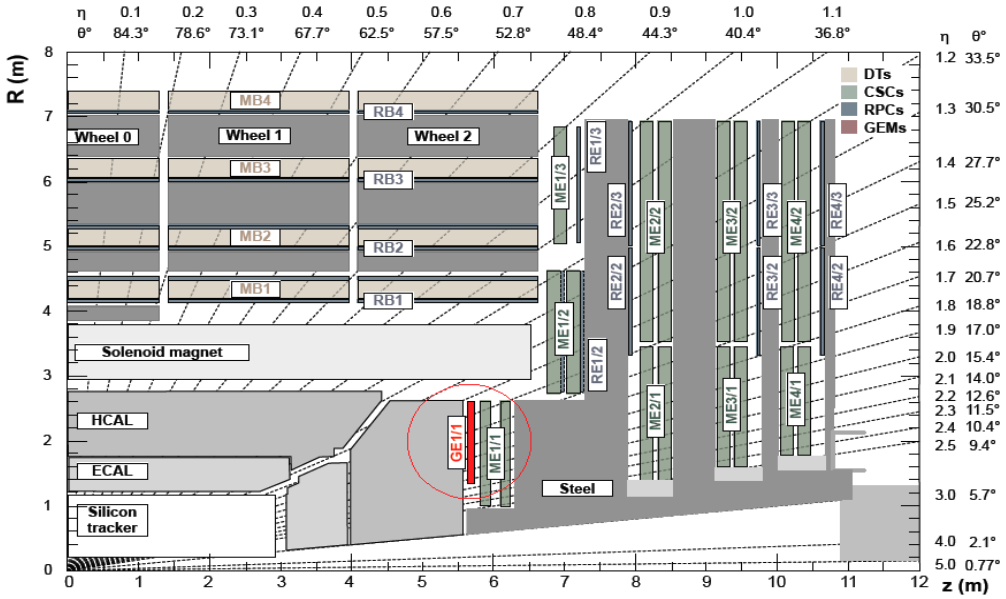

Figure 3.17: A visual representation of one-fourth of the CMS longitudinal cross-section, showcasing the current muon spectrometer and the GE1/1 project [29].

with five GE1/1 superchambers was installed in CMS during the YETS 2016/2017, referred to as "Slice Test" and discussed in detail in Chapter 5.

3.7.1.2 GE1/1 Performance Requirement

The primary objective was to optimize the CSC system to achieve efficient reconstruction and selection after the high-luminosity upgrade of the LHC, all while maintaining an acceptable L1 trigger rate. CMS had established minimum requirements, as outlined in Table 3.2, based on the desired trigger and physics performance standards [30]. The CMS GEM project utilized a two-phase approach: an initial research and development (R&D) phase focuses on exploring triple-GEM technology and developing GE1/1 detectors that meet the specific requirements of CMS. This was succeeded by the production and rigorous QC processes for the final set of 144 detectors, culminating in their integration into the CMS.

3.7.1.3 Detector Overview

Each GE1/1 detector consists of a trapezoidal gas volume that accommodates three large trapezoidal GEM foils, spaced a few millimeters apart between a drift board and

Table 3.2: Specifications and parameters for the technical design and operation of the CMS GE1/1 detector [31].

Properties	CMS Requirements
Rate capability	> 10 kHz/cm^2
Single Chamber Efficiency (MIP)	$> 97\%$
Angular resolution	< 300 µrad
Single Chamber Time Resolution	< 10 ns
Gain uniformity	> 85 %
Longevity	> 60 mC/cm^2

a readout board. The GEM foils are produced from copper-clad Kapton, perforated with a high-density pattern of truncated double-cone holes arranged hexagonally. This complex fabrication is achieved through both the double-mask and single-mask photolithographic techniques, pioneered by the CERN PCB workshop [32]. The GEM

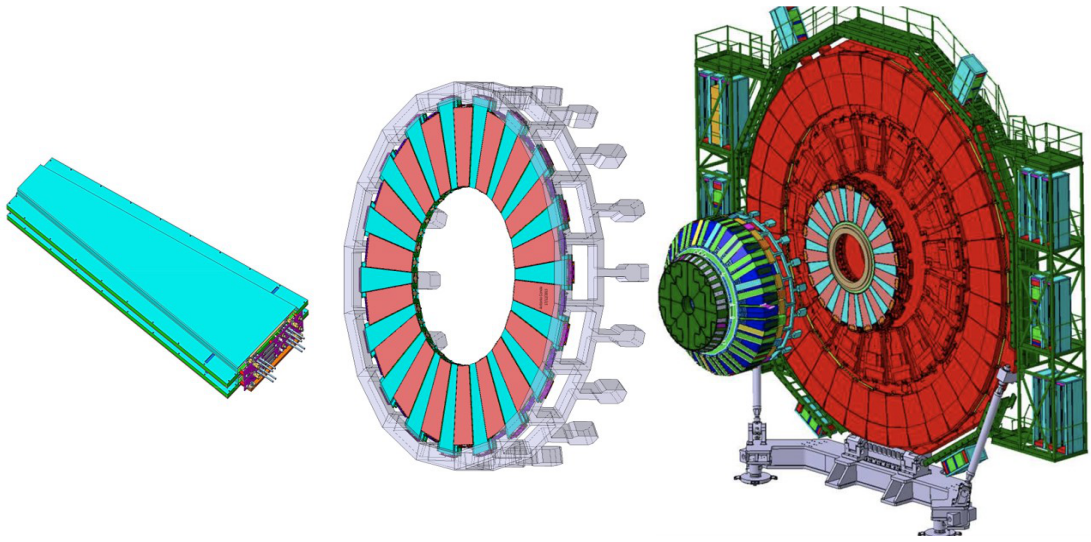

Figure 3.18: Left: GE1/1 super chamber. Middle: GE1/1 super-chamber arranged into the forward station. Short-type chambers (orange) have the readout board facing the outer side, while long-type chambers (azure) position the readout board towards the IP. Right: Integration of GE1/1 detectors in the CMS endcap [30]

holes in the GE1/1 triple-GEM detector foils take the form of truncated double cones with outer diameters around 70 µm and inner diameters around 50 µm, arranged in a hexagonal pattern with a pitch of 140 µm. The electric field strength inside these GEM holes can reach 80 kV/cm. optimized for CMS experiment, the detector incorporates specific thicknesses in various regions to achieve optimal time resolution. This includes

a 3 mm drift region, 1 mm and 2 mm spaces in electron transfer gaps, and a 1 mm space in the signal induction region. The baseline gas mixture for operation is 70% Arand 30% CO_2. The technical specifications for both short and long versions of the GE1/1 detectors are detailed in Table 3.3.

3.7.2 GE2/1 Upgrade

The novel detector system involves the installation of 18 "super-chambers" per endcap within the region $1.6 < |\eta| < 2.4$. Each super-chamber consists of two trapezoidal-shaped triple-GEM layers, collectively covering 20° in ϕ, as illustrated in Figure 3.19. Each GE2/1 chamber covers an area of 1.45 m^2, contributing to a combined active

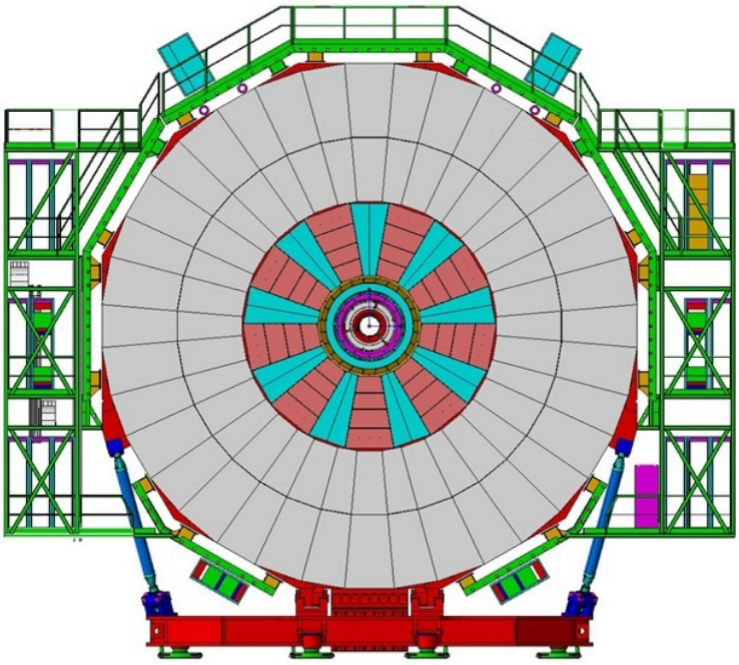

Figure 3.19: The 18 GE2/1 detectors (indicated in blue and red) are positioned on the back of the yoke disks YE ± 1. The chambers of neighboring super chambers overlap in ϕ to prevent acceptance holes [33].

area of 105 m^2. The chamber is segmented into four modules in R, with each module containing 12 sectors. Each sector is monitored by 128 radial strips, resulting in approximately 6000 strips per chamber. Strip pitches range from 0.5 mm to 1.2 mm. The nominal voltage is approximately 3200 V, corresponding to an effective gas gain of

Table 3.3: Specifications and parameters for the technical design and operation of the CMS GE1/1 detector [31].

Specification/Parameter	GE1/1
Detector technology	Gaseous detector (MPGD)
Charge amplification element	GEM foil (triple, cascaded, tensioned at ≈ 5 N/cm)
Number of chambers	144 (72 in each endcap)
Chamber shape (active readout area)	Trapezoidal opening angle 10.15°
Active area overlap in adjacent chambers	2.6 mrad ($\sim$ to 5.7 readout strip pitches)
Short chamber dimensions (active vol.)	L:106.1 cm (center line) W:(23.1-42.0) cm, D: 0.7 cm
Long chamber dimensions (active vol.)	L: 120.9 cm (center line) W: (23.1 - 44.6) cm, D: 0.7 cm
Total chamber thickness	D: 3.5 cm
Active readout area	0.345 m^2 (short chamber) 0.409 m^2 (long chamber)
Active chamber volume	2.6 liters (short chamber) 3 liters (long chamber)
Radial distance from beam line	130.2 cm (at inner edge of active readout area)
Geometric acceptance in η	1.61 - 2.18 (short chamber) 1.55 - 2.18 (long chamber)
Signal readout structure	Truly radial readout strips
Readout strip dimensions	230 µrad angular strip width 463 µrad angular pitch
Number of η-segments in readout	8
Number of readout strips per η-segment	384
Number of readout strips per chamber	3072

$1 - 2 \times 10^4$. The anticipated spatial resolution varies, ranging from 200 µm to 410 µm from the inner to outer radius.

3.7.3 ME0 Upgrade

The detection system comprises 18 modules on each endcap, with each module constructed using 6 layers of trapezoidal-shaped triple-GEM detectors. Consequently, a total of 216 chambers are required for the entire system. This station will be positioned behind the recently upgraded HGCAL calorimeter, taking advantage of the newly available space created by this enhancement. The covered region extends from $2 < |\eta| < 2.8$, maximizing the muon spectrometer's acceptance. It overlaps with existing CSCs systems and new RPCs stations up to $|\eta| = 2.4$, within mechanical constraints. The ME0 upgrade encompasses a total active area of 105 m^2. Each layer

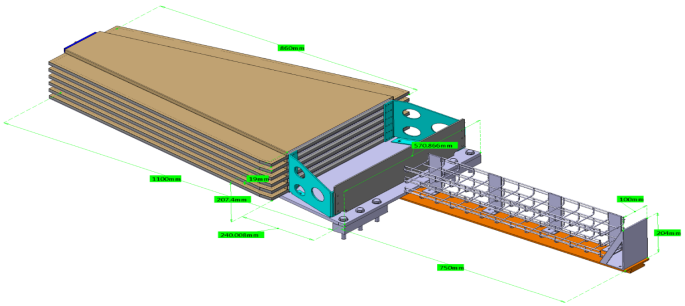

Figure 3.20: The arrangement of the ME0 stack, featuring six triple-GEM layers, is depicted in the lower right section of the figure. These six layers are staggered in a manner that causes the active areas of neighboring stacks to overlap in the ϕ direction [33].

of a single chamber is segmented into 8 rings in η and 3 sectors in ϕ. The sectors are further divided into 128 radial strips. The construction details mirror those of the GE2/1 chambers, with enhanced spatial resolution: 160 μm at the inner radius and 390 μm at the outer radius. For more details on the ME0 upgrade project, refer to [33].

3.8 Conclusions

The technology of gaseous detectors offers a high degree of adaptability concerning size, shape, configuration, mode of operation, and sensitivity to energetic particles. Due to these attributes, gaseous detectors play a crucial role in various applications within HEP. The recent advancements in MPGDs now make it feasible to utilize gaseous detectors that exhibit exceptional detection performance in high-rate scenarios.

One particularly captivating MPGD is the GEM structure, which has undergone extensive exploration in the last decade and found applications in numerous significant HEP experiments. Drawing upon their prior experience with GEM technology, the CMS GEM Collaboration has developed a specialized version of large triple-GEM detectors for upgrading the front CMS muon endcaps, contributing valuable insights to the field.

Bibliography

[1] Glen Knoll. *Radiation Detection and Measurement (4th ed.)* Hoboken, NJ: John Wiley, 2010. ISBN: 978-0-470-13148-0.

[2] L.E. Porter. "The Barkas-Effect Correction to Bethe–Bloch Stopping Power". In: *Theory of the Interaction of Swift Ions with Matter. Part 2*. Vol. 46. Advances in Quantum Chemistry. Academic Press, 2004, pp. 91–119. DOI: https://doi.org/10.1016/S0065-3276(04)46004-3. URL: https://www.sciencedirect.com/science/article/pii/S0065327604460043.

[3] William R. Leo. *Techniques for Nuclear and Particle Physics Experiments*. Springer, 1994. ISBN: 978-3-540-57280-0, 978-3-642-57920-2. DOI: 10.1007/978-3-642-57920-2.

[4] Donald E. Groom, Nikolai V. Mokhov, and Sergei I. Striganov. "Muon stopping power and range tables 10-MeV to 100-TeV". In: *Atom. Data Nucl. Data Tabl.* 78 (2001), pp. 183–356. DOI: 10.1006/adnd.2001.0861.

[5] Jeremie Alexandre Merlin. "Study of long-term sustained operation of gaseous detectors for the high rate environment in CMS". PhD thesis. Strasbourg U., Apr. 2016.

[6] H.L. Bradt and B. Peters. In: *Physical Review Letters* 74 (1948), p. 1828. DOI: 10.1103/PhysRev.74.1828.

[7] Florian Zenoni. "Study of Triple-GEM detectors for the CMS muon spectrometer upgrade at LHC and study of the forward-backward charge asymmetry for the search of extra neutral gauge bosons". PhD thesis. U. Brussels, U. Brussels (main), Apr. 2016.

[8] Alessandra Puglisi. "Ab-initio study of x-ray spectroscopy of molecular ions". Theses. Université Pierre et Marie Curie - Paris VI, Sept. 2017. URL: https://theses.hal.science/tel-01755939.

[9] R. Serber. "Nuclear Reactions at High Energies". In: *Phys. Rev.* 72 (1947), pp. 1114–1115. DOI: 10.1103/PhysRev.72.1114.

[10] M. L. Goldberger. "The Interaction of High Energy Neutrons and Heavy Nuclei". In: *Physical Review* 74.10 (Nov. 1948), pp. 1269–1277. DOI: 10.1103/physrev.74.1269. URL: https://doi.org/10.1103/physrev.74.1269.

[11] M. P. Guthrie, R. G. Alsmiller, and H. W. Bertini. "Calculation of the capture of negative pions in light elements and comparison with experiments pertaining to cancer radiotherapy". In: *Nucl. Instrum. Meth.* 66 (1968), pp. 29–36. DOI: 10.1016/0029-554X(68)90054-2.

[12] Aatos Heikkinen, Nikita Stepanov, and Johannes Peter Wellisch. "Bertini intranuclear cascade implementation in GEANT4". In: *eConf* C0303241 (2003), MOMT008. arXiv: nucl-th/0306008.

[13] Victor F. Weisskopf. "Statistics and nuclear reactions". In: *Physical Review* 52.4 (Aug. 1937), pp. 295–303. DOI: 10.1103/physrev.52.295. URL: https://doi.org/10.1103/physrev.52.295.

[14] F. Sauli. "Principles of Operation of Multiwire Proportional and Drift Chambers". In: (May 1977). DOI: 10.5170/CERN-1977-009.

[15] H. J. Hilke and W. Riegler. "Gaseous Detectors". In: *Particle Physics Reference Library: Volume 2: Detectors for Particles and Radiation*. Ed. by Christian W. Fabjan and Herwig Schopper. Cham: Springer International Publishing, 2020, pp. 91–136. ISBN: 978-3-030-35318-6. DOI: 10.1007/978-3-030-35318-6_4. URL: https://doi.org/10.1007/978-3-030-35318-6_4.

[16] C. W. Fabjan and H. Schopper, eds. *Elementary Particles. Detectors for Particles and Radiation.: Part 1: Principles and Methods*. Vol. 21B1. Landolt-Boernstein - Group I Elementary Particles, Nuclei and Atoms. Springer, 2011. ISBN: 978-3-642-03605-7, 978-3-642-03606-4. DOI: 10.1007/978-3-642-03606-4.

[17] Giacomo Mauri. "Development and characterization of detectors for large area application in neutron scattering and small area application in neutron reflectometry". In: (May 2019). arXiv: 1905.12311 [physics.ins-det].

[18] R. Guida et al. "Optimization strategies for the greenhouse gas consumption of the resistive plate chamber detectors at the CERN LHC experiments". In: *Nuclear Instruments and Methods in Physics Research Section A: Accelerators, Spectrometers, Detectors and Associated Equipment* 1055 (2023), p. 168444. ISSN: 0168-

9002. DOI: https://doi.org/10.1016/j.nima.2023.168444. URL: https://www.sciencedirect.com/science/article/pii/S0168900223004345.

[19] Georges Charpak et al. "The Use of Multiwire Proportional Counters to Select and Localize Charged Particles". In: *Nucl. Instrum. Meth.* 62 (1968), pp. 262–268. DOI: 10.1016/0029-554X(68)90371-6.

[20] Maxim Titov. "Gaseous Detectors". In: *Handbook of Particle Detection and Imaging*. Ed. by Claus Grupen and Irène Buvat. Berlin, Heidelberg: Springer Berlin Heidelberg, 2012, pp. 239–264. ISBN: 978-3-642-13271-1. DOI: 10.1007/978-3-642-13271-1_11. URL: https://doi.org/10.1007/978-3-642-13271-1_11.

[21] Fabio Sauli and A Sharma. "Micro-pattern gaseous detectors". In: *Nucl. Instrum. Methods Phys. Res., A* 477.1-3 (2002), pp. 1–7. DOI: 10.1146/annurev.nucl.49.1.341. URL: https://cds.cern.ch/record/431069.

[22] T Beckers et al. "Optimization of microstrip gas chamber design and operating conditions". In: *Nucl. Instrum. Methods Phys. Res., A* 346 (1994), pp. 95–101. DOI: 10.1016/0168-9002(94)90691-2. URL: https://cds.cern.ch/record/259630.

[23] Roger Bouclier et al. "Performance of gas microstrip chambers on glass substrates with electronic conductivity". In: *Nucl. Instrum. Methods Phys. Res., A* 332 (1993), pp. 100–106. DOI: 10.1016/0168-9002(93)90745-4. URL: https://cds.cern.ch/record/245234.

[24] Fabio Sauli. "Development of high rate MSGCS: overview of results from RD28". In: *Nucl. Phys. B, Proc. Suppl.* 61B (1998), pp. 236–243. DOI: 10.1016/S0920-5632(97)00568-9. URL: https://cds.cern.ch/record/321533.

[25] A J Barr et al. ""Diamond" over-coated Microstrip Gas Chambers for high rate operation". In: (1997). DOI: 10.1016/S0920-5632(97)00580-X. URL: https://cds.cern.ch/record/322022.

[26] B Boimska et al. *Investigation of discharge limits in diamond coated microstrip gas chambers*. Tech. rep. Geneva: CERN, 1996. URL: https://cds.cern.ch/record/687363.

[27] C Krauss. "Charged particle tracking with the HERA-B detector". In: (2002). URL: https://cds.cern.ch/record/643265.

[28] S Bachmann et al. "Discharge studies and prevention in the gas electron multiplier (GEM)". In: *Nucl. Instrum. Methods Phys. Res., A* 479.2-3 (2002), pp. 294–308. DOI: 10.1016/S0168-9002(01)00931-7. URL: https://cds.cern.ch/record/483487.

[29] M. Abbas et al. "Benchmarking LHC background particle simulation with the CMS triple-GEM detector". In: *JINST* 16.12 (2021), P12026. DOI: 10.1088/1748-0221/16/12/P12026. arXiv: 2107.03621 [physics.ins-det].

[30] A Colaleo et al. *CMS Technical Design Report for the Muon Endcap GEM Upgrade*. Tech. rep. 2015. URL: https://cds.cern.ch/record/2021453.

[31] Thomas Hebbeker and Andrey Korytov. "The Phase-2 Upgrade of the CMS Muon Detectors". In: (Sept. 2017).

[32] Rui DE OLIVEIRA and Serge DUARTE PINTO. "A METHOD OF MANUFACTURING A GAS ELECTRON MULTIPLIER". Pat. WO/2009/127220. Oct. 2009. URL: https://patentscope.wipo.int/search/en/detail.jsf?docId=WO2009127220.

[33] *The Phase-2 Upgrade of the CMS Muon Detectors*. Tech. rep. This is the final version, approved by the LHCC. Geneva: CERN, 2017. URL: https://cds.cern.ch/record/2283189.

Chapter 4

Assembly and Quality Control of GE1/1 Detectors

"Science is a beautiful gift to humanity; we should not distort it."
— A P J Abdul Kalam, 1931–2015

4.1 Introduction

In this chapter, we will discuss the assembly and QC of GE1/1 detectors, which was part of the GE1/1 project. Approval for the project was granted by the CMS collaboration in 2015, as detailed in the preceding chapter (Chapter 3). The execution of the project was planned to coincide with the muon upgrade during LS2 in 2018. Within the GE1/1 project framework, 144 individual chambers underwent assembly and testing at various production sites before being transported to CERN for conclusive validation. The primary objective was to assess the effectiveness and resilience of the triple-GEM technology. A thorough QC protocol was systematically implemented at both production sites and the CMS GEM facility at CERN. This protocol aimed to ensure the attainment of superior quality and optimal functionality for each chamber.

As a member state of CERN, India assumed the responsibility for assembling a total of 17 GE1/1 short chambers. The Panjab University GEM (PUGEM) group, assigned to assemble and test 8 of these chambers, utilized a dedicated cleanroom facility named Cleanroom-100 for assembly and a testing lab for QC3 and QC4.

4.2 GE1/1 Detector Mass Production

The optimization of large-scale GE1/1 detector production had advanced through collaborative initiatives spanning several years, engaging various research institutions and associated industries [1]. The assembly and QC procedures for GE1/1 detectors were spread across numerous production sites, with a notable emphasis on CERN serving as the primary center for essential R&D laboratory functions, manufacturing operations, and GEM-foil production [2]. This testing encompassed evaluations of both raw materials and the incorporation of detectors into the muon endcap regions of the CMS experiment.

Moreover, the CMS-GEM collaboration had identified alternative manufacturing and QC sites. This initiative relied on the expertise in detector development and received support from the respective home institutes for the GE1/1 project:

- Bhabha Atomic Research Centre (BARC), Delhi University and Panjab University - India
- Florida Institute of Technology (FIT) - USA
- Ghent University (UGent) - Belgium
- INFN Laboratori Nazionali di Frascati (LNF) - Italy
- INFN Sezione di Bari and Bari University – Italy
- National Center for Physics (NCP) – Pakistan

The University of Aachen in Germany hosted a secondary facility conducting QC assessments for GE1/1 detectors from both CERN and UGent manufacturing sites. The primary industry partners involved in the CMS-GEM project are outlined in Table 4.1.

Numerous additional research institutes and industrial entities actively participated in the CMS-GEM project, spanning countries such as Belgium, Bulgaria, China, Colombia, Egypt, Finland, France, Germany, Hungary, India, Italy, Korea, Pakistan, Qatar, and the US. The comprehensive list of institutions and their collaborators can be found in [3]. Figure 4.1 illustrated the entire mass production chain of GE1/1 detectors. Suppliers in the industrial sector provided components for GE1/1 detectors to CERN, where they underwent thorough visual inspection and specialized testing. As the

Table 4.1: Key industry partners in the CMS-GE1/1 Project. The tabulated data has been extracted from [1].

Suupliers	**Detector Components**
MicroPack Pvt. Ltd.	Drift and Readout PCBs
Eltos S.p.A	Internal and External Frames
Mansner Oy Hienomekaniikka	Pull-outs
Bossard Group	Screws and Washers
Angst & Pfister SA	Viton O-ring
Parker Legris	Gas Plugs
Peninunsula	Panasonic Connectors Assembly
Hybrid SA	High Voltage (HV) Dividers
Farnell/Mouser Electronics	SMD components
Fixtest	High Voltage Pins
Kerb-Konus/Titanox	Brass Insert (Internal/Flanges)

exclusive facility for manufacturing and QC, CERN ensured adherence to standards before distribution. Accepted components were utilized for assembly either at CERN or other designated sites. All GE1/1 detectors, regardless of their origin (CERN or external sites), underwent precise in-situ testing to ensure robust performance in the CMS experiment. QCs encompassed assessments such as gas tightness, electric tests, noise analysis, gas gain, and RU.

Externally manufactured GE1/1 detectors that passed intermediate checks were sent back to CERN for additional QCs. CERN evaluated both externally manufactured and on-site assembled detectors. The assembly of two GE1/1 detectors resulted in a superchamber, which was exclusively assembled and quality-controlled by CERN. Following mechanical assembly, essential parameters were measured, and the superchamber was deemed ready for final installation in the CMS Muon Spectrometer.

The production of GE1/1 detectors commenced in April 2017 at the CERN production facility and in the autumn of 2017 at the majority of production and QC facilities. Initially scheduled for completion in 2020, the installation of these detectors in the CMS experiment's Muon Spectrometer was contingent upon the assembly and certification of all superchambers at the CERN manufacturing facility. However, due to the unprecedented Corona-virus Disease-2019 (COVID-19) situation, this timeline experi-

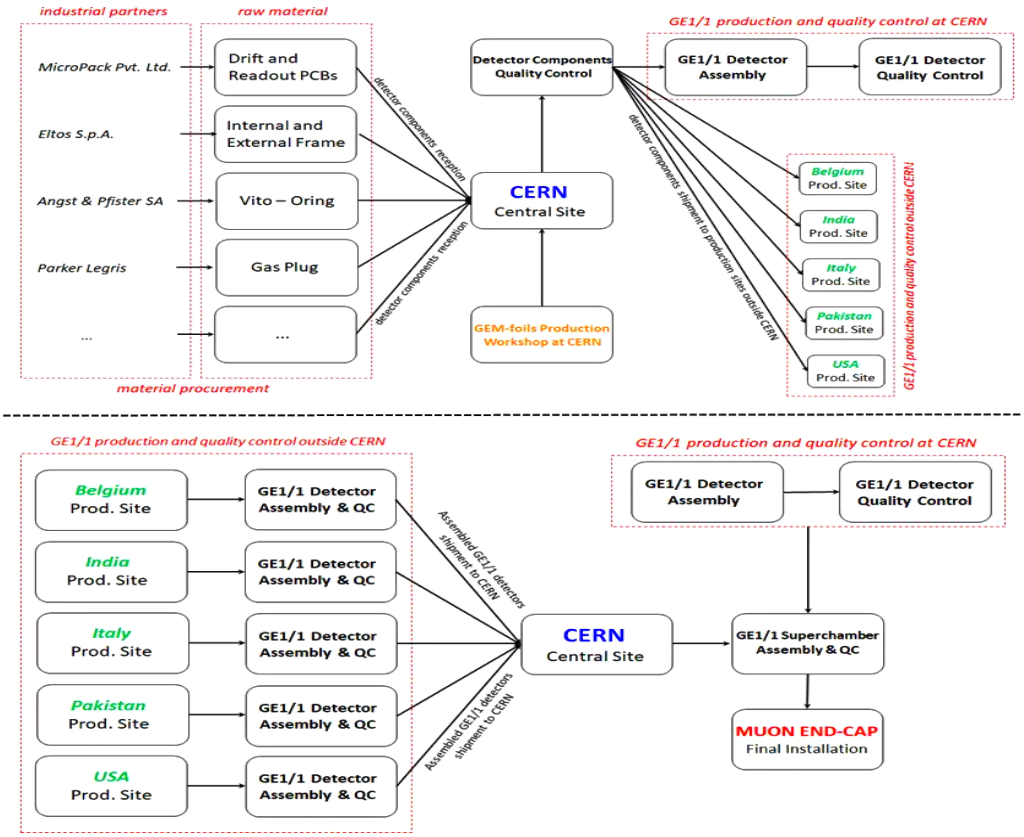

Figure 4.1: The GE1/1 detector mass production chain, incorporating production facility and/or industrial enterprises overseeing the process along with production and QC phases, is illustrated [1].

enced delays. The installation of GE1/1 detectors was ultimately carried out during the LS2 upgrade period, concluding in 2022. Sections 4.4 and 4.5 provides a detailed, step-by-step description of the GE1/1 detector assembly and quality certification methods.

4.3 GE1/1 Detector Components and Design

4.3.1 Technical Design

The structure of the CMS GE1/1 detector encompasses three identical large trapezoidal GEM foils situated within a gas volume that adopts the trapezoidal shape, delineated by the external frame, readout board, and drift board. The integrity of this gas volume is maintained by two Viton O-rings positioned within the groove of the exterior

frame. The mechanical design of a CMS GE1/1 triple-GEM detector is depicted in an exploded view in Figure 4.2, emphasizing essential components from the bottom: a 3 mm internal frame, the first GEM foil, a 1 mm internal frame, the second GEM foil, a 2 mm internal frame, the third GEM foil, a 1 mm internal frame, the first O-ring, the exterior frame, the second O-ring, and the readout board.

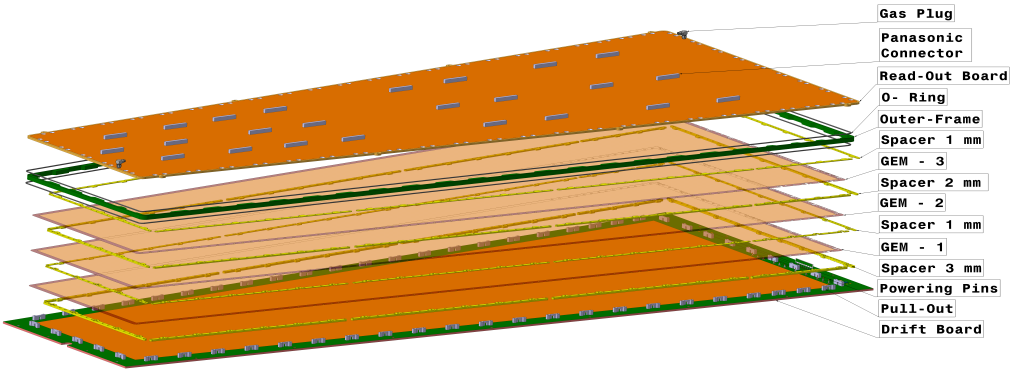

Figure 4.2: An exploded depiction of the mechanical design of a GE1/1 triple-GEM detector and its primary assembly components [4].

As a result of inherent spatial limitations in the existing mechanical framework of the forward region of the muon endcap within the CMS experiment, intentional measures have been taken to reduce the dimensions of the CMS GE1/1 detectors. Furthermore, in response to mechanical constraints in the GE1/1 station and to improve detection coverage, two different detector variants have been implemented: the Long and the Short. Comprehensive technical specifications for both the short and long versions of the GE1/1 detectors are thoroughly outlined in Table 4.2.

4.3.2 Drift Board Design

The drift board, a Printed Circuit Board (PCB), integrates the trapezoidal drift electrode, as depicted in the Figure 4.3 (left), providing a clearer understanding of its mechanical configuration. The active region of the board, coated with a copper layer, directly interfaces with the active gas volume of the detector. The Figure 4.3 (right) showcases the actual drift board, providing an enlarged view of its base that highlights crucial components.

Within the board, spring-loaded HV pins are incorporated to supply power to the GEM foils. A total of 12 HV pins are strategically positioned, with 4 pins energizing

Table 4.2: Short and Long GE1/1 detector technical specifications and characteristics.

Specification	Short	Long
Chamber Shape	Trapezoidal	Trapezoidal
	L: 106.1 cm	L: 120.9 cm
Chamber Dimensions	W: (23.1-42.0) cm	W: (23.1-44.6) cm
	D: 0.7 cm	D: 0.7 cm
Chamber Thickness	3.5 cm	3.5 cm
Active readout area	0.345 m^2	0.409 m^2
Active chamber volume	2.6 liters	3 liters
Geometric acceptance in η	1.61-2.18	1.55-2.18

each foil based on its HV pads. The height of these pins is determined by the position of the foil. Perimeter through-holes on the board serve the purpose of mounting stainless steel Pull-Outs, essential components for mechanically stretching GEM foils (discussed in Section 4.4.5). Supplementary elements include HV distribution traces, a dedicated protection resistor pad of 10 MΩ, and pads for a decoupling Resistance-Capacitance (RC) circuit. The protective resistor serves to safeguard against electrical damage from high voltage, while the RC circuit, comprising a 100 kΩ resistor and a 330 pF capacitor, isolates signals during measurements from the bottom of the third GEM foil. The components described here are illustrated in Appendix B.

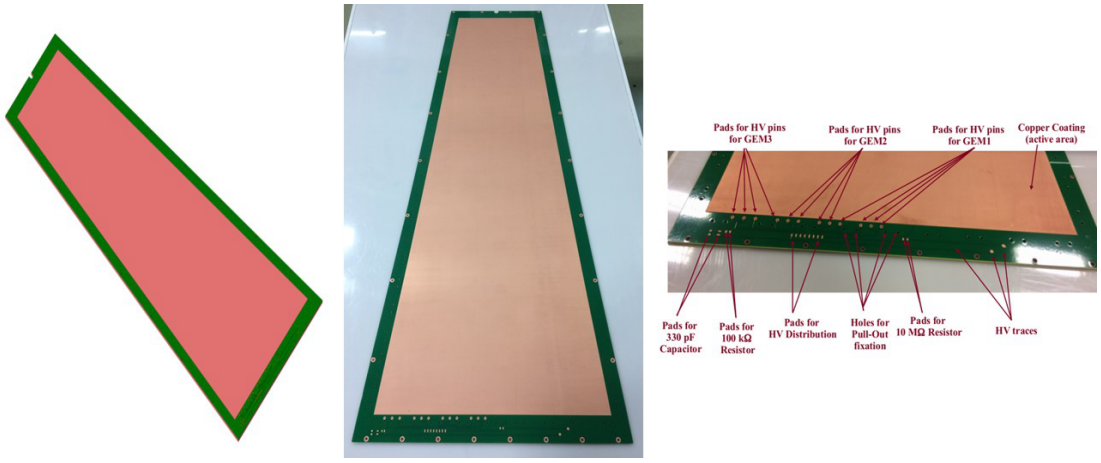

Figure 4.3: Left: Mechanical design of the GE1/1 drift board. Middle: Image of the GE1/1 the drift board. Right: A close-up of the larger base of the GE1/1 drift board (right).

4.3.3 External Frame Design

The trapezoidal-shaped external frame, depicted in Figure 4.4, is constructed from halogen-free glass-epoxy material. Manufactured as a single piece to minimize material non-homogeneity, its primary role is to create a gas-tight seal for the chamber by enclosing the active gas volume between the drift and readout boards.

To improve gas-tightness without causing damage, the external frame includes a small groove positioned peripherally to accommodate the Viton O-ring. This O-ring compresses between the drift and readout boards, with notches strategically placed around the frame to accommodate Pull-Outs. Additionally, a protective layer of Nuvovern® polyurethane varnish is applied to seal in particulates, preventing contamination during the assembly and operation of the detector.

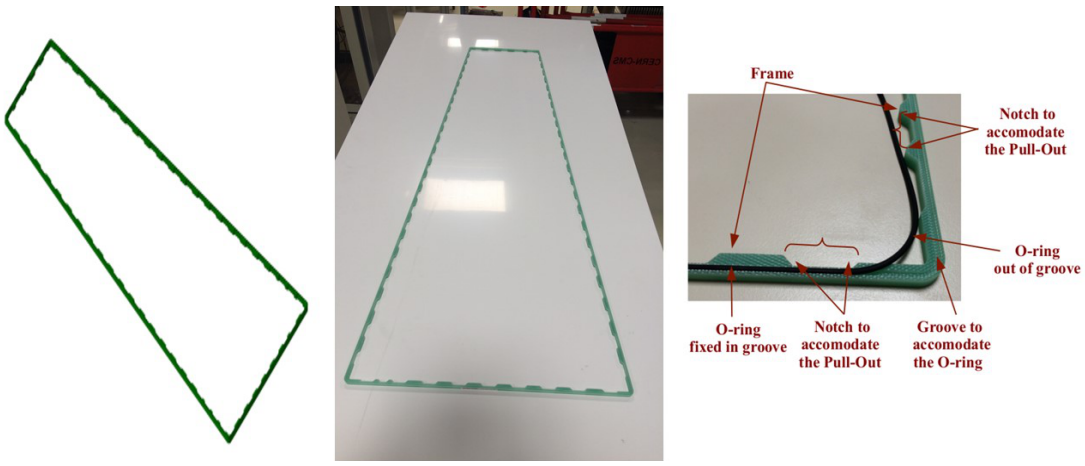

Figure 4.4: Left: Mechanical design of the external frame. Middle: Image of the exterior frame. Right: A close-up shows the exterior frame's groove, an O-ring in and out of its groove, and notches on the inner side of the frame to allow the Pull-Outs. These images are taken from [1].

4.3.4 Internal Frame Design

Internal frames play a vital role in determining the distances between the drift board, GEM foils, and readout board. Comprising four layers of halogen-free epoxy glass with thicknesses of 3 mm, 1 mm, 2 mm, and 1 mm, totaling 10 parts as shown in Figure 4.5, these frames are crucial components. To safeguard against the potential dislodgment of glass epoxy particles during assembly, a coating process is applied

to the frames using Nuvovern® polyurethane varnish. This procedure ensures a contamination-free environment within the detector and the cleanroom. The presence of sparks and electrical shorts on GEM foils, resulting from such particles, poses a risk of GEM foil destruction. The attachment of the three GEM foils to the frames is facilitated by M2 screws strategically positioned around their perimeter. Integrated into the 3 mm frame are threaded M2 brass inserts, designed to prevent the release of epoxy glass particles during assembly. This precaution serves to diminish the likelihood of sparks, electrical shorts, and damage to the GEM foils. The M2 screws and M2 brass inserts can be seen in Appendix B.

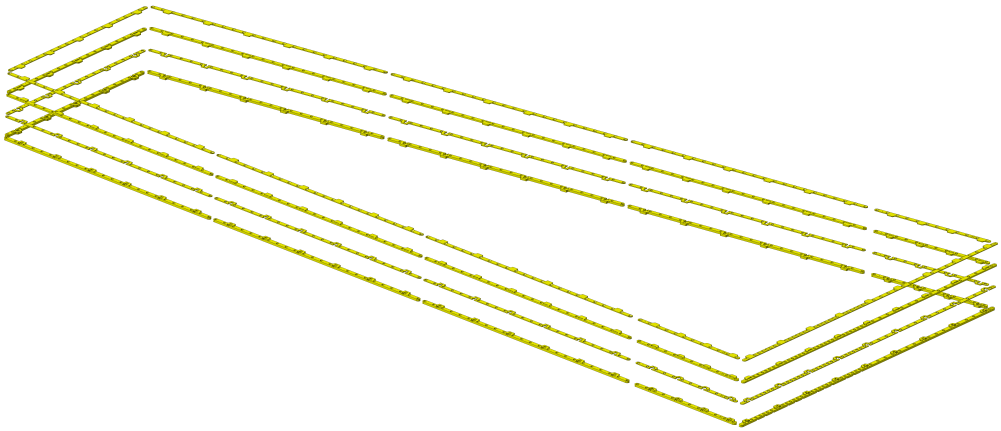

Figure 4.5: Internal frame mechanical design [1].

4.3.5 GEM Foil Design

The GE1/1 detector utilizes three trapezoidal GEM foils that are identical, as shown in Figure 4.6. The manufacturing process for these GEM foils involves the use of a traditional photolithography technique, a method extensively employed in the printed circuit sector.

4.3.5.1 Double-Mask Photolithography

The double-mask photolithography process, as described in references [5] and [6], entails applying a 15 µm thick photoresistive layer on both sides of a copper-clad polyimide substrate. The GEM-hole design is transferred onto flexible masks through UV-light exposure, and subsequent wet-etching selectively removes copper from the

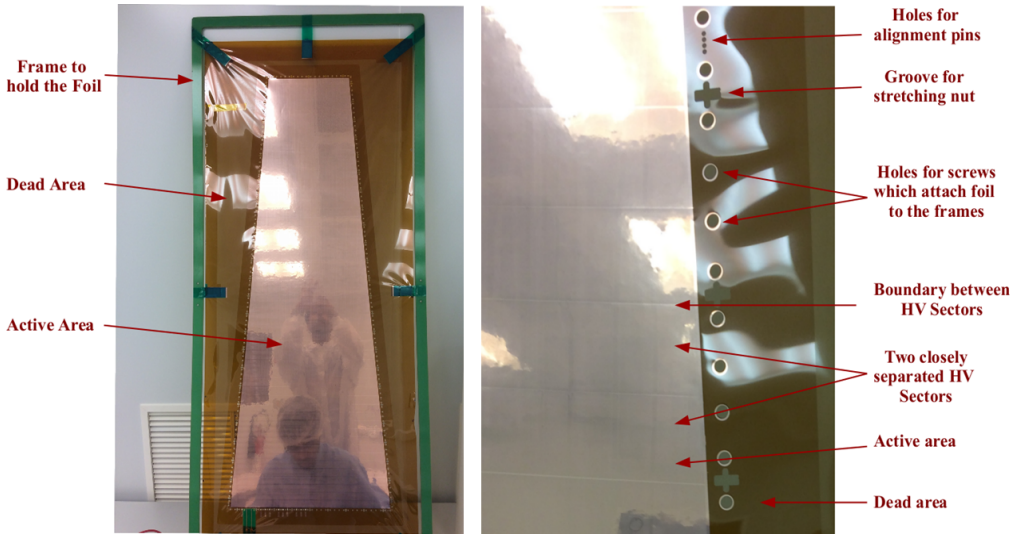

Figure 4.6: Left: GEM foil design for GE1/1 detector. Right: Foil strip with small holes for alignment pins during GE1 detector installation, larger holes for screw passage connecting the foil to internal frames, and plus-shaped slots for stretching nuts and HV sectors [1].

holes while preserving concealed areas. Ensuring an alignment error within 10 µm between the top and bottom masks is essential to maintain a uniform hole shape across the GEM foil. Nevertheless, manual alignment becomes impractical for foil sizes beyond approximately 40 cm. To address this challenge for larger GEM foils, single-mask photolithography emerges as a feasible alternative.

4.3.5.2 Single-Mask Photolithography

The single-mask photolithography procedure, as described in references [5] and [6], involves duplicating the GEM-hole design onto one side of the copper-clad polyimide substrate, eliminating the necessity for alignment. A 15 µm thick photoresistive layer is created, and the hole pattern functions as a mask for chemically etching holes in the top copper layer. Following the removal of the photoresist, the holes in the top copper layer act as a mask for polyimide etching. Subsequently, the bottom copper layer is etched following the polyimide, using the polyimide holes as a mask. A second polyimide etching from the bottom alters the hole geometry, resulting in the characteristic bi-conical shape. All GE1/1 detectors integrate GEM foils manufactured at CERN using the single-mask photolithography technique.

Figure 4.7 illustrates the procedural steps in the photolithography process for both the single-mask and double-mask techniques, both of which were formulated by the CERN PCB Workshop [5, 6].

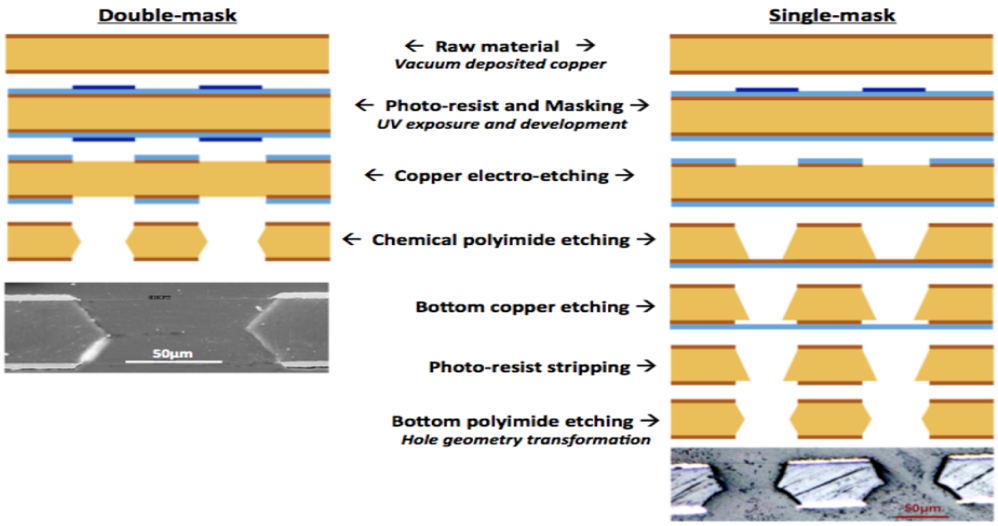

Figure 4.7: Left: Schematic comparison of processes for fabricating double-mask GEM-foils. Right: Single-mask GEM-foils [5] [6].

In contrast to the segmented surface of the GEM foil facing the drift board, the side directed towards the readout boards operates as a continuous conductor. These sectors, aligned parallel to the trapezoid's base, decrease in width from the narrow to the wide end, aiming to preserve an area of approximately 100 cm^2 for each sector. This method, known as the Blank-Hole Segmentation, has been utilized in the production of GE1/1 foils [7]. The segmentation introduced by this technique is implemented to restrict the maximum charge during a discharge, consequently diminishing the overall energy impact. In cases of extreme events, like a destructive discharge affecting a specific HV sector, only that particular sector is impacted, preventing harm to the entire foil. However, the use of this segmentation approach requires distinct HV supplies for each sector.

To meet this demand, a shared connection point is designated for the external HV supply, and an HV trace runs along the edge of the GEM foil. Common connection points, coupled with two redundant points, are situated at the wide end. Surface-mounted 10 MΩ protection resistors establish connections from the HV trace to each HV sector, effectively mitigating discharges, decoupling capacitance, and limiting the current drawn from the HV supply. In anticipation of the ME0 upgrade, the GEM

collaboration has introduced a novel strategy called Random-Hole Segmentation, which will be discussed further in Chapter 6.

4.3.6 Readout Board Design

In accordance with Figure 4.8, the takes on a trapezoidal shape as a PCB, featuring 3072 readout strips arranged radially along the longer dimension of the detector's inner side. This configuration defines the active area, marked by a 10.15° angle, facilitating a 2.6 milliradian (mrad) overlap (equivalent to approximately 5.67 strips) between successive active areas of the detector. Connections between the readout strips and the opposite side of the board are established through metalized vias, leading to 8 partitions in (i_η, i_ϕ), each containing 128 strips. The strip pitch varies from 0.6 mm at the narrow end to 1.2 mm at the broad end of the detector. Furthermore, the readout

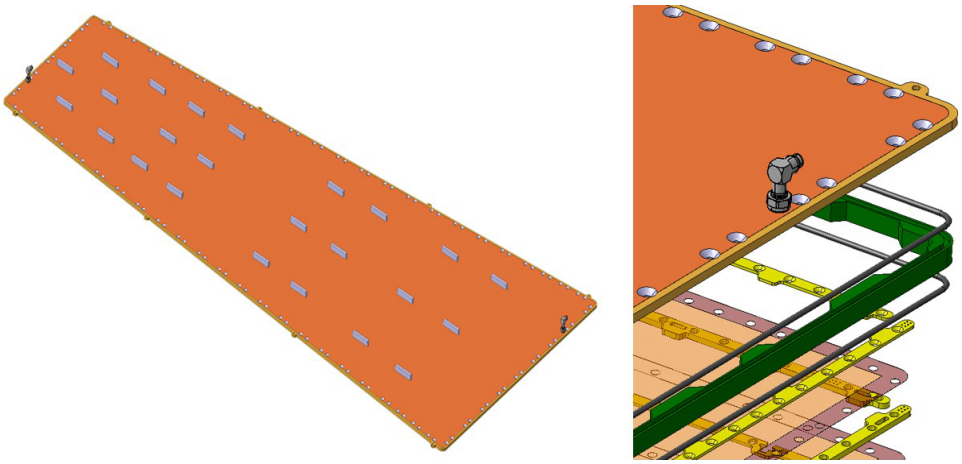

Figure 4.8: Left: Mechanical design of the Readout Board. Right: A close-up of readout board showing the gas plug [1].

board is equipped with two diagonally opposed holes at the corners to accommodate gas plugs, serving as the inlet and outlet. The gas distribution system for the GE1/1 chambers consists of an inlet and an outlet. The mechanical configuration of the gas stopper attached to the readout board is shown in Figure 4.8 (right). The gas mixture enters the detector diagonally through the inlet, and within the GEM-foil stack, distribution occurs through holes in the foil and gaps in the internal frames.

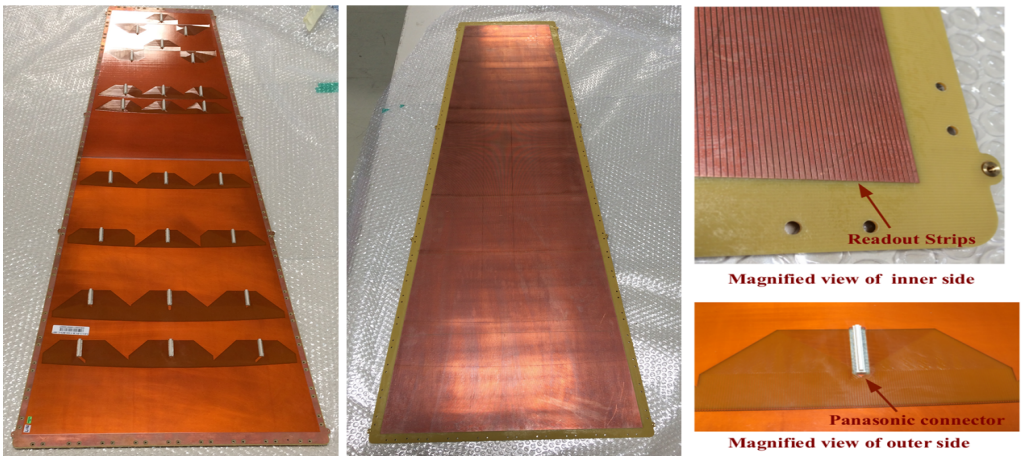

Figure 4.9: Left: The GE1/1 readout board's external side features 24 (i_η, i_ϕ) readout sectors with male Panasonic adapters, two holes for gas plugs, and perimeter holes for securing screws. Middle: Inner side of readouit board. Readout strips are visible on the inside. Right: A close-up of the inside view with readout strips and the external Panasonic connection [1].

4.4 Assembly Procedure

The functionality of GEM technology heavily relies on the precision-etched, micron-level perforations of the GEM-foils, and preserving their integrity is of utmost importance. Even the smallest particle contamination can lead to unpredictable functioning or permanent damage to the detector. Consequently, assembly takes place exclusively within a cleanroom rated at a minimum class-1000 standard. Tools that have lubricated shafts, soldering equipment requiring volatile flux heating, motors, vacuum pipes with out-gassing oils, and other potential sources of contamination are strictly forbidden in the assembly area.

Those participating in the assembly strictly adhere to cleanroom protocols, encompassing the use of aprons, dust-free gloves, facial masks, shoe coverings, hair caps, and similar precautions. Figure 4.2 presents a schematic overview of the assembly process, highlighting key steps. The additional insights and technical details regarding CMS GE1/1 detector construction methods, can be found in [8].

4.4.1 Drift Board Preparation

The preparation of the drift board involves attaching the stainless steel pull-outs and soldering the 12 HV-pins responsible for powering each layer. Given the inherent risk

of contamination associated with soldering and hand screw fastening, this specific step is executed outside the cleanroom. The heights of each pair of HV-pins are precisely aligned with the positions of the corresponding GEM-foils and are methodically placed on the drift board to establish a gas-tight seal. Each pull-out is securely attached to the drift board using two A2 stainless steel M3 $\times$ 6 $\times$ 8 screws and polyamide washers. Additionally, at this stage, the Surface-Mount Device (SMD) 10 MΩ protective resistor and the decoupling RC circuit, consisting of a 100 kΩ resistor and a 330 pF capacitor, are positioned in their designated locations. Before securing them, all screws and washers undergo a meticulous cleaning process in an ultrasonic bath to eliminate any potential dirt or contaminants.

The HV-pins are positioned on the drift board within the gas volume to ensure an optimal and dependable power supply to each foil. Their spring-loaded design ensures uninterrupted contact with the corresponding pads of the GEM-foil when placed in the stack. Figure 4.10 provides a visual representation of the HV circuit architecture on the drift board. The HV-pins are attached to pads located outside the gas volume,

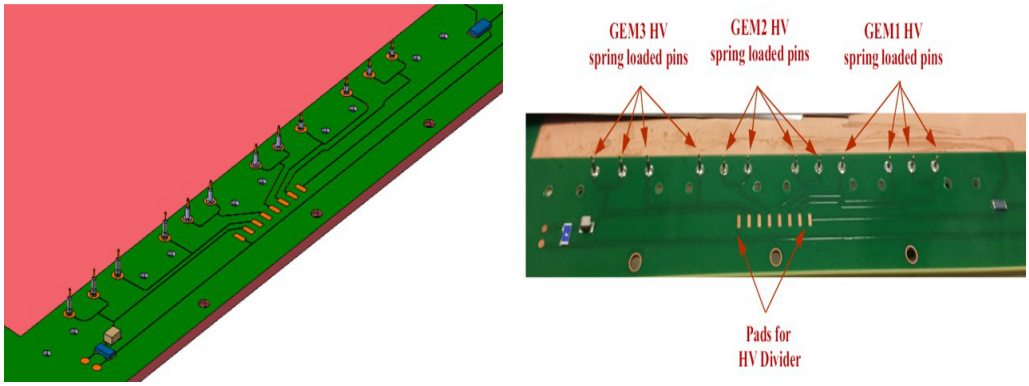

Figure 4.10: Left: Schematic of the HV circuit with twelve pins on the drift board. Right: Concise arrangement of the high-voltage circuit on the drift board with twelve HV-pins, ensuring proper contact with corresponding GEM-foil pads [1].

specifically designed to be compatible with both single-channel and multi-channel power supplies. In situations where a single-channel power source is employed, a resistive high-voltage divider network is applied to ensure the appropriate distribution of voltage within the detector. The design and layout of the HV-pins on the drift board, along with their positions in relation to the GEM-foil stack, are illustrated in Figure 4.11 (left). The schematic of the HV divider circuit for the 3/1/2/1 mm gap configuration can be found in Figure 4.11 (right).

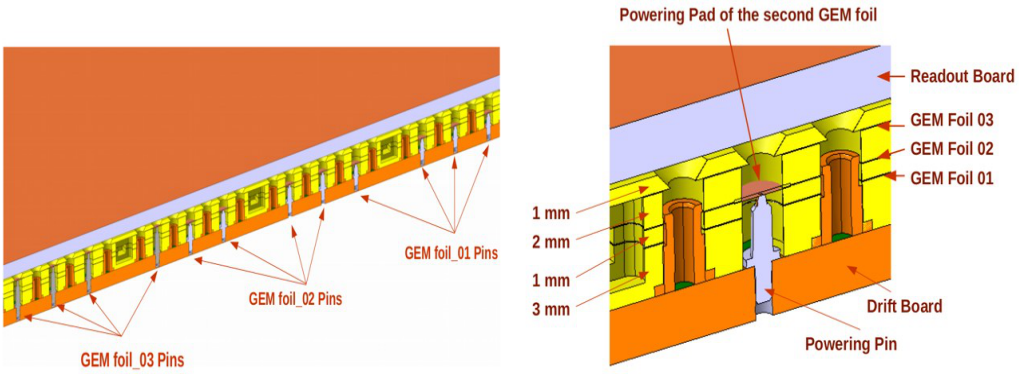

Figure 4.11: Left: A sectional view of the spring-loaded twelve HV-pins on the drift board and their relation to the GEM-foils. Right: Detailed view of an HV-pin showcasing the stack of GEM-foils, internal frames with thicknesses of 3 mm, 1 mm, 2 mm, and 1 mm, the power pad of the second GEM-foil, the lone HV-pin in contact with the power pad of the second GEM-foil, and the readout board [1].

4.4.2 Readout Board Preparation

The preparation of the GE1/1 readout board involved a series of steps, including the installation of brass inserts in the lateral flanges, threading gas holes, and attaching gas connectors with adhesive. Initial cleaning utilized a vacuum cleaner, followed by placing the board on a table with strips facing up, avoiding direct contact with bare fingers. To protect Panasonic connectors from scratching, a soft material or foam sheet was utilized. Clamping brass inserts in designated holes was done securely with a clamping hand. Using a 3 mm tap on the opposite side of the board created a thread pattern for the gas connector as shown in Figure 4.12 (left). Dust removal and ethanol cleaning with tissue paper were conducted on both sides around the hole. On a metallic surface cleaned with ethanol, epoxy glue components were mixed to an opaque, uniform consistency. The Teflon washer was removed from gas plugs, and a metallic stick applied a thin ring of glue between the body and the threaded part of the connector. Gently screwing the gas connector onto the readout board until the base touched ensured the formation of a neat and smooth glue ring around the connector base shown in Figure 4.12 (right).

4.4.3 GEM Stack Assembly

In the critical assembly phase of the GEM-stack, ensuring precise and contamination-free alignment is important. This procedure occurs within a controlled environment,

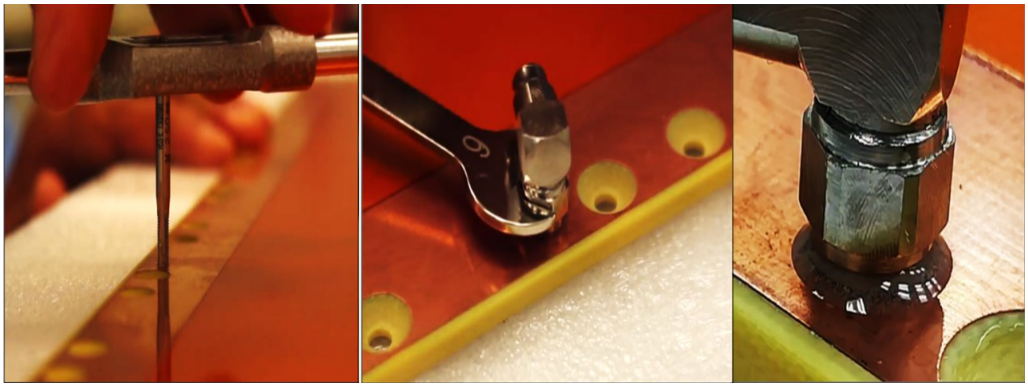

Figure 4.12: Left: Creating the thread in the gas inlet/outlet. Middle: Affixing the gas connector to the board through the application of adhesive. Right: Close of the gas connector after drying the adhesive [1].

utilizing alignment pins on a Plexiglass base. The 3 mm internal frame components, illustrated in Figure 4.13 (right), are strategically positioned over alignment pins before inserting the initial GEM-foil. Before aligning the foil on the initial external frame

Figure 4.13: Left: GEM-foil cleaning in progress with an adhesive roller, effectively eliminating micron-level dust particles due to its strong sticking capacity. Right: First GEM-foil placement on Plexiglass base with positioned 3 mm internal frames [1].

layer as shown in Figure 4.13 (left), a thorough cleaning process takes place. This cleaning is facilitated by an anti-static adhesive roller. Following this, QC2 is executed for each GEM foil utilizing a Multi Mega-ohmmeter MEGGER MIT420 insulation tester. A potential difference of 550 V is applied across the foils, creating a substantial electric field within the GEM-holes. The impedance of the foils should surpass 10 GΩ, and the count of sparks is recorded every 30 seconds for the subsequent 10 minutes. The spark rate should not surpass 2 Hz in the last two or three minutes of the test, depending on relative humidity. Sparks, stemming from microscopic particles, function as an additional cleaning method. Nevertheless, excessive sparking indicates

dust pollution, requiring a repetition of basic foil cleaning procedures. Post-test, electrostatically charged foils undergo discharge to prevent detrimental discharges during the subsequent stretching process, a critical step in preventing foil damage.

As a precaution, GEM-foils undergo manual stretching and temporary fixation using tape between the extended outer holding frame (to be removed later) and the Plexiglass base. This prevents sagging and contact during stack alignment before stretching. Foil alignment is achieved with holes and secured to internal frames using a specific pattern as shown in Figure 4.5. The stack is secured by M2 $\times$ 6 screws against M2 brass inserts depicted in Figure 4.14. During assembly, stainless steel nuts are

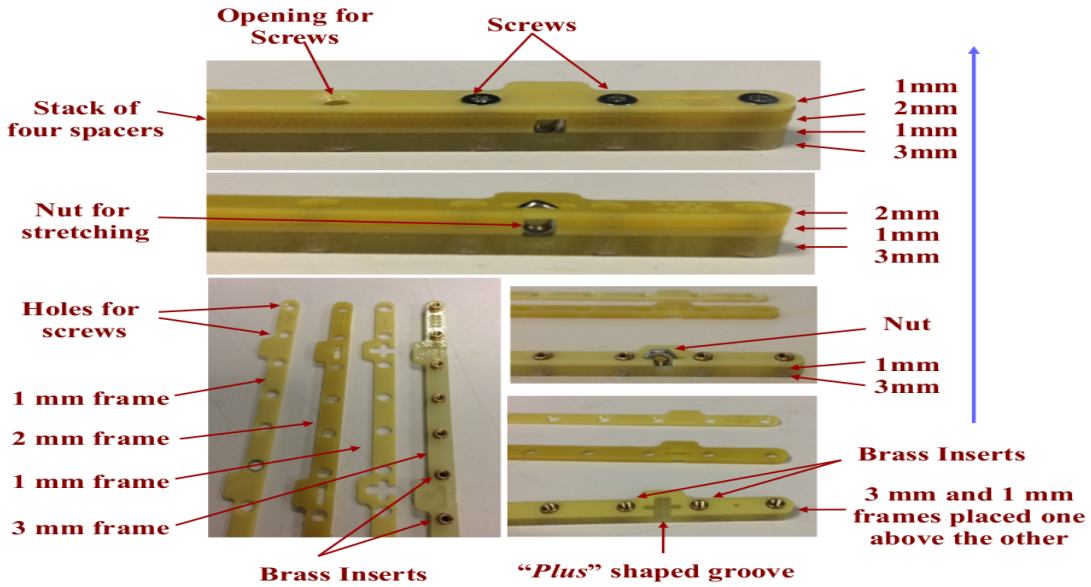

Figure 4.14: The GE1/1 detector's four internal frames, stacked in a 3/1/2/1 mm gap configuration, include brass inserts, stretching nut grooves, and fastening screw positions [1].

placed within specifically designed plus-shaped grooves on the internal frames. Their axes are positioned perpendicular to the axes of the brass inserts within the internal frame. This step follows the addition of the second GEM foil to the stack, followed by the attachment of the 2 mm frame. The nuts, combined with the pull-out and specialized screws, play a role in the stretching mechanism described in Section 4.4.5. The construction of the GEM-foils stack is finalized by eliminating the void spaces (kapton) around the GEM-foils. Figure 4.15 visually illustrates these stages.

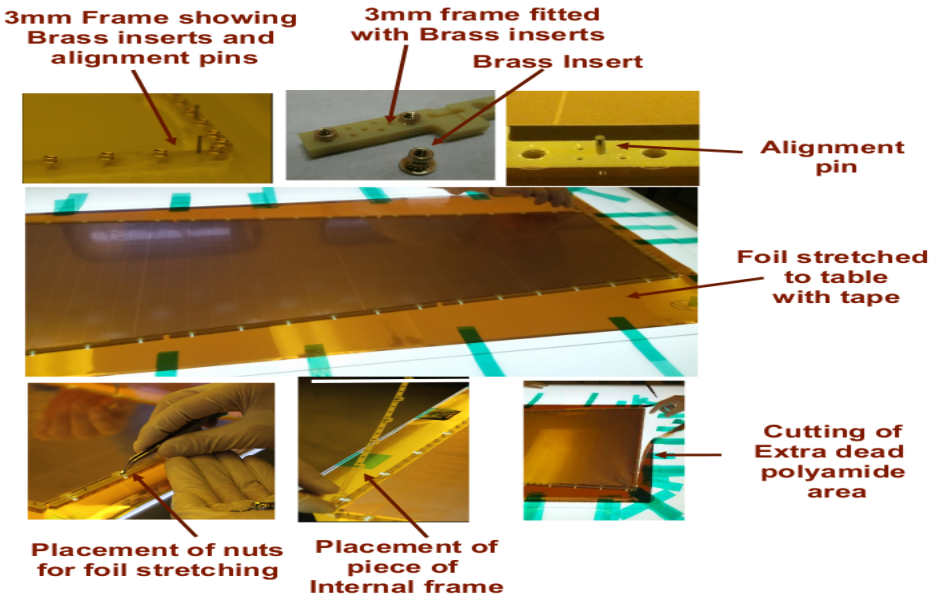

Figure 4.15: The step-by-step process in assembling the stack formation [1].

4.4.4 GEM Stack Placement

The assembly procedure initiates with the placement of the GEM-foils stack onto the drift board. To ensure operational stability, the drift board is affixed to the Jig using aluminum bars secured with fixation bolts, as illustrated in Figure 4.16. The Jig assumes a pivotal role in preserving the level of the drift board, mitigating potential deformations that might arise during the stretching of the GEM-foils stack or the fixation of the readout board.

4.4.5 Stretching Mechanism

Upon situating the stack onto the drift board, screws of dimensions M2.5 $\times$ 8 $\times$ 8 are strategically arranged along the stack's perimeter and manually tightened into pre-installed perpendicular nuts within the internal frame grooves. These screws undergo manual tightening with a closely monitored torque set between 8-10 cN·m. Consequently, the GEM-foils experience uniform tension as the inner frame extends outward, reaching the pull-outs, as illustrated in Figure 4.17. Precision adherence to torque parameters is crucial due to inherent technology tolerances impacting gas gain uniformity and time response. Ensuring consistent stretching during assembly is vital for achieving a uniform response across the detector.

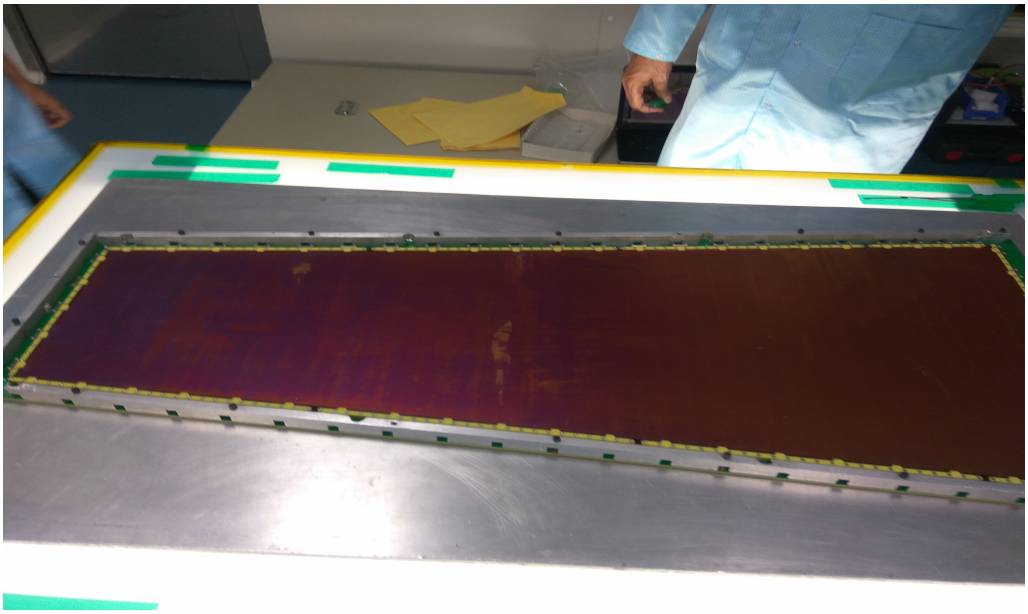

Figure 4.16: The arrangement of the GEM-foils stack on the drift board, accompanied by securing the drift board against the Jig using aluminum bars [1].

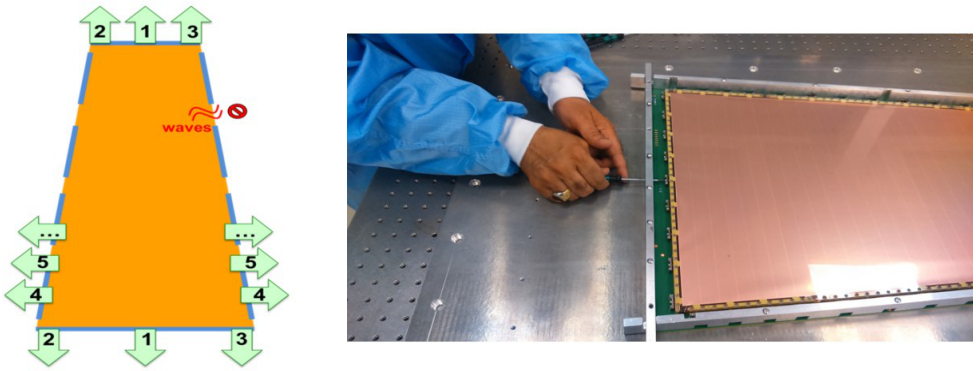

Figure 4.17: Left: Explanation of the stretching process. Right: Actual stretching of the foils [1].

Following the stretching process, a thorough connection check is conducted to assess impedance between the gaps and across the GEM-foils using a MEGGER MIT420 insulation tester. The HV traces on the drift board, located outside the gas volume, facilitate the application of a 550 V potential difference between the gaps and across the GEM-foils. An expected impedance range of $100-150$ GΩ is anticipated at 30% RH, with potential variations at higher humidity levels.

4.4.6 Chamber Closure

The GEM-foils stack is encased within the external frame using an O-ring, and the readout board is positioned above the external frame. A2 stainless steel M3 $\times$ 6 $\times$ 8 screws, equipped with polyamide washers, are employed to affix the readout board to the pull-outs. This process results in the deformation of the O-ring, effectively sealing gaps and creating a gas-tight barrier. The final chamber configuration is illustrated in Figure 4.18 (left). In this setup, the induction gap can be assessed by connecting the Panasonic-to-Lemo adapter to one of the readout sectors. Applying 550 V between the GEM3 bottom and the signal pad of the Panasonic-to-Lemo converter while holding the chamber vertically, as demonstrated in Figure 4.18 (right), allows for the inspection of impedance, which should rapidly reach 100 GΩ.

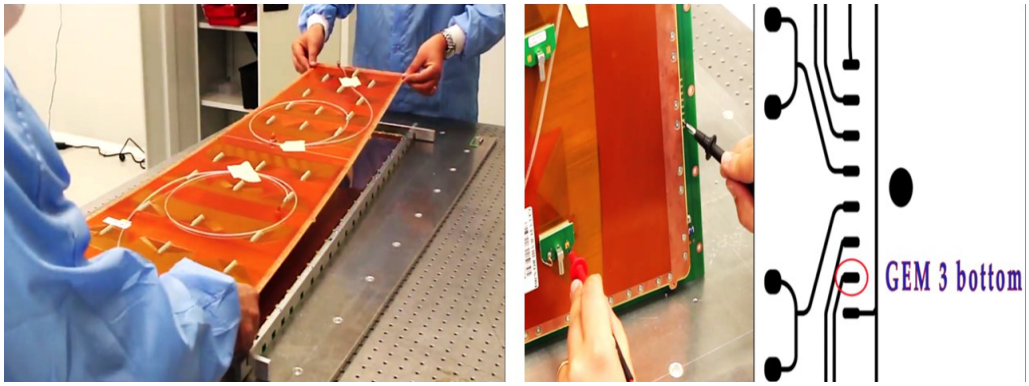

Figure 4.18: Left: Attaching the readout board to the stack. Right: Testing the induction gap with an insulation meter (MEGGER).

4.5 GE1/1 Quality Assurance

4.5.1 Overview of the QA/QC

The QA and QC processes are integral in ensuring the effective delivery of GE1/1 detectors, ensuring optimal operation upon integration into the Muon Spectrometer of the CMS experiment. The ultimate quality and performance of the detector hinge on both the quality of manufacturing and the precision of assembly operations. Rigorous QA and QC methods have been formulated to avert potential mechanical or electrical

flaws that might jeopardize detector performance. These methods are crafted to maintain a high level of consistency across all manufacturing and QC facilities.

A total of 8 GE1/1 short chambers underwent full assembly and testing (QC2 to QC4) at Panjab University. Subsequently, QC5 was conducted at Delhi University, as India was having only one X-ray and SRS system facility available.

In Figure 4.19, there is a depiction of a flowchart delineating the general procedures for QA and QC in the GE1/1 project. This entire process is segmented into three primary stages:

- Assembly and QC of components at the CERN production site.
- Assembly and QC of single GE1/1 detectors at manufacturing locations.
- Assembly and QC of superchambers at the CERN production site before delivery for installation at the CMS Muon System.

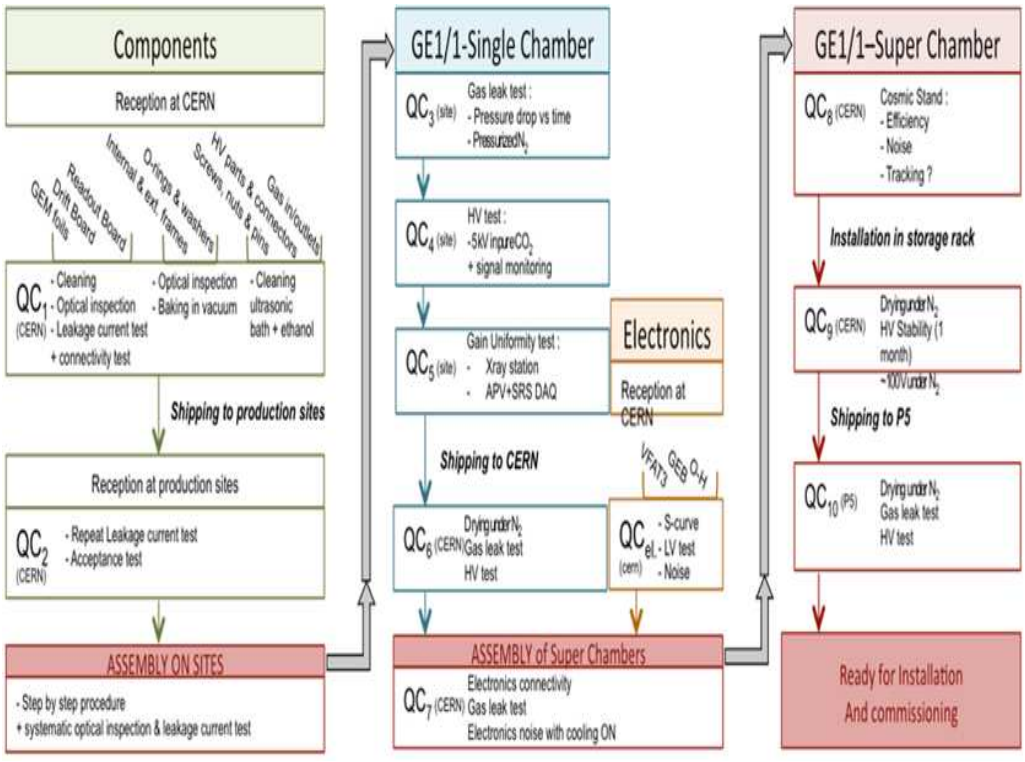

Figure 4.19: Schematic summary of the QA and QC processes for GE1/1 detectors [9].

The following sections describe the main QA and QC procedures utilized for the GE1/1 detectors produced at the CERN manufacturing sites.

- Assembly components: QC1 – GE1/1 Detectors Components Inspection and Readout Board Connectivity Test.
- GEM-foils: QC2 – Leakage Current Test.
- GE1/1 detector: QC3 – Gas Leak Test in CO_2.
- GE1/1 detector: QC4 – HV Test in CO_2.
- GE1/1 detector: QC5 – Gas Gain Calibration Test in Ar/CO_2 (in percentage ratio 70/30).

4.5.2 QC1 – GE1/1 Detectors Components Inspection

Manufacturers produce GE1/1 detector components, sent to CERN for immediate defect verification. Post-cleaning includes visual inspection using deionized water and processes like ultrasonic baths, baking, and sandblasting to ensure quality. Subsequent sections outline initial inspections and tests on these components.

- **Frame**: Optical inspection identifies cracks and defects in the epoxy glass of internal and external frames. Frame dimensions, including groove measurements, are accurately assessed using a digital caliper and dial indicator, ensuring enhanced gas-tightness in the detector shown in Figure 4.20 (left and middle).

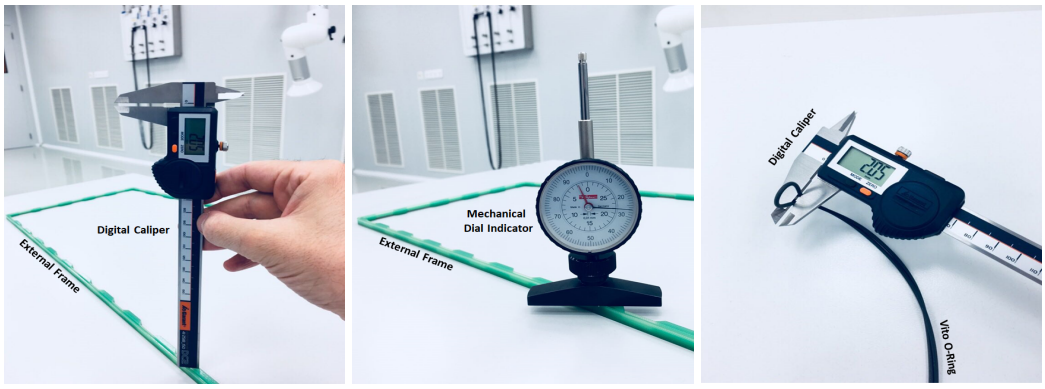

Figure 4.20: Left: Using a high-resolution digital caliper, the width and depth of the external frame measurement. Middle: Using mechanical dial indicator. Right: Assessing the external diameter of the O-ring using caliper [1].

- **O-ring**: Ensuring Viton O-ring integrity involves optical examination and specialized cleaning. The external diameter is precisely measured with a high-resolution

digital caliper for proper coupling with the external frame, ensuring gas-tightness shown in Figure 4.20 (right).

- **Drift Board**: Optical inspection identifies mechanical damage and surface irregularities. A high-pressure nitrogen cannon removes dust and residues.
- **Readout Board**: The initial check on the readout board's flatness is done on an optical table. Bending is assessed by measuring the board's height at various points using a high-resolution digital caliper 4.21. Optical inspection identifies defects in readout strips or Panasonic adapters. Due to small sizes, visual inspection alone doesn't guarantee integrity. A dedicated QC test uses an ARDUINO Mega 2560 to simultaneously check all strips for shorts or open connections. The ARDUINO platform, plugged into each Panasonic connector, manages data acquisition and system control for electrical testing. The readout board is rejected if more than 4 defects (short circuits) are found across the entire board or more than 3 faulty channels within the same connector.

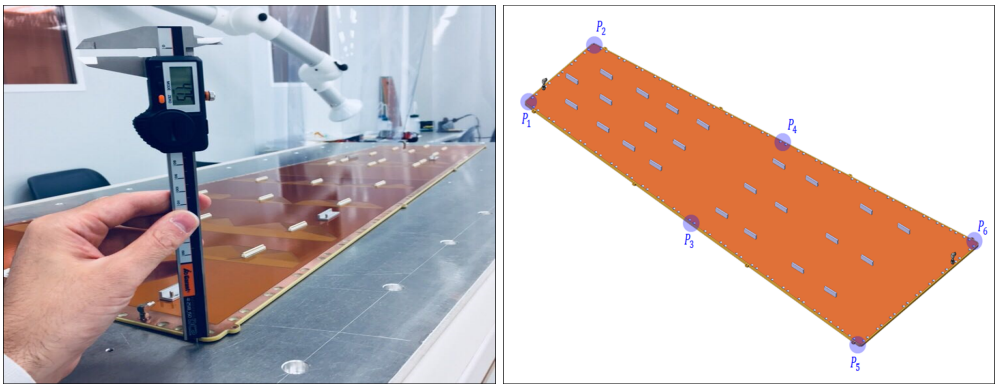

Figure 4.21: Left: Precise height measurements at various points along its perimeter on a flat optical table using a high-resolution digital caliper. Right: different points for measurements [1].

Once meeting the specified acceptance criteria, entire assembly sets are either utilized for assembly at the CERN production site or sent to alternative production and QC facilities.

4.5.3 QC2 — Leakage Current Test

During chamber operation, applying high voltage to GEM foil's surfaces can create lower-resistance paths within the holes, resulting in leakage current. Manufacturing

defects and environmental factors (humidity, temperature) can enhance this current, impacting data quality. Continuous monitoring is necessary. Leakage current is an indicator of foil health. Conducting the QC2 test before and after chamber assembly ensures undamaged foils and prevents dust deposition.

The QC2 process involves 4 key steps to ensure optimal GEM-foil functionality.

1. **QC2 Fast Test**: A MEGGER, applies a 550 V potential difference between the top and bottom surfaces of the foil for 10 minutes. Measurements include leakage current, impedance, and spark count. Conducted in a cleanroom, the test is successful if the foil's impedance surpasses 10 GΩ with fewer than 2 sparks in the last three minutes. Significant damage caused by sparks would be evident in both impedance and spark rate.

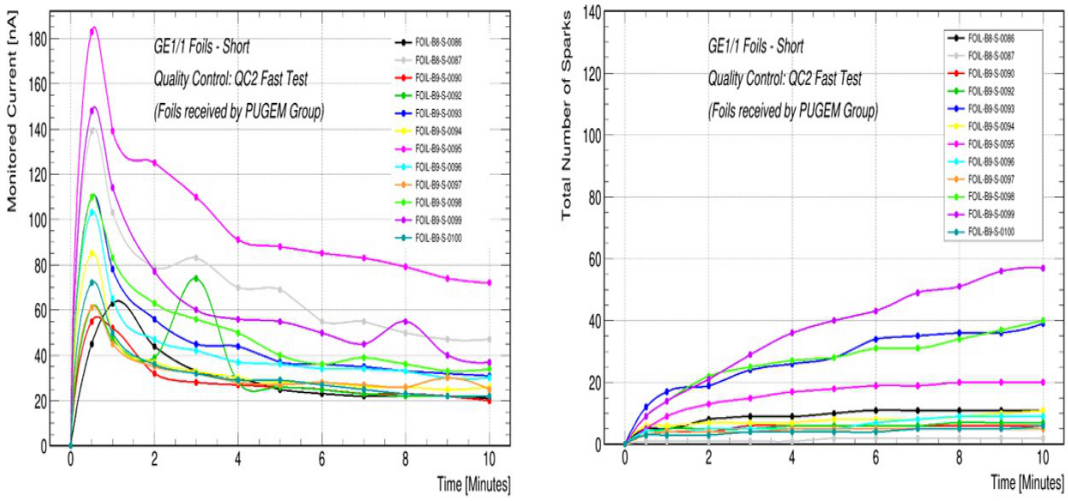

Figure 4.22: Left: QC2 fast test leakage current results for few foils received by Panjab University from CERN for GE1/1 Assembly. Right: Total sparks count during test is plotted against time.

2. **QC2 Long Test**: In a cleanroom, the test places the foil in a nitrogen-filled box with a 50 L/h flux, reducing humidity below 7%. A programmable power supply applies a 600 V high voltage to both faces. Success is defined by a leakage current of approximately 3 nA and fewer than 3 sparks in the last 6 hours at this voltage.

3. **QC2 Fast Dry Gas Test**: This pre-assembly test, also utilized for examining chambers under suspicious conditions, includes purging the chamber with pure CO_2 for 5 hours to prevent discharge-related damage. Subsequently, the QC2

fast post-assembly procedure is executed, with the requirement that foil and gap impedances exceed 20 GΩ and 100 GΩ, respectively.

4. **QC2 Post-Assembly**: Performed outside the cleanroom, this test safeguards against the impact of assembly dust on foil operation. Similar to the QC2 fast test, 550 V was applied one pair at a time to both foil faces and electrodes, generating an electric field in the gaps. Successful completion requires foil and gap impedances to surpass 10 GΩ and 100 GΩ, respectively, with no sparks observed in the last ten minutes. A failed test mandates opening the chamber in the cleanroom for issue identification and resolution.

4.5.4 QC3 — Gas Leak Test

QC3 is designed to identify and measure gas leakage in a GE1/1 chamber. The process involves introducing pure CO_2 into the detector, generating a 25 mBar overpressure by closing the gas output valve. After reaching this state, the input valve is shut, commencing the measurement of internal overpressure. Simultaneously, environmental conditions, including pressure and temperature, are continuously observed to guarantee a precise estimation of internal overpressure.

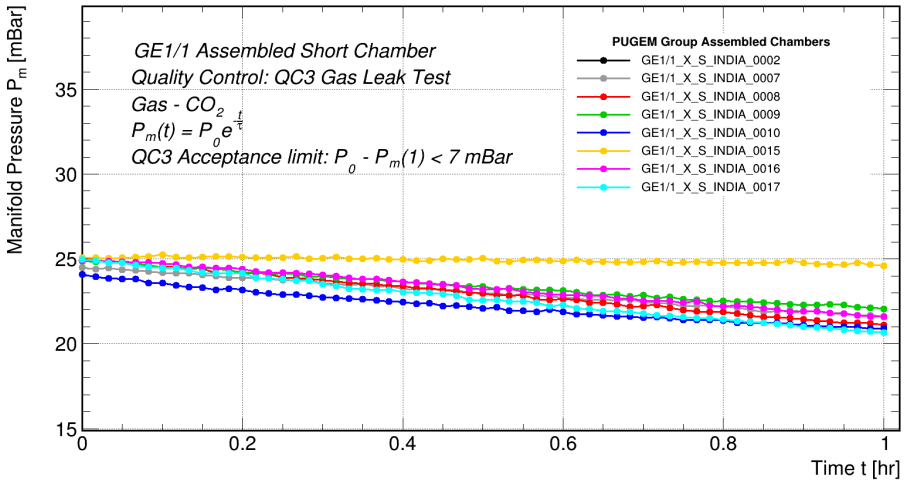

Figure 4.23: QC3 gas leak rate test performed for PUGEM group assembled chambers. All the chambers passed the QC3 test.

The internal overpressure decreases exponentially over time according to the equation

$$P(t) = P_0 e^{-\frac{t}{\tau}} \tag{4.1}$$

where P_0 is the internal overpressure at t = 0 and τ is the gas leak time constant, indicating the rate of overpressure decrease. The test is considered successful if the internal overpressure drop is less than 7 mBar per hour.

4.5.5 QC4 — HV Test in CO_2

The QC4 test involves purging the detector with pure CO_2 at a rate of 5 L/h. Its objectives are to detect potential defects in the HV circuit by measuring the I-V curve and to quantify the intrinsic noise rate. During the test, HV is supplied to individual electrodes using a resistive divider power supply shown in Figure 4.24 (left). The I-V curve is generated by varying the voltage from 0 V to 3.0 kV in 200 V increments, and then up to 4.9 kV in 100 V steps. Calculating the measured resistance $R_{Measured}$ from the curve enables a comparison with the expected resistance $R_{Expected}$. This initial test is considered successful if the percentage difference between the resistances is below 2%.

$$\frac{|R_{Measured} - R_{Expected}|}{R_{Expected}} < 0.02 \tag{4.2}$$

To evaluate the intrinsic noise rate, a dedicated configuration, illustrated in Figure 4.24 (right), captures the signal originating from the GEM3 bottom face and logs the signals detected over a continuous 1-minute operation at a consistent HV level. This process is replicated for the voltage values employed in the I-V curve scan. The test is considered successful if the noise rate at 4.9 kV is less than 0.02 Hz/cm^2.

4.5.6 QC5 — Effective Gain and Response Uniformity

The QC5 test involves measuring the effective gas gain generated by the detector under a consistent voltage applied through a resistive divider, coupled with an assessment of RU. In this test, a Silver target X-ray gun emits photons within the energy range of 22 to 25 keV. The detector, located within a copper enclosure designed for radiation con-

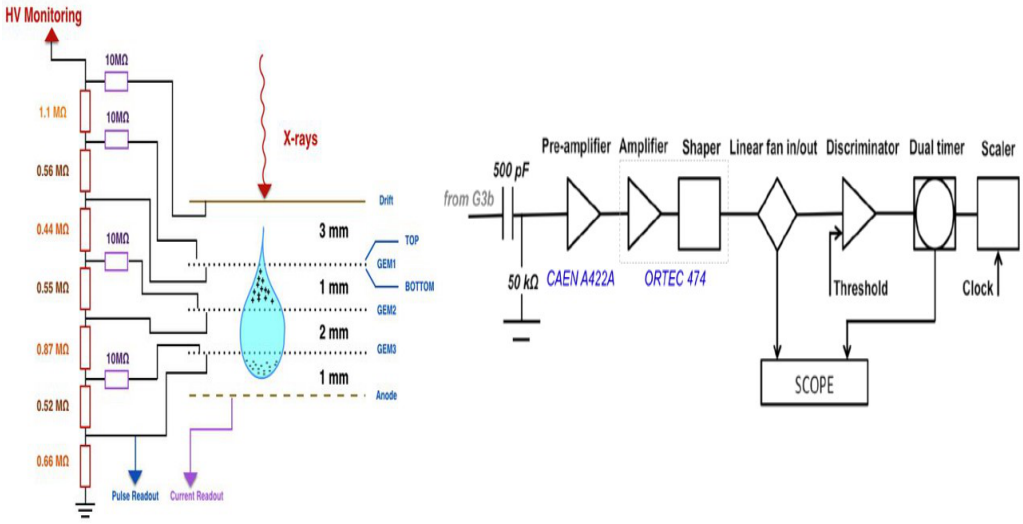

Figure 4.24: Left: Schematic of the resistive divider utilised in QC4 tests. Channels for each connection are indicated on the right: Drift, GEM1 Top, GEM1 Bottom, GEM2 Top, GEM2 Bottom, GEM3 Top, GEM3 Bottom. Right: The setup for measuring noise rate in QC4 is depicted in the diagram [1].

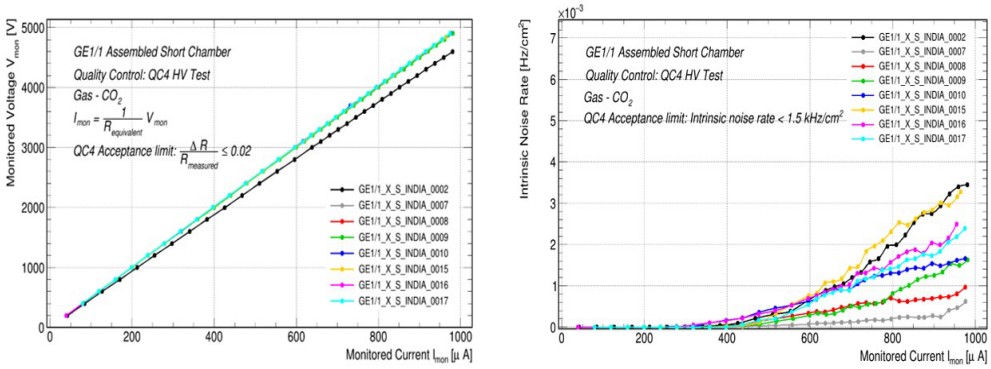

Figure 4.25: Left: Results from the QC4 HV Test on the PUGEM group assembled chambers indicate a current-voltage relationship with an equivalent resistance (R_{equiv}) of about 5 $M\Omega$ for all the chambers except GE1/1-X-S-INDIA-0002 in which HV Filter was not used. Right: The intrinsic noise rate for the assembled chambers.

tainment as shown in Figure 4.26, undergoes flushing with the standard Ar/CO_2 (in percentage ratio 70/30) at a flow rate of 5 L/h. Upon interaction with the copper layer of the drift board, X-ray gun photons are absorbed, resulting in copper de-excitation and the emission of photons at 8.03 keV. This Cu fluorescence becomes integrated into the detector gas, giving rise to the emission of primary electrons. Subsequently, these electrons undergo multiplication through the three GEM foils, leading to the generation of a signal on the readout strips. The electrical charge generated on the readout strips undergoes amplification through APV25 analog readout chips [10],

followed by digitization through Analog to Digital Converter (ADC). Subsequently, the recorded data is processed by Front-End Concentrator cards (FECs), integral parts of the RD51 Scalable Readout System (SRS) [11]. A schematic representation of this test setup is provided in Figure 4.26.

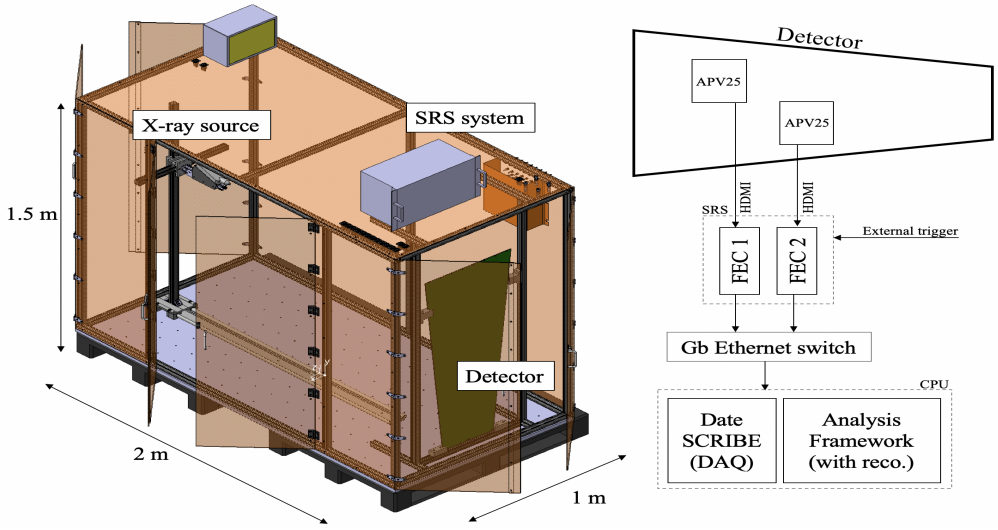

Figure 4.26: Left: Schematic representation of the X-ray station utilized in the QC5 RU test. Right: Standard data flow within the SRS DAQ, extending from the front-end APV25 to the analysis framework [12].

4.5.6.1 Effective Gas Gain

The G_{eff} is determined using the relation

$$G_{eff} = \frac{I_a}{R \cdot n_e \cdot e} \tag{4.3}$$

where I_a is the current from multiplication electrons on the anode, R is the photon interaction rate, n_e is the number of primary electrons, and e is the charge of the electron. Gain measurement occurs consistently in the sector (i_η, i_ϕ) = (4, 2), can be correlated from Figure 4.27 (left), with voltage values applied sequentially, ranging from a divider current of 550 µA to 700 µA in 10 µA increments. The number of primary electrons is calculated using the formula:

$$n_e = E_\gamma \left(\frac{f_{Ar}}{W_i(Ar)} + \frac{f_{CO_2}}{W_i(CO_2)} \right) \tag{4.4}$$

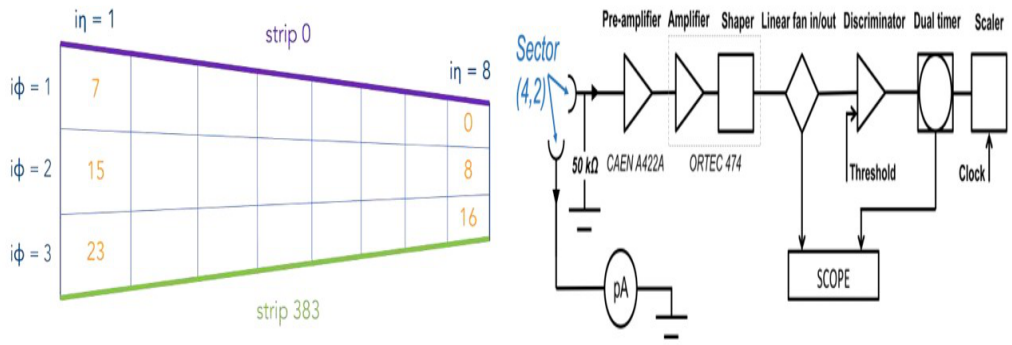

Figure 4.27: Left: Assignment of VFATs to specific locations on the covered readout sectors is determined [13]. Right: Diagram of the configuration utilized for measuring the effective gas gain in QC5 [1].

Here,

- E_γ = 8.03 keV represents the photon energy within the gas.
- $W_i(Ar)$ = 26 eV and $W_i(CO_2)$ = 33 eV denote the work functions for Ar and CO_2.
- The numerators in the fractions contain gas concentrations in the mixture: f_{Ar} = 0.70 and f_{CO_2} = 0.30.

The amplified current (I_a) on readout sector strips is measured using a pico-ammeter. The photon interaction rate (R) is determined through an experimental setup shown in Figure 4.27 (right), counting signals on readout strips within a 60-second interval. For accurate R and I_a measurements, background subtraction is utilized, using counts and currents observed under the same conditions with the X-ray gun turned off. A typical GE1/1 detector gain at a 700 μA divider current is 3.5×10^4, and the results for PUGEM group assembled short chambers are depicted in Figure 4.28.

4.5.6.2 Response Uniformity

To conduct a comprehensive evaluation of gas gain across the detector, the previously outlined procedure becomes impractical due to time constraints. Instead, the adopted approach involves irradiating the entire detector with an X-ray gun and recording signals on each strip. This test also occurs within the copper box. To prevent electronics saturation and facilitate the detection of gain differences between nearby regions in a similar setup except, the chamber operates at a low gain of $\sim$ 600.

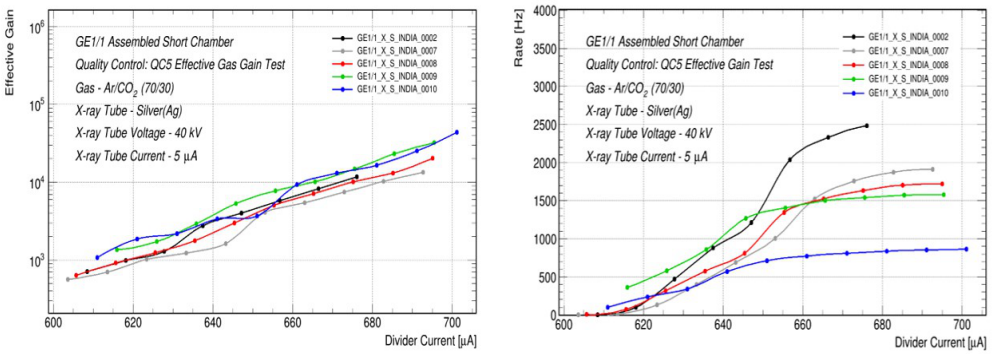

Figure 4.28: Left: QC5-effective gain test results of few assembled GE1/1 short chambers. Right: Photon interaction rate measured during the test.

The GE1/1 detector geometry is defined, with 768 slices created for gas gain evaluation. Each slice represents a division of the η-partition into 96 slices, each containing 4 strips. Cluster charge for each slice is added to a histogram, and noise events are rejected based on charge and cluster size criteria. A spectrum of charge collected by strip clusters is fit to extract the copper fluorescence photopeak position. The mean position of the photopeak for each slice is used to generate a distribution for the entire detector area, with a Gaussian fit used to extract the mean (μ) and standard deviation (σ). The RU is calculated as the ratio of σ to μ, multiplied by 100. Maintaining RU below 30% ensures stable operation efficiency (98%) and time resolution (< 10 ns) across all detector sectors.

In the data analysis phase, the accumulated charge from each strip cluster that produces a signal is employed to generate a uniformity map. This map calculates the average effective gas gain across the entire detector, along with its standard deviation. Additional details can be found in [1].

4.5.7 QC6 — HV Stability Test

After passing the QC5 test, chambers undergo transport to CERN, where mechanical stress and potential dust ingress during transit may impact HV stability. Therefore, a new QC test, QC6, is conducted in pure CO_2 with the following steps:

- Measure the impedance of each foil with a MEGGER, passing if the impedance is over 10 GΩ in one minute for each foil.

- Perform I-V curve measurements for HV electrodes (foils, transfer regions, induction and drift gaps) using a multichannel power supply with an A1515TG board, identifying defects in T-filter circuits or distribution issues.
- Evaluate foil stability by applying 580 V with a current threshold ($I_0 = 2\mu A$) one foil at a time. The test passes if the trip rate (current exceeding the threshold resulting in voltage turn-off) is below 1 trip/hour, requiring potentially lengthy testing to remove contaminants on the foils.

Contaminants can create a conductive pathway inside a GEM hole, persisting until removed. Dust can be vaporized by applying a prolonged voltage difference or using a MEGGER. In severe cases, such as when copper drops are melted and deposited in a hole during a discharge, a permanent short circuit between the top and bottom copper layers can occur. This leads to a voltage drop and reduced gain in the affected foil sector. Concurrently, the power supply channel feeding the foil experiences increased current, causing voltage reduction in other sectors due to a portion of the voltage falling on the filter resistors [14].

4.5.7.1 Superchamber Formation

Following the successful passage of QC7, two chambers with comparable gains are conjoined in parallel using aluminum holders. This decision is guided by the configuration of the GEM HV system within CMS, which channels power to both layers of a superchamber through the same HV board channels. Given that the voltage applied to the electrodes of both layers remains identical, it is imperative for the chambers to exhibit similar gains, ensuring consistent behavior.

4.5.8 QC7 — Electronics Test

Following the QC6 test, the chambers undergo the integration of electronic components, including the GEB, 24 VFATs, 9 FEASTs, and the OptoHybrid board. The QC7 focuses on verifying the correct operation of these components. I contributed to this effort during my time at CERN. The main objectives of QC7 include establishing the optimal configuration of the VFAT in terms of the global charge threshold level and identifying any electronic issues, such as dead channels or disconnections.

4.5.8.1 Two Test Phases in QC7

The QC7 test is conducted twice before formally affirming the validation of the chamber:

- In the absence of the cooling plate, during this stage, the chamber is solely furnished with the electronics. Cooling for the electronic components is maintained by affixing heat sinks to each component, connecting them with a thermal pad using a non-conductive thermal paste. Additionally, a fan positioned above the chamber expeditiously dissipates heat as shown in Figure 4.29.

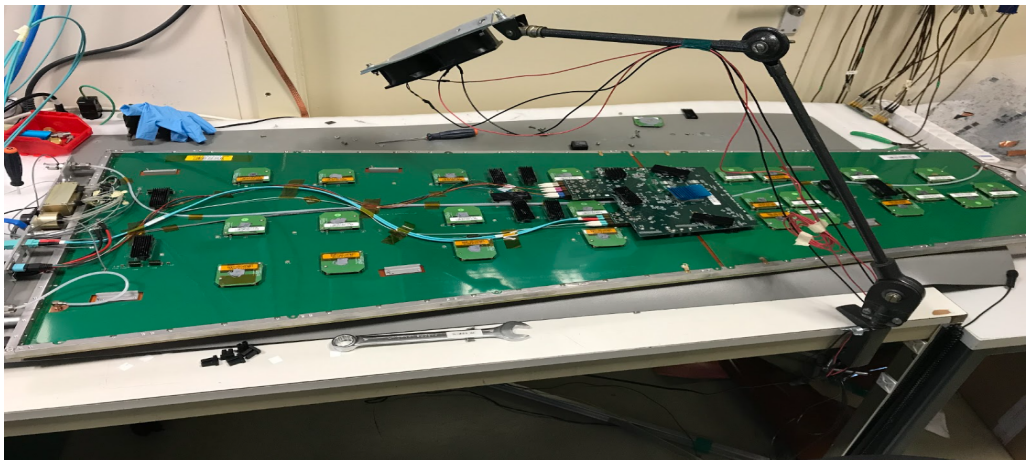

Figure 4.29: A GE1/1 Long chamber positioned on a QC7 stand featuring fan cooling.

- Incorporating both the cooling plate and the chamber's chimney, the latter is coated with a Kapton foil on its inner surface to guarantee electrical insulation between the chimney and the cooling plate.

The procedure remains consistent in both scenarios. The test is reiterated to confirm the proper functioning of the electronics in both chamber equipment configurations. This involves checking whether the application of the cooling plate has affected the noise level of the VFATs or if any of them has become partially unplugged.

4.5.8.2 Procedure

As demonstrated in the following paragraphs, the QC7 procedure involves:

- Connectivity test

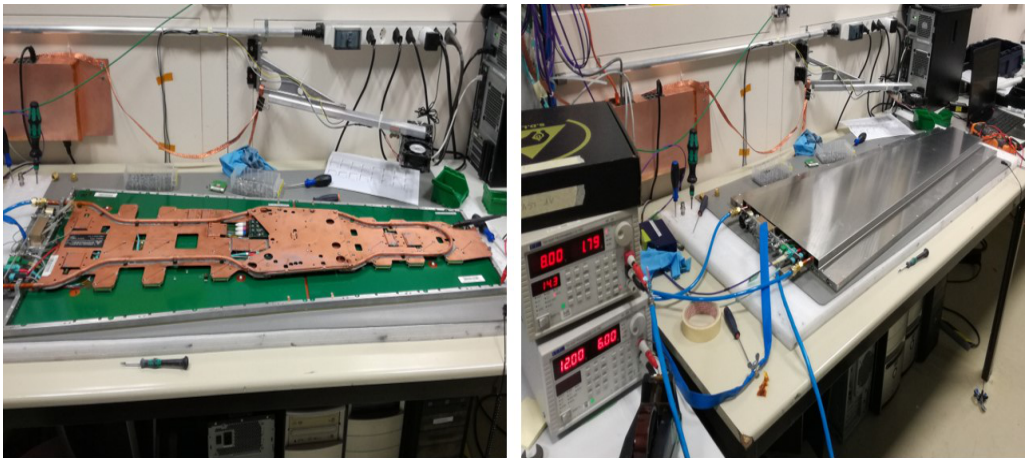

Figure 4.30: Left: Chamber with cooling plate. Right: Chamber with cooling and chimney for thermal scanning.

- Initial S-curve scan
- S-bit scan
- Subsequent S-curve scan
- Threshold scan

This process is replicated for both chamber equipment configurations.

4.5.8.3 Preparation For Test

During this stage, the chamber is situated on the stand, where:

- The back-end fibers (trigger and data path) are connected to the chamber patch panel.
- The LV cable is connected, providing 8 V through a portable power supply. If the chamber functions correctly, the current drawn at power-up is $\sim$ 1.75 A.
- If the cooling plate is not yet installed, heat sinks are placed on FEASTs, Giga-Bit Transceivers (GBTs), and the FPGA, and the fan above the chamber is activated. Alternatively, if the cooling plate is installed, the flow of cooling water within the cooling pipe is activated.

4.5.8.4 Connectivity test

The procedure starts by verifying communication between the front-end electronics (VFAT chips and OptoHybrid board). Next, the VFAT Digital to Analog Converter (DAC) are calibrated to determine the correspondence between a DAC threshold value and an applied bias voltage. A VFAT chip acts as a comparator, returning a logic 1 if the input signal exceeds a certain threshold and a logic 0 otherwise. This threshold, common to all 128 channels of the VFAT, is set in a register called CFG_THR_ARM by a DAC, with an 8-bit resolution (0-255 in decimal). Setting this threshold determines the amplitude required for the input signal to pass the VFAT's selection, affecting its noise rate. The following QC7 tasks involved measuring VFAT noise rates and analyzing response efficiency to varying signal intensities.

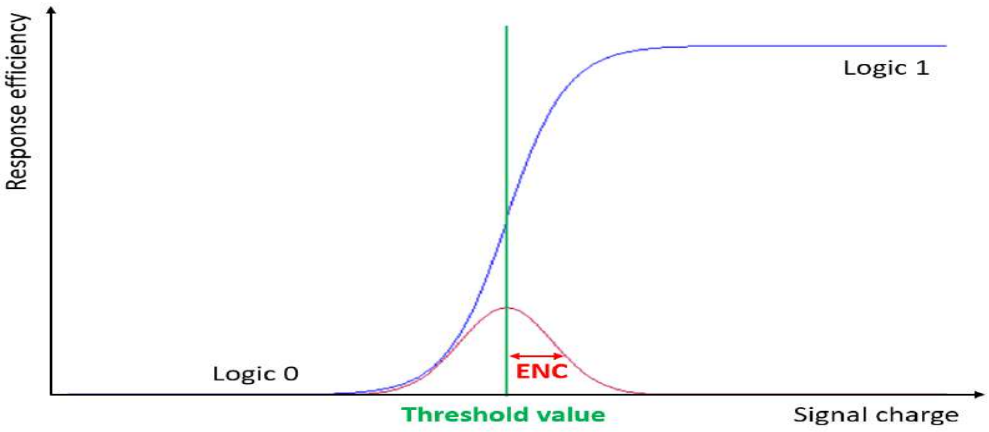

Figure 4.31: Diagram depicting VFAT channel response efficiency to an input charge signal amid noise. The blue curve shows the s-curve response, a step response affected by white noise. The green line indicates the charge threshold value at 50% efficiency. The red curve represents noise, including its standard deviation ENC [14].

4.5.8.5 First S-curve scan

Observing VFAT channel responses to fixed charge input signals is fundamental, achieved through an S-curve scan involving 100 pulses for each charge value from the internal VFAT pulse generator. Ideally, all channels should exhibit a logical one above a certain charge value set by CFG_THR_ARM, resulting in a step response. However, manufacturing variations in channel characteristics and intrinsic noise introduce complexity, shaping the response into a sigmoid curve due to convolution

with Gaussian noise. The threshold charge value is determined by a 50% efficiency response, and the standard deviation becomes the ENC depicted in Figure 4.31. An excessively low ENC in some channels indicates improper response, possibly due to disconnection or dead channels. The first QC7 S-curve scan, with CFG_THR_ARM set to 100, assesses VFAT response and identifies dead or non-communicating channels. The test passes if fewer than three issues are found; otherwise, it is repeated after attempting to resolve the identified problems. If issues persist, solutions may include re-plugging the VFAT after cleaning the connector or replacing it with a functional one. A sample s-curve at CFG_THR_ARM = 100 is depicted in Figure 4.32, illustrating a VFAT's behavior during the last step of QC7 validation with cooling and chimney installed.

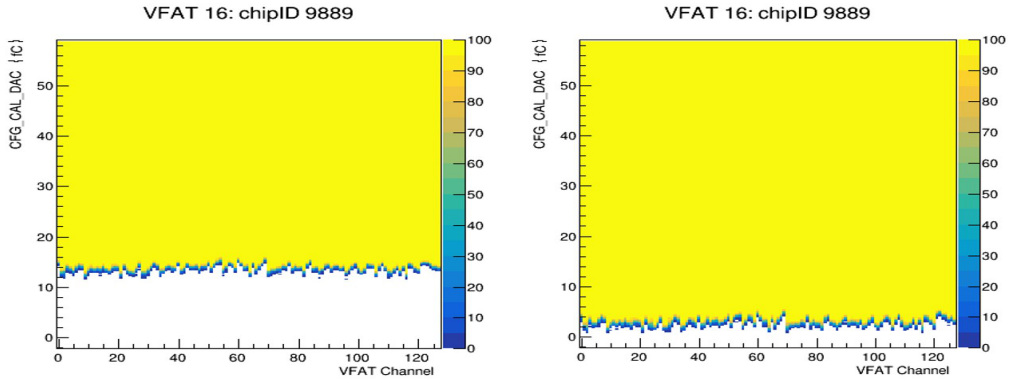

Figure 4.32: Left: S-curves of VFAT 16 in chamber GE11-X-L-CERN-0007, equipped with the cooling plate and chimney corresponding to CFG_THR_ARM = 100. Right: The curve obtained after applying a 100 Hz noise threshold value [14].

4.5.8.6 S-Bit Rate Scan

This phase aims to set the global threshold of the VFAT to restrict the accepted noise signals by the front-end electronics. Considering the anticipated maximum total hit rate of $\sim$ 1.5 kHz/cm^2 for GE1/1 detectors during their operation in CMS in the HL-LHC phase, a noise limit of 100 Hz has been established for each VFAT. The procedure involves counting trigger hits for 1 second in the VFAT readout sector at a fixed CFG_THR_ARM value. This counting is repeated for each of the 256 values of CFG_THR_ARM. The resulting noise trigger hit rate vs VFAT threshold curve, as depicted in Figure 4.33 (left), is used to extract the VFAT threshold expressed in DAC units corresponding to a 100 Hz noise hit rate.

The curve typically exhibits an initial plateau due to electronics saturation at low DAC threshold values, followed by a gradual decline for increasing DAC threshold values. Any deviation from this expected behavior may indicate issues in VFAT connections or the presence of faulty channels. An example is shown in Figure 4.33 (right), where the S-bit rate curve for VFAT 5 in chamber GE11-X-S-FIT-0004 is displayed, revealing a broken S-bit line. This issue prompted the removal of GE11-X-S-FIT-0004 from CMS and its return to QC7 for resolution. The broken S-bit line behavior is often caused by a faulty connection of the VFAT to the Panasonic connector on the readout board or the OptoHybrid board to the SAMTEC connector on the GEB. Re-plugging these electronic components, after cleaning the Panasonic connector with ethanol, typically resolves the problem. However, if the issue lies with the SAMTEC connector, necessitating GEB replacement, becomes the main solution.

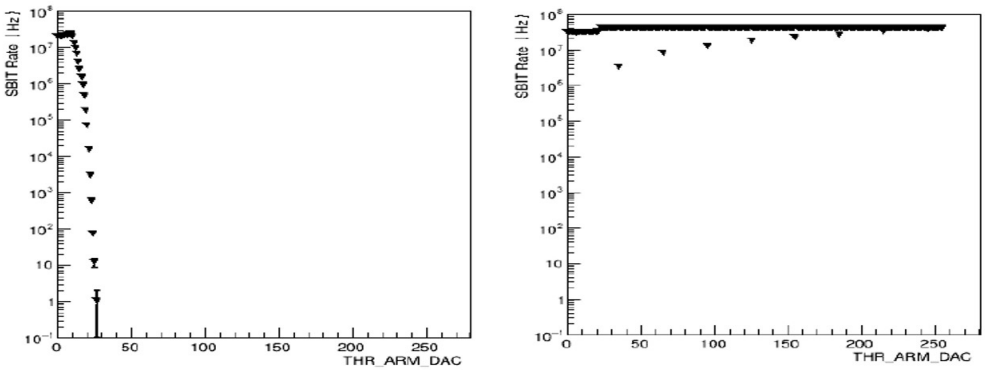

Figure 4.33: Left: S-bit rate curves for VFAT 16 in chamber GE11-X-L-CERN-0007 with cooling plate and chimney. Right: Broken S-bit curve for VFAT 5 in chamber GE11-X-S-FIT-0004. The latter was previously installed in CMS, then re-extracted and returned to QC7 for resolution, involving re-plugging the OptoHybrid board and the VFAT [14].

4.5.8.7 Second S-curve Scan

Upon determining the threshold DAC value corresponding to 100 Hz noise for each VFAT installed in the chamber, these thresholds are employed to configure the VFATs. Subsequently, a new S-curve scan is conducted, generating updated S-curve plots for all 24 VFATs. During this phase, verification of the correct response from all channels and measurement of their noise levels are carried out. The validation criteria include ensuring that the average ENC for all channels within a VFAT is below 0.7 fC, and the average ENC for individual channels is under 1.5 fC; otherwise, the channel is

masked. Additionally, no more than three masked channels are permissible within the same η-partition. Failure to meet these conditions necessitates repeating the QC7 test, replacing VFATs that do not meet the test requirements. Figure 4.33 (right) provides a summary plot of ENC values as an example. The decision to accept or reject the test at specific charge values is influenced by intrinsic noise amplitude and the flexibility provided by bias voltage to adjust global and per-channel VFAT thresholds [13].

Figure 4.34 (left) depicts a summary of charge threshold values derived from VFAT channels after applying the 100 Hz DAC threshold. Notably, the thresholds increase from the narrow (VFAT 0, 8, and 16) to the wide side (VFAT 7, 15, and 23) of the chamber as per VFAT numbering in Figure 4.27 (left). This observed increase is attributed to the strip area's influence, which maintains consistent radial angular spacing. Consequently, the wider η readout sectors exhibit a larger area covered by the strips, leading to increased strip intrinsic capacitance and, subsequently, higher noise collection.

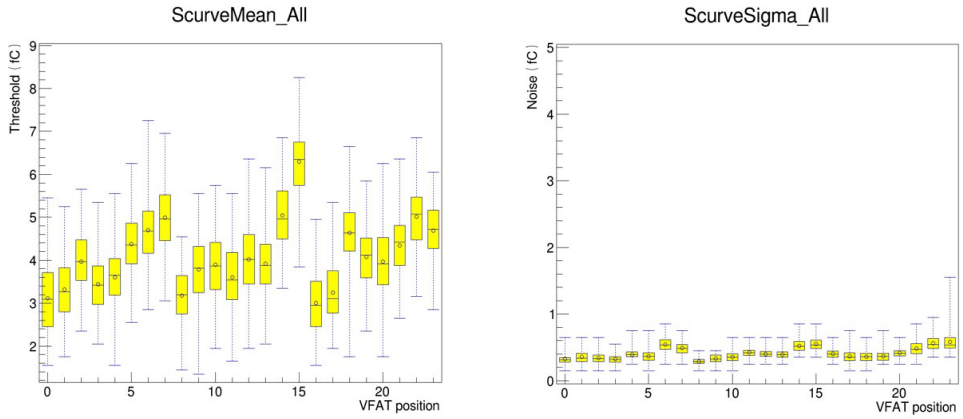

Figure 4.34: Left: A box plot for charge threshold values. Right: The ENC values using a standard box plot with the yellow box indicating values from the first quartile to the third quartile (25%-75%), the central line denoting the median, and a small circle representing the mean[14].

4.5.9 QC8 — Cosmic Ray Stand Test

The final chamber undergoes validation at CERN's GEM lab in a cosmic ray stand located in the 904 building. The objectives of this setup are to:

- Confirm proper functioning of chambers, services, and components.
- Evaluate chamber detection efficiency and tracking throughput.
- Examine mid-term stability, focusing on the HV system (especially GEM foils) and LV system electronic components over about two weeks.

For QC8 clearance, a superchamber must exhibit an average detection efficiency exceeding 95% in both layers. A cosmic ray stand, measuring $200 \times 200 \times 200\ cm^3$ constructed with aluminium profiles, comprises seven shelves is used to conduct the test. This stand can simultaneously test up to 15 superchambers. The top and bottom shelves utilize plastic scintillators for muon triggering, while the remaining five accommodate superchambers identified by shelf row and column numbers. Each superchamber layer is equipped with cooling and gas systems. HV and LV systems are integrated with CAEN boards, and the DAQ system utilizes μ-TCA electronics for data handling. QC8 involves preparation, data collection (5 runs with varied HV configurations), and analysis (identifying dead/hot strips, event certification, efficiency calculations), computing an averaging of efficiency for 24 VFAT readout sectors to validate or discard a chamber based on efficiency. The dedicated QC8 tool retrieves operational parameters for offline analysis and real-time anomaly detection, utilizing inputs such as mapping, usage periods, monitored chambers, and monitoring duration. It executes operations like reading mapping files, connecting to the DCS Oracle database, and executing SQL queries to retrieve and store relevant data. Output files, comprising current, voltage, and status data presented through plots and histograms, register values in the database during significant variations. For HV channels, a consistent labeling convention is followed, and monitoring plots aid in understanding system behavior during ramps and operations. The LV system, utilizing a 16-bit status code, displays current levels in standby, run, and scan modes, providing a concise yet comprehensive assessment of chamber health and performance.

4.6 Conclusion

In total, 161 GE1/1 detectors were assembled and subjected to rigorous QC tests at multiple production sites. Of these, 156 detectors successfully passed through all the QC processes outlined in this thesis. Following this validation, 144 detectors were

subsequently installed in the CMS muon endcaps, while an additional 12 detectors were retained as spares [12].

The PUGEM group assembled and tested a total of 8 chambers. These detectors were labeled as "GE1/1-X-S-INDIA-00NN", with NN representing specific values like 02, 07, 08, 09, 10, 15, 16, and 17, which were serial numbers assigned to India for identifying the assembled detectors. All of these chambers passed through the entire QC processes and were paired with other chambers, either from the same production site or a different one, to create superchambers. These superchambers were then strategically installed in the muon endcap of the CMS experiment and are currently collecting data in Run-3.

Chapter 5

Estimation and Comparison of Background Radiations for GE1/1 Detector

"We do not look upon nuclear energy as a source of power only; we look upon it as a great source of energy to be used for the benefit of humanity."

— V A Sarabhai, 1919–1971

5.1 Introduction

In this chapter, we present an extensive simulation study focused on estimating the background hit-rate for the GE1/1 detector for LHC Run-2, followed by a detailed comparison with data from the GE1/1 Slice Test [1]. Section 5.2 briefly discusses the GE1/1 Slice Test, offering contextual insights. In Section 5.3, a thorough exploration unfolds, emphasizing measurements and results derived from CMS background radiations. Addressing the crucial task of evaluating background particles for the overall study, Section 5.4 provides additional depth. Section 5.5 undertakes a simulation study, specifically examining the response of a single Triple-GEM detector to various particles and the associated simulation framework. This analysis involves comparing the variations in response concerning the energy and incident angle of particles with findings from previous simulation studies. In Section 5.5.2, the results pertaining to the response of superchambers for a specific geometry and the actual readout conditions

during the Slice Test are presented. Predictions of hit rates, along with their systematic uncertainties derived from FLUKA [2] simulations, are outlined in Sections 5.6. The subsequent section, Section 5.7, thoroughly details the comparison between these predictions and the measurements obtained during LHC running, ensuring a robust evaluation of the simulation study against real-world data.

5.2 GE1/1 Slice Test

The GE1/1 project was initiated in 2017 through the implementation of a Slice Test, with the primary objectives of accumulating knowledge for installation and commissioning, demonstrating operational conditions, and seamless integration into the CMS online system. During the 2016-2017 YETS, a total of five superchambers, out of the 36 in the negative muon endcap, were installed referred as "Gemini". Among them, one was horizontally positioned at 3 o'clock position (Gemini01), while the remaining four were vertically positioned at 6 o'clock position (Gemini27 through Gemini30), collectively forming a 50° region of the negative endcap. The detector in the superchamber that is closest to the IP is labeled as Layer-1, while the other is identified as Layer-2. As described in Chapter 4, GE1/1 chambers exhibit two variants; Gemini01, Gemini27, and Gemini29 were short, while Gemini28 and Gemini30 were long detectors, as illustrated in Figure 5.1.

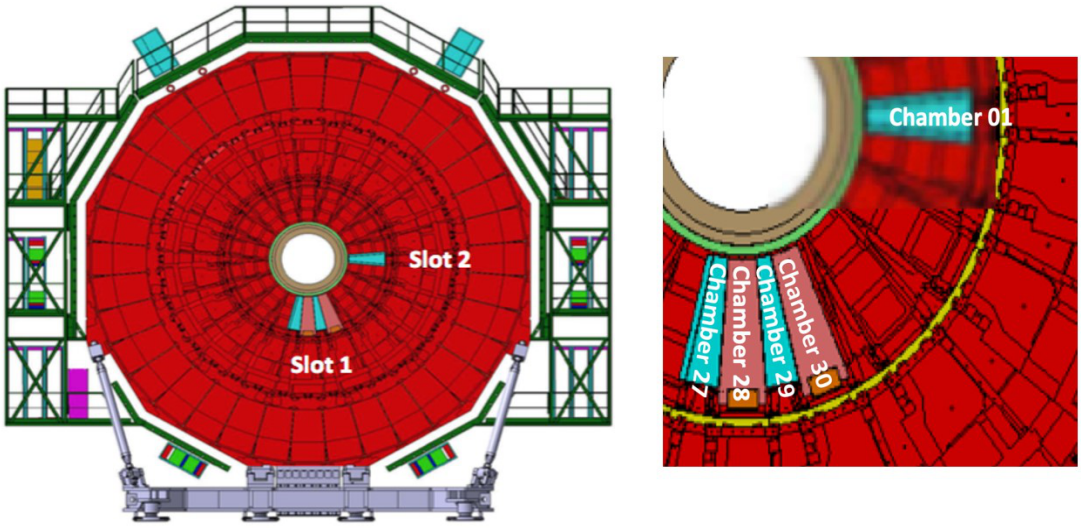

Figure 5.1: Left: Diagram illustrating the negative muon endcap with a focus on the placement of the five slice test uperchambers. Right: A close-view showing five superchambers with their numbers.

5.2.1 High voltage

In the case of Gemini27 to Gemini30, a single high voltage channel from a CAEN A1526N module, commonly used in HEP experiments, with voltage transmitted to detector electrodes through a ceramic divider. In contrast, Gemini01 is powered by a CAEN A1515TG module, a multi-channel power supply with 14 HV channels (7 channels per layer), individually energizing each of the seven electrodes in a Gemini chamber. The Slice Test utilizes a mixed HV system, eliminating the need for additional HV cables in the existing CMS endcap for single-channel chambers. Gemini01 is equipped with the multi-channel power supply to accumulate experience. This module, specifically designed for GEM detectors, provides advantages such as voltage adjustment for each electrode, individual condition monitoring, and potential removal of problematic channels while keeping others powered. Despite its simplicity, the single-channel supply lacks sensitivity to discharges, maintaining a current near 700 μA. In contrast, the multi-channel supply, despite its drawbacks, enhances sensitivity to discharges and offers flexibility in voltage control for individual electrodes. However, the latter requires the development of new interfaces, control systems, and automation within the CMS experiment [1].

5.2.2 Readout System and Low Voltage

The initial Slice Test chamber readout system utilized VFAT2 ASICs [3], which were operational in four chambers (Gemini27 to Gemini30). In contrast, Gemini01, which was replaced in early 2018, featured the latest on-detector DAQ) electronics based on VFAT3 ASICs [4], available in both Version-2 and Version-3. Figure 5.2 illustrated the version-2 GEM DAQ electronics configuration. The GEM Electronics Board (GEB) integrated on-board electronics throughout the detector, housing 24 VFAT2 hybrids and an Optohybrid (OH) board with a Virtex-6 FPGA for data collection and slow control functions. The μTCA crate at the rear end houses an AMC13 card responsible for Trigger Timing and Controls (TTC) signal transmission to the CTP7 mezzanine card. The CTP7 card, located within the μTCA crate, connects to the OH board through fiber connections. The evolution from version 2 to version 3 electronics encompasses progress in ASIC chip technology, a revamped GEB, and an upgraded OH board. The VFAT3 ASIC in version-3 delivers improved performance and communication protocols specifically designed for HL-LHC operations and the upgraded CMS detector.

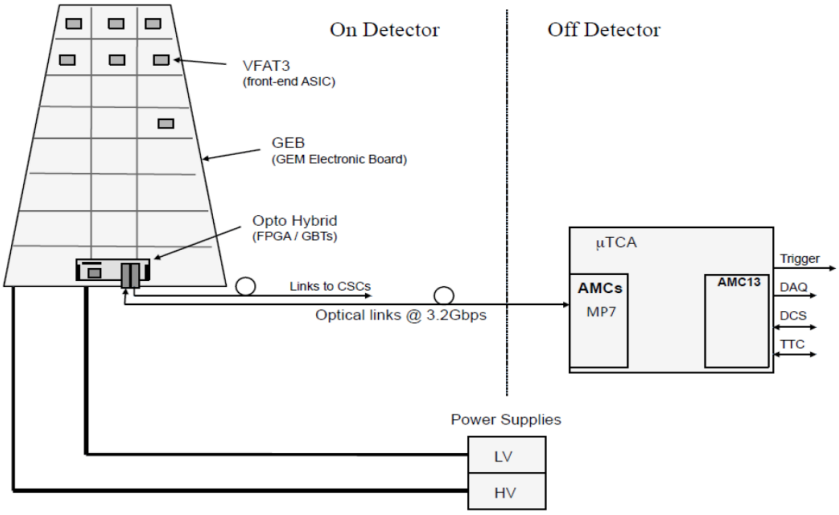

Figure 5.2: Version-2 DAQ electronics schematic: 24 readout sectors with VFAT2 chips, OH board on GEB, and TCA back-end crate [5].

The latest GEB design is bifurcated into two components, facilitating more efficient production and assembly. This modification necessitated adjustments to the OH board, which is now centrally positioned within the chamber. Importantly, the back-end electronics exhibit consistency across both versions [5].

5.2.3 RADMON

During the Slice Test, radiation background measurements at Slot-1 of GE1/1 were conducted using a single radiation monitor (RADMON) positioned at the center of the GEM chamber. The RADMON, depicted in Figure 5.3 (left) and captured in

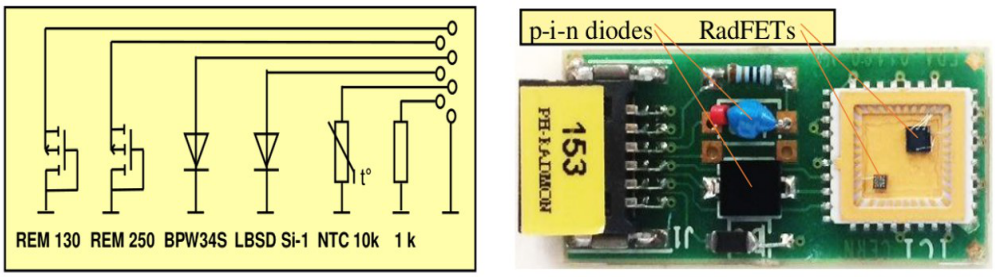

Figure 5.3: Left: Schematic representation of the RADMON PCB. Right: Actual photograph [6]

Figure 5.3 (right), integrates four radiation sensors: two RadFETs (REM 250 and REM 130) for total radiation dose measurement, and two p-i-n diodes for evaluating the

1 MeV neutron equivalent fluence [7]. Additionally, a 10 kΩ thermistor regulates sensor temperature, while a 1 kΩ resistor ensures connection quality. After analyzing

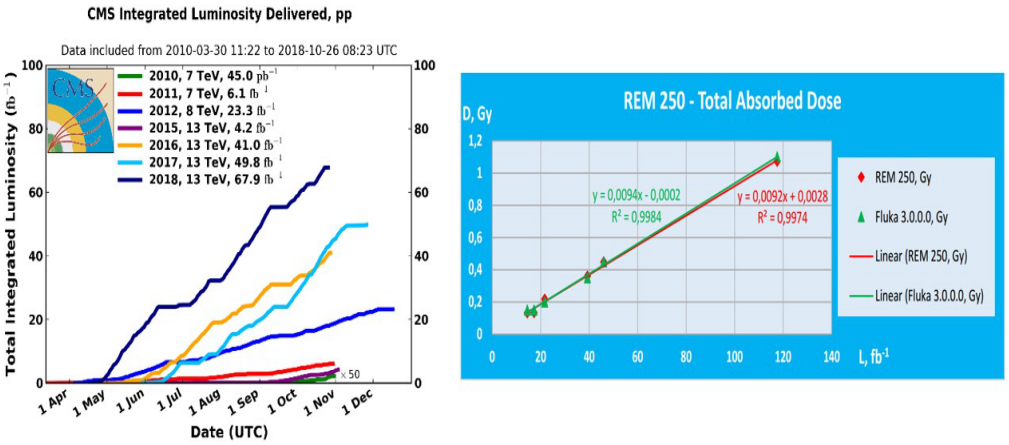

Figure 5.4: Left: Annual integrated luminosities delivered to CMS. Right: Comparison of Experimental and Simulated Absorbed Dose Data around Slot-1 in GE1/1 [6]

the combined data from the 2017 and 2018 LHC runs, the total delivered luminosity is determined to be 117.7 fb^{-1}, as illustrated in Figure 5.4 (left). The absorbed dose, measured by REM 250, demonstrates a notable alignment with the 2017 results [8] and closely corresponds to FLUKA v.3.0.0.0 simulations, depicted in Figure 5.4 (right). The substantial agreement between FLUKA data and experimental results attests to the reliability of the CMS Beam Radiation, Instrumentation, and Luminosity (BRIL) group dose simulation at the GE1/1 position.

5.2.4 Channel Loss

In the course of the Slice Test, superchamber equipped with VFAT2 exhibited channel loss, in contrast to those with VFAT3 [9]. This issue poses a potential threat to the operational integrity of the GE1/1 project, potentially limiting detection efficiency and capabilities. Consequently, the GEM management group launched the GEM Sustained Operations campaign [10] to thoroughly investigate and address channel loss before the GE1/1 LS2 installation without disrupting established detector balance.

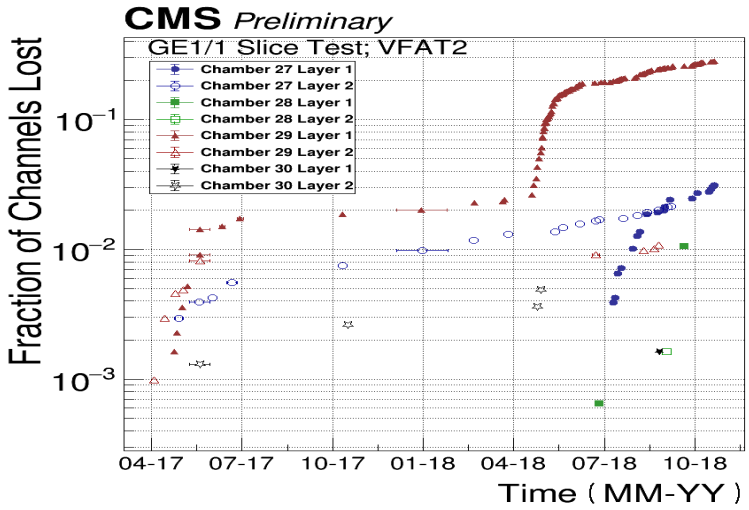

Figure 5.5: VFAT2 superchamber channel loss over time in the Slice Test [10]

5.3 Measurement of CMS Muon Background

5.3.1 Measurement Technique

The background rate, obtained through the demonstration detector, is a crucial measurement that represents the estimated rate of non-primary particles (excluding muons) passing through the GEM detector in correlation with luminosity - an essential parameter for precise detector simulation. To measure this rate, Run-319347 (205.4 pb^{-1}) with zero-bias conditions was conducted, and the dataset was gathered from the output of randomly triggered bunch crossings [11].

In the process of computing the event hit-rate, various calibration steps were introduced. The hit-rate is computed using the following formula:

$$\text{Hit-Rate}(\text{Hz}/\text{cm}^2) = \frac{N_{\text{hit}}}{N_{\text{event}} \times T_{\text{window}} \times A_{\text{effective}}} \tag{5.1}$$

where N_{event} represents the number of events, T_{window} is the readout time window of the GE1/1 detector set at 100 ns, and $A_{\text{effective}}$ stands for the effective readout area.

The initial step involved excluding inactive or noisy channels to focus solely on active channels. Two separate data cleaning procedures were applied. For channel selection, channels with no hits during the run were eliminated, and those with over 2% of their VFAT's total hits (considering each VFAT has 128 strips, equivalent to

around 0.78% of the VFAT's total hits per channel) were then excluded from the remaining dataset.

Despite the removal of noisy channels, residual intrinsic noise persisted, randomly affecting entire VFATs during data collection. To address this, luminosity blocks with hits exceeding 2 sigma from the average number were discarded. Blocks with at least one hit during five consecutive luminosity blocks were considered operational. These operational luminosity blocks define the VFAT's active time, allowing for the computation of the event hit-rate as the ratio of hits to the product of the active time and active area. The combination of these criteria facilitated the calculation of the effective readout area of the chambers for each luminosity block, ensuring a refined dataset for subsequent analysis. The active area of the readout was determined by multiplying the overall area of the GEM detectors by the proportion of active channels that remained after eliminating noisy and inactive channels.

Events originating from an unstable beam were systematically excluded from the analysis. The assessment of the $\mathcal{L}$ distribution for each luminosity block was conducted, and if the standard deviation exceeded 0.01×10^{34} cm^{-2}s^{-1}, the corresponding luminosity block was omitted from further consideration.

5.3.2 Measurement Results

5.3.2.1 Linear Dependence on Instantaneous Luminosity

The analysis yielded the environmental background hit-rate of GE1/1 Slice Test Chamber-28 Layer-2, analyzing its variation as a function of $\mathcal{L}$. The rate is calculated for each η partition of the GE1/1 detector, and adjustments are applied to account for the effective readout area calculated in the previous section. Data points associated with each η partition are subjected to fitting procedures utilizing a linear function, providing a numerical representation of the relationship between the environmental background hit-rate and $\mathcal{L}$ within each η partition.

A linear relationship has been identified between the measured GE1/1 hit-rate and the $\mathcal{L}$ of the LHC , spanning from 0.1×10^{34} cm^{-2}s^{-1} to 1.7×10^{34} cm^{-2}s^{-1}, as depicted in Figure 6.5 (left). This linear correlation remains consistent across each individual η-sector.

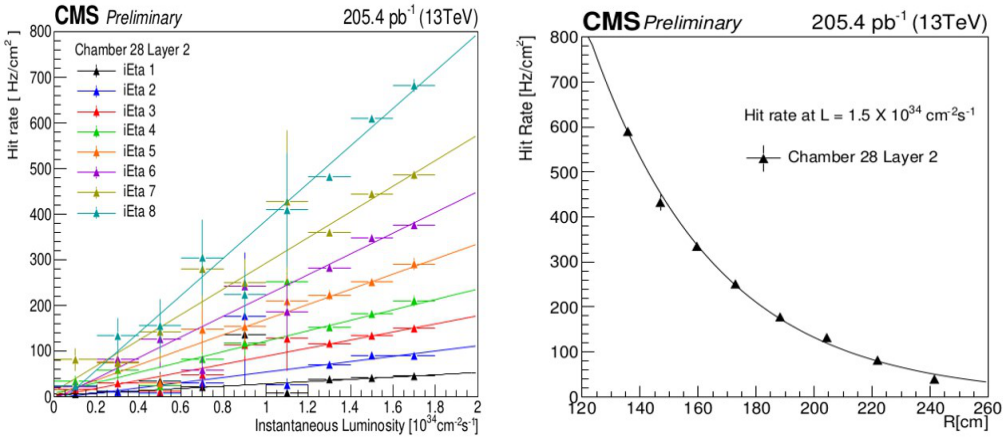

Figure 5.6: Left: The correlation between the hit-rate and instantaneous luminosity, measured in data and fitted with a linear function. Right: In-situ measurement of the background hit-rate during the 2018 Slice Test with respect to distance from beam-pipe [11].

5.3.2.2 Background as a Function of R

Another result involves the investigation of the background hit-rate dependence on the distance from the beam pipe to the center of η-partitions (cylindrical radius R). Data points, recorded at an $\mathcal{L}$ of 1.5×10^{34} cm^{-2}s^{-1}, are determined through a linear fit to the hit rate. Each data point is presented with an error bar, representing uncertainties derived from the linear fit. In the dataset, the diverse radii are acquired by utilizing the hit-rate for an individual η-partition and plotting it at the mean radius. Consequently, it will effectively represent an average across the radial extent of the η-partition. The correlation between the environmental background hit-rate and its spatial-dependent factors is thoroughly depicted in Figure 6.5 (right), where the hit-rate is plotted against R.

5.4 Evaluation of CMS Muon Background

The predominant factor influencing the background levels in the CMS cavern, determining the hit-rate and occupancy in the muon detectors, is attributed to neutrons and secondary particles resulting from neutron interactions with matter. This background persists for an extended period as neutrons can travel for seconds without encountering interactions. Neutrons originate from the interactions of hadrons gen-

erated in primary p-p collisions with the materials of the beam pipe and structures situated in the very forward region, such as the very forward calorimeter (HF), beam collimator, and shielding. The spectrum of these long-lived neutrons spans from the thermal region to a few GeV [12]. The precise evaluation of anticipated background rates holds critical importance, particularly in the CMS forward region, where intense backgrounds of neutrons and secondary particles are prevalent. The gradual capture of slow neutrons by nuclei, followed by photon emission in the detector material, produces photons, and subsequently, electrons and positrons capable of generating detectable ionization in gas detectors as shown in Equation 5.2.

$$n(\text{thermal}) \rightarrow \gamma \rightarrow e^{+}e^{-} \tag{5.2}$$

The radiation environment significantly influences detector technology and design. Elevated occupancy and hit rates can cause detector inefficiencies, degraded resolutions, and momentum mismeasurements, rendering the detector inoperable. Additionally, the high flux of particles can lead to radiation damage in electronics, causing disruptions (single event upsets) or component destruction (single event damage). In the Phase-II of the LHC , the increased collision rate and the intense radiation environment present challenges for signal identification, given the rise in background particle rates. Evaluating background flux is crucial to understanding its impact on detector and trigger performance, as well as the aging of detectors and electronics.

Assessing improvements in the CMS detector's performance, incorporating the GE1/1 system, relies on a detailed simulation integrated into the GEANT-based CMSSW framework. CMSSW involves GEANT-based particle propagation, digitization packages for emulating detector and electronics response, trigger simulation, and event reconstruction. However, simulating long-lived backgrounds in one go with particles from a p-p collision is not feasible due to a propagation time cut-off in CMSSW, reducing CPU time. To include long-lived background contributions, the rate and properties of hits are evaluated separately, and their contribution will embedded into CMSSW simulated data events. The CMS adaptation of the FLUKA package calculates particle fluxes, convoluted with the GE1/1 detector response parameterization obtained from a dedicated GEANT4 simulation study [12].

5.4.1 FLUKA Simulation

The assessment of the persistent cavern background is estimeted using the FLUKA simulation tool, enabling the calculation of long-lived neutron and secondary particle fluxes resulting from neutron interactions with the detector material.

The CMS adaptation of the FLUKA package provides a detailed breakdown of dimensions and material composition for various detector subsystems, such as tracker, calorimeters, and the muon system. The validation of FLUKA predictions in the CMS environment involves analyzing Run-1 data, with initial comparisons outlined in [13]. To estimate particle flux, we utilized the Run-2 configuration (CMS geometry version v3.31.4.2), incorporating planned upgrades to the central beampipe and muon chamber shielding compared to Run-1. Figure 5.7 depicts the CMS geometry version v3.31.4.2 interfaced with FLUKA. This geometry is used for simulations under Run-2 data-taking conditions. A dedicated FLUKA simulation, configured with a 6.5 TeV beam energy and assuming a minimal bias event structure extrapolated from low-energy experimental data, was conducted to estimate energy and angular distributions of background particles (neutrons, photons, electrons, positrons, and charged hadrons) at the surface of the GE1/1 station. Simulation results are saved as flux maps for each particle type, exemplified in Figure 6.2 (left) showcasing the neutron flux map around the future GE1/1 detector location. The fluence estimation through Monte

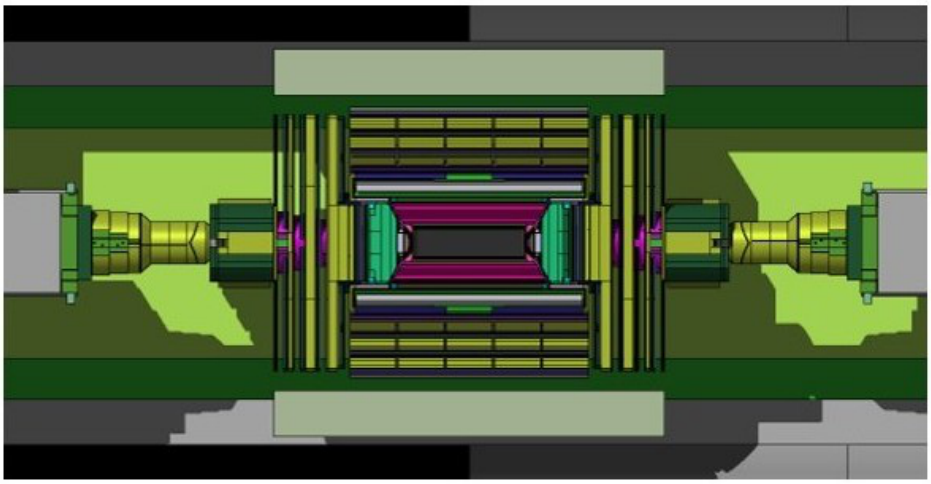

Figure 5.7: CMS geometry used in FLUKA simulation run version 3.31.4.2 [11].

Carlo simulations considers energy variations for different particles at CMS using FLUKA. The defined cut-offs include 100 keV for hadrons, 10 keV for neutrons, 3 keV

for photons, and 30 keV for electrons. It's important to note that photons and electrons have higher cut-offs in specific regions, excluding inside the tracker but encompassing heavy parts. FLUKA Simulation employs the same Run-2 geometry as v3.41.4.2, with updates since v3.13.0.0, detailed in [14]. These updates involve the implementation of the Phase-1 pixel, a shift of the RPC detectors to the inner radius of Muon Barrel-4, and modifications to the material budget in ECAL Barrel and ECAL Endcap.

5.4.2 Results from FLUKA Simulation

The primary sources of background involves various particles and phenomena. Penetrating hadrons, which emerge from the inner detectors, and muons originating from machine-generated background contribute to the overall background signal. Additionally, the presence of neutrons, generated either from showers or leaks in the forward shielding, poses a concern due to their low rate but substantial impact on segment reconstruction and detector longevity. Another significant contributor to background hits is the production of photons during the de-excitation of nuclei. This process involves the excitation of nuclei through the capture of low-energy neutrons, establishing it as a major source of unwanted signals in the GE1/1 detectors. Understanding and addressing these primary sources of background are crucial for improving the accuracy and reliability of GE1/1 detector measurements.

A crucial parameter derived from this simulation is the particle flux, representing the number of particles per unit area per unit time. Equation 5.3 describe the formulation of flux calculation at a specific $\mathcal{L}$ using the results from FLUKA simulation.

$$\underbrace{\Phi(\mathrm{cm}^{-2}\mathrm{s}^{-1})}_{\text{Prediction}} = \underbrace{\phi(\mathrm{cm}^{-2})}_{\text{FLUKA result}} \cdot \overbrace{\underbrace{\mathcal{L}(\mathrm{mb}^{-1}\mathrm{s}^{-1})}_{\text{User configured}} \cdot \underbrace{\sigma_{\mathrm{inel}}(\mathrm{mb})}_{\text{Energy dependent}}}^{\text{Normalisation factor}} \tag{5.3}$$

Here Φ represents the particle flux at a specific $\mathcal{L}$, ϕ repesents the flux for a single p-p collision and σ_{inel} is the inelastic cross section for LHC Run-2. Figure 5.8 showcasing the all particle flux 2D map in a CMS quadrant. An inelastic cross section of 80 mb [15] is utilized for normalizing the flux to $\mathcal{L} = 1.5 \times 10^{34}\ \mathrm{cm}^{-2}\mathrm{s}^{-1}$.

These particle fluxes, rescaled by a factor depending on the detector's response, play a role in the hit-rate calculation. The predicted distribution of flux as a function of R at $\mathcal{L}$ of $1.5 \times 10^{34}\ \mathrm{cm}^{-2}\ \mathrm{s}^{-1}$ for different background particles is shown in Figure 5.9.

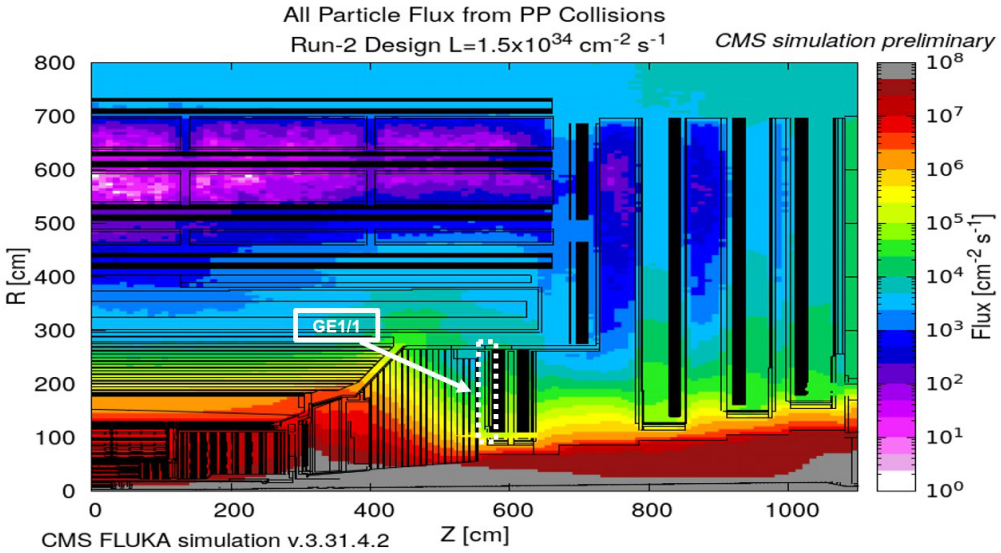

Figure 5.8: FLUKA simulation of particle flux in a CMS detector quadrant. A 2D flux map, normalized to an $\mathcal{L}$ of 1.5×10^{34} cm^{-2}s^{-1}, overlaid on the diagram depicting detector elements and GE1/1 region is shown with dotted lines [16].

The simulation results are obtained for R-value 120-160 cm and for Z-value 565-574 cm which corresponds to the GE1/1 position in Slot-1 Chamber-28 in CMS geometry.

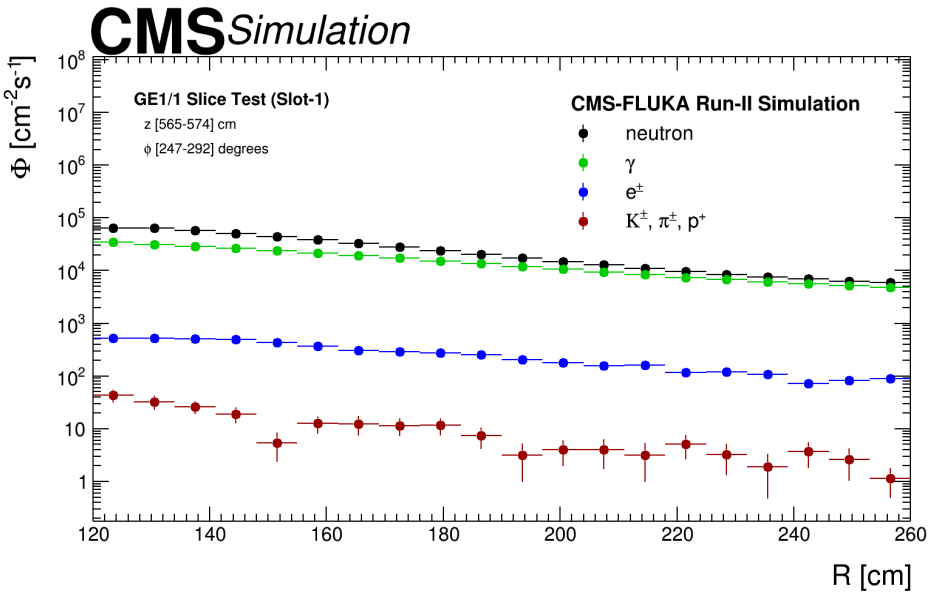

Figure 5.9: Particle flux reaching at the GE1/1 volume normalized to $\mathcal{L}$ of 1.5×10^{34} cm^{-2} s^{-1} [11].

Figure 5.9 predicted flux of neutrons and charged hadrons within the volume corresponding to the GE1/1 chamber location plotted against R. In the same, the simulation predicts the flux of photons and electrons resulting from neutron interactions in the material around the enclosure where the GE1/1 chambers were situated.

A comparison of neutron flux in Slot-1 and Slot-2 is shown in Figure 5.10. There are very slight variations in neutron particle flux between Slot-1 and Slot-2.

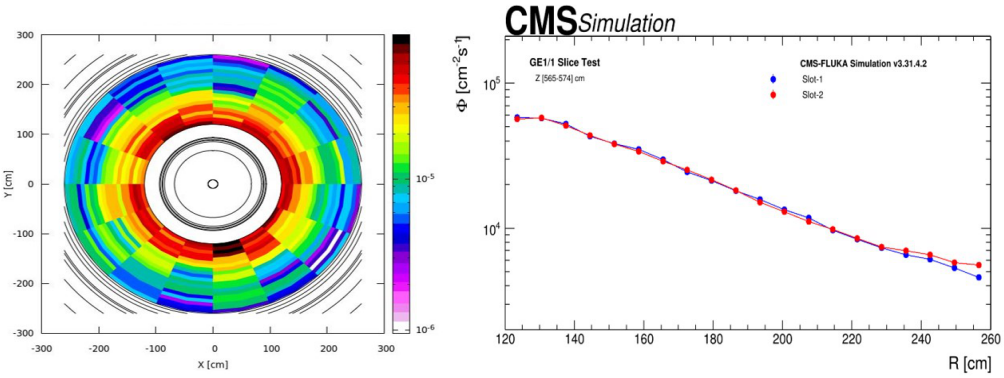

Figure 5.10: Cross-sectional view of A 2D map of neutron flux in a cross-section view at Z-value 565-574 cm (region in which GE1/1 is installed) of CMS geometry.

The essential distributions characterizing incoming particles include both their energy distribution, as shown in Figure 5.11, and their incident angle distribution, presented in the Figure 5.12.

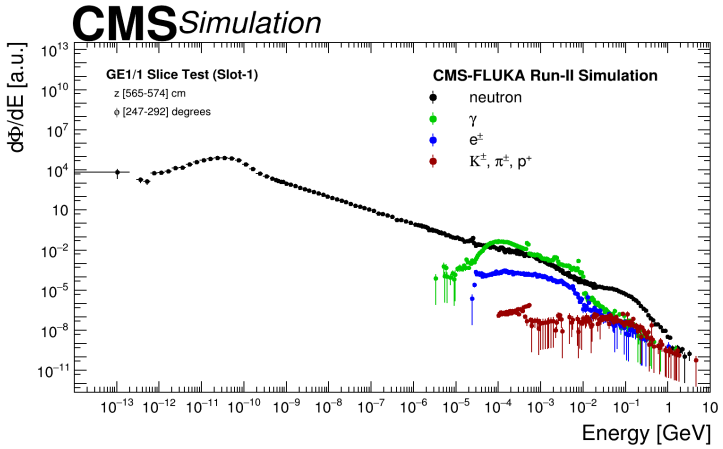

Figure 5.11: Left: The energy spectra of incoming particles are depicted [17].

These distributions play a crucial role in guiding subsequent GEANT simulations. These findings are in line with and build upon a previous study that used FLUKA simulations [18].

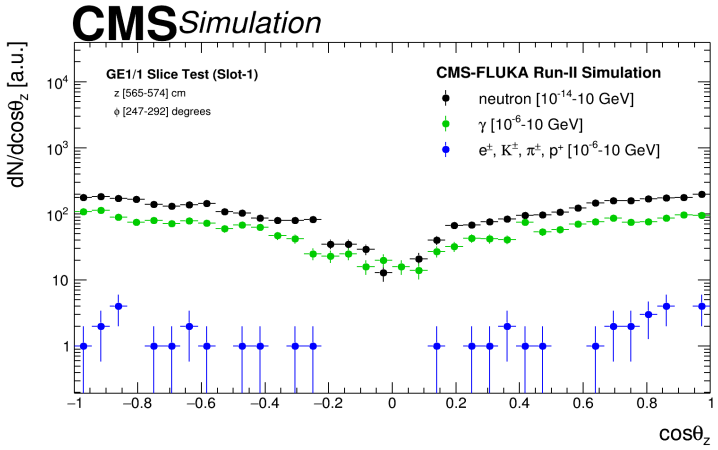

Figure 5.12: The distribution of direction cosine concerning the normal to the detector surface [17].

In the region containing the GE1/1 detectors, primary contributions come from low-energy neutrons, photons, electrons, positrons, and charged hadrons, as indicated in Table 5.1. Negligible contributions from sources such as muons, originating from gauge boson decays, are disregarded, as their production cross-sections are an order of magnitude lower than those illustrated in Figure 5.11 and 5.12.

Table 5.1: Energy range of the background particle resulted from the FLUKA simulation.

Background Particle	Energy-Range
neutrons	$10^{-11} - 10^{4}$ MeV
photons	$10^{-3} - 10^{4}$ MeV
$e^{\pm}$	$10^{-2} - 10^{4}$ MeV
charged hadrons ($K^{\pm}$, $\pi^{\pm}$, proton)	$10^{-3} - 10^{4}$ MeV

5.5 Detector Response Evaluation for Background Particles

In this section, we explore the sensitivities of a triple-GEM detector designed in accordance with the CMS GE1/1 specifications in two configurations. The first configuration involves a simplified geometry, featuring a single triple-GEM detector. The second configuration, described in Section 5.5.2, comprises a superchamber arrangement with two triple-GEM detectors, replicating the actual geometry of the GE1/1 Slice Test detector. The adoption of this simplified geometry enables an exploration of the interactions between detector materials and particles, providing valuable insights into the behavior of the service volume, which includes the front-end electronics and the cooling system. Subsequent sections will show the significance of the cooling system in influencing the sensitivity to neutrons and photons.

Table 5.2 list the Long and Short Chamber variants of GE1/1 detector. A Long chamber variant's geometry is chosen for both the configuration discussed above. The

Table 5.2: Dimensions of long and short trapezoidal-shaped triple-GEM detector.

Configuration	Long (Even) Chamber	Short (Odd) Chamber
Height	1283.0 mm	1135.0 mm
Short Base Length	282.2 mm	282.2 mm
Long Base Length	510.0 mm	483.7 mm

characterization of the detector response is achieved by utilizing the term "sensitivity". In this context, sensitivity is defined as the probability of a particle depositing energy within the sensitive volume, for example, in an Ar/CO_2 gas mixture, and generating primary ionized electrons [19]. The interaction mechanisms of different particles in context to gaseous detector and CMS, are previously discussed in Chapter 4. These primary electrons undergo a multiplication process, ensuring that the resulting charge is of sufficient magnitude for detection by a readout system with specified charge thresholds. The determination of the charge threshold is linked to the energy deposit necessary to differentiate signal from noise. Hence, the sensitivity can be expressed as

follows:

$$\text{Sensitivity} = \frac{N_{hits}}{N_{total}} \tag{5.4}$$

Here, N_{total} represents the total number of incoming particles reaching the active surface of a GEM detector from any direction. On the other hand, N_{hits} signifies the number of registered "hits" that exceeds a specified energy threshold discussed in Section 5.5.1.3. These registered hits are accumulated for a specific incident particle at a given incident energy and angle while traversing the triple-GEM detector.

5.5.1 Single Triple-GEM Detector

5.5.1.1 Geometry

The probabilities of hits occurring in the GE1/1 detector are influenced by the description of the material budget. To assess sensitivities, we utilized a simplified geometry depicted in Figure 5.13, which represents a single triple-GEM detector, excluding considerations for back-end electronics and the cooling system (service volume). This comparison allows us to evaluate and understand the impact of the material budget specifically service volume on hit probabilities in the detector.

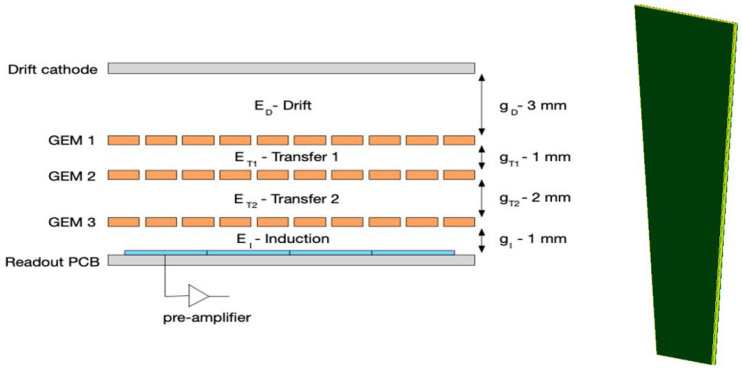

Figure 5.13: Left: Representation of a transverse view of a triple-GEM detector [17]. Right: A geometrical volume representation of single triple-GEM volume taken from GEANT4 visualisation.

Table 5.3 gives the detailed material composition and dimensaion of the single Triple-GEM detector as described in the GE1/1 Technical Design Report [12]

Table 5.3: The material composition and dimensions of distinct layers within a single Triple-GEM detector.

Layer	z-Dimensions	Material
Drift Board	35 μm / 3.2 mm / 35 μm	Copper / FR4 / Copper
Drift Gap	3 mm	Ar / CO_2
GEM1	5 μm / 50 μm / 5 μm	Copper / Kapton / Copper
Transfer-1 Gap	1 mm	Ar / CO_2
GEM2	5 μm / 50 μm / 5 μm	Copper / Kapton / Copper
Transfer-2 Gap	2 mm	Ar / CO_2
GEM3	5 μm / 50 μm / 5 μm	Copper / Kapton / Copper
Induction Gap	1 mm	Ar / CO_2
Readout Board	35 μm / 3.2 mm / 35 μm	Copper / FR4 / Copper

5.5.1.2 GEANT4 Simulation

In this simulation, we utilized GEANT4 version 10.6 along with the FTFP_BERT_HP physics list, which is specifically designed and recommended for standard HEP processes. This comprehensive physics list encompasses a range of fundamental interactions, including standard electromagnetic processes. For hadrons with energy below 5 GeV, the simulation incorporates the Bertini-style cascade, while at higher energies surpassing 4 GeV, the FTF (Fritiof) model is used. Additionally, the simulation includes a dedicated model designed for accurately representing neutron interactions occurring below 20 MeV [20]. This choice of physics list ensures a thorough and accurate representation of particle interactions across a broad energy spectrum in the simulation.

The incident background particles are generated to exhibit properties consistent with those generated in p-p collisions at the LHC . The simulation setup incorporates "source planes" generating primary particles as shown in Figure 5.14, matching the size of the GEM detector's drift board and positioned 3 mm away from the detector on both sides. This configuration captures diverse incident angles and path lengths of primary particles striking the detector's surface and traversing its sensitive volume. The detector's response to primary incident particles is separately estimated on each side for each source plane, and the average is employed to determine the final detector response. Although the simulation considers particle interactions and

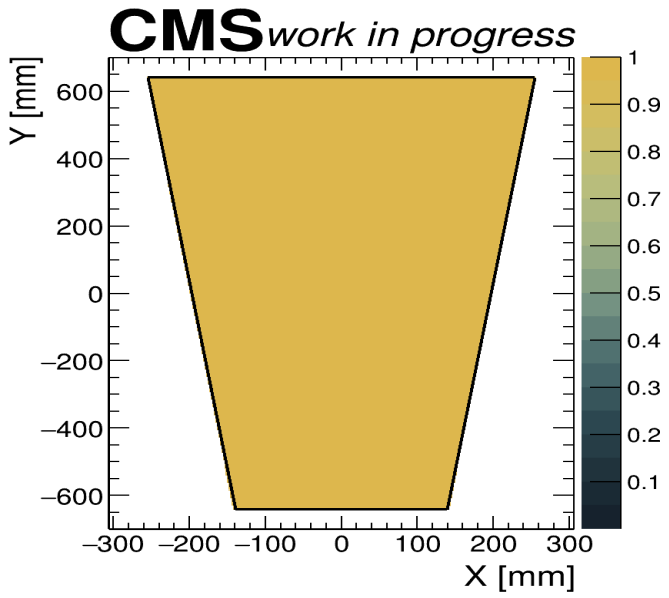

Figure 5.14: A uniform source plane of size equivalent to GE1/1 drift board.

secondary creation in different gaps of the triple-GEM detector, the detector response is extracted from the first two gas gaps, specifically the drift and transfer-1 gaps. The probability of signal origin maximum for drift gap and minimum for Transfer-2 and Induction gap as shown in Table 5.4. Signal induction arises from the generation of a

Table 5.4: Probability of signal origin in various gas gaps [21].

Gas Gap	Probability of Signal Origin
Drift	$\sim 80\%$
Transfer-1	$\sim 17\%$
Transfer-2	$\sim 3\%$

charged particle within the detector, originating from the interaction with neutral or charged background particles (e.g. neutrons, photons, electrons, and charged hadrons). Processes crucial to signal evolution, including electron drift, multiplication, charge transfer, and electronic response, are beyond the scope of this study. Detailed design considerations for the CMS GEM detectors were informed by optimization studies for signal detection using alternative simulation packages [22].

The acquired sensitivities are then juxtaposed with research carried out at the CHARM facility [19]. It is crucial to emphasize that the response of this specific

triple-GEM detector is closely connected to the existence of other triple-GEM detectors within the encompassing superchamber. The interaction of materials among these detectors adds an extra layer of complexity to the sensitivity assessment, necessitating meticulous consideration in our analysis.

5.5.1.3 Energy Threshold For Signal

The energy depositions simulated in the first two gaps of a triple-GEM detector are converted into charge depositions using the relevant amplification factor, and they must exceed the minimum threshold value of the VFAT chip. Despite the readout electronics having a threshold of 3 fC, a value of 1.69 fC is applied - equivalent to one electron in the drift gap. This choice is made to investigate the impact of low levels of noise. Subsequently, in Section 5.5.2.3, the energy thresholds are adjusted to align with the operational configuration of the GE1/1 Sice Test chambers in CMS.

The estimation of the minimum energy deposits required is outlined as follows:

- The gas gain amplification (G) was configured at 1.0×10^4, corresponding to 24, 22, and 20 multiplications during GEM1, GEM2, and GEM3, respectively.
- Setting the readout thresholds for the strips to 1.69 fC for i_η = 1 to 8 necessitates approximately 10547 electrons (see Appendix C) to surpass this threshold.
- The minimum average number of electrons required to be generated in the drift gap and the transfer-1 gap are 1 (calculated as $10547/G$) and 24 (calculated as $10547/G^{2/3}$), respectively.
- The effective average energy necessary to remove an electron due to ionization in an Ar/CO2 gas mixture (in the ratio of 70/30) is denoted as $\langle Wi \rangle$ = 28.1 eV [23, 24]. Consequently, energy losses listed in Table 5.7 are imperative for registering "hits" in the drift and transfer-1 gaps, respectively.
- Electrons produced in the drift and transfer-1 gaps undergo amplification by factors of 10^4 and 440, respectively, at the readout strips. In the event that the energy loss of a particle, simulated by GEANT4, exceeds the designated threshold, a "hit" is tallied for (N_{hits}) in Equation 5.4.

Given that GEANT4 excludes charged particles with a track length less than 0.7 mm [25], we adopt an alternative approach for our analysis. Instead of tallying secondary

charged particles, we establish criteria based on the energy deposited in the gaps. This methodology aligns with the methodology presented in prior research [19].

Table 5.5: The energy thresholds and related parameters used in the simulation of the drift and the transfer-1 gaps of the triple-GEM detector configuration. The effective gain is set to 1.0×10^4 and the charge threshold for readout is 1.69 fC.

Parameters	Drift Gap	Transfer-1 Gap
Minimum no. of electrons in the gap	1	24
Energy thresholds	28.1 eV	674.4 keV

5.5.1.4 Simulation Result

The response of a detector depends on the particle's characteristics, including its type, kinematics, and the medium in which interactions occur. Neutrons primarily lose energy through inelastic scattering at high energies (> 10 MeV), elastic scattering at intermediate energies (between 10^{-5} and 10 MeV), and neutron capture at low energies (< 10^{-5} MeV). Photons (γs) mainly undergo pair production at high energies (> 10 MeV), Compton scattering at intermediate energies (ranging from 10^{-1} to 10 MeV), and the photoelectric effect at lower energies (< 10^{-1} MeV). Electrons and positrons ($e^{\pm}$ particles) primarily emit bremsstrahlung at high energies (> 1 MeV) and cause ionization at lower energies (< 1 MeV).

Neutral particles, such as neutrons and γ particles, interact before giving rise to a charged particle. The calculated sensitivity, depicted in a two-dimensional map concerning kinetic energy and angle, is presented for neutrons in Figure 5.15 (left) and γ particles in Figure 5.15 (right).

A one-dimensional representation of sensitivity, elucidating the dependence on incident energy for various particles under normal incidence to the detector, is illustrated in Figure 5.16 (left). Furthermore, Figure 5.16 (right) portrays the sensitivity as a function of the incident angle for different particle types at two energy levels (1 and 100 MeV).

The sensitivity exhibits a pronounced dependence on both the energy and incidence angle. The likelihood of an interaction is intricately linked to the detector's width and the angle of incidence. An increase in the incidence angle results in the particle

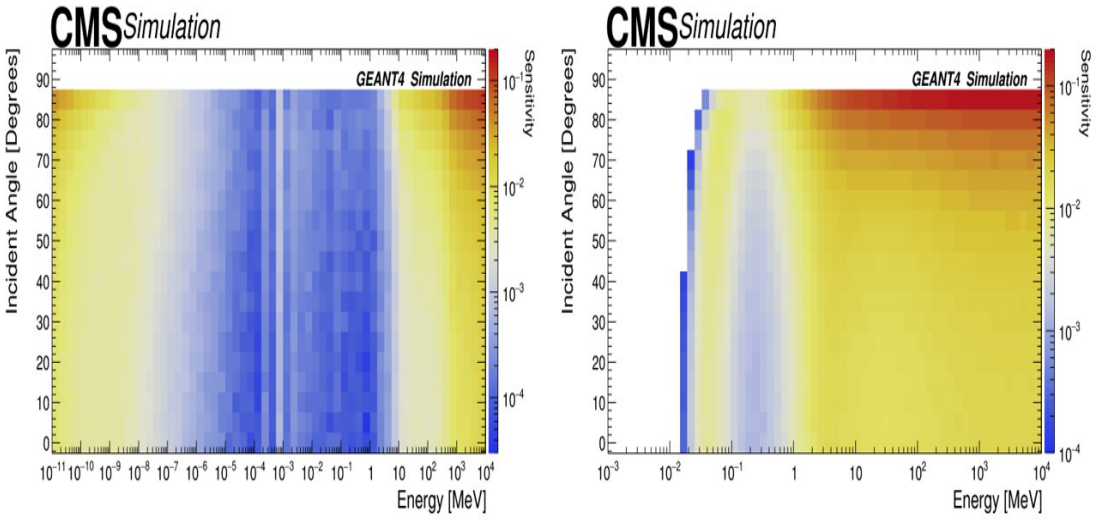

Figure 5.15: Left: 2D-Map depicting sensitivity for neutrons with horizontal axis corresponds to kinetic energy, while the vertical axis represents the incident angle. Right: 2D-Map depicting sensitivity for photons with horizontal axis corresponds to kinetic energy, while the vertical axis represents the incident angle.

traversing a greater distance within the detector, thereby presenting more material as a potential target for interaction. Furthermore, the probability of interaction is contingent upon the specific interaction process and the energy of the particle. In assessing sensitivity, we consider the energy spectrum of incident particles, the energy-dependent probability of interaction, and the corresponding path length.

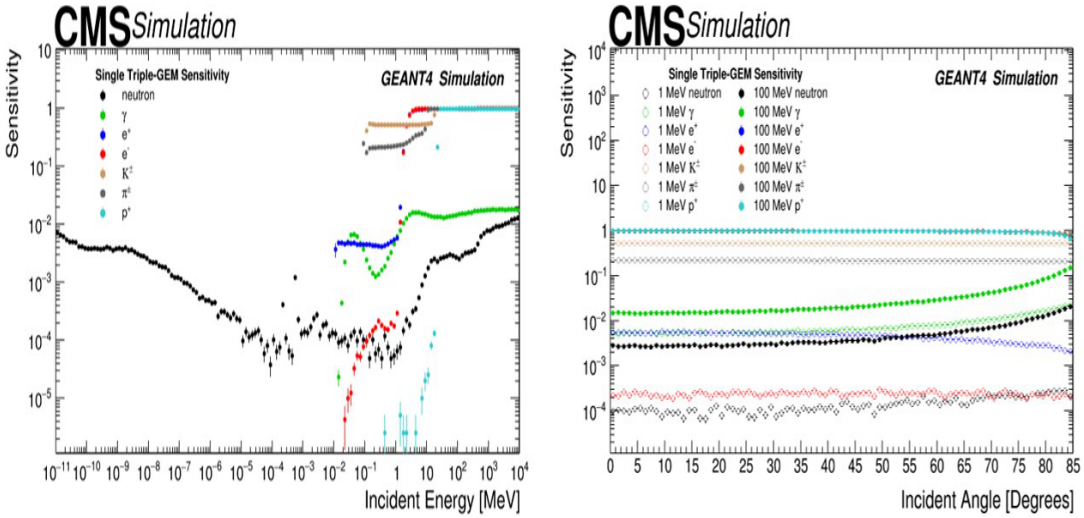

Figure 5.16: Left: Sensitivity plotted against kinetic energy for neutrons, photons, and electrons at normal incidence to the detector. Right: Sensitivity charted against incident angle for various particle types at energy values of 1 MeV and 100 MeV.

Sensitivities were determined through extensive simulations with large samples, involving on the order of $\mathcal{O}(10^7)$ events. The magnitude of statistical uncertainty is contingent upon both the particle type under investigation and the specific region within the sensitivity map. Statistical uncertainties span from 0% to 16% for neutrons, 0% to 2.1% for γ particles, and 0% to 10.0% for $e^{\pm}$.

It is crucial to underscore that these sensitivities were derived without imposing constraints from a specific radiation environment. The sole consideration was the energy range corresponding to each particle type. Consequently, the outcomes are applicable to any facility equipped with similar triple-GEM detectors [19].

The sensitivity outcomes for an individual triple-GEM detector, as illustrated in Figure 5.16 (left), remain invariant with respect to the detector's surface geometry. These results exhibit both qualitative resemblance and quantitative compatibility with those presented in the work [19] as compared in Figure 5.17.

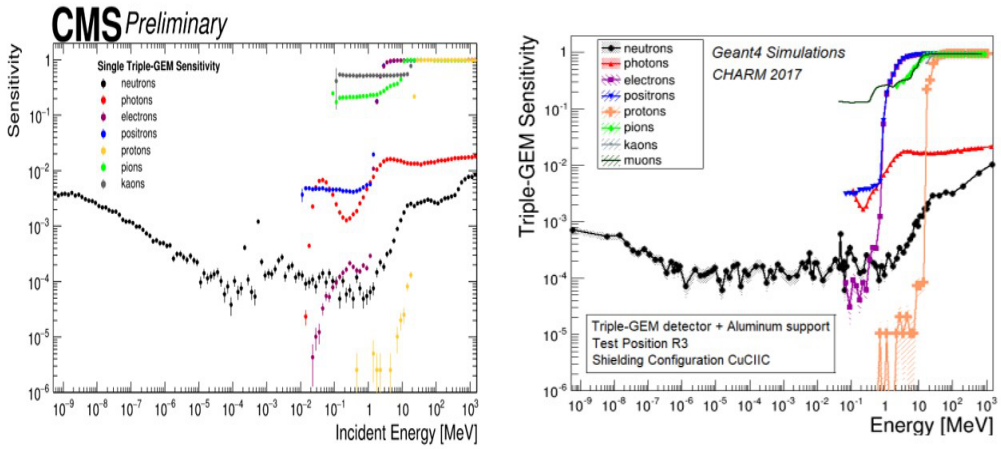

Figure 5.17: Comparison of sensitviity of neutron, photons, $e^{\pm}$ and charged hadrons with the previous study [19]. Left: Sensitivity plotted against energy using the present study GEANT4 simulation. Right: Sensitviity plot from taken from [19].

The predicted sensitivity for photons in the present study is in agreement with the outcomes of the prior investigation. It should be noted that the response of a GEM detector, when incorporated into a superchamber within the CMS experiment, may differ from that of the solitary chamber analyzed in this context. The ensuing sections of this thesis will elaborate on the modifications made to the background modeling, aligning it with the unique radiation conditions of the CMS experiment and the specific geometry of the GE1/1 muon upgrade project detector.

Noteworthy distinctions, particularly in neutron sensitivity at low energies, can be attributed to several factors. Firstly, the current simulation employs an updated GEANT4 version that incorporates enhanced modeling for thermal neutrons as shown in Figure 5.18 for the even configuration. Additionally, energy thresholds for the drift and transfer-1 gaps were applied in this study but were absent in the previous one. Lastly, the earlier study simulated a detector featuring an extra layer of Kapton (50 μm) and FR4 (1.2 mm).

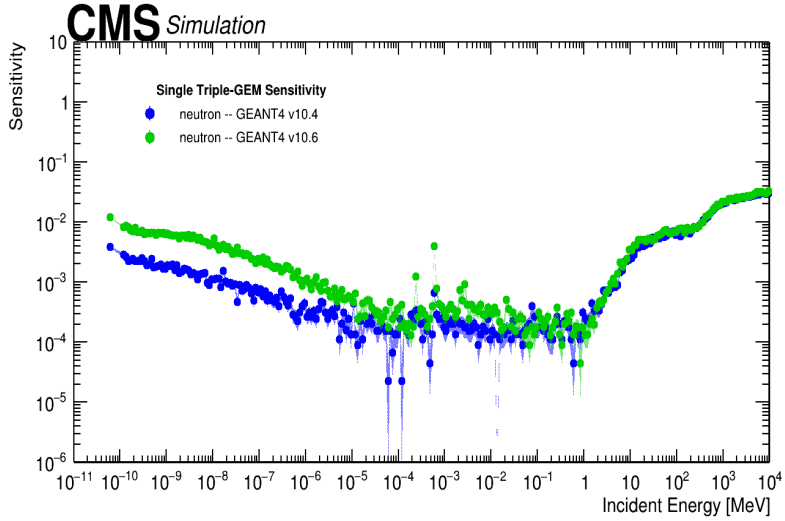

Figure 5.18: Comparison of sensitviity of neutrons predicted by two versions; GEANT4 v10.4 and v10.6.

5.5.2 Superchamber Detector

5.5.2.1 Geometry of Superchamber

The response of the detector to background radiation is contingent on the entirety of materials comprising the triple-GEM detector, encompassing the electronics, cooling system, and mechanical support. Notably, the triple-GEM detectors deployed in the CMS experiment exhibit additional components beyond the basic triple-GEM configuration as given in Table 5.3. Essential supplementary elements and their specifications are listed in Table 5.6. For this investigation, a long chamber configuration is adopted, as delineated in Tables 5.2. The superchamber, characterized by a total thickness of 73.1 mm, incorporates a 3.7 mm interspace between the two detectors. Each unit of

Table 5.6: Additional materials and their dimensions, including the layers, used in the triple-GEM detector configuration for the GEANT simulation.

Layer	z-Dimensions	Material
GEB	0.1 mm / 0.9 mm	Copper / FR4
VFAT and Opto-Hybrid	1 mm / 1.6 mm	FR4 / FR4
Cooling Pads	1 mm	Copper
Cooling Pipes	⌀ 8 mm, ⌀ 6 mm	Copper (Filled with H_2O)
Spacers	3 mm/1 mm/2 mm/1 mm	FR4
External Frame	7.2 mm	FR4
Aluminium Frame	11.5 mm	Aluminium
Cover	1 mm	Aluminium

the triple-GEM detector comprises a GEB housing readout electronics and a cooling system equipped with cooling pads and pipes containing circulating chilled water. Copper, a choice for its high thermal conductivity, is employed for both cooling pipes and pads. A pivotal element of the readout electronics for a superchamber consists of VFAT-3 ASICs, a refinement of the earlier VFAT ASICs [3, 4], accompanied by an Opto-Hybrid board. The VFAT3 play a crucial role in reading, digitizing, and processing signals from the 384 strips within each η-sector of a superchamber layer. The Opto-Hybrid board, integrated into the GEB, incorporates GBT chip sets, optical receivers and transmitters, and a FPGA. Detailed information regarding the front-end electronics is available in [12]. Figure 5.19 provides a GEANT4-based representation of a Superchamber utilised in this study.

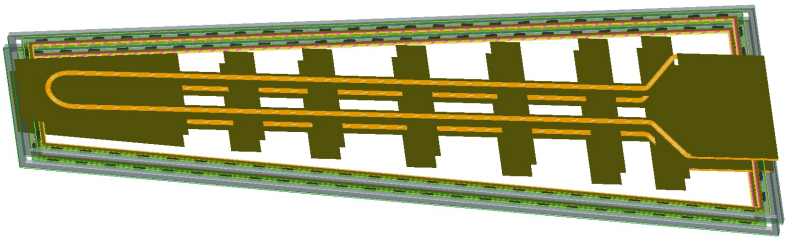

Figure 5.19: GEANT4 visualization of a superchamber featuring two triple-GEM detectors.

5.5.2.2 GEANT4 Simulation of Superchamber

The simulation technique used for sensitivity estimation is similar to that described in Section 5.5.1.2, with the primary difference being the presence of a superchamber and additional material due to the extra triple-GEM detector. This variation affects the sensitivity of other detector layers, as sensitivity is assessed for incident particles arriving at the superchamber surface from various directions. The simulation generates incident background particles with energy and angular spectra as predicted by the FLUKA simulation outlined in Section 5.4.2. The energy ranges for the particles are chosen based on the information provided in Table 5.1 for each particle.

The setup includes "source planes" that emit primary particles, positioned 3 mm away from the GEM detector's drift board on both sides, to mimic background particles over the GE1/1 detector. This configuration is based on the simplified geometry outlined in Section 5.5.1.2. The detector's response to primary incident particles is calculated separately for each side and each source plane, and the resulting average response is used to determine the final detector response. The angular spectrum shown in Figure 5.12 is utilized for particle generation to ensure a realistic scenario. The simulation focuses on the response of the initial two gas gaps in the triple-GEM detector - the drift and transfer-1 gaps, as discussed in Section 5.5.1.2.

5.5.2.3 Energy Threshold For Signal

Energy thresholds for calculating "hits" are determined following the methodology outlined in Section 5.5.1.3, with adjustments for a VFAT threshold of 3 fC. The energy deposit threshold used in the calculation aligns with the 3 fC threshold employed in the Slice Test [11], as shown in Table 5.7.

Table 5.7: Energy thresholds and simulation parameters for the triple-GEM detector's drift and transfer-1 gaps. Effective gain: 1.0×10^4, readout charge threshold: 3 fC

Parameters	Drift Gap	Transfer-1 Gap
Minimum no. of electrons in the gap	2	43
Energy thresholds	56.2 eV	1.21 keV

5.5.2.4 Simulation Results For Superchamber

The sensitivity at a given particle energy is computed as the fraction of all generated events in which a signal is observed, separately for each of the two detectors comprising a superchamber. The sensitivity values obtained for the two layers in a superchamber are not the same. The energy-dependent sensitivities thus obtained for Layer-1 and Layer-2 are shown in Figure 5.20, with the error indicating the statistical uncertainty. A 1D representation of sensitivity as a function of energy for various particles is shown in Figure 5.20.

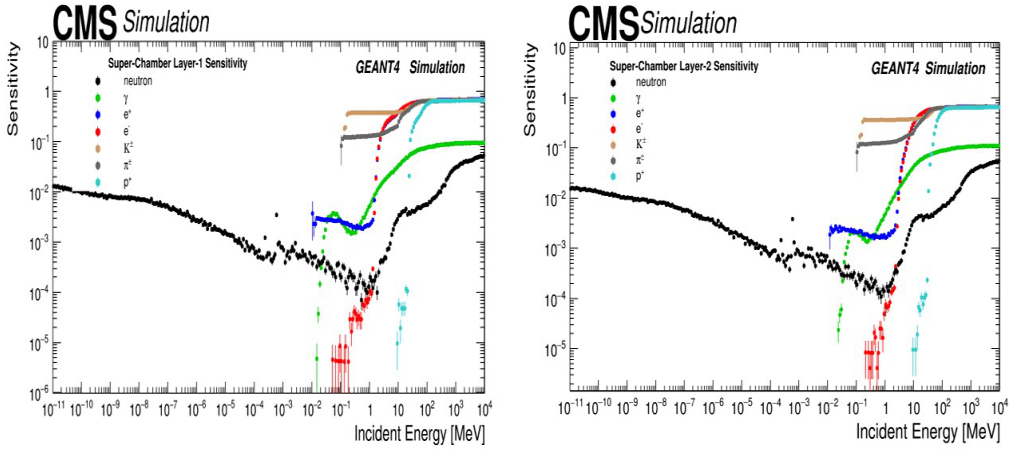

Figure 5.20: Left: Layer-1 sensitivity plotted against incident energy for various particles, with convolution performed over all potential incident angles. Right: Layer-2 sensitivity plotted against incident energy.

5.6 Calculation of Background Hit Rate

The hit-rate is defined as the number of particles detected per unit of time per unit area in a single chamber. In the Slice Test conducted on the GE1/1 superchambers, the hit-rate was measured, taking into account the instantaneous luminosity and detector area as variables as discussed in Secton 5.3. This measurement is crucial for detector calibration and monitoring. The hit-rate is influenced by the multiplication of particle flux and average sensitivity for each particle type (neutrons, photons, $e^{\pm}$, charged hadrons), considering their energy and incident angle dependencies, as detailed in

Equation 5.5.

$$\text{Hit Rate} = \sum_i \text{Sensitivity}(i, E, \theta) \otimes \text{Flux}(i, E, \theta, R) \tag{5.5}$$

Here i denotes the category of particle (e.g., neutrons, photons, $e^{\pm}$, and charged hadrons), E represents the energy of the incident particle, and θ indicates the angle relative to the normal to the detector surface.

Particle flux is estimated using FLUKA, as depicted in Figure 5.9, and is then multiplied by an average sensitivity. The average sensitivity is discussed in the next section.

5.6.1 Average Sensitivity

Average Sensitivity is determined by convoluting the sensitivity at a specific energy and incident angle with the normalized abundance of particles at that energy and incident angle. The convolution over a given energy range yields the average sensitivity. Figure 5.11 provides energy sepectrum for all possible particle types arriving from different directions at the surface of GE1/1 detector. This enenrgy spectrum is normalized to 1 to get a normalized enenrgy spectrum as shown in Figure 5.21 (left). Average sensitivity is the integration of the convolution of this normalized flux and one of the sensitivity curve (Layer-1 or Layer-2) shown in Figure 5.20.

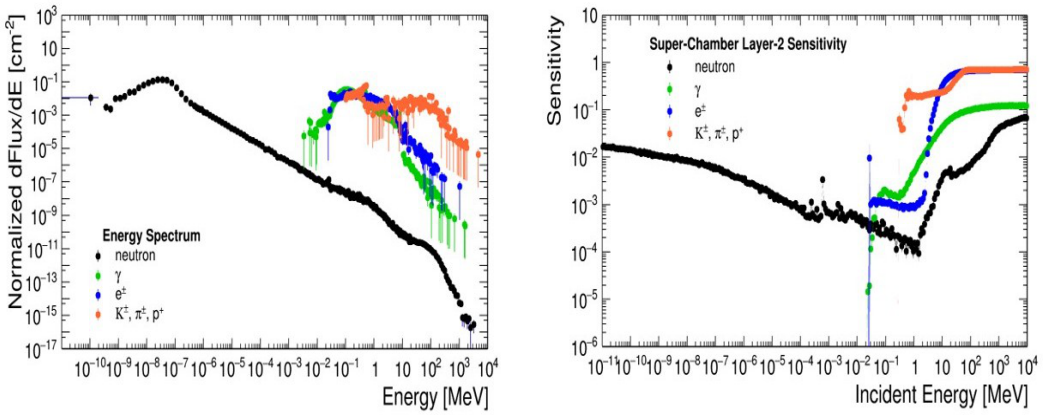

Figure 5.21: Left: A normalized energy spectrum of the background particles. Right: Sensitivity plotted against incident energy for various particles with convolution performed over all potential incident angles.

The average sensitivity, estimated using the energy spectrum of the incident background particles, and the sensitivity for different energies are presented in Table 5.8 for both Layer-1 and Layer-2. The method of using the average sensitivity for GE1/1 detector as a whole is preferred over obtaining the sensitivity for different η-sectors because the detectors have a uniform response for each η-sector, as verified with X-rays during quality control tests [26]. The impact of detector material and configura-

Table 5.8: Average sensitivity for each particle type in Layer-1 and Layer-2 of the superchamber configuration employed during the 2018 GE1/1 Slice Test data-taking.

Particle	Average Sensitivity of Layer-1 (%)	Average Sensitivity of Layer-2 (%)
Neutron	0.64 ± 0.01 (stat.)	0.76 ± 0.01 (stat.)
Photons	0.28 ± 0.01 (stat.)	0.22 ± 0.01 (stat.)
$e^{\pm}$	1.24 ± 0.04 (stat.)	0.31 ± 0.01 (stat.)
Charged Hadrons ($K^{\pm}$, $\pi^{\pm}$, p)	26.29 ± 1.24 (stat.)	24.29 ± 1.14 (stat.)

tion on sensitivity becomes apparent when contrasting Figure 5.16 (left) representing the simplified geometry with Figure 5.20 depicting the superchambers in the CMS experiment.

5.6.1.1 Comparison of Average Sensitivity from Previous Studies

In the previous study [12], a GE1/1 superchamber was simulated, with particles of fixed energy and type crossing the outer surfaces of the superchamber with uniform density over the outer surface of the chamber frame, and incident angles were distributed according to an angular distribution obtained from a previous FLUKA simulation study. The method chosen at that time was the same as described in this chapter, except the minimum energy thresholds for secondary particle production in GEANT were set to about 1 keV for all types of particles except protons and nuclei, for which the threshold was removed entirely. The average sensitivity from the previous study and this one are compared in Table 5.9. The difference between the two studies

Table 5.9: Comparison of TDR and Chamber 28 Layer-2 studies

Parameter	TDR	Present Study)
Triple-GEM Geometry	superchamber	Precise superchamber[1]
GEANT4 Version	v9.6	v10.06
Neutrons (%)	0.18 $\pm$ 0.05	0.76 $\pm$ 0.01
Photons (%)	0.97 $\pm$ 0.04	0.22 $\pm$ 0.01
$e^{\pm}$ (%)	8 $\pm$ 3	0.31 $\pm$ 0.01
Charged Hadrons (%) ($K^{\pm}$, $\pi^{\pm}$, p^{+})	–	24.3 $\pm$ 1.1

is attributed to an updated version of GEANT and a more accurate geometric representation of the GE1/1 detector in this study. GEANT4 v10.06 is an updated version with improved thermal neutron modeling.

5.6.2 Systematic Uncertainties

5.6.2.1 Systematics for GEANT4 Simulation

The precision of sensitivity estimates hinges on accurately describing physics processes and employing realistic detector modeling. The physics processes employed in this simulation are widely recognized and have undergone validation within the GEANT4 framework through multiple studies that include comparisons with experimental data [27, 28]. To assess the influence of detector modeling on sensitivity estimates, the simulation varies the following parameters.

- Drift Gap Width (DGW) variations may arise from mechanical deformations during detector assembly. The simulation incorporates variations [12] of $\pm$10% for both layers of the superchamber. The resulting impact on the average sensitivity of Layer-2 is presented in Table 5.10.
- Gas Mixture Proportion (GMP) for the Ar/CO_2 gas (in the ratio 70/30) was consistently monitored during detector operation and quality control testing, revealing negligible deviations. However, conservative variations of (60/40) and

[1] includes two triple-GEM in superchamber configurtion with pulouts, Alluminium zig, cover, spacers, VFATs and cooling system.

(80/20) are considered in the simulation. The associated impact on the estimated average sensitivity of Layer-2 is detailed in Table 5.10.

- Z-Position (ZPOS) of the primary source surface from the detector is varied by ± 2 mm from the nominal value of 3 mm, and the subsequent re-calculation of average sensitivity measures the impact on the hit rate. The variation in the average sensitivity is presented in Table 5.10
- Surface Area of Primary (SAR) is another systematic uncertainty arises from variations in the x-y dimensions of the source planes. We used a source plane exactly having dimension of drift board as can be seen in Figure 5.14 for the simulation. When the source planes are enlarged by $\pm 10\%$, there is a variation in the average sensitivty for each particle reported in Table 5.10.

Table 5.10: Effect of simulation parameter variations on average sensitivity, relative to the baseline determined by average sensitivity of Layer-2 given in Table 5.8.

Parameters	Variation Values	Impact on average sensitivity of Layer-2 (in %)			
		Neutron	Photon	$e^{\pm}$	Charged Hadrons
DGW	Drift Gap: 2.7 mm	0.6	1.4	1.0	0.5
	Drift Gap: 3.3 mm	0.3	0.4	0.0	0.6
GMP	Ar/CO_2 (60/40)	1.0	0.4	0.3	0.5
	Ar/CO_2 (80/20)	0.1	0.9	0.9	0.2
ZPOS	1 mm	0.6	0.4	0.9	4.0
	5 mm	1.0	1.4	0.9	9.9
SAR	-10%	6.7	6.4	5.4	4.8
	+10%	1.0	0.9	1.0	1.3

The impact of parameter variations depends on the incident particle type, kinetic energy, and incident angle. A single detector exhibits lower sensitivity compared to the experimental configuration. The sensitivity's dependence on parameter variations across different energy ranges is also evaluated.

For neutrons, energy ranges include low energy (LE) from 10^{-11} to 10^{-2} MeV , intermediate energy (IE) from 10^{-2} to 1 MeV , and high energy (HE) from 1 to 10^{4} MeV . Energy ranges for γ's, $e^{\pm}$, and charged hadrons comprise LE from 10^{-2} to 1 MeV and HE from 1 to 10^{4} MeV.

For neutrons, the maximum sensitivity variation due to GMP variations is 1.0% for LE, 5.6% for IE, and 4.6% for HE. Meanwhile, for photons, $e^{\pm}$, and charged hadrons, the sensitivity variation in LE (HE) is estimated to be 0.8% (0.5%), 2.1% (0.3%), and 1.2% (0.1%), respectively. DGW uncertainties show variations similar to GMP, except for the neutron case in the IE region, where statistics are limited.

The uncertainties outlined in Table 5.10 for various incident particle types translate into uncertainties in the hit rate. Notably, the overall uncertainty on the hit-rate is primarily influenced by contributions from neutrons and photons.

5.6.2.2 Systematics for FLUKA Simulation

To assess the systematic uncertainty related to particle flux, a comparison is made between the Run-2 scenario in FLUKA and an alternative scenario. In this alternative setup, the shielding material in front of the Hadron Forward (HF) calorimeter is modified, with borated polyethylene being replaced by non-borated polyethylene. This change directly influences the number of particles reaching the muon stations. The uncertainty is quantified by analyzing the particle flux differences between the two scenarios. Depending on the parameter R, the variation falls within the range of 10% to 20%, with a mean value of 15%. This mean value is established as the indicative uncertainty associated with the particle flux.

The uncertainties in the hit-rate arising from both the FLUKA simulation and the GEANT4 detector simulation are combined in quadrature. The resultant total systematic uncertainty is estimated to be approximately 14.5%.

5.6.3 Hit-Rate for Different Particles

Determining the hit-rate associated with a particular particle involves the multiplication of its average sensitivity, as indicated in Table 5.8, by the corresponding particle flux. In this procedure, the average sensitivity values from Table 5.8 are utilized to scale the particle flux represented in Figure 5.9 (right). The resulting particle-specific hit rates are illustrated in Figure 5.22, providing a detailed breakdown of contributions from various particle types to the overall hit-rate for Layer-2. Significantly, neutrons constitute the predominant contribution, while photons contribute approximately

$\sim$15%. Contributions from charged hadrons and $e^{\pm}$ are notably minimal, each contributing approximately 1%.

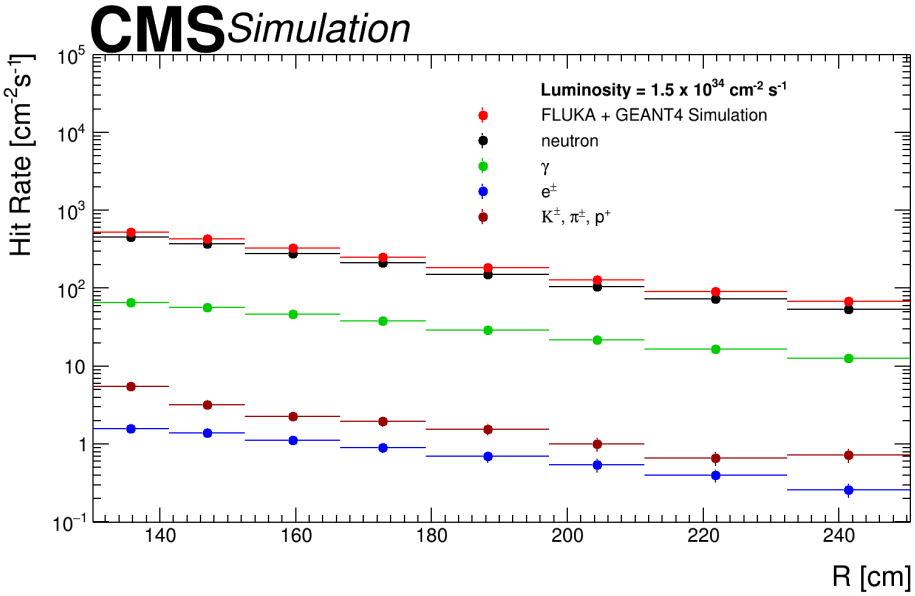

Figure 5.22: Prediction from simulation for hit-rate contribution from different background particles at Layer-2 of superchamber Gemini28.

5.7 Comparison of Data vs Simulation

This investigation employs a comparative analysis between simulation and measurement to validate the presented model. In Figure 5.23, the measured hit-rate of Layer-2 for superchamber Gemini28 is compared with the simulation prediction. The simulated hit-rate is calculated as outlined in the preceding Section 5.6.3. The hit rates, as depicted in Figure 5.22, for various background particles are aggregated for each R point to determine the total hit-rate at that specific point. This aggregation is necessary because data measurement provides the overall hit rate, irrespective of the particle type. Each data point in Figure 5.23 corresponds to different perpendicular distances R from the beamline to the centers of the η-sectors. As expected, the hit-rate is elevated at lower R (higher η), indicative of the heightened collision flux in this region.

The bottom panel of Figure 5.23 presents the ratio of data to simulation along with the estimated systematic uncertainty. The observed hit rates for the triple-GEM detector align with the simulated predictions within the specified uncertainty, with

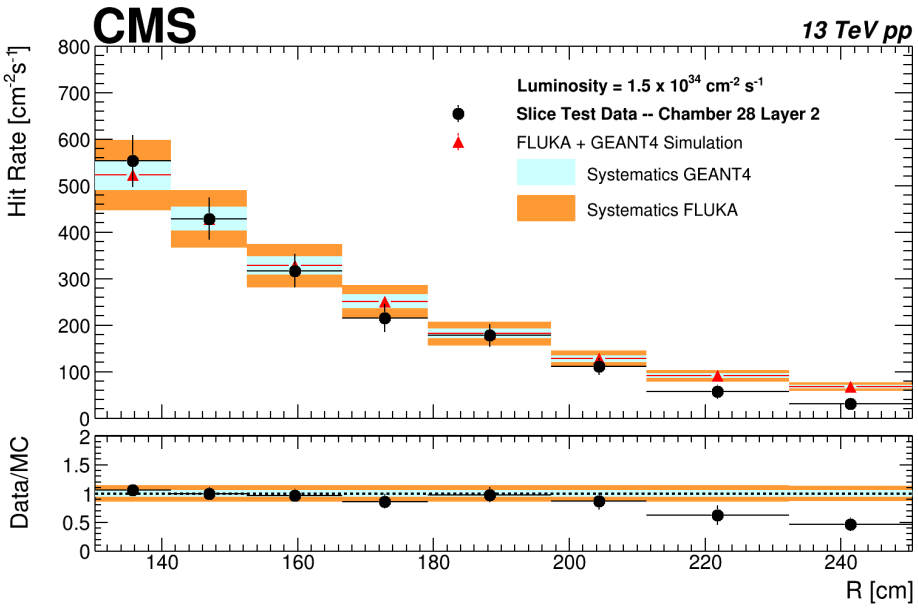

Figure 5.23: Comparison between measured and simulated hit rates on Layer-2 of supercham-ber Gemini28 in the slice test. Blue bands represent systematic uncertainties from GEANT4 detector modeling, while orange bands result from adding FLUKA flux modeling uncertainties in quadrature with those in the blue bands. The bottom panel illustrates the ratio of measured to simulated hit rates.

the exception of η-sectors 1 and 2. In these sectors, data were acquired using readout thresholds higher than the nominal values. The overall uncertainty encompasses both statistical and systematic uncertainties, as detailed in the preceding section, and is computed by combining these uncertainties in quadrature. The uncertainty in the hit-rate for the experimental data includes statistical uncertainty and uncertainties associated with the measurement of instantaneous luminosity.

In Figure 5.23, the hit-rate data for i_η = 1 and 2 (sectors with R > 210 cm) deviate below the predicted values. This deviation can be attributed to elevated thresholds used in the VFAT-3 readout electronics during data acquisition. Specifically, the thresholds for i_η = 1 and 2 were 8.8 fC and 4.0 fC, respectively, corresponding to 6 and 3 electrons per strip in the drift gap. For i_η = 1, a minimum energy loss of 168.6 eV (= 6 × 28.1 eV) is required to register as a "hit", leading to reduced sensitivity. Consequently, the applied thresholds induce a distortion in the strip multiplicity distributions for i_η = 1 and 2. The detection efficiency is notably impacted by the heightened threshold at the strip level for muons at i_η = 1 . While a 3 fC threshold aligns well with our simulation model, a threshold of 8.8 fC proves inadequate, particularly given the non-linear nature of particle interactions with Ar/CO_2 gas (energy loss rate) and

electron multiplication (gas gain). Replicating these non-linear effects within the current simulation framework is challenging, but future studies could benefit from a comprehensive description of electron multiplication (avalanche), potentially using the Garfield [29] software package, along with a simulation of the electronics. The Garfield package is discussed in the next chapter and is used for the simulation of GEM detector for electrode segmentation of GEM foil.

5.8 Conclusion

In this chapter, we examined the measurement of background particles in the context of the GE1/1 detector and replicated the results using FLUKA and GEANT4 simulations to enhance our understanding of the background rate. The assessment of collision-induced background hit rates in the CMS triple-GEM detector during p-p collisions at the LHC involved a modeling approach, utilizing the FLUKA and GEANT4 simulation packages. The FLUKA simulation provided distributions of kinetic energy and angular information for incident particles within the radiation environment, while the GEANT4 simulation characterized particle interactions by employing an accurate material description for each GEM detector. The combined simulated hit rates, determined by integrating sensitivity and particle flux, were then compared with experimental measurements at a luminosity of $1.5 \times 10^{34} \text{cm}^{-2}\text{s}^{-1}$ at $\sqrt{s}$ = 13 TeV. Notably, the predicted hit rates aligned with the experimental data within their respective uncertainties, especially for detector sectors operating under nominal parameters.

The framework introduced in this paper is adaptable, allowing for the assessment of hit rates for alternative detectors at the High-Luminosity LHC . Future research in this field may extend to similar simulations for GE2/1 detectors and, notably, the more intricate ME0. Given ME0's configuration with six detection planes, it requires specialized computing power to capture processes generating signals in each plane. This capability contributes to an enhanced understanding of trigger rates and the robustness of detectors across various experimental configurations.

Bibliography

[1] Martina Ressegotti. "Micropattern Gas Detectors for the CMS Experiment's Muon System Upgrade: Performance Studies and Commissioning of the first GEM Detectors". PhD thesis. Pavia U., 2019.

[2] Alfredo Ferrari et al. "FLUKA: A multi-particle transport code (Program version 2005)". In: (Oct. 2005). DOI: 10.2172/877507.

[3] P Aspell et al. "VFAT2: A front-end system on chip providing fast trigger information, digitized data storage and formatting for the charge sensitive readout of multi-channel silicon and gas particle detectors". In: (2007). DOI: 10.5170/CERN-2007-007.292. URL: http://cds.cern.ch/record/1069906.

[4] P Aspell et al. "VFAT3: A Trigger and Tracking Front-end ASIC for the Binary Readout of Gaseous and Silicon Sensors". In: (2019), p. 8824655. DOI: 10.1109/NSSMIC.2018.8824655. URL: https://cds.cern.ch/record/2706411.

[5] M. Abbas et al. "Detector Control System for the GE1/1 slice test". In: *JINST* 15.05 (2020), P05023. DOI: 10.1088/1748-0221/15/05/P05023.

[6] L. Dimitrov et al. "Results of the Radiation Dose Study Around the Tested GEM Muon Detector at CMS". In: *Proceedings of the XXVI International Symposium on Nuclear Electronics & Computing (NEC 2019)*. Ed. by V. Korenkov, T. Nechaevskiy A. ans Strizh, and T. Zaikina. Budva, Montenegro: CEUR Workshop Proceedings, Sept. 2019, pp. 153–158.

[7] F. Ravotti et al. "Radiation monitoring in mixed environments at CERN: From the IRRAD6 facility to the LHC experiments". In: *IEEE Trans. Nucl. Sci.* 54 (2007), pp. 1170–1177. DOI: 10.1109/TNS.2007.892677.

[8] L. Dimitrov et al. "First Results of the Radiation Monitoring of the GEM Muon Detectors at CMS". In: *Proceedings of the XXVI International Symposium on Nuclear Electronics & Computing (NEC 2017)*. Ed. by Vladimir Korenkov and Andrey Nechaevskiy. Budva, Montenegro: CEUR Workshop Proceedings, Sept. 2017, pp. 318–323.

[9] Elizabeth Rose Starling. *Status of the Readout Electronics for Triple-GEM Detectors of the CMS GE1/1 System and Performance of the Slice Test in the 2017-18 LHC Run*. Tech. rep. Geneva: CERN, 2019. DOI: 10.22323/1.343.0132. URL: https://cds.cern.ch/record/2645759.

[10] Francesco Ivone. "Discharge mitigation strategies for GE11 detectors in the CMS Experiment". Presented 19 Jul 2019. PhD thesis. Bari U., 2019. URL: https://cds.cern.ch/record/2689967.

[11] M. Abbas et al. "Performance of a triple-GEM demonstrator in pp collisions at the CMS detector". In: *JINST* 16.11 (2021), P11014. DOI: 10.1088/1748-0221/16/11/P11014. arXiv: 2107.09364 [physics.ins-det].

[12] A Colaleo et al. *CMS Technical Design Report for the Muon Endcap GEM Upgrade*. Tech. rep. 2015. URL: https://cds.cern.ch/record/2021453.

[13] Serguei Chatrchyan et al. "The Performance of the CMS Muon Detector in Proton-Proton Collisions at $\sqrt{s}$ = 7 TeV at the LHC". In: *JINST* 8 (2013), P11002. DOI: 10.1088/1748-0221/8/11/P11002. arXiv: 1306.6905 [physics.ins-det].

[14] "1-D plot covering CMS tracker, showing FLUKA simulated 1 MeV neutron equivalent in Silicon including contributions from various particle types." In: (2015). URL: https://cds.cern.ch/record/2039908.

[15] Albert M Sirunyan et al. "Measurement of the inelastic proton-proton cross section at $\sqrt{s} = 13$ TeV". In: *JHEP* 07 (2018), p. 161. DOI: 10.1007/JHEP07(2018)161. arXiv: 1802.02613 [hep-ex].

[16] Cecilia Uribe Estrada et al. "Simulation studies of the impact of the CMS radiation environment on RPC detectors". In: *PoS* LHCP2019 (2019). Ed. by Pablo Roig Garcés et al., p. 049. DOI: 10.22323/1.350.0049.

[17] M. Abbas et al. "Benchmarking LHC background particle simulation with the CMS triple-GEM detector". In: *JINST* 16.12 (2021), P12026. DOI: 10.1088/1748-0221/16/12/P12026. arXiv: 2107.03621 [physics.ins-det].

[18] D. Abbaneo. "Impact of the radiation background on the CMS muon high-eta upgrade for the LHC high luminosity scenario". In: *PoS* TIPP2014 (2014), p. 086. DOI: 10.22323/1.213.0086.

[19] M. Abbas et al. "Triple-GEM discharge probability studies at CHARM: simulations and experimental results". In: *JINST* 15.10 (2020), P10013. DOI: 10.1088/1748-0221/15/10/P10013.

[20] Sunanda Banerjee and Vladimir Ivanchenko. "Validation of Physics Models of Geant4 Versions 10.4.p03, 10.6.p02 and 10.7.p01 using Data from the CMS Experiment". In: *EPJ Web of Conferences* 251 (Jan. 2021), p. 03010. DOI: 10.1051/epjconf/202125103010.

[21] Florian Zenoni. "Study of Triple-GEM detectors for the CMS muon spectrometer upgrade at LHC and study of the forward-backward charge asymmetry for the search of extra neutral gauge bosons". PhD thesis. U. Brussels, U. Brussels (main), Apr. 2016.

[22] M. Abi Akl et al. "Uniformity studies in large area triple-GEM based detectors". In: *Nucl. Instrum. Meth. A* 832 (2016), pp. 1–7. DOI: 10.1016/j.nima.2016.06.026.

[23] Archana Sharma. "Properties of some gas mixtures used in tracking detectors". In: (July 1998).

[24] F. Sauli. "Principles of Operation of Multiwire Proportional and Drift Chambers". In: (May 1977). DOI: 10.5170/CERN-1977-009.

[25] Makoto Asai et al. "Recent developments in Geant4". In: *Annals Nucl. Energy* 82 (2015), pp. 19–28. DOI: 10.1016/j.anucene.2014.08.021.

[26] M. Abbas et al. "Performance of prototype GE1 / 1 chambers for the CMS muon spectrometer upgrade". In: *Nucl. Instrum. Meth. A* 972 (2020), p. 164104. DOI: 10.1016/j.nima.2020.164104. arXiv: 1903.02186 [physics.ins-det].

[27] Alexander Howard et al. "Validation of neutrons in Geant4 using TARC data - production, interaction and transportation". In: *2008 IEEE Nuclear Science Symposium and Medical Imaging Conference and 16th International Workshop on Room-Temperature Semiconductor X-Ray and Gamma-Ray Detectors*. 2008, pp. 2885–2889. DOI: 10.1109/NSSMIC.2008.4774970.

[28] J. Apostolakis et al. "Validation and verification of Geant4 standard electromagnetic physics". In: *J. Phys. Conf. Ser.* 219 (2010). Ed. by Jan Gruntorad and Milos Lokajicek, p. 032044. DOI: 10.1088/1742-6596/219/3/032044.

[29] R. Veenhof. "GARFIELD, recent developments". In: *Nucl. Instrum. Meth. A* 419 (1998). Ed. by M. Krammer et al., pp. 726–730. DOI: 10.1016/S0168-9002(98)00851-1.

Chapter 6

GEM Foil Electrode Segmentation and Detector Performance

"I have often pondered over the roles of knowledge or experience, on the one hand, and imagination or intuition, on the other, in the process of discovery. I believe that there is a certain fundamental conflict between the two, and knowledge, by advocating caution, tends to inhibit the flight of imagination. Therefore, a certain naivete, unburdened by conventional wisdom, can sometimes be a positive asset."

— H C Mehrotra, 1923–1983

6.1 Introduction

In this chapter, we will explore the detailed aspects of electrode segmentation in large-area GEM foils and its significant impact on the performance of GEM detectors. GEM detectors, such as the GE1/1 detector, utilized foils with electrodes oriented towards the readout board (reffered as bottom electrode of GEM foil), forming a continuous conductor. However, the electrodes facing the drift board (reffered as top electrode of GEM foil) are segmented into HV sectors of varying widths, with a charge flow limit of approximately 2 microcoulomb (μC) per foil [1]. This segmentation design is crucial for high-rate applications as it effectively constrains the capacitance between opposing electrodes, minimizing the energy released in a discharge event.

Another notable approach to foil segmentation involves electrically isolating both the top and bottom electrodes of GEM foils into distinct sectors. This strategy, proposed for the upcoming CMS Muon upgrade ME0 detector foils, presents a promising solution to further enhance the performance and reliability of these detectors.

In Section 6.2, we will thoroughly explain both types of segmentation methods, shedding light on their underlying principles and operational advantages. Following this, Section 6.3 will present the comprehensive Test-Beam results for both segmentation methods, providing valuable insights for their practical implementation. These results will be thoroughly compared with simulations, the details of which will be discussed in Section 6.4. The simulation results, presented in these sections, will offer a comprehensive understanding of the expected performance enhancements and operational efficiencies achieved through electrode segmentation.

Furthermore, Section 6.5 will showcase detailed electric field maps, providing a visual representation of the electric field distribution with the segmented GEM foils. Additionally, Sections 6.6 and 6.7 will present the electron T_e and muon efficiency, respectively, offering a quantitative analysis of the segmentation's impact on detector performance.

Finally, we will culminate our discussion by comparing the simulation results with the Test-Beam data in Section 6.8, providing a comprehensive evaluation of the segmentation strategies and their implications on the overall performance and reliability of GEM detectors.

6.2 GEM Foil Segmentation

The energy stored in large-area GEM foils with high capacitance can potentially damage the foils in the event of a discharge [2]. Discharges can also spread to anodes, leading to failures in readout electronics. Segmentation of GEM foils divides the active surface into numerous sectors, each independently supplied by protective resistors, to address this issue, as shown in Figure 6.1. This division lowers the energy of successive discharges due to their reduced capacity. Segmentation has become a common approach in many experimental settings, such as muon detection in large-area GEM detectors for the ongoing CMS upgrade [1, 3].

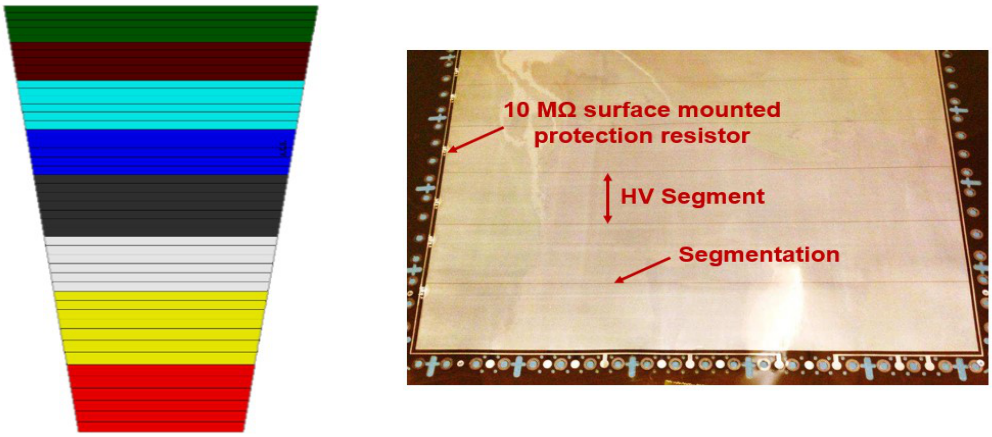

Figure 6.1: Left: Diagram showing HV segmentation of long GE1/1 GEM foil into 47 sectors on the side of the foil facing the drift board. The color scheme indicates which HV segments correspond to the 8 η-sectors of the detector. Right: The GE1/1 GEM foil features traces running along the active area, which route HV to the HV segments through 10 MΩ protection resistors [4].

Segmentation is commonly achieved by inserting an insulating zone devoid of holes on one side of a GEM foil between two electrode sectors. The metal is removed in this location, revealing the insulating substrate (polyimide). The width of such insulating gaps is typically 100-200 μm, resulting in an electric field distortion in this region. Electrons traveling towards the GEM foil may be lost or caught in the holes of the surrounding electrode sectors, deviating from their intended pathways.

However, segmentation causes signal distortion and efficiency loss in the region of the insulating gap between sectors. Such distortions have been observed in the COMPASS [5] triple-GEM tracking detector [6]. To reduce distortions at sector gaps, an alternate design has been proposed for the ME0 detector upgrade that preserves the hole pattern even in the insulating zone. While the electrode segmentation is maintained by removing metal along a strip, the hole pattern is not disturbed, and holes can be found in the insulating gap as well. Although the electric field is distorted in this region, this design may result in some electric field lines pass through the insulating zone's perforations, allowing some electrons to follow their initial pathways and undergo multiplication.

Moreover, reducing the size of each sector mitigates the current induced on the electrodes during irradiation by avalanche charges, which traverse the high-voltage protection resistors, thereby constraining the detector's rate capability. The two types of segmentation methods are discussed below.

6.2.1 Blank Electrode Segmentation

The blank electrode segmentation in GEM foil involves a segmented electrode, creating an exposed polyimide region devoid of holes. This electrode segmentation is typically achieved by introducing an insulating region without GEM holes between two adjacent electrode sectors during manufacturing. However, the conventional practice of electrode segmentation leads to a distortion in the electric field configuration, potentially resulting in a consequential deterioration of detection efficiency within the segmentation gap.

The utilization of blank electrode segmented foils is accompanied by two principal drawbacks:

- The introduction of narrow dead zones between two sectors may hinder the optimal functionality of the detector, as we will discuss further.
- The manual alignment of the segmentation pattern with the GEM hole pattern during the manufacturing process of GEM foils is necessary, but it poses the risk of potential errors.

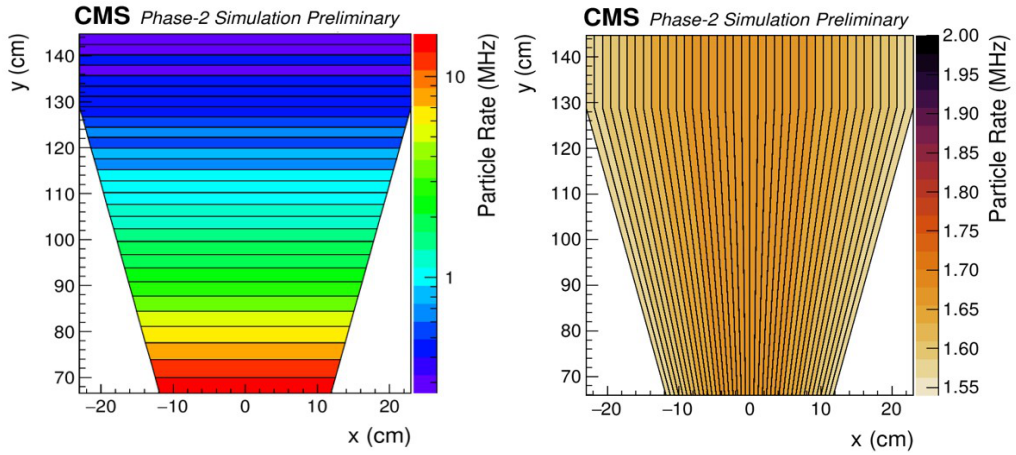

Figure 6.2: Left: Diagram illustrating the transverse segmentation of a GEM foil in an ME0 detector relative to the LHC beamline, displaying the anticipated background particle rate per sector. Right: Diagram depicting the design of the adopted azimuthal segmentation for the ME0 detectors, illustrating the anticipated background particle rate per sector within the CMS environment. [7].

The imperative to address these considerations is particularly pronounced in the realm of high-rate systems, exemplified by the CMS Phase-II upgrade at the LHC. The impending installation of the ME0 detector station within the CMS muon spectrometer during the LHC LS3 necessitates the assembly of 18 stacks of triple-GEM detectors

for each of the two endcaps. An evaluation of the rate capability of these triple-GEM detectors, designed to cover extensive areas, has revealed their inadequacy for the high-flux conditions of the ME0 station in the CMS experiment [8]. This limitation arises from the presence of resistive protection circuits, which leads to a decreasing rate capability as the total irradiated detector area increases. To address this, a proposed solution involves restoring the original gas gain of the detector through electrode-by-electrode voltage compensation.

In the initial configuration of the ME0 detector at CMS, the triple-GEM detectors experienced a gain drop exceeding 40%, accompanied by a sector-by-sector gain non-uniformity of 50% under irradiation as shown in Figure 6.2.

The solution to this problem comes with another metod of segmentation is reffered as “random electrode” segmentation discussed next.

6.2.2 Random Electrode Segmentation

The proposed solution is reviving an earlier concept from Sauli, Rui, and the RD51 team [9] called random electrode segmentation. This involves introducing a random alignment between the hole pattern and the sector gap, a concept recently revisited by the RD51 team [10]. The potential of this alternative design lies in its promise for the

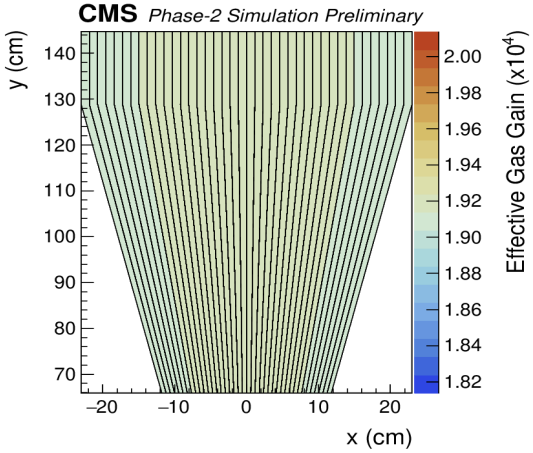

Figure 6.3: Gain variations in the ME0 detector due to the implementation of azimuthal segmentation.

manufacturing of large area foils. Unlike traditional methods, this technique does not demand precise alignment of the sector gap with the hole pattern.

The conventional segmentation of electrodes leads to an alteration of the electric field, potentially causing a decline in detection efficiency within the sector gap. To address the potential loss in efficiency at these sector gaps, R&D group revisited the alternative design concept of random electrode segmentation.

Sauli introduced the concept two decades ago but abandoned it due to local copper detachment near the insulating gap. The design involves a unique surface with GEM-holes, maintaining electrode segmentation by removing the copper layer along a strip with a random alignment between the hole pattern and sector gap. The layout allows for holes in the insulating gap and rims, with partial copper coverage, potentially enabling some electric field lines to pass through the sector gap, leading to electron multiplication.

In addressing the problem discussed in the previous section, the implementation of an azimuthal segmentation in relation to the LHC beam line is expected to reduce both gain loss and its non-uniformity as shown in Figure 6.3 [8].

- The segmentation is (nearly) radially symmetric, ensuring high gain uniformity.
- The gain drop can be minimized by increasing the number of sectors. This approach is simulation-agnostic, independent of knowledge about the background flux.

Achieving precise azimuthal segmentation requires careful alignment of photolithographic masks to create insulating gaps in sectors. This precision is crucial due to the misalignment of hole patterns with the ME0 trapezoidal shape. Additionally, each sector has a slight variation in inclination relative to the vertical line ($\pm 10^{\circ}$), causing holes to partially overlap with the segmentation area. Consequently, removing these overlapping holes increases the dead area, raising it from the standard 200 μm to approximately 600 μm. This change has implications for the overall performance of the detector.

Conclusively, initial Test-Beam results for a segmented detector with random electrode in the ME0 station are discussed in the next section, and its muon efficiency is compared with that of a triple-GEM prototype with blank segmentation.

6.3 Test Beam Efficiency Measurement

At CERN North Area, an experimental evaluation of 10×10 cm^2 prototype involved subjecting it to rigorous testing using 80 GeV muons in the Test-Beam. Employing a sophisticated two-dimensional triple-GEM tracker with a point space resolution of 75 µm, a thorough analysis was conducted to derive a high-resolution efficiency map for the detector [11]. The construction of this efficiency map involved finely binning the propagated track positions with sub-millimeter precision.

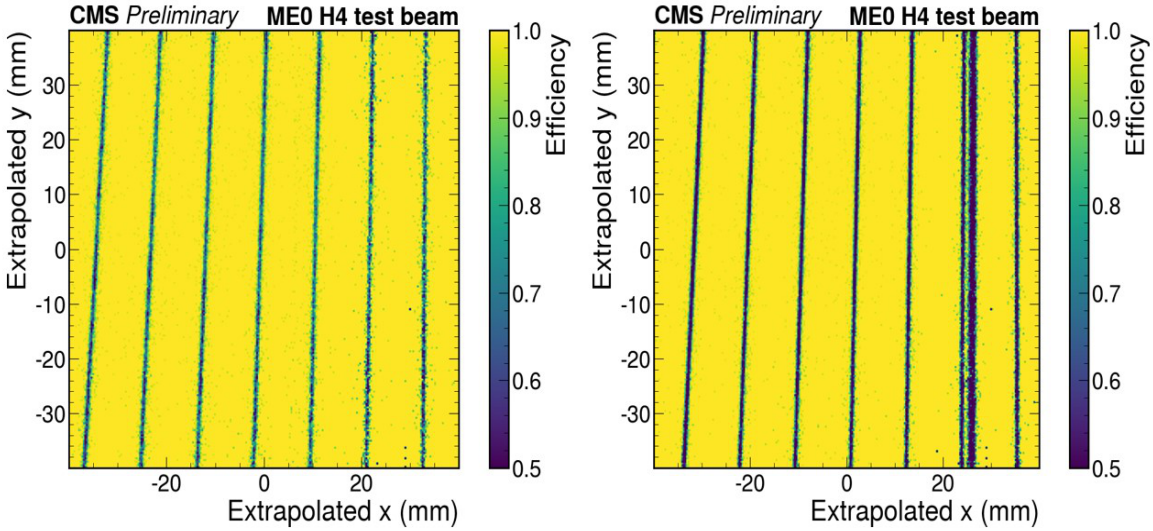

Figure 6.4: Left: Efficiency map depicting the wide side of the ME0, with the blank-segmented configuration. Right: Efficiency map depicting the wide side of the ME0, with the random electrode segmented design [11].

In assessing the influence of random electrode segmentation on efficiency, a CMS ME0 detector equipped with GEM foils featuring random electrode segmentation was subjected to testing in tandem with a counterpart blank electrode segmented ME0 detector. The ME0 detectors, characterized by a trapezoidal shape with approximate bases measuring 23 cm and 46 cm and a height of 73 cm, are further segmented into 40 sectors along the vertical direction. This experimental setup allowed for a direct comparison of the performance impact resulting from the adoption of random electrode segmentation in the GEM foils.

In Figure 6.4, a comparative analysis of efficiency maps is presented for both the blank-segmented ME0 and the random-hole segmented ME0, focusing on the 10×10 cm^2 area covered by the tracker. These maps depict the profile of the GEM foil segmentation, revealing notable differences in efficiency losses between the two

configurations. Specifically, the efficiency losses in the dead regions of the random-hole segmented prototype appear to be lower than those observed in the blank-segmented detector.

To provide a more detailed perspective, a cross-sectional view of the efficiency profile along the y-axis is illustrated in Figure 6.5. This slice of the efficiency profile underscores that in the blank-segmented detector, efficiency loss reaches up to 75%, emphasizing significant degradation. Conversely, in the random-segmented prototype, the efficiency loss is notably more limited, reaching approximately 40%. These findings underscore the comparative advantages of the random-hole segmentation approach, indicating a potential improvement in overall detector performance, particularly in mitigating efficiency losses in critical regions.

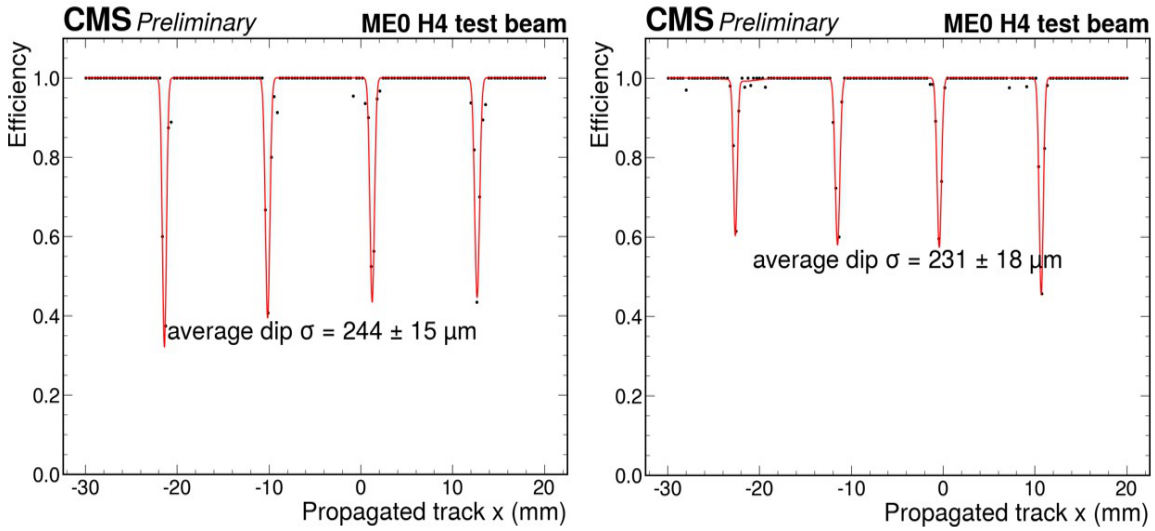

Figure 6.5: Left: Cross-sectional efficiency profile for the wide side of the ME0, with the blank-segmented configuration. Right: With the random-segmented configuration [11].

6.4 Simulation Setup

The simulation of the triple-GEM detector, aiming to replicate and examine both types of segmentation, utilizes ANSYS [12] and Garfield++ software [13]. 'This simulation studies the complex processes of electron drift and diffusion in gas mixtures, particularly Ar/CO_2 (in percentage ratio 70/30), under an electric field. It primarily focuses on analyzing the deformations of the electric field and evaluating the decrease in muon

detecton efficiency. To deepen our understanding of these phenomena, a thorough comparison is performed between the simulation data and experimental results.

For complex geometries, external software such as COMSOL [14] and neBEM [15] can be used to compute the electric field and detector geometry. The resulting field map from these applications is then used as input for Garfield++. This simulation framework interfaces with two additional codes: MagBoltz [16], which solves the Boltzmann transport equation for electrons in gas under the influence of electric and magnetic fields, and High-Energy Electro-Dynamics (HEED) [17], which simulates the ionization of gas molecules by incident charged particles. A schematic diagram illustrating the simulation workflow is provided for clarity.

6.4.1 ANSYS

ANSYS is renowned for its versatility in various analyses, including electromagnetic studies, structural stability assessments, fluid dynamics, and heat transfer analyses. In our simulation, we utilized ANSYS Mechanical ANSYS Parametric Design Language (APDL) to generate electric field maps for our detector. This process involves computing the electric potential at each point within the detector, considering both the internal applied electric field and the geometry of the GEM. ANSYS utilises the Finite Element Method (FEM) to solve Maxwell's equations of electrodynamics, providing a numerical solution to complex boundary conditions within the GEM.

Calculating the electric field in a single or triple-GEM setup is complex due to the detector's complex structure and numerous boundary conditions. ANSYS uses the FEM with the SOLID123 technique, which is a 10-node solid element capable of quadratic displacement behavior, to subdivide the geometry, enabling the derivation of approximate solutions. This method, which utilises quadric curved tetrahedra for each element, improves the accuracy of the simulation, particularly in modeling the complex bi-conical shape of holes in the GEM foil.

6.4.1.1 Geometry

Geometry typically used for general simulations involves replicating a single unit cell with two one-fourth holes as shown in Figure 6.6 [18]. We have designed a larger area GEM foil detector to accommodate segmentation effects. The segmentation

periodicity is ≈ 25 mm in case longitudinal segmentation of GE1/1 and ≈ 15 mm for the proposed azimuthal segmetation in ME0 foils. To study segmentation precisely and apply boundary conditions that replicate the solution to a larger volume, we utilized a larger area GEM detector. In constructing the geometry, we employed

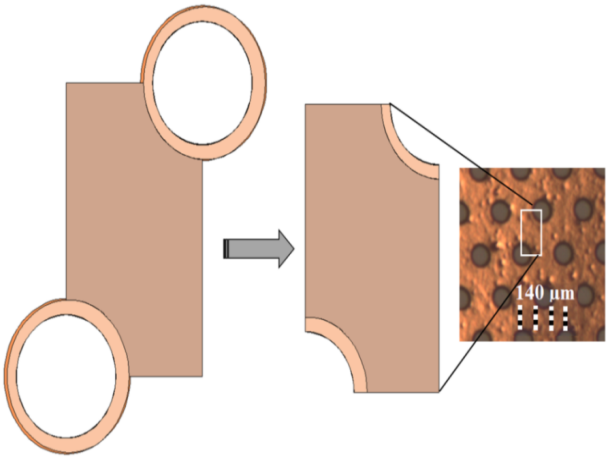

Figure 6.6: Top view of ANSYS-generated GEM foil holes, with the central part representing a segment of an actual GEM foil (white rectangle). [18].

50 µm thick Kapton with 5 µm Copper layers on the top and bottom. A segmentation with a width of 200 µm was introduced to replicate a small section of the segmented GEM foil, facilitating the generation of the complete foil-type scenario. In the initial phase, three samples, each with dimensions of 2.52×0.242 mm^2, were created, as depicted in Figure 6.7. One sample remained non-segmented, serving as a reference, while the other two, identical in dimensions, featured segmentations at the middle of the sample at angles of 20° and 0° with respect to the Y-axis. The GEM materials are defined with dielectric constants: gases like CO_2, and Ar have a nearly constant value around 1, Copper plates possess a high dielectric constant of approximately 10^{10}, and insulator material Kapton has a dielectric constant of 4. These rectangular hole patterns, with a 140 µm pitch, were repeated three times along the Z-axis to form a complete triple-GEM detector. The samples were extracted from a GEM foil section with segmentations at 0° and 20°, as illustrated in Figure 6.8. The proposed ME0 foil incorporates multiple segments at various angles ranging from 0° to 20°. For simplification, we will designate the sample with no segmentation as Sample-1, the sample with a 20° segmentation as Sample-2, and the sample with a 0° segmentation as Sample-3.

For obtaining accurate and precise estimations, it is crucial to establish boundary conditions that closely resemble the actual scenario. All the samples, with the exception

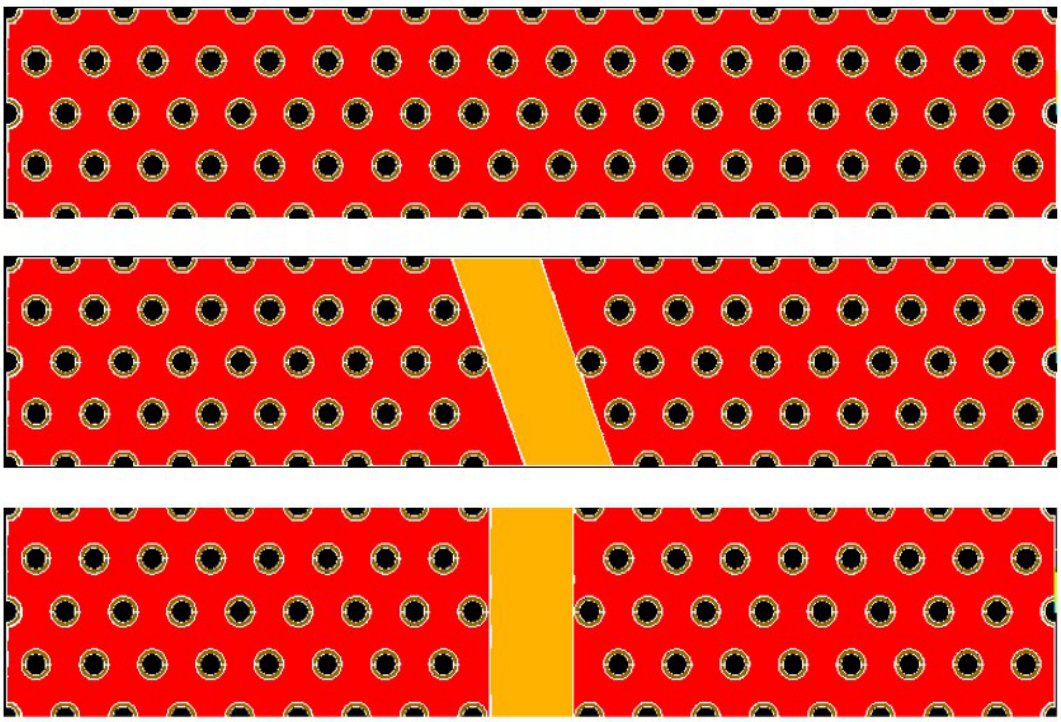

Figure 6.7: Top: Sample with no Segmentation. Middle: Sample with 20° segmentation by removing copper strip of width 200 μm from both sides of GEM foil. Bottom: Sample with 0° segmentation (bottom) by removing copper strip of width 200μm from both sides used for the electric field calculation.

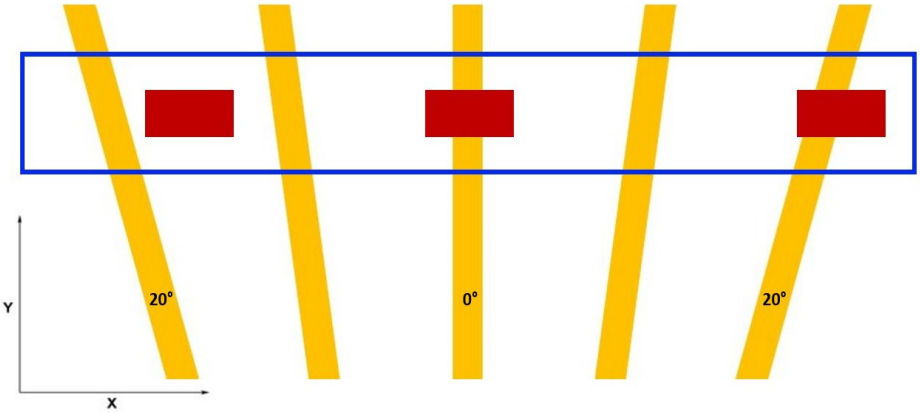

Figure 6.8: Region of ME0 foil imitated in ANSYS geometry for simulation.

of Sample-2, can be effectively utilized for applying boundary conditions and obtaining accurate results. However, replicating Sample-2's nodal solution in the X-axis or Y-axis (a method available in Garfield++) presents challenges. In Sample-2, the segmented region is inclined at an angle of 20°, complicating the establishment of X or Y symmetry.

To address this challenge, extensive efforts were dedicated to finding a viable solution. A repeating pattern was identified for Sample-2, aligning the segmented area with the Y-axis, while the hole pattern is rotated at an angle of 20°, as depicted in Figure 6.9. Again for simlification, we are designating this geometry as Sample-2′. This approach allows for extending the solution beyond the sample boundary, ensuring a more accurate representation of the actual conditions. This sample can be

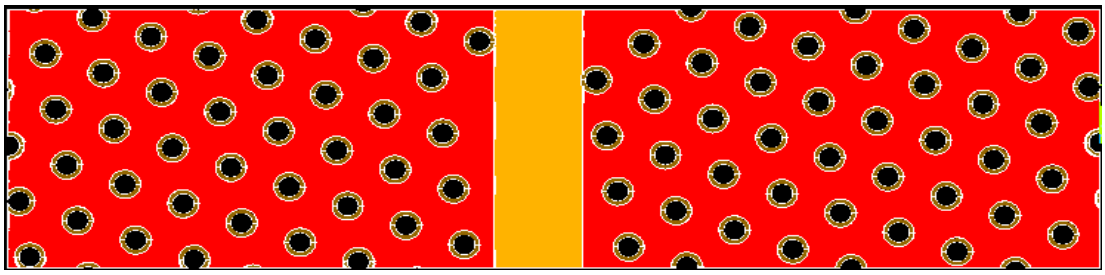

Figure 6.9: New sample with 20° segmentation by rotating the hole patterned to 20° clockwise through Z-axis.

used to extend the solution beyond the sample boundary in the X and Y directions. The straightforward periodicity method is applied for extending the field solution beyond the sample's boundaries. For both the single-GEM and triple-GEM detector

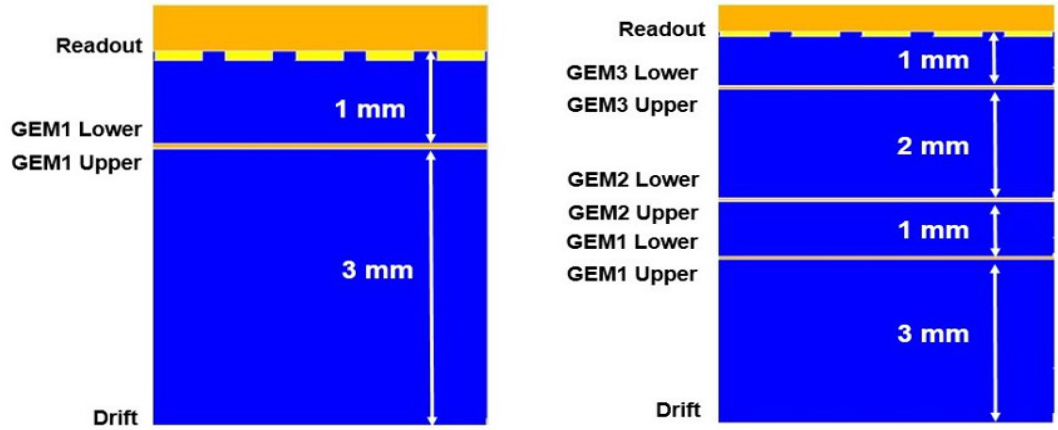

Figure 6.10: Left: ANSYS geometry view of singe-GEM detector with gap configuration 3:1 in mm. Right: ANSYS geometry view of triple-GEM detector with gap configuration 3:1:2:1 in mm.

configurations with gap ratios of 3:1 in mm and 3:1:2:1 in mm, respectively, all samples were encoded using the APDL.

Table 6.1: Voltages used for the different electrodes of a single GEM detector using the current setting at 700μA.

Single-GEM Detector	Z-Position (cm)	Triple-GEM Detector	Z-Position (cm)
Readout	0	Readout	0
Induction Gap	0.0 to - 0.1000	Induction Gap	0.0 to - 0.1000
GEM Lower	- 0.1000 to - 0.1005	GEM3 Lower	- 0.1000 to - 0.1005
Kapton	- 0.1005 to - 0.1055	Kapton3	- 0.1005 to - 0.1055
GEM Upper	- 0.1055 to - 0.1060	GEM3 Upper	- 0.1055 to - 0.1060
Drift	- 0.1060 to - 0.4060	Trnasfer2 Gap	- 0.1060 to - 0.3060
		GEM2 Lower	- 0.3060 to - 0.3065
		Kapton2	- 0.3065 to - 0.3115
		GEM2 Upper	- 0.3115 to - 0.3120
		Transfer1 Gap	- 0.3120 to - 0.4120
		GEM1 Lower	- 0.4120 to - 0.4125
		Kapton1	- 0.4125 to - 0.4175
		GEM1 Upper	- 0.4175 to - 0.4180
		Drift Gap	- 0.4180 to - 0.7180

6.4.1.2 GEM Applied Voltages

A GEM detector demands individual biasing at each of its electrodes to ensure proper functionality. The detector is characterized by discrete electric field regions: Drift, GEM, and Induction in the case of a single-GEM detector, and Drift, GEM1, Transfer1, GEM2, Transfer2, GEM3, and Induction in the case of a triple-GEM detector. The electric field strength within the drift region ranges from 250 to 300 V/mm, while the GEM regions exhibit a field strength between 5800 to 6500 V/mm. The transfer and induction regions are characterized by an electric field strength falling within the range of 400 to 450 V/mm.

To determine the requisite voltages for the Drift, GEM Upper, and GEM Lower electrodes, a voltage divider setting is implemented. A specified electric current of 700 microamperes (μA) is applied to ascertain the voltages across the electrodes. The

Table 6.2: Voltages used for the different electrodes of a single GEM detector using the current setting at 700 μA.

Electrode	Divider Resistance (MΩs)	Voltage Drop (V)	Voltage w.r.t. Readout (V)
Readout	—	—	0
GEM Lower	0.6259	(700 × 0.6259) = - 438.13	- 438.13
GEM Upper	0.5255	(700 × 0.5255) = - 367.85	(- 438.13 - 367.85) = - 805.98
Drift	1.1257	(700 × 1.1257) = - 787.99	(- 805.98 - 787.99) = - 1593.97

drift region receives the highest negative voltage, and the remaining voltages are adjusted based on the resistor distribution within the potential divider. The readout plane is grounded in this configuration. The applied voltages are determined based

Table 6.3: Voltages used for the different electrodes of a single GEM detector using the current setting at 700 μA.

Electrode	Divider Resistance (MΩs)	Voltage Drop (V)	Voltage w.r.t. Readout (V)
Readout	—	—	0
GEM3 Lower	0.6259	(700 × 0.6259) = - 438.13	- 438.13
GEM3 Upper	0.5255	(700 × 0.5255) = - 367.85	(- 438.13 - 367.85) = - 805.98
GEM2 Lower	0.8758	(700 × 0.8758) = - 613.06	(- 805.98 - 613.06) = - 1419.04
GEM2 Upper	0.5503	(700 × 0.5503) = - 385.21	(- 1419.04 - 385.21) = - 1804.25
GEM1 Lower	0.4378	(700 × 0.4378) = - 306.46	(- 1804.25 - 306.46) = - 2110.71
GEM1 Upper	0.5632	(700 × 0.5632) = - 394.24	(- 2110.71 - 394.24) = - 2504.95
Drift	1.1257	(700 × 1.1257) = - 787.99	(- 2504.95 - 787.99) = - 3292.94

on experimental settings. The resultant voltage values, thoroughly distilled from these experimental configurations, are comprehensively presented in Table 6.2 for single-GEM detector and in Table 6.3 for triple-GEM detector. These values serve as critical inputs for both the field calculation and the subsequent Garfield simulation.

6.4.1.3 Meshing

In the computational realm of field calculation and simulation meshing, the development of the 3D electric field model involves the intricate assembly of a mesh comprising tetrahedral elements. The adjustability of these elements within the mesh throughout the simulation is a crucial feature, directly influencing both the precision of results and the temporal dynamics of the simulation. This mesh adapts to the inside surface geometry, partitioned into tetrahedra. The electric potential is computed at each mesh node. The tetrahedra size decreases based on geometry complexity, ensuring efficient coverage of irregular shapes, particularly near GEM holes. The trade-off becomes evident, where the integration of finer mesh elements enhances result accuracy but concurrently elongates the overall simulation duration.

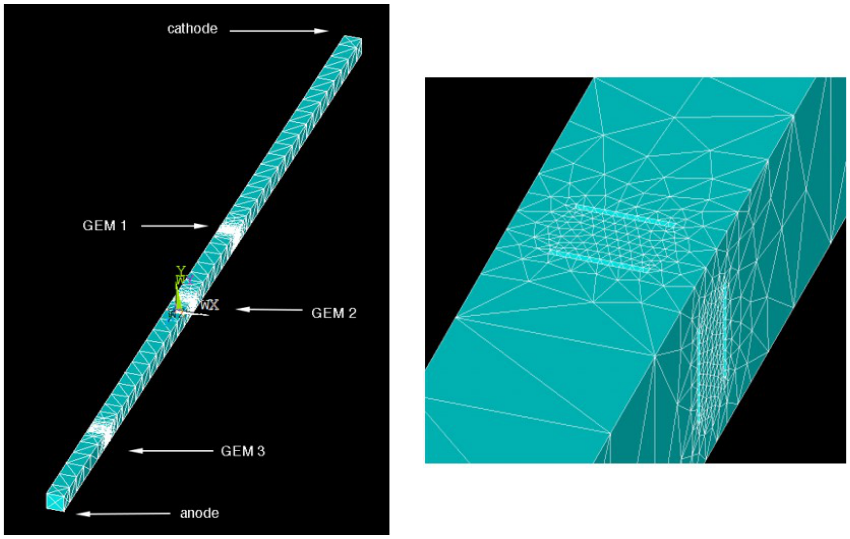

Figure 6.11: Left: Mesh of the vertical unit generated using ANSYS. The meshing method employed is SOLID123, with each element consisting of ten nodes. This method is optimized for accurately modeling round shapes, such as the holes in a GEM foil. Right: Close-up of the vertical unit's outer edges, highlighting a finer mesh around a single GEM foil. To accurately model the surface of the holes and the copper components, it is necessary to decrease the element sizes near the GEM foils, as their dimensions along the x-axis and y-axis are much smaller than the thickness of the triple-GEM [19].

The mesh yields solutions at each node, considering polygon shapes as shown in Figure 6.11. We use curved tetrahedrals with 10 nodes, each linked to a shaping function. Through extrapolation, the software solves the entire problem, providing electric potential values for determining corresponding electric field lines. The simulation duration, ranging from days to weeks, depends on factors like sample size, high

voltage, and mesh size. For increased accuracy, the simulation strategically uses the smallest mesh size, recognizing its crucial role in achieving precision.

6.4.1.4 Result

After solving the electrostatic field, a field map can be saved, encapsulating information about FEM cells and potential. Four output files are commonly generated:

- ELIST.lis: maps FEM elements.
- NLIST.lis: stores node coordinates.
- MPLIST.lis: defines materials and their properties.
- PRNSOL.lis: records potential at each node.

Typically, a single GEM results in approximately 10,000 elements and 15,000 common nodes. Element concentration is higher in areas with significant structural variations. Additionally, the weighting field generates extra Drift.lis and Readout.lis files for the calculation of signal output for the drift and readout containing nodal solutions for the potential, with the field map and FEM elements being identical.

6.4.2 Garfield

Garfield++ is a versatile software package for detailed simulations of gaseous and silicon particle detectors. Initially released in 1984 as Garfield in FORTRAN, it focused on simulating gaseous detectors. In the late nineties, it underwent an update and transitioned to C++, incorporating the capability to simulate semiconductor detectors. This evolution led to the creation of Garfield++, a comprehensive simulation tool covering primary ionizations to signal processing. The software offers flexibility through various algorithms and customizable simulation environments. This section outlines the fundamental principles of these simulations, with more detailed information available in the user manual, source code, and on the official website. Figure 6.12 provides an overview of the Garfield++ class structure, with the program relying extensively on the ROOT [20] software package developed at CERN for simulation and analysis. HEED is an independent simulation tool developed by I. Smirnov in Fortran and later in C++ [16]. It intricately simulates the primary ionization process based on the Photo-Absorption Ionization (PAI) model [21]. Specifically, it calculates gas parameters

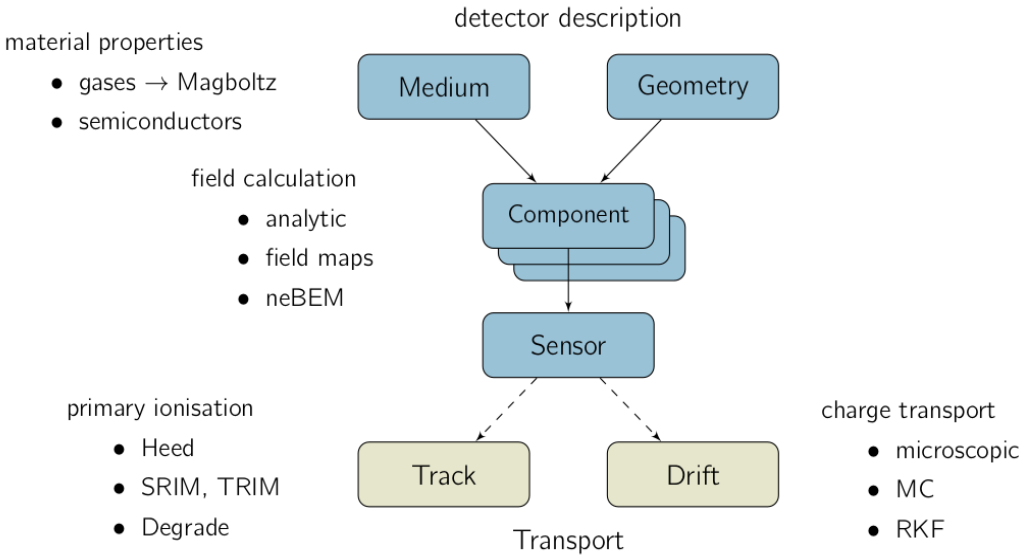

Figure 6.12: Main classes and their interactions in Garfield++.

like cluster density, W_i-value, and stopping power, as well as the location and energy transfer of ionization clusters. Additionally, it determines the positions of primary and secondary electrons originating from δ-electrons.

HEED accommodates a variety of incident particles such as muons, pions, electrons, positrons, and α-particles. For photons, it provides the position of primary electrons, but the energy of primary and secondary electrons is set to zero due to the absence of detailed transport of δ-electrons in HEED.

HEED enhances accuracy by using individual electron cross sections based on electron shell data from experiments, assuming the energy from a charged particle is absorbed solely by a single electron. The accuracy of HEED is extensively discussed in the main paper [16], demonstrating close agreement with experimental data. For instance, simulated cluster density matches experimental curves for pions, protons, and electrons over an energy equivalent to $\beta\gamma = 10^5$ with high precision.

6.4.2.1 Geometry

The geometry for GEM detector, along with electrostatics, must be loaded from ANSYS output files. The FEM elements are parsed to load the GEM unit cell in Garfield++. Subsequently, an active medium or gas volume is assigned and characterized by

its permittivity (ϵ_r = 1 for the gas volume). Only the active medium is used in the simulation, while other volumes (metal and kapton layers) are neglected due to the absence of transport models in solids (except for semiconductors).

A gas mixture of Ar/CO_2 is assigned to the gas volume via the Magboltz class, acting as a link between Garfield++ and the standalone Magboltz simulation tool. The Component class integrates geometry and gas medium classes, providing a unified description of the detector, including the electric field. The potential is loaded from ANSYS output files, and the field is computed by E = -ΔV(r).

Once the geometry and fields are integrated into a Component object, the Track and charge transport classes can simulate primary ionization and the transport of primary electrons, respectively. The Sensor class serves as the global connection, linking all the different sub-classes and enabling the calculation of induced signals and convolutions with transfer functions[1].

6.4.2.2 Simulation

Utilizing ANSYS-derived results, we conducted simulations on single-GEM and triple-GEM detectors, utilising electrons and muons as primary particles.

The electron simulation specifically targeted the computation of G_{int} and G_{eff}. In this context, we simulated precisely 50,000 electrons, each initialized with an energy of 0.5 eV. These electrons were introduced with randomized directions, resulting in momentum aligned with the positive Z-direction. Systematic variations in initial Z-position were applied within the drift volume, and distinctions in X and Y-positions were introduced across multiple samples, as depicted in Figure 6.13.

As previously discussed, the simulation of Sample-2 involves utilizing Sample-2', depicted in Figure 6.9. To achieve an equivalent effect to that of Sample-2, we executed a precise rotation of the X-Y area of the primary track's initial position, exemplified in Figure 6.14.

For muon simulations in the triple-GEM detector, we modeled 5,000 muons, each interacting with foils representing distinct sample types. The muon tracks were generated using the HEED model, utilizing the same primary track initial positions as

[1] a function reprensenting readout elctronics output.

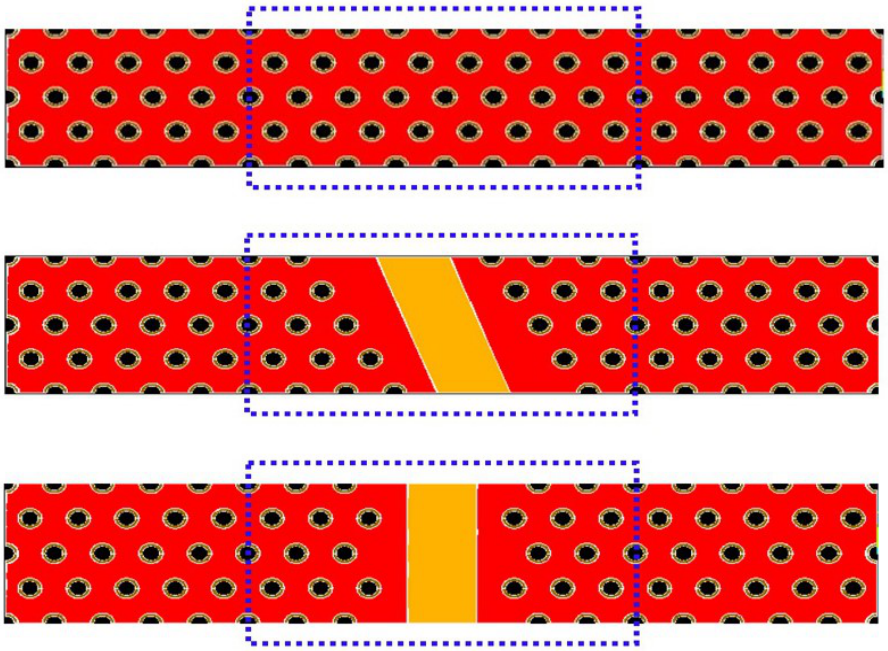

Figure 6.13: Top: Parimary track generation area in X-Y plane for sample-1. Middle: Parimary track generation area in X-Y plane for sample-2. Bottom: Parimary track generation area in X-Y plane for sample-3.

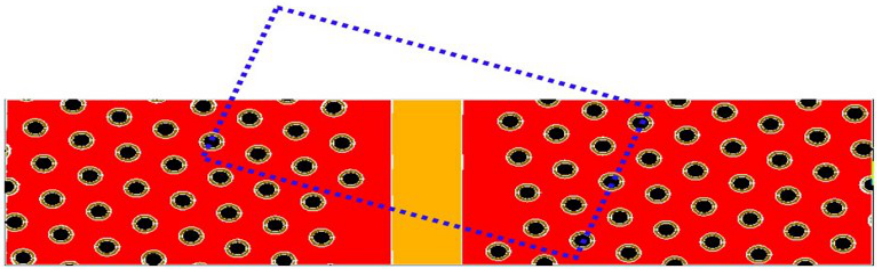

Figure 6.14: Parimary track generation area in X-Y plane for sample-2 used for the simulation as discussed.

utilised for the electron simulation. Given the absence of strips in the ANSYS geometry, the entirety of the sensor was utilized for electron collection and signal generation.

The Sensor class assumes a pivotal role as the overarching entity, establishing connections with diverse sub-classes. Its primary function lies in coordinating the computation of induced signals and their convolutions with the VFAT3 transfer func-

tion [22], a crucial step detailed below:

$$F(t) = \left(\frac{t}{\tau}\right)^{n} \cdot \exp\left(\frac{-n \cdot t}{\tau}\right) \tag{6.1}$$

In the context of VFAT3, a transfer function with parameters n = 3 (for VFAT2, n = 2) and peaking time τ = 25 ns is used for the convolution process.

6.5 Electric Field Map

Using Garfield++, the ANSYS solution has generated an electric field map. Different configurations of GEM foil have been studied.

6.5.1 No segmentation

The electric field map for the non-segmented sample shows electric field lines from readout to drift with high intensity in the holes. This is an expected normal field map for a normal single-GEM detector.

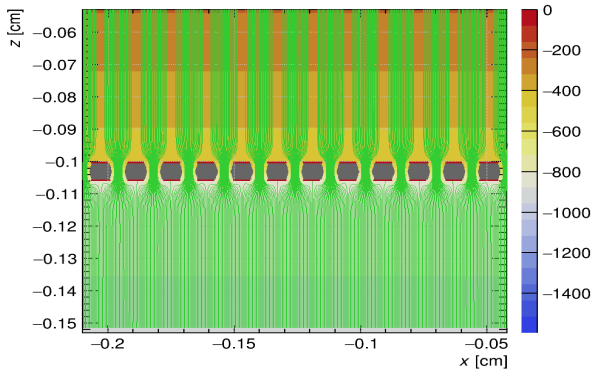

Figure 6.15: A zoomed electric field map for single GEM detector with a GEM foil having no segmentation.

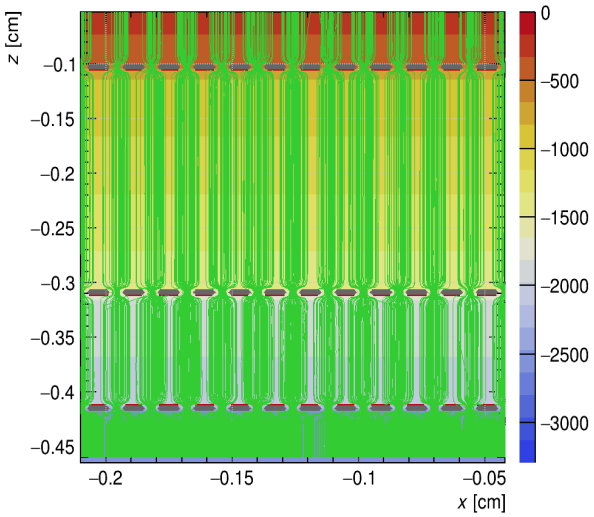

Figure 6.16: A zoomed electric field map for single GEM detector with a GEM foil having no segmentation.

6.5.2 Double segmentation

6.5.2.1 Blank Segmentation

The electric field map of the double-segmented sample illustrates intense electric field lines extending from the readout to the drift region, particularly concentrated in the holes away from the segmented area. Conversely, the field lines converge towards the exposed Kapton within the segmented region. The influence of segmentation at two distinct angles (0° and 20°) can be anticipated through the consideration of T_e and G_{eff}.

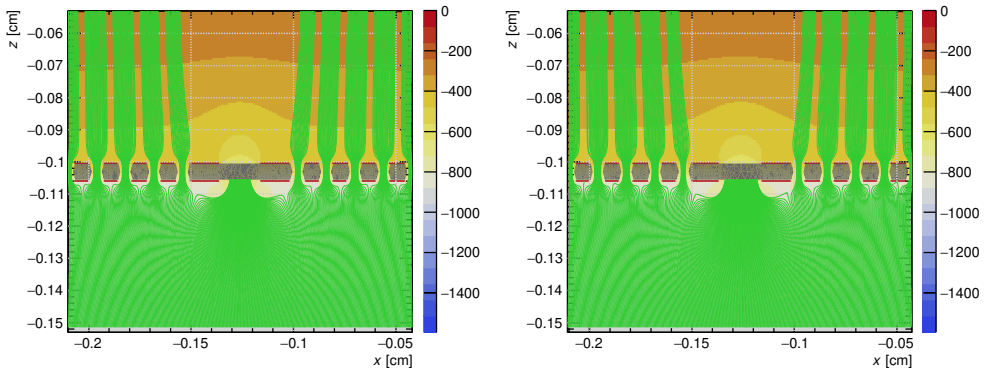

Figure 6.17: Left: A electric field map for single GEM detector with a GEM foil having double segmentation of blank type by removing a copper strip of width 200 μm from both sides at 0°. Right: For segmentation at 20°.

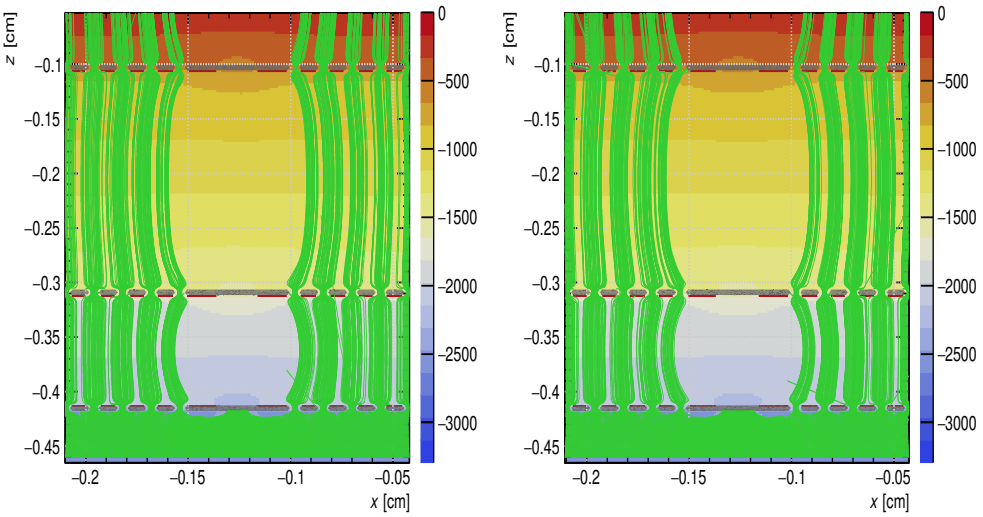

Figure 6.18: Left: A electric field map for triple GEM detector with a GEM foil having double segmentation of blank type by removing a copper strip of width 200μm from both sides at 0°. Right: For segmentation at 20°

6.5.2.2 Random Segementation

The electric field map for the double-segmented sample with holes grooved in the segmented area shows electric field lines from readout to drift with high intensity in the holes away from the segmented area, but field lines converge towards the exposed kapton of the segmented area. Some of the converged field lines pass through the holes grooved in the segmented area.

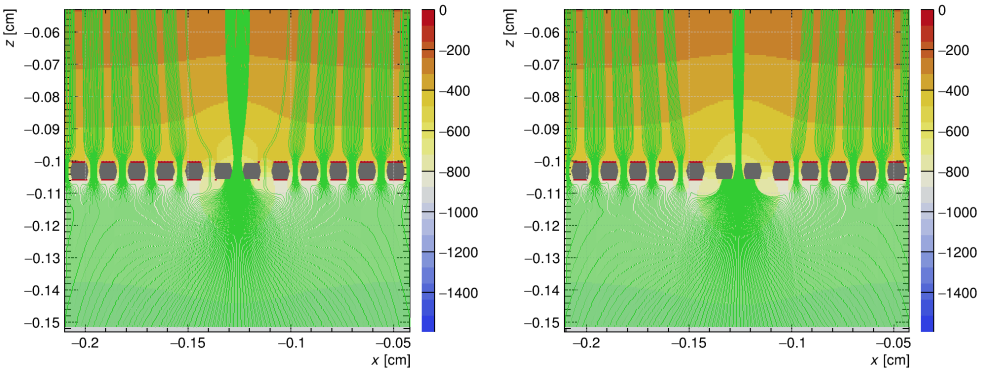

Figure 6.19: Left: A electric field map for single GEM detector with a GEM foil having double segmentation of random electrode type by removing a copper strip of width 200μm from both sides at 0°. Right: For segmentation at 20°

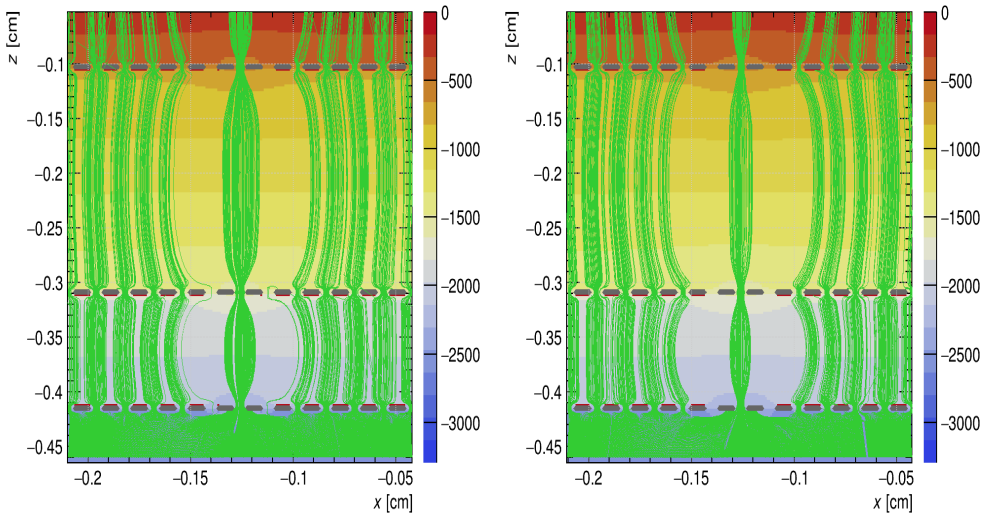

Figure 6.20: Left: A electric field map for triple GEM detector with a GEM foil having double segmentation of random electrode type by removing a copper strip of width 200μm from both sides at 0°. Right: For segmentation at 20°

6.5.3 Single Segmentation

6.5.3.1 On Drift Side

6.5.3.1.1 Blank Segmentation

The electric field map for the drift side single-segmented samples for the blank segmented foil shows electric field lines from readout to drift with high intensity in the holes away from the segmented area, but no fieldlines in the segmented area. The results for the single-GEM and triple-GEM for both the cases (0° and 20°) are shown in Figure 6.21 and 6.22 respectively.

6.5.3.1.2 Random Segmentation

The electric field map for the drift side single-segmented samples for the random segmented foil shows electric field lines from readout to drift with high intensity in the holes away from the segmented area, but few fieldlines passes through the GEM foil(s) in the segmented area. The results for the single-GEM and triple-GEM for both the cases (0° and 20°) are shown in Figure 6.23 and 6.24 respectively.

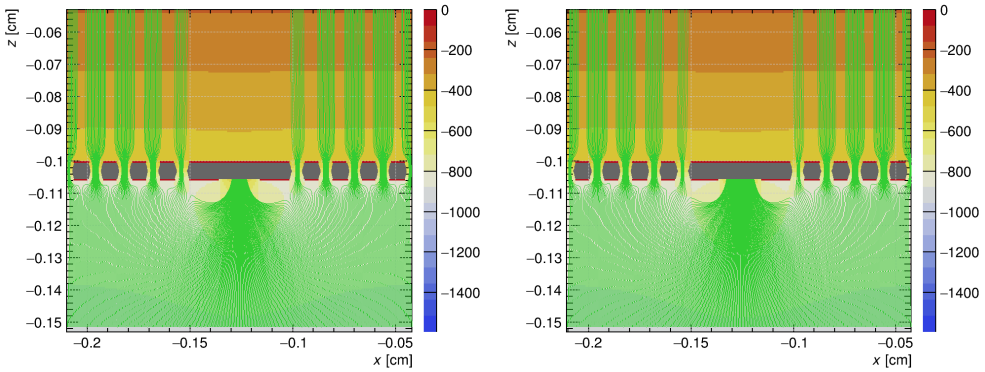

Figure 6.21: Left: A electric field map for single GEM detector with a GEM foil having single segmentation on drift side of blank type by removing a copper strip of width 200 µm from both sides at 0°. Right: For segmentation at 20°.

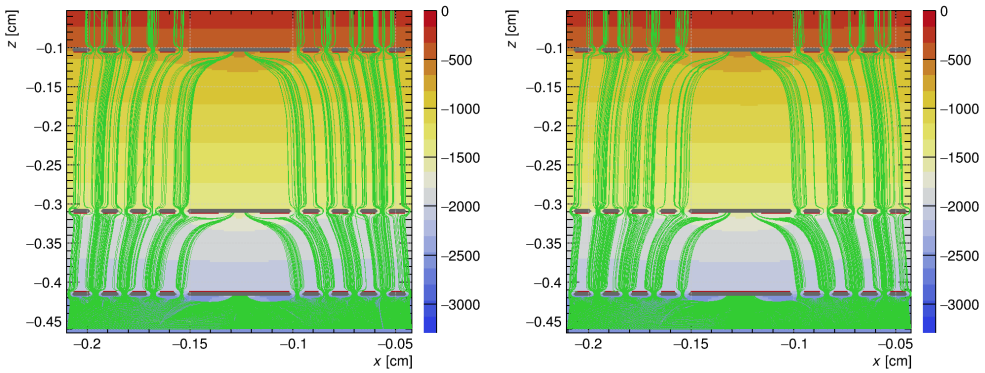

Figure 6.22: Left: A electric field map for triple GEM detector with a GEM foil having single segmentation on drift side of blank type by removing a copper strip of width 200 µm from both sides at 0°. Right: For segmentation at 20°.

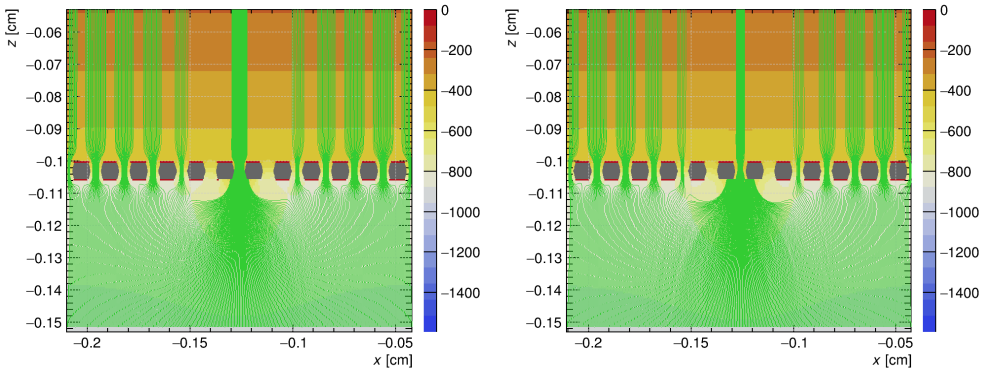

Figure 6.23: Left: A electric field map for single GEM detector with a GEM foil having single segmentation on drift side of random electrode type by removing a copper strip of width 200 µm from both sides at 0°. Right: For segmentation at 20°.

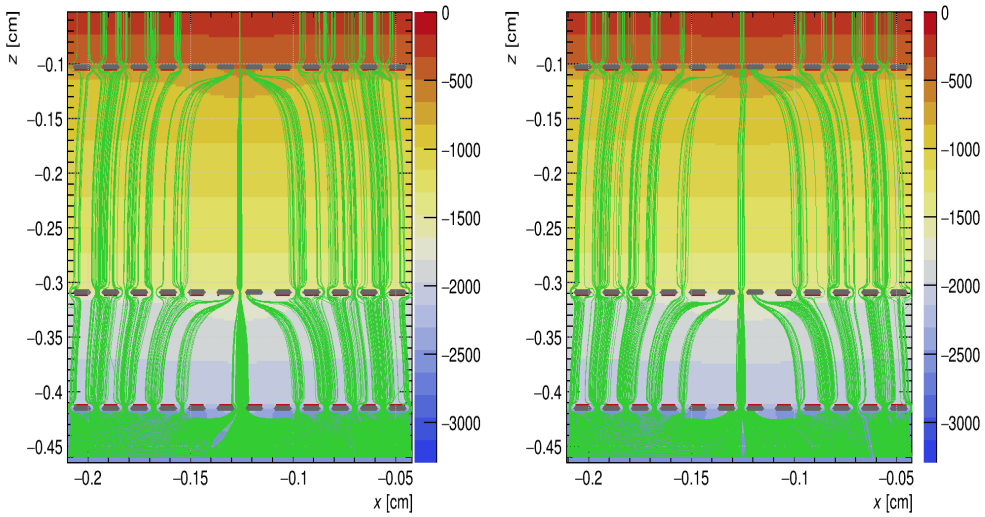

Figure 6.24: Left: A electric field map for triple GEM detector with a GEM foil having single segmentation on drift side of random electrode type by removing a copper strip of width 200 µm from both sides at 0°. Right: For segmentation at 20°.

6.5.3.2 On Readout Side

6.5.3.2.1 Blank Segmentation

The electric field map for the readout side single-segmented samples for the blank segmented foil shows electric field lines from readout to drift with high intensity in the holes away from the segmented area, but no fieldlines in the segmented area. The results for the single-GEM and triple-GEM for both the cases (0° and 20°) are shown in Figure 6.25 and 6.26 respectively.

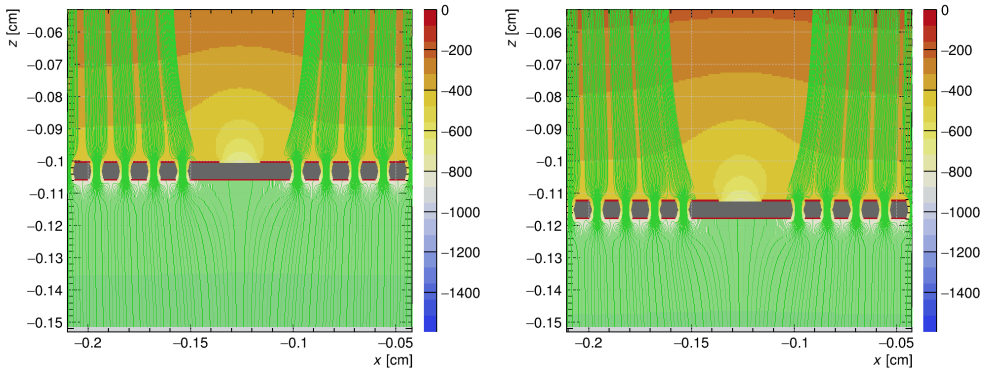

Figure 6.25: Left: A electric field map for single GEM detector with a GEM foil having single segmentation on readout side of blank type by removing a copper strip of width 200 µm from both sides at 0°. Right: For segmentation at 20°.

The dead region became increased in the case of triple-GEM detector.

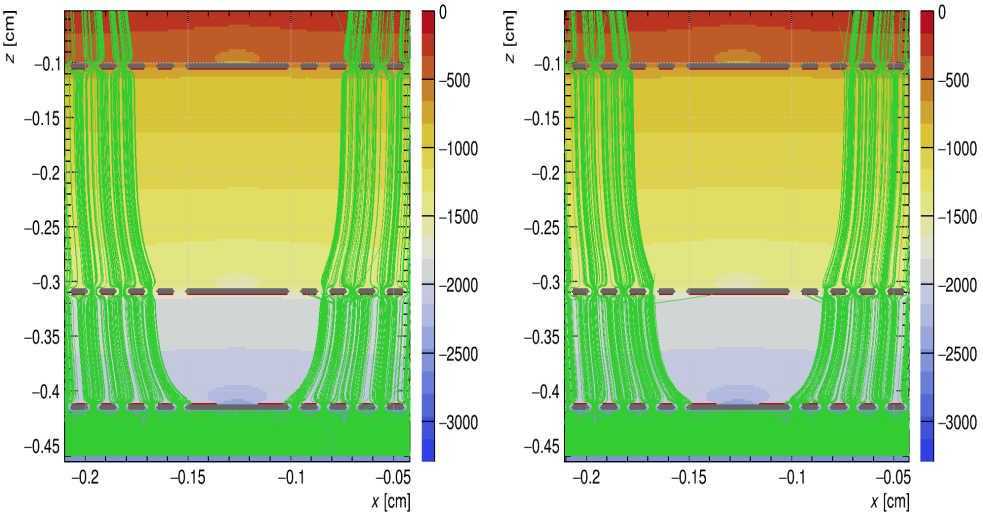

Figure 6.26: Left: A electric field map for triple GEM detector with a GEM foil having single segmentation on readout side of blank type by removing a copper strip of width 200 μm from both sides at 0°. Right: For segmentation at 20°.

6.5.3.2.2 Random Segmentation

The electric field map for the readout side single-segmented samples for the random segmented foil segmented shows electric field lines from readout to drift with high intensity in the holes away from the segmented area, but few fieldlines pass through the holes grooved in the segmented area and reach to drift plane. the results for the single-GEM and triple-GEM for both the cases (0° and 20°) are shown in Figure 6.27 and 6.28 respectively.

6.6 Electron Transparency

6.6.1 Collection and Extraction Efficiency

Before we can analyze the factors that influence gas gain, we must first define the sort of gain that we are interested in. That is, in most circumstances, we assess the G_{eff} rather than the genuine, intrinsic gas gain (G_{int}). This is an important distinction since the G_{eff}, defined as the ratio of the detected charge to the main ionization charge, is

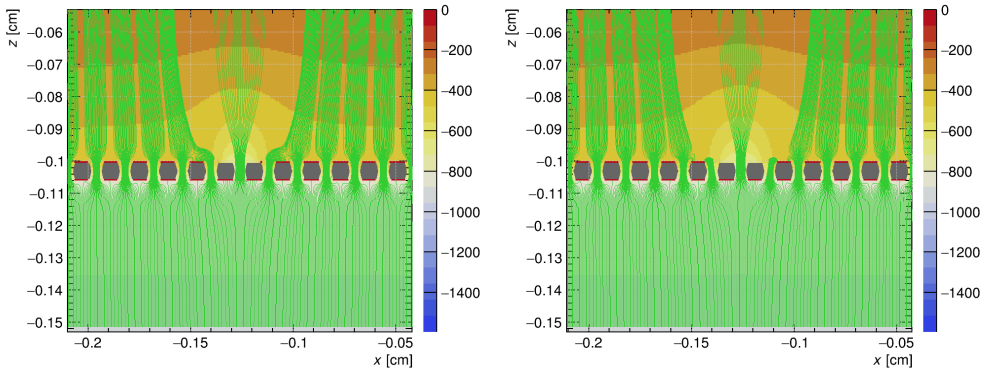

Figure 6.27: Left: A electric field map for single GEM detector with a GEM foil having single segmentation on readout side of random electrode type by removing a copper strip of width 200 µm from both sides at 0°. Right: For segmentation at 20°.

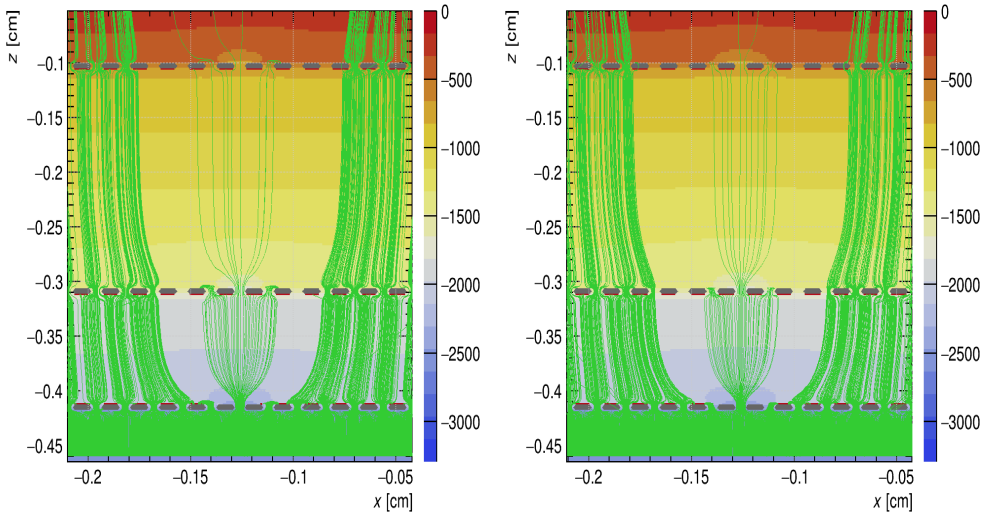

Figure 6.28: Left: A electric field map for triple GEM detector with a GEM foil having single segmentation on readout side of random electrode type by removing a copper strip of width 200 µm from both sides at 0°. Right: For segmentation at 20°.

often smaller than the amplification stage's true gas gain. To investigate the causes for this, we must first specify various parameters.

First, in Equation 6.2, we define ϵ_{coll} as the ratio of the number of primary electrons created above the GEM foil to the number of electrons that actually enter a GEM foil hole:

$$\epsilon_{coll}(\epsilon_{coll}) = \frac{\text{electrons collected in the holes}}{\text{electrons produced above the holes}} \tag{6.2}$$

If the electric field lines are not adequately focussed into the GEM foil holes, or if electron diffusion above the foils is inadequate, the ϵ_{coll} will be lowered [23]. Because of this, some of the primary electrons are caught on the top GEM foil electrode or enter the hole but strike the polyimide surface between the two electrodes and are collected there rather than multiplying in and passing through the hole. These effects correspond to a 20 % and 5 % loss in gain, respectively, for an $Ar/CO_2/CF_4$ (45/15/40) gas combination [24].

Furthermore, extra losses can occur prior to multiplication in electronegative gas mixtures due to recombination. In the case of an $Ar/CO_2/CF_4$ (45/15/40) gas mixture, the strong electric field around the hole (~ 10 kV/cm) might result in the recombination of the primary electron due to the high electron attachment compared to the initial Townsend coefficient. This recombination process adds a 10% loss in gain to the two previously stated effects, resulting in a total collecting efficiency of 65% [25].

The ϵ_{ext}, given in Equation 6.3 as the ratio between the number of electrons created within the holes during the multiplication stage and the number of electrons retrieved from the holes, is the second metric we may define.

$$\epsilon_{ext}(\epsilon_{ext}) = \frac{\text{electrons extracted from the holes}}{\text{electrons produced inside the holes}} \tag{6.3}$$

Again, diffusion contributes to the loss of efficiency in this scenario. Because of diffusion, the multiplication electrons are not localized to the center of the GEM foil hole. As a result, in circumstances when the electric field below the GEM foil is relatively low, some of these electrons may be caught on the foil's bottom electrode rather than being transmitted to the anode or the next GEM foil. In simulation study [26], given an induction field of 5 kV $\cdot$ cm^{-1}, 3% of electrons are retained at the top of the hole owing to diffusion, 10% are ion caught within close proximity of the bottom of the hole, and 50% of the remaining electrons are lost to the lower GEM foil electrode, resulting in a 35% ϵ_{ext}.

$$G_{eff} = \frac{\text{electrons extracted from the holes}}{\text{electrons produced inside the holes}} \tag{6.4}$$

6.6.2 Transparency of GEM Foil

The T_e of a GEM foil can be defined as the fraction of generated electrons that reach the readout plane. This can be calculated using the ϵ_{coll} and ϵ_{ext}. However, not all electrons produced during the avalanche formation reach the holes of the GEM foil. Some electrons get attached to the copper layer of the GEM and the Kapton part in the hole. Therefore, the overall number of charges reaching the readout plane is an important parameter for predicting the gain of a GEM detector.

$$T_e = \prod_n \epsilon_{coll}^n \times \epsilon_{ext}^n \tag{6.5}$$

Here n is the number of GEM foil used in the GEM detector i.e. for single GEM detector n = 1, for triple GEM detector n = 3.

ϵ_{coll}, ϵ_{ext}, T_e, G_{int} and G_{eff} for all the cases are listed in Appendix D.

6.7 Muon Detection Efficiency

To find an efficient segmentation method, one needs to calculate the muon detection efficiency for the different configurations of the GEM detector. As we discussed in Section 6.4.2.2, 5000 muons were generated at the base of the drift region for the muon detection effieciency. The idea of the selection of the generation point is that experimentally the muon will come from outside the detector and will/may traverse the whole depth of the sensitive volume of the detector. The energy of the muons were fixed at 80 GeV and we used two momentum direction; one with angle 0° and another with angle 10° w.r.t. perpendicular to the surface of the detector. The selection of these two angles for the simulation is to acomodate the effect of muons coming from oblique directions. The VFAT threshold used for simulation results is 0.1 fC. The reason for choosing this value is to make selection cuts in accordance with the test beam conditions. Due to electronic noise (below 0.3 fC), a VFAT threshold of 0.4 fC was used for the data [27]. We have not added any noise during the simualation, so we used a VFAT threshold of 0.1 fC for the comparison to the test beam results. For another specific case, we can use a higher value depending on the case study.

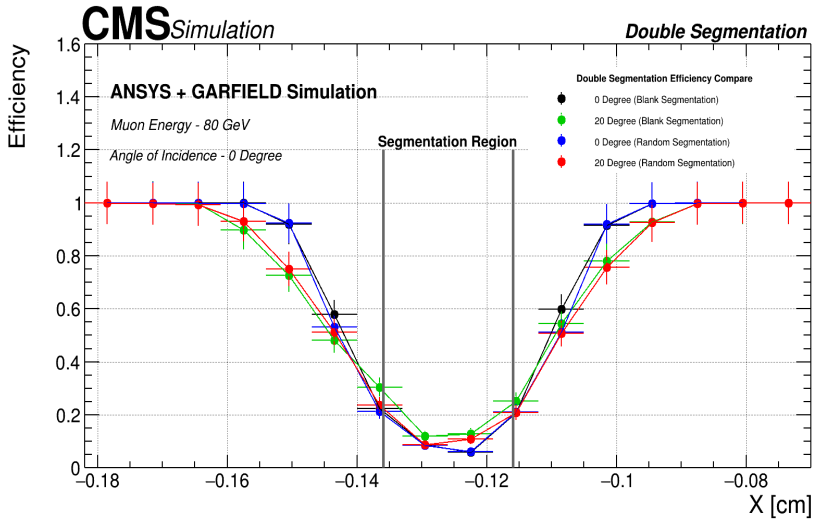

Figure 6.29: A comparison muon detection efficiency for a triple-GEM comprising double segmented GEM foils. All the cases for blank and random segmentation are shown here. These results are for the angle of incidence 0° for all the cases.

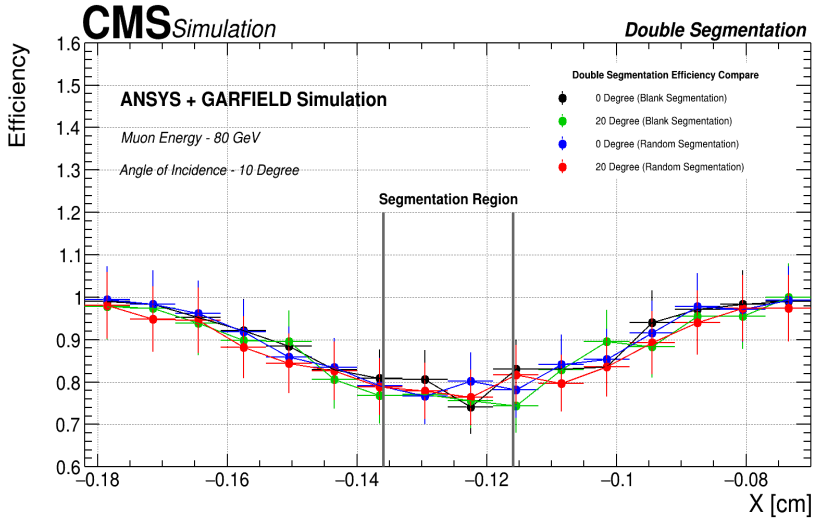

Figure 6.30: A comparison muon detection efficiency for a triple-GEM comprising double segmented GEM foils. All the cases for blank and random segmentation are shown here. These results are for the angle of incidence 10° for all the cases.

6.8 Conclusion

In this chapter, we examined the Test-beam results of ME0 prototype detector and predicted the results using ANSYS and Garfield++ simulations to enhance our understanding of the GEM foil segmentation. The T_e and muon detection efficiency for blank and random electrode segmented foils were studied using the ANSYS and Garfield

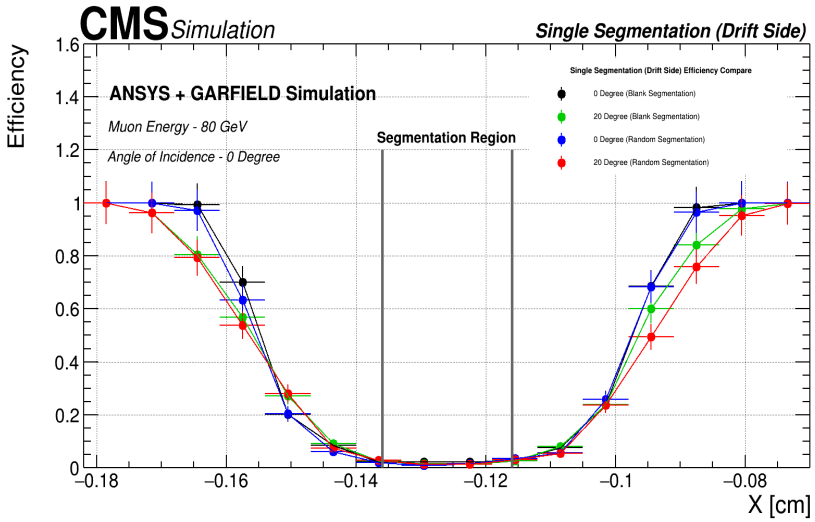

Figure 6.31: A comparison muon detection efficiency for a triple-GEM comprising drift side single segmented GEM foils. All the cases for blank and random segmentation are shown here. These results are for the angle of incidence 0° for all the cases.

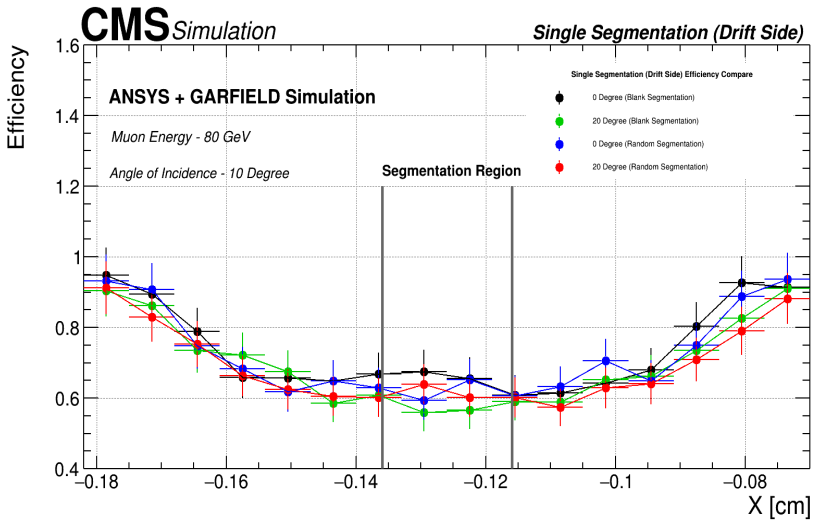

Figure 6.32: A comparison muon detection efficiency for a triple-GEM comprising drift side single segmented GEM foils. All the cases for blank and random segmentation are shown here. These results are for the angle of incidence 10° for all the cases.

simulation. The muon detection effeciency for both the cases reflects the same trend showed by the Test Beam results. There is a drop in the efficiency in the segmented region, but the width of the region get improved in the randon electrode segmentation method. The losses in muon detection efficiency at different angles shown in Figure 6.5 are comparable to the results shown in the previous section.

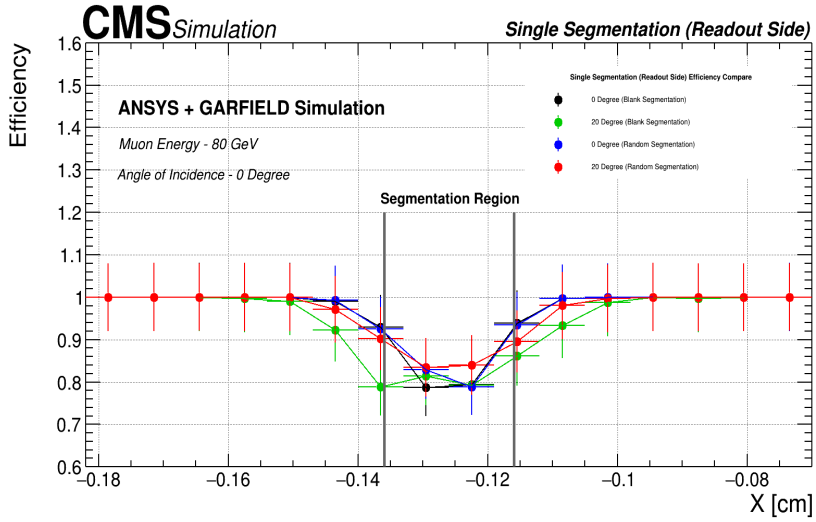

Figure 6.33: A comparison muon detection efficiency for a triple-GEM comprising readout side single segmented GEM foils. All the cases for blank and random segmentation are shown here. These results are for the angle of incidence 0° for all the cases.

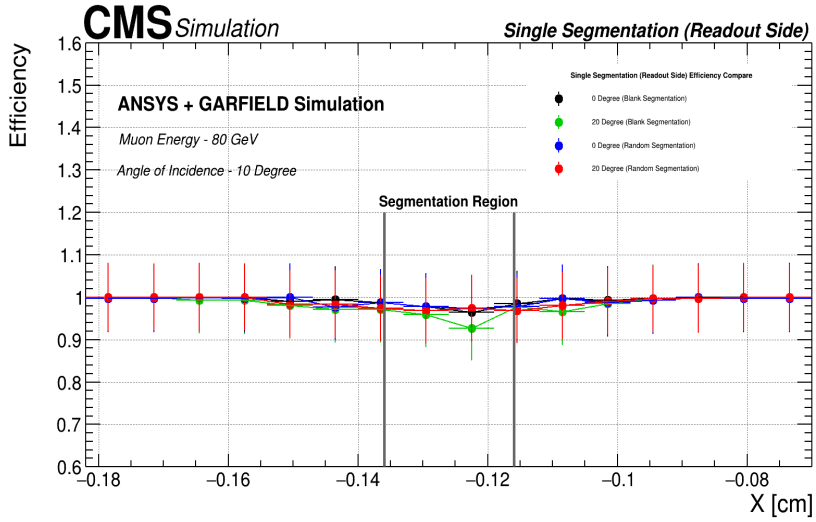

Figure 6.34: A comparison muon detection efficiency for a triple-GEM comprising readout side single segmented GEM foils. All the cases for blank and random segmentation are shown here. These results are for the angle of incidence 10° for all the cases.

Bibliography

[1] M. A. Akl et al. "CMS Technical Design Report for the Muon Endcap GEM Upgrade". In: (June 2015). Ed. by A. Colaleo et al.

[2] S. Bachmann et al. "Discharge mechanisms and their prevention in the gas electron multiplier (GEM)". In: *Nucl. Instrum. Meth. A* 479 (2002), pp. 294–308. DOI: 10.1016/S0168-9002(01)00931-7.

[3] D. Abbaneo et al. "GEM based detector for future upgrade of the CMS forward muon system". In: *Nucl. Instrum. Meth. A* 718 (2013). Ed. by Franco Cervelli et al., pp. 383–386. DOI: 10.1016/j.nima.2012.10.058.

[4] A Colaleo et al. *CMS Technical Design Report for the Muon Endcap GEM Upgrade*. Tech. rep. 2015. URL: https://cds.cern.ch/record/2021453.

[5] Oleg M. Kouznetsov. "The COMPASS experiment at CERN". In: *18th International Seminar on High Energy Physics*. Oct. 2014.

[6] C. Altunbas et al. "Construction, test and commissioning of the triple-GEM tracking detector for COMPASS". In: *Nucl. Instrum. Meth. A* 490 (2002), pp. 177–203. DOI: 10.1016/S0168-9002(02)00910-5.

[7] Michele Bianco et al. *Rate capability of large-area triple-GEM detectors and new foil design for the innermost station, ME0, of the CMS endcap muon system*. Tech. rep. Geneva: CERN, 2021. DOI: 10.1109/NSS/MIC44867.2021.9875626. arXiv: 2201.09021. URL: https://cds.cern.ch/record/2797720.

[8] M. Bianco et al. "High rate capability studies of triple-GEM detectors for the ME0 upgrade of the CMS Muon Spectrometer". In: *J. Phys. Conf. Ser.* 2374.1 (2022), p. 012141. DOI: 10.1088/1742-6596/2374/1/012141.

[9] A. P. Marques et al. "Minimizing distortions with sectored GEM electrodes". In: *Nucl. Instrum. Meth. A* 961 (2020), p. 163673. DOI: 10.1016/j.nima.2020.163673.

[10] Marcus Ziegler. "Development of a triple GEM detector for the LHCb experiment". PhD thesis. Zurich U., 2002.

[11] Antonello Pellecchia et al. "Production and characterization of random electrode sectorization in GEM foils". In: *JINST* 18.07 (2023), p. C07001. DOI: 10.1088/1748-0221/18/07/C07001. arXiv: 2303.06355 [physics.ins-det].

[12] ANSYS. *ANSYS Fluent - CFD Software | ANSYS*. 2016. URL: http://www.ansys.com/products/fluids/ansys-fluent.

[13] H. Schindler. "Garfield++: status and plans". In: VCI2022 - Vienna Conference on Instrumentalisation. INSTRUMENTATION RELATED TO NUCLEAR SCIENCE AND TECHNOLOGY. Austria, 2022, p. v. URL: http://inis.iaea.org/search/search.aspx?orig_q=RN:53124958.

[14] COMSOL Multiphysics. "Introduction to COMSOL multiphysics®". In: *COMSOL Multiphysics, Burlington, MA, accessed Feb* 9 (1998), p. 2018.

[15] N. Majumdar, S. Mukhopadhyay, and S. Bhattacharya. "Computation of 3D electrostatic weighting field in Resistive Plate Chambers". In: *Nuclear Instruments and Methods in Physics Research Section A: Accelerators, Spectrometers, Detectors and Associated Equipment* 595.2 (2008), pp. 346–352. ISSN: 0168-9002. DOI: https://doi.org/10.1016/j.nima.2008.07.033. URL: https://www.sciencedirect.com/science/article/pii/S0168900208010139.

[16] I. B. Smirnov. "Modeling of ionization produced by fast charged particles in gases". In: *Nucl. Instrum. Meth. A* 554 (2005), pp. 474–493. DOI: 10.1016/j.nima.2005.08.064.

[17] S. F. Biagi. "Monte Carlo simulation of electron drift and diffusion in counting gases under the influence of electric and magnetic fields". In: *Nucl. Instrum. Meth. A* 421.1-2 (1999), pp. 234–240. DOI: 10.1016/S0168-9002(98)01233-9.

[18] A. Karadzhinova et al. "Impact of GEM foil hole geometry on GEM detector gain". In: *JINST* 10.12 (2015), P12014. DOI: 10.1088/1748-0221/10/12/P12014.

[19] Antonio Bianchi. "Characterization of gaseous detectors at the CERN Gamma Irradiation Facility: GEM performance in presence of high background radiation". MA thesis. Turin, INFN, Oct. 2016.

[20] Rene Brun et al. *root-project/root: v6.18/02*. Version v6-18-02. June 2020. DOI: 10.5281/zenodo.3895860. URL: https://doi.org/10.5281/zenodo.3895860.

[21] J. Apostolakis et al. "An implementation of ionisation energy loss in very thin absorbers for the GEANT4 simulation package". In: *Nucl. Instrum. Meth. A* 453 (2000), pp. 597–605. DOI: 10.1016/S0168-9002(00)00457-5.

[22] Thierry Maerschalk. "Study of Triple-GEM detector for the upgrade of the CMS muon spectrometer at LHC". PhD thesis. U. Brussels, Brussels U., 2016.

[23] C. Richter et al. "On the efficient electron transfer through GEM". In: *Nucl. Instrum. Meth. A* 478 (2002), pp. 538–558. DOI: 10.1016/S0168-9002(01)00896-8.

[24] Francesco Fallavollita. "Triple-Gas Electron Multiplier technology for future upgrades of the CMS experiment: construction and certification of the CMS GE1/1 detector and longevity studies". Presented 18 Jan 2019. PhD thesis. Pavia U., 2018. URL: https://cds.cern.ch/record/2658126.

[25] Davide Pinci. "A triple-GEM detector for the muon system of the LHCb experiment". PhD thesis. Cagliari U., 2006.

[26] W. Bonivento et al. "A complete simulation of a triple-GEM detector". In: *IEEE Trans. Nucl. Sci.* 49 (2002). Ed. by J. D. Valentine, pp. 1638–1643. DOI: 10.1109/TNS.2002.805170.

[27] Antonello Pellecchia, Piet Verwilligen, and Anna Stamerra. "Performance of triple-GEM detectors for the CMS Phase-2 upgrade measured in test beam". In: *Nucl. Instrum. Meth. A* 1046 (2023), p. 167618. DOI: 10.1016/j.nima.2022.167618. arXiv: 2207.09906 [physics.ins-det].

Chapter 7

Application of GEM in Medical Imaging

"An equation for me has no meaning, unless it expresses a thought of God."
— S I Ramanujan, 1887–1920

7.1 Introduction

Medical imaging is the field in which radiation is used for qualitative or quantitative imaging of the diseased organ/body of the patient for diagnostics and treatment procedures. For this purpose, many such systems have been developed to serve the man kind. X-Ray radiography, Computed Tomography (CT), Ultrasonography (USG), Magnetic Resonance Imaging (MRI), Nuclear Medicine Imaging and Positron Emission Tomography (PET) are some techniques used in medical imaging. PET is widely used for the staging, restaging, drug, and therapy response of the patients diagnosed with cancer. PET enables us to obtain morphological imaging of the biodistribution of positron-emitting radionuclides or radiopharmaceuticals injected into the patient's body [1].

In this chapter, we discuss the application of GEM detectors in medical imaging. GEM detctors can be used for the low-energy X-ray imaging. In this study, we are seeking the use for PET imaging. In Section 7.2, we will give an overview of

PET detection technique and in Section 7.3, we will discuss the physics of positron annihilation.

Compton scattering is sensitive to both circular and linear polarization. Notably, in the case of linear polarization measurements, a polarized target is not obligatory, as required in circular polarization measurements. The study utilizes GEANT4 Monte Carlo simulations to model a source-detector system. Employing a dual-head Compton detector model, the investigation capitalizes on the angular correlation of Compton-scattered 511 keV photon pairs.

7.2 PET Detection Technique

In PET, a positron-emitting radiopharmaceutical is administered to the patient's organ through various means, such as inhalation or IV injection. The radiopharmaceutical is prepared by combining a positron-emitting radionuclide, such as ^{18}F or ^{15}O, with a pharmaceutical compound, typically a chelating agent specific to the target organ. The radiopharmaceutical is taken up more by the tissues of the target organ[1] compared to normal tissues, producing a suitable signal-to-noise ratio for imaging. The positrons emitted by these radionuclides in the target organ annihilate with electrons of biomolecules, producing pairs of counter-propagating 511 keV photons.

The PET detection method uses a coincidence detection technique to correlate two annihilation photons resulting from positron-electron annihilation. This is captured by a scintillation-based detection system arranged in a ring configuration. To refine the raw data, an energy acceptance criterion [2] and time-of-flight information [3] are applied. This process reduces false coincidences and improves the signal-to-noise ratio. Discrimination of true coincidence events from false scatter, random, and multiple events is critical, as false coincidences can introduce noise and result in contrast loss in the generated images [4].

In addition to these parameters, the polarization correlation between the two annihilation photons is a noteworthy factor. These photons, in a Quantum Entangled (QE) state [5] exhibit linear polarization with orthogonal orientations. This polarization correlation can serve as a discriminatory tool for authenticating true annihilation

[1] A specific organ or tissue within the body that is the focus of the imaging study

coincidences in PET. Estimating linear polarization is achieved through Compton scattering using the Klein-Nishina formula [6].

7.3 Physics

7.3.1 Mechanisms of Positronium Formation

Positronium is a unique atom formed by an electron and a positron. Positrons are generated, for instance, during the decay of radioactive nuclei. As they traverse through matter, they initially lose energy by interacting with electrons in the surrounding atoms. Once thermalized, positrons can either directly annihilate with electrons in the medium or form a bound state known as positronium (e^+e^-). Positronium has two lowest bound states: Para-positronium and Ortho-positronium, depending on the relative orientation of the spins of the electron and positron in the system:

- Para-positronium has anti-parallel spins (e^+ and e^-), resulting in a singlet state with total spin 0 ($^1S_0$).
- Ortho-positronium has parallel spins (e^+ and e^-), leading to a bound state with total spin 1 ($^3S_1$).

This system is inherently unstable, and the electron (e^-) and positron (e^+) annihilate quickly. In the singlet state, annihilation produces a pair of photons with a lifetime (τ) of 1.24×10^{-10} seconds ($^1S_0 \rightarrow 2\gamma$).

If the system is in a triplet state, annihilation produces three photons with a τ of 1.38×10^{-7} seconds ($^3S_1 \rightarrow 3\gamma$), or it may first de-excite to the singlet state before annihilating into two photons. We will study events exclusively from the annihilation of Para-positronium.

7.3.2 The Annihilation Photons

The wave function of the e^+ and e^- in the singlet state can be written as:

$$\Psi_{e^+e^-} = \frac{1}{\sqrt{2}} \left(|\uparrow^-, \downarrow^+\rangle - |\downarrow^-, \uparrow^+\rangle \right), \tag{7.1}$$

where + and - designate positron and electron, and $\uparrow$ and $\downarrow$ denote up and down spin projections.

The endpoint energy of the positron originating from the ^{22}Na decay is 546 keV, indicating that the e^+e^- system is formed with zero momentum. Consequently, according to momentum conservation, at least two particles are emitted when this system annihilates. However, the spin of the system is zero, implying that only an even number of photons could combine in a way that their spins add up to zero. The diagram below illustrates the two possible configurations of spin and momentum for the emitted photons, where γ^{R} and γ^{L} denote right and left circularly polarized photons, respectively.

$$\xleftarrow{\gamma_1^R \Longleftarrow} \xrightarrow{\gamma_2^R \Longrightarrow} \qquad \xleftarrow{\gamma_1^L \Longrightarrow} \xrightarrow{\gamma_2^L \Longleftarrow} \tag{7.2}$$

There are two wave functions that correctly describe the two-photon state:

$$\Psi_{\pm} = \frac{1}{\sqrt{2}}\left(\gamma_1^R\gamma_2^R \pm \gamma_1^L\gamma_2^L\right) \tag{7.3}$$

The parity invariance of the electromagnetic interaction imposes additional constraints on these wave functions. Parity transformation affects the initial state, and the fermion-antifermion parity is determined by $(-1)^{L+1}$.

$$\mathrm{P}|\Psi_{\mathrm{e^+e^-}}\rangle = -|\Psi_{\mathrm{e^+e^-}}\rangle \tag{7.4}$$

So, the final state, namely the two-photon state, should exhibit the same change under parity. Of the two possible wave functions Ψ_- and Ψ_+, only the first has an eigenvalue -1.

$$\mathrm{P}|\Psi_-\rangle = -|\Psi_-\rangle \tag{7.5}$$

This function represents two photons with planes of polarization perpendicular to each other. The energy of the photons is 511 keV since the positronium is at rest when the e^+ and e^- annihilate.

7.3.3 Compton Scattering

In Compton scattering, a photon undergoes a collision with an electron, experiencing a loss of energy and subsequently being deflected from its initial direction of travel as depicted in Figure 7.1. The fundamental theory governing this phenomenon, assuming the electron is initially free and at rest, is provided by the Klein-Nishina formula. The

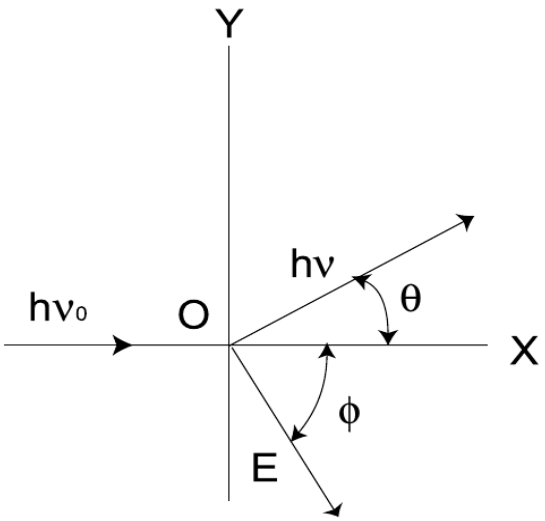

Figure 7.1: Compton scattering with a free electron at rest

relationship between photon deflection and energy loss in Compton scattering is established through the conservation of momentum and energy between the photon and the recoiling electron. This relationship is expressed as:

$$
\begin{aligned}
E' &= \frac{E}{1+\frac{E}{m_e c^2}\left(1-\cos(\theta)\right)} \\
E_{recoil} &= m_e c^2 \frac{2E^2\cos(\phi)^2}{(E+m_e c^2)^2 - E^2\cos(\phi)^2} \\
\tan(\phi) &= \frac{1}{1+\frac{E}{m_e c^2}}\cot\left(\frac{\theta}{2}\right)
\end{aligned}
\tag{7.6}
$$

Here, E represents the energy of the incident photon, E' is the energy of the scattered photon, E_{recoil} is the energy of the recoiling electron, m_e is the rest mass of an electron, and c is the speed of light. The angles θ and ϕ characterize the scattering process.

This mathematical representation provides a comprehensive understanding of the energy and angular distributions involved in Compton scattering, essential for

interpreting experimental results and predicting the behavior of photons interacting with matter.

7.3.4 Compton Scattering Cross-Section

Using the framework of QED, Klein and Nishina derived [6] a formula describing the probability of finding a photon scattered off an electron in a particular direction:

$$\frac{d\sigma(E,\theta,\eta)}{d\Omega} = \frac{r_0^2}{2}\left(\frac{E'}{E}\right)^2\left(\frac{E}{E'}+\frac{E'}{E}-2\sin^2\theta\cos^2\eta\right) \tag{7.7}$$

Here, r_0 denotes the classical electron radius, E is the energy of the incident photon, E′ is the energy of the scattered photon, θ is the angle between the initial photon momentum and the scattered photon momentum, and η is the angle between the plane of scattering and the plane of polarization of the initial photon.

Examining the equation reveals that for a given value of θ, the scattering cross-section achieves a maximum when the photon is scattered at 90° with respect to its initial electric field polarization vector. This observation implies that by identifying a photon in a given direction, its initial polarization can be determined.

The energy E′ of the scattered photon is related to its initial energy E and the scattering angle θ by rearranging the Equation 7.6:

$$E' = E\frac{m_e}{m_e + E[1-\cos\theta]} \tag{7.8}$$

Considering the experiment where the energy of the photon equals the rest mass of the electron, the ratio E'/E simplifies to:

$$\frac{E'}{E} = \frac{m_e}{m_e + E[1-\cos\theta]} = \frac{1}{2-\cos\theta} \tag{7.9}$$

To simplify calculations, the variable $\epsilon = E'/E$ is introduced. Consequently, the differential cross-section is expressed as:

$$\frac{d\sigma(E,\theta,\eta)}{d\Omega} = \frac{r_0^2}{2}\epsilon^2\left[\epsilon+\frac{1}{\epsilon}-\sin^2\theta[1+\cos^2\eta]\right] \tag{7.10}$$

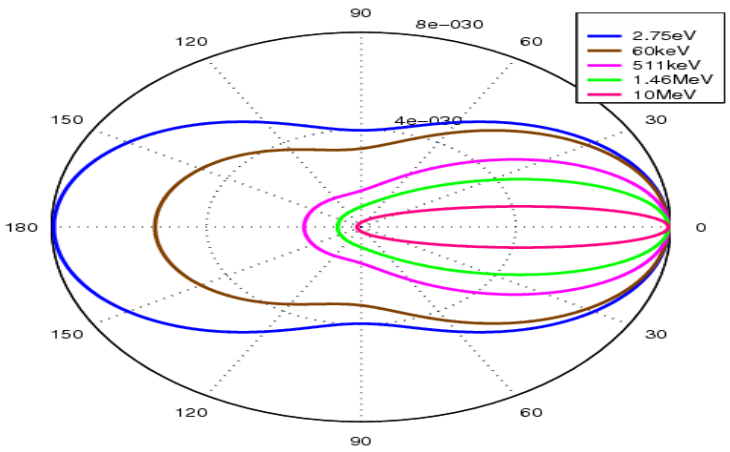

Figure 7.2: Klein-Nishina cross section for different energies.

Upon averaging over initial states and summing over final states, the differential cross-section for Compton scattering of non-polarized photons is obtained:

$$\left(\frac{d\sigma(E,\theta,\eta)}{d\Omega}\right)_{NP} = \frac{r_0^2}{2}\epsilon^2\left[\epsilon + \frac{1}{\epsilon} - \sin^2\theta\right] \tag{7.11}$$

Combining Equation 7.10 and 7.11:

$$\frac{d\sigma(E,\theta,\eta)}{d\Omega} = \left(\frac{d\sigma(E,\theta,\eta)}{d\Omega}\right)_{NP}[1 - \zeta(\theta)\cos 2\eta] \tag{7.12}$$

where

$$\zeta(\theta) = \frac{\sin^2\theta}{\epsilon + \frac{1}{\epsilon} - \sin^2\theta} \tag{7.13}$$

Notably, this function reaches its maximum value when $\theta = 82^\circ$ [7].

7.3.5 Probability of Finding Two Scattered Photons

We are investigating the probability, denoted as $P_{12}(E_1, E_2, \phi_1, \phi_2)$, which represents the likelihood of detecting two photons scattering simultaneously at angles θ_1, ϕ_1, θ_2, and ϕ_2. The detailed calculations for this probability can be found in references [8, 9].

In this work, we focus on presenting the final result:

$$P_{12}(E_1, E_2, \phi_1, \phi_2) = \left(\frac{d\sigma(E_1, \theta_1, \eta_1)}{d\Omega_1}\right)_{NP} \left(\frac{d\sigma(E_2, \theta_2, \eta_2)}{d\Omega_2}\right)_{NP} [1 - \zeta(\theta_1)\zeta(\theta_2)\cos 2\Delta\eta] \tag{7.14}$$

where $\Delta\eta = \eta_1 - \eta_2$. This equation is derived under the assumption that the two photons are relatively polarized at 90°. As demonstrated in the previous section, in Compton scattering, a polarized photon tends to deflect perpendicularly to its initial polarization. Therefore, observing two photons that preferentially scatter at 90° relative to each other suggests that their initial polarizations were relatively perpendicular.

If the photons are uncorrelated, meaning there is no relation between their polarizations before Compton scattering, the probability P_{12} simplifies to the product of the two non-polarized cross-sections. In this case, P_{12} does not exhibit any dependence on the relative difference of η_1 and η_2. In our current experiment, we will measure the coincidence rates of scattered photons detected by two detectors positioned at various relative angles $\Delta\eta$.

7.4 Detection Technique

Compton scattering of photons by polarized electrons exhibits sensitivity to circular photon polarization. In the case of linear photon polarization, the electrons in the scattering target may remain unpolarized. The Klein-Nishina formula provides the differential cross section for this process, and Lipps and Tolhoek [10, 11] derived a Compton cross-section explicitly dependent on the polarization states of all particles involved. The detection of linear polarization through Compton scattering arises from a term in the cross-section formula that explicitly involves the cosine squared of the angle between the polarization vector and the scattering plane.

For polarized photons, this leads to an asymmetric photon angular distribution after scattering, a characteristic extensively utilized in γ-ray polarimeters. In the case of an initially unpolarized beam of photons, the scattered photons become partially polarized. The degree of polarization, denoted as P, is given by the expression:

$$P = \frac{I_\perp - I_\parallel}{I_\perp + I_\parallel} = \frac{\sin^2\theta}{\epsilon + \frac{1}{\epsilon} - \sin^2\theta} \tag{7.15}$$

Here, $I_{\perp}$ and $I_{\parallel}$ represent the intensities of the scattered photons perpendicular and parallel to the initial photon polarization, respectively, and θ is the scattering angle. The parameter (ϵ) relates to the energy transfer in the scattering process.

7.4.1 Single Photon Polarization via Compton Scattering

The angular distributions of photons scattered on an electron are described by the Klein–Nishina differential cross-section Equation 7.7. Two crucial limits are apparent from Equation 7.7: when the scattering angle θ is close to zero or 180°, the cross-section variation with η becomes unobservable. A scattering at $\eta = 90^{\circ}$ maximizes the last term, but the energy of the outgoing photon also depends on the Compton scattering angle θ given in Equation 7.8. Consequently, the visibility, representing the interference contrast of the oscillation in η, is a function of both energy and scattering angle for the Compton scattering process.

For 511 keV photons, the optimal scattering angle θ is 82°, maximizing visibility for azimuthal angle η variation. In Figure 7.3, the cross section is shown for two scenarios: an arbitrarily chosen small angle ($\theta = 10^{\circ}$) and the optimal angle ($\theta = 81.66^{\circ}$). The Klein–Nishina formula shown in Equation 7.7 emphasizes a preference for small Compton scattering angles (θ), as depicted in Figure 7.1. Furthermore, an azimuthal asymmetry in the scattered radiation is evident, favoring scatterings around ($\eta = \pm 90^{\circ}$) over ($\eta = 0^{\circ}$) and ($\eta = 180^{\circ}$). This asymmetry can be explained physically: a polarization vector component normal to the scattering plane retains its orientation for the outgoing photon, while a component in the scattering plane undergoes a change of ($\cos\theta$) to align with the new momentum vector. Due to varying cross-section values for photons scattered under different Compton angles θ, we introduce the normalization $P(E, \theta, \eta)$ to compare the likelihoods of scattering parallel and normal to polarization. This normalization, for fixed initial energy E and Compton scattering angle θ, can be understood as the probability density distribution of the angle η:

$$P(E, \theta, \eta) = N(E, \theta) \frac{d\sigma(E, \theta, \eta)}{d\Omega} \tag{7.16}$$

where the normalization factor $N(E, \theta)$ is defined as:

$$N(E, \theta) = 1 / \int_{-\pi}^{\pi} \frac{d\sigma(E, \theta, \eta)}{d\Omega} \tag{7.17}$$

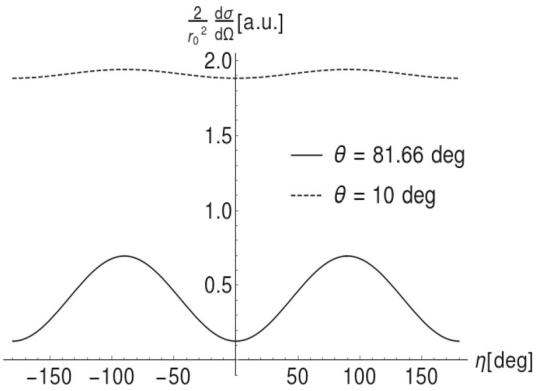

Figure 7.3: Klein–Nishina cross section plots for 511 keV photons at optimal ($\theta = 81.66^\circ$) and small ($\theta = 10^\circ$) scattering angles, as a function of (η) [12].

For $\theta \approx 81.66^\circ$, scattering probability peaks at $\eta = \pm 90^\circ$. The normalized Klein–Nishina differential cross-section, interpreted as a deviation probability, provides a practical limit for resolving the polarization direction of 511 keV photons scattered under $\theta = 81.66^\circ$ (Figure 7.3). The obtained σ values, derived from fitting a Gaussian function to positive η distributions, highlight a lack of polarization direction determinability for forward ($\theta = 0^\circ$) and backward ($\theta = 180^\circ$) Compton scattering, yielding a standard deviation close to 52°, akin to a uniform distribution [12].

7.4.2 Double Photon Polarization via Compton Scattering

The polarization correlation of annihilation photons undergoes a transformation into an angular correlation following Compton scattering, governed by the Klein–Nishina differential cross section for linearly polarized photons. The differential double cross-section for a pair of Compton-scattered annihilation photons is precisely described by Equation 7.14. When considering fixed scattering angles θ_1 and θ_2, the joint Probability Density function (PDF) reaches its maximum when $|\eta_1 - \eta_2| = 90^\circ$ which indicates that annihilation photons in orthogonal polarization states exhibit a preference for scattering in directions perpendicular to their initial polarization directions.

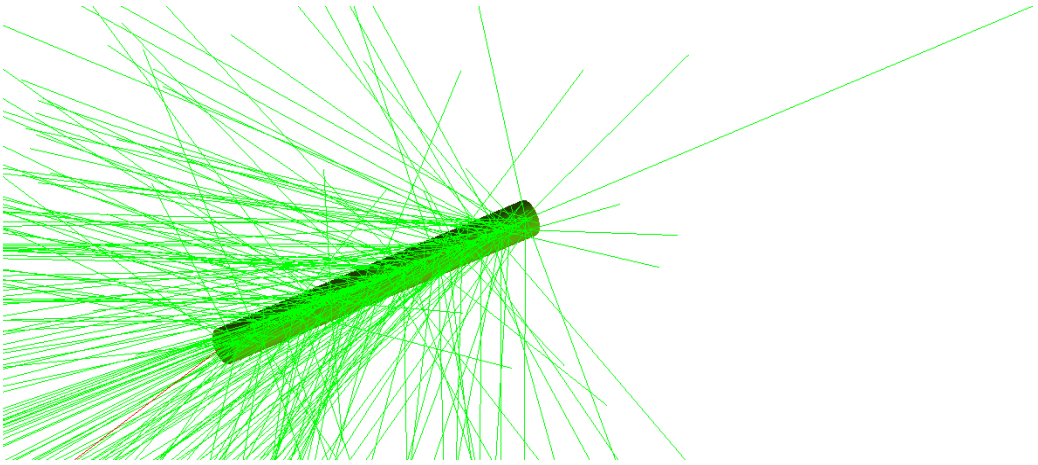

Figure 7.4: A GEANT4-constructed geometry for cross-section calculation.

7.5 Simulation

7.5.1 Cross-Section Calculation

In the process of confirming the fidelity of GEANT4 in simulating the angular correlation of scattered annihilation photons, a thorough approach is undertaken. The Klein-Nishina cross-section, a fundamental aspect of quantum physics governing Compton scattering, is computed. This calculation is performed within the confines of a simplified cylindrical volume, which serves as a representative space containing the material sensitive to Compton interactions.

The interaction dynamics are explored by determining the point where the scattered γ-ray engages with the virtual environment. To facilitate this analysis, the scattering point is strategically shifted to the center of the cylindrical volume. Following this adjustment, the position of the scattered γ ray in relation to a virtual plane detector is computed.

This methodological precision is essential for obtaining accurate insights into the behavior of scattered annihilation photons. The distributions derived from these calculations are then scrutinized to ensure their alignment with the theoretical expectations dictated by the Klein-Nishina cross-section. By systematically evaluating various scenarios, this process serves as a comprehensive validation of GEANT4's capability to accurately model the intricate angular correlation of scattered annihilation photons.

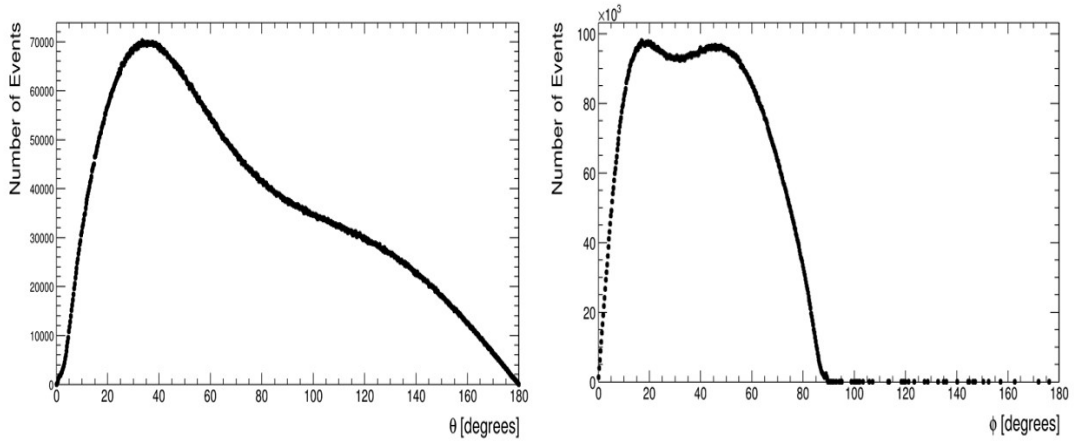

Figure 7.5: Left: Spectrum of scattering angle (θ). Right: Spectrum recoil angle ϕ.

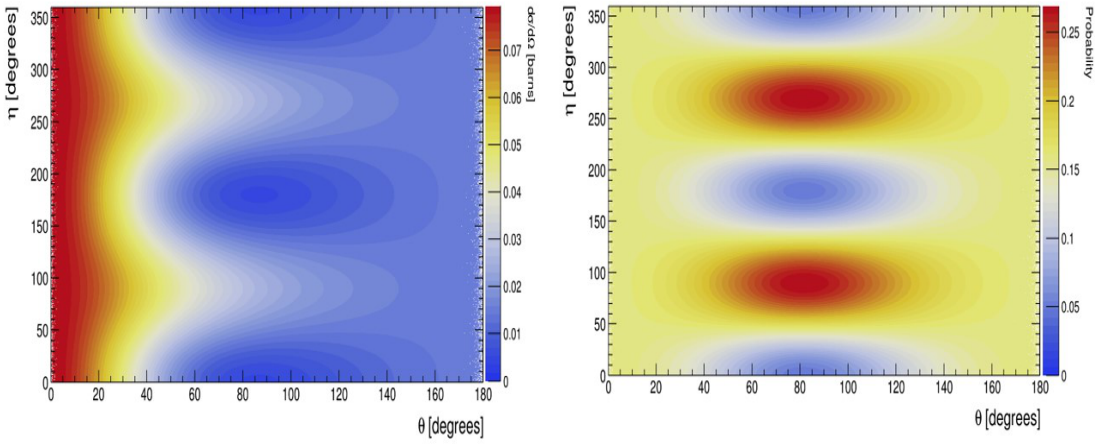

Figure 7.6: Left: A 2D plot of θ and η with a color map as the differential cross section. Right: A 2D plot of θ and η with a color map as probability.

7.5.2 Simple Dual Head PET Simulation

A detector system featuring two oppositely directed planar Compton cameras was simulated using GEANT4. Each Compton camera comprises a scatter detector (gas medium) and an absorber (scintillator) positioned in air. Gas medium used in simulation is $Xe/CO_2/C_4F_{10}$ (in percentage proportion 50, 15 and 35). The gas medium so chosen here contains Xenon, which is the highest density Noble gas and can be used for the proportional chambers. The C_4F_{10} is used as a radiator gas in Ring Imaging Cherenkov (RICH) detectors at LHCb [13], but we are using here in the gas mixture due to ots high density. The GEANT4 Low Energy Electromagnetic Physics package [14], specifically the Livermore library, was activated to incorporate key interaction processes: Compton scattering, Rayleigh scattering, photoelectric effect, and pair production for photons. Additionally, interaction processes such as ionization, multiple scattering, and bremsstrahlung were considered for secondary charged particles.

To account for the polarization effect on Compton scattering, the GEANT4 class for polarized Compton model `G4LivermorePolarizedComptonModel` was employed. The simulation of each annihilation event involved generating a pair of oppositely directed 511 keV photons from an isotropic point source. These photons possessed orthogonal linear polarization vectors relative to each other, with the linear polarization vectors randomly assigned in the transverse plane while adhering to the orthogonality constraint for each annihilation pair.

To devise and evaluate a coincidence acceptance/rejection scheme based on the azimuthal angle (here α) of Compton-scattered pairs, simulations were performed. The initial step involved confirming that GEANT4 accurately models the angular correlation of scattered annihilation photons according to theoretical expectations. This verification is crucial, especially because GEANT4 incorporates a more realistic simulation of Compton scattering, considering effects arising from atomic electron binding energies and Doppler broadening resulting from atomic electron orbital energies [15, 16].

This comprehensive simulation approach ensures that the simulated data align with theoretical expectations, taking into account the complexities of Compton scattering and associated phenomena within the GEANT4 framework.

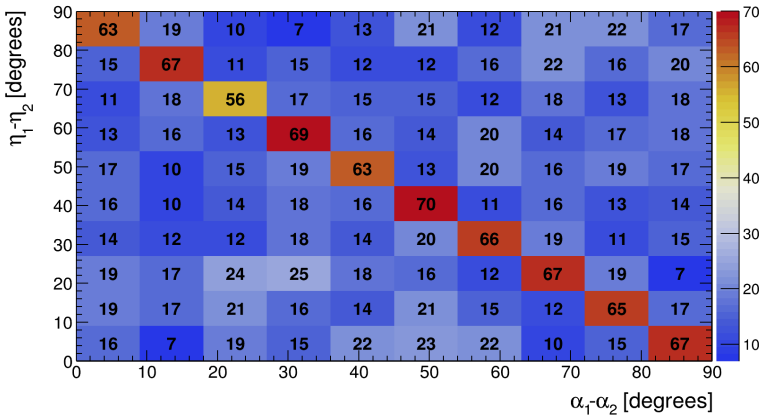

Figure 7.7: A 2D plot of differene in η and difference in α with 100 % pure state.

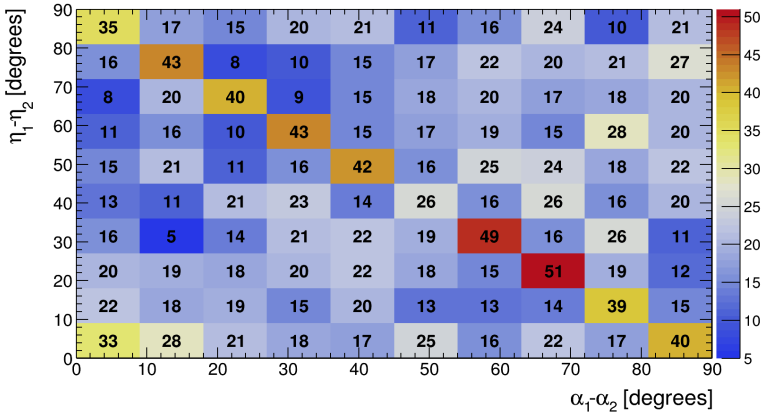

Figure 7.8: A 2D plot of differene in η and difference in α with 50 % pure state + 50 % random state.

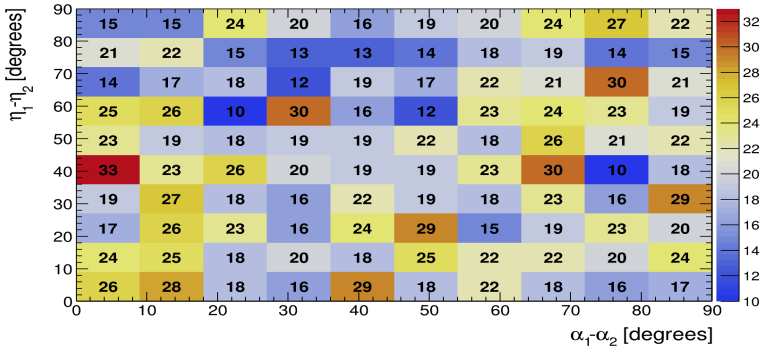

Figure 7.9: A 2D plot of differene in η and difference in α with 100 % random state.

7.6 Conclusion

The polarization measurement technique serves as a discriminative tool for identifying annihilation photons. Our current study suggests a probability of photon interaction in the gaseous detection medium to be approximately 0.02. We are making efforts to enhance this interaction probability and refine the image reconstruction process from the raw data.

Our ongoing work involves improving the interaction probability through the analysis of simulation data and conducting simulations to obtain the necessary differential cross-section data for polarization calculations. We anticipate providing updates and publishing the results with hardware tests to verify the simulation results in the near future.

Bibliography

[1] Jacob Trotter et al. "Positron Emission Tomography (PET)/Computed Tomography (CT) Imaging in Radiation Therapy Treatment Planning: A Review of PET Imaging Tracers and Methods to Incorporate PET/CT". In: *Advances in Radiation Oncology* 8.5 (2023), p. 101212. ISSN: 2452-1094. DOI: https://doi.org/10.1016/j.adro.2023.101212. URL: https://www.sciencedirect.com/science/article/pii/S2452109423000416.

[2] H. Zaidi and K. F. Koral. "Scatter Correction Strategies in Emission Tomography". In: *Quantitative Analysis in Nuclear Medicine Imaging*. Ed. by Habib Zaidi. Boston, MA: Springer US, 2006, pp. 205–235. ISBN: 978-0-387-25444-9. DOI: 10.1007/0-387-25444-7_7. URL: https://doi.org/10.1007/0-387-25444-7_7.

[3] S Surti and J S Karp. "Experimental evaluation of a simple lesion detection task with Time-of-Flight PET". In: *Physics in Medicine & Biology* 54.4 (2009), p. 1087. DOI: 10.1088/0031-9155/54/4/C01. URL: https://dx.doi.org/10.1088/0031-9155/54/4/C01.

[4] G.B. Saha. *Basics of PET Imaging: Physics, Chemistry, and Regulations*. Springer New York, 2004. ISBN: 9780387213071. URL: https://books.google.co.in/books?id=_Hbw6X6aLUMC.

[5] Alexander Ivashkin et al. "Testing entanglement of annihilation photons". In: *Scientific Reports* 13.1 (2023), p. 7559. ISSN: 2045-2322. DOI: 10.1038/s41598-023-34767-8. URL: https://doi.org/10.1038/s41598-023-34767-8.

[6] Yuji Yazaki. "How the Klein-Nishina formula was derived: Based on the Sangokan Nishina Source Materials". en. In: *Proc Jpn Acad Ser B Phys Biol Sci* 93.6 (2017), pp. 399–421.

[7] M Toghyani et al. "Polarisation-based coincidence event discrimination: an in silico study towards a feasible scheme for Compton-PET". en. In: *Phys Med Biol* 61.15 (July 2016), pp. 5803–5817.

[8] C. S. Wu and I. Shaknov. "The Angular Correlation of Scattered Annihilation Radiation". In: *Phys. Rev.* 77 (1950), pp. 136–136. DOI: 10.1103/PhysRev.77.136.

[9] L. R. Kasday, J. D. Ullman, and C. S. Wu. "Angular correlation of compton-scattered annihilation photons and hidden variables". In: *Nuovo Cimento B Serie* 25.2 (Feb. 1975), pp. 633–661. DOI: 10.1007/BF02724742.

[10] F.W. Lipps and H.A. Tolhoek. "Polarization phenomena of electrons and photons. I: General method and application to Compton scattering". In: *Physica* 20.1 (1954), pp. 85–98. ISSN: 0031-8914. DOI: https://doi.org/10.1016/S0031-8914(54)80018-8. URL: https://www.sciencedirect.com/science/article/pii/S0031891454800188.

[11] F. W. Lipps and H. A. Tolhoek. "Polarization phenomena of electrons and photons. II: Results for Compton scattering". In: *Physica* 20.1 (Jan. 1954), pp. 385–405. DOI: 10.1016/S0031-8914(54)80054-1.

[12] P. Moskal et al. "Feasibility studies of the polarization of photons beyond the optical wavelength regime with the J-PET detector". In: *Eur. Phys. J. C* 78.11 (2018), p. 970. DOI: 10.1140/epjc/s10052-018-6461-1. arXiv: 1809.10397 [physics.ins-det].

[13] E. Albrecht et al. "Performance of a prototype RICH detector using hybrid photo-diodes". In: (Apr. 2001).

[14] G.O. Depaola. "New Monte Carlo method for Compton and Rayleigh scattering by polarized gamma rays". In: *Nuclear Instruments and Methods in Physics Research Section A: Accelerators, Spectrometers, Detectors and Associated Equipment* 512.3 (2003), pp. 619–630. ISSN: 0168-9002. DOI: https://doi.org/10.1016/S0168-9002(03)02050-3. URL: https://www.sciencedirect.com/science/article/pii/S0168900203020503.

[15] Jeremy Brown et al. "A low energy bound atomic electron Compton scattering model for Geant4". In: *Nuclear Instruments and Methods in Physics Research Section B: Beam Interactions with Materials and Atoms* 338 (Nov. 2014), 77–88. DOI: 10.1016/j.nimb.2014.07.042.

[16] C Z Uche, M J Cree, and W H Round. "GEANT4 simulation of the effects of Doppler energy broadening in Compton imaging". en. In: *Australas Phys Eng Sci Med* 34.3 (May 2011), pp. 409–414.

General Conclusion

Upon joining both the CMS GEM Collaboration and the Panjab University Experimental High Energy Group, I participated in the assembly phase of the GE1/1 project within CMS and at Panjab University.

During this stage, critical project aspects remained undetermined, prompting the need to showcase the suitability of GE1/1 technology for upgrading CMS end-caps. This involved conducting measurements of fundamental characteristics of the world's largest triple-GEM detectors to ensure their compatibility with the CMS forward environment. The CMS GEM Collaboration aimed to demonstrate that GE1/1 prototypes fulfilled CMS requirements for both the L1 trigger system and offline reconstruction. Additionally, it was essential to study the long-term operation of GE1/1s to guarantee their durability over several decades in challenging environments.

Beyond considerations related to the detector, it was imperative to highlight the resources, experience, and manpower of the CMS GEM Collaboration for such a significant project. The collaboration developed numerous tools and techniques to facilitate the integration of the GE1/1 project into the CMS system, including the establishment and validation of production plans and quality control measures for the chambers.

My Ph.D. work, proposed in this context, encompassed four main projects. The first project is focussed on assmbly and QC of GE1/1 detectors. The second project focused on studying the background radiation for the GE1/1 triple-GEM detectors, addressing discrepancies in the low pseudorapidity region. The third project extensively examined the effect of blank and random electrode segmentation on the performance of GEM detectors. The fourth project centered on the application of GEM detectors in medical imaging and therapy assembly.

The successful completion of my Ph.D. work resulted in good agreement between the GE1/1 Slice Test data and simulation, leading to the application of the same

methodology for the GE1/1 Run-3 background estimation. The results are currently being utilized by the GEM-DPG for the simulation and estimation of Run-3 background data. The exploration of segmentation effects on detector performance has opened avenues for further research and development to minimize losses, with some groups actively working on these advancements.

Reflecting on my experiences, I consider myself fortunate to have worked at CERN, where I encountered diverse detection technologies and collaborated with exceptional teams. Involvement in this groundbreaking project equipped me with valuable skills, and after three years of intense work, I am eager to continue my career in scientific research.

Appendix A

Neutron Cross-Section Libraries

The primary neutron cross-section databases are the United States Evaluated Nuclear Data File (ENDF) from the National Nuclear Data Centre (NNDC), the European Joint Evaluated Fission and Fusion Library (JEFF) managed by the Nuclear Energy Agency, and the Japanese Evaluated Nuclear Data Library (JENDL) developed by the Japan Atomic Energy Agency. These databases, maintained by their respective organisations, are regularly updated on their websites. Notably, the latest ENDF and JEFF libraries now extend their coverage to 150 MeV for specific isotopes.

Appendix B

GE1/1 Detector Assembly Components

Figure B.1: Left: Gas connectors. Right: Viton O-ring.

Figure B.2: Brass inserts.

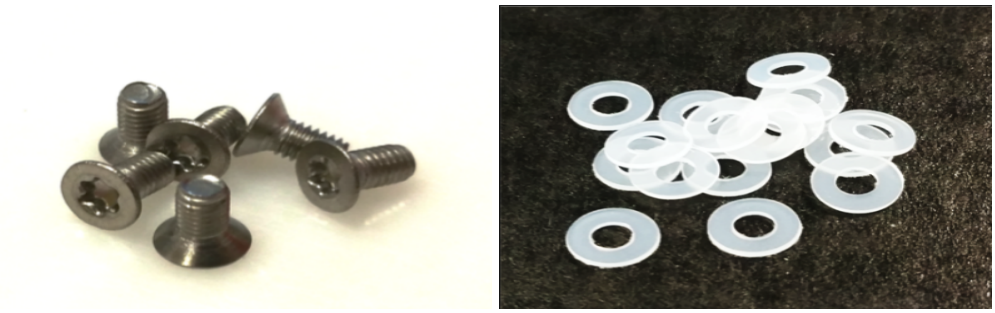

Figure B.3: Left: Nylon washers. Right: M3 × 6 screws.

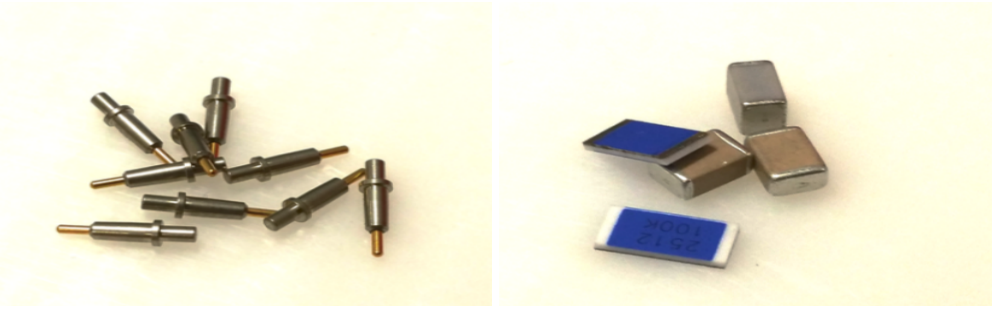

Figure B.4: Left: HV contact pins. Right: SMD components.

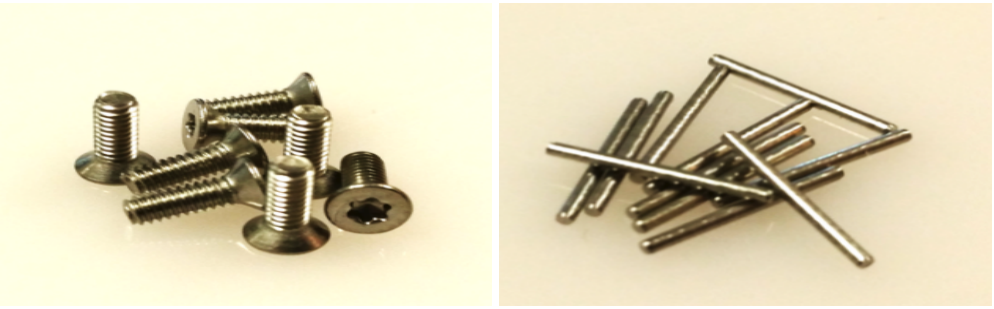

Figure B.5: Left: M2 × 6 screws. Right: ring

Figure B.6: Left: M2.5 nuts. Right: M4 × 6 long screws.

Appendix C

Radiation Background Parametres

C.1 Calculation for 3 fC

N_{Min} = Number of minimum electrons should be collected at the readout.
N_{Drift} = Number of electrons should be produced in Drift.
$N_{\text{Transfer1}}$ = Number of electrons should be produced in Transfer1.
ED_{Drift} = Energy deposit required in Drift.
$ED_{\text{Transfer1}}$ = Energy deposit required in Transfer1.
G = Gain = 10560 (For Slice Test)
$Q_e = 1.602\,176\,634 \times 10^{-19}\,\text{C}$
Threshold = 3 fC = $3 \times 10^{-15}\,\text{C}$

$$\text{N}_{\text{Min}} = \frac{\text{Threshold}}{\text{Q}_\text{e}} = \frac{3\text{e}{-}15}{1.602176634\text{e}{-}19} = 1.87245272234 \times 10^4 \approx 18725$$
$$\text{N}_{\text{Drift}} = \frac{\text{N}_{\text{Min}}}{\text{G}} = \frac{18725}{10560} = 1.77320075758 \approx 2$$
$$\text{N}_{\text{Transfer1}} = \frac{\text{N}_{\text{Min}}}{(\text{G}^{1/3})^2} = \frac{18725}{(10^4)^{2/3}} = \frac{18725}{440} \approx 42.556818818 \approx 43$$
$$\text{ED}_{\text{Transfer1}} = \text{N}_{\text{Transfer1}} \times \text{W}_{\text{Ar/CO}_2} = 43 \times 28.1\ \text{eV} = 1208.3\ \text{eV} = 1.2083\ \text{keV}$$

C.2 Average Energy Deposit

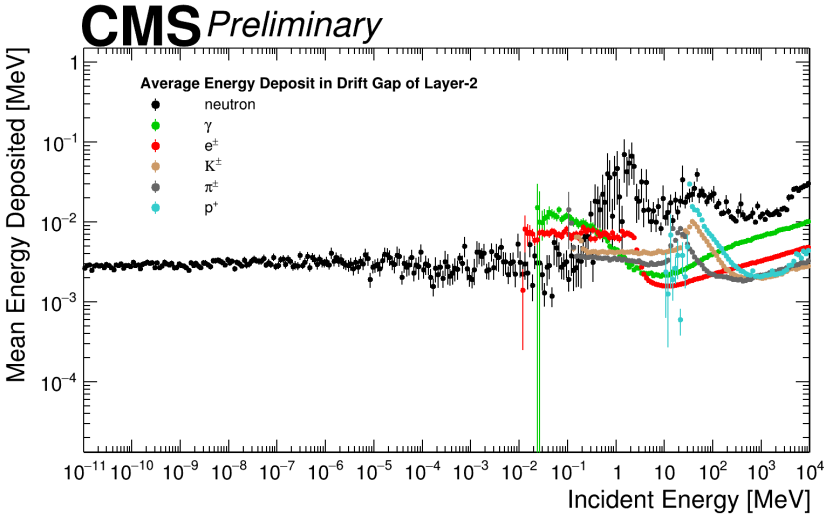

Figure C.1: Mean energy deposit in drift gap of layer-2 of GE1/1 superchamber for different particles.

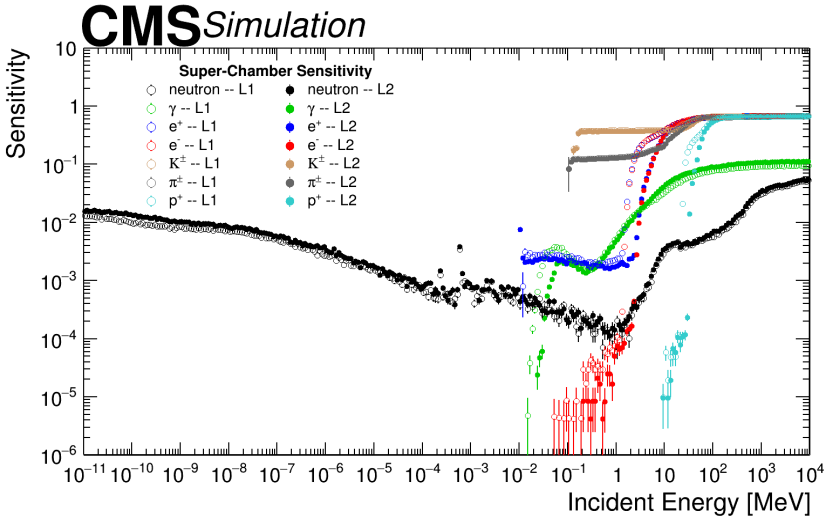

Figure C.2: A comparison of sensitvity of GE1/1 dtector Layer-1 and Layer-2.

Appendix D

GEM Foil Segmentation Study

D.1 No segmentation

Table D.1: ϵ_{coll}, ϵ_{ext}, T_e, G_{int} and G_{eff} for single-GEM detector having non-segmented GEM foil.

Parameters	Value
ϵ_{coll}	99.06 %
ϵ_{ext}	42.68 %
T_e	42.28 %
G_{int}	28.123
G_{eff}	11.890

Table D.2: ϵ_{coll}, ϵ_{ext}, T_e, G_{int} and G_{eff} for triple-GEM detector having non-segmented GEM foils.

Parameters	No Segmentation GEM foil			
	GEM 1	GEM 2	GEM 3	Cumulative
ϵ_{coll}	98.85 %	63.51 %	61.70 %	—
ϵ_{ext}	35.73 %	35.20 %	41.73 %	—
T_e	35.32 %	22.35 %	25.74 %	2.03 %
G_{int}	—	—	—	11664.8
G_{eff}	—	—	—	236.708

D.2 Double segmentation

Table D.3: ϵ_{coll}, ϵ_{ext}, T_e, G_{int} and G_{eff} for single-GEM detector having double segmentated foils with detector configuration 3:1 mm.

Parameters	Double Segmentation			
	Blank Segmentation		Random Segmentation	
Sample View				
ϵ_{coll}	39.93%	35.97%	96.68%	96.37%
ϵ_{ext}	40.85%	40.90%	40.40%	39.54%
T_e	16.31%	14.71%	39.06%	38.10%
G_{int}	14.35	12.74	14.26	12.63
G_{eff}	2.34	1.87	5.57	4.81

Table D.4: ϵ_{coll}, ϵ_{ext}, T_e, G_{int} and G_{eff} for triple-GEM detector with detector configuration 3:1:2:1 mm having double segmented foils at 20° orientation.

Parameters	Triple GEM Detector							
	Blank Segmentation				Random Segmentation			
Sample View								
	GEM1 [%]	GEM2 [%]	GEM3 [%]	Total	GEM1 [%]	GEM2 [%]	GEM3 [%]	Total
ϵ_{coll}	33.11	54.17	52.50	—	96.12	59.77	59.82	—
ϵ_{ext}	29.87	29.17	41.05	—	32.75	32.57	40.70	—
T_e	9.89	15.80	21.55	0.34 %	31.48	19.47	24.35	1.49 %
G_{int}	—	—	—	3097.66	—	—	—	2984.84
G_{eff}	—	—	—	10.43	—	—	—	44.54

Table D.5: ϵ_{coll}, ϵ_{ext}, T_e, G_{int} and G_{eff} for triple-GEM detector with detector configuration 3:1:2:1 mm having double segmented foils at 0° orientation.

Parameters	Triple GEM Detector							
	Blank Segmentation				Random Segmentation			
Sample View								
	GEM1 [%]	GEM2 [%]	GEM3 [%]	Total	GEM1 [%]	GEM2 [%]	GEM3 [%]	Total
ϵ_{coll}	37.21	52.86	54.11	—	96.08	59.08	56.47	—
ϵ_{ext}	29.13	28.82	40.10	—	31.93	31.19	39.87	—
T_e	10.84	15.23	21.70	0.36 %	30.68	18.43	22.52	1.27%
G_{int}	—	—	—	4183.92	—	—	—	3785.14
G_{eff}	—	—	—	14.99	—	—	—	48.19

D.3 Single segmentation

D.3.1 On Drift Side

Table D.6: ϵ_{coll}, ϵ_{ext}, T_e, G_{int} and G_{eff} for single-GEM detector with detector configuration 3:1 mm having drift side single segmented foils.

Parameters	Double Segmentation			
	Blank Segmentation		Random Segmentation	
Sample View				
ϵ_{coll}	15.62%	13.51%	95.71%	95.65%
ϵ_{ext}	44.72%	44.43%	43.02%	42.64%
T_e	6.98%	6.00%	41.17%	40.79%
G_{int}	10.56	9.36	10.33	8.66
G_{eff}	0.74	0.56	4.25	3.53

Table D.7: ϵ_{coll}, ϵ_{ext}, T_e, G_{int} and G_{eff} for triple-GEM detector with detector configuration 3:1:2:1 mm having drift side single segmented foils at 20° orientation.

Parameters	Triple GEM Detector							
	Blank Segmentation				Random Segmentation			
Sample View								
	GEM1 [%]	GEM2 [%]	GEM3 [%]	Total	GEM1 [%]	GEM2 [%]	GEM3 [%]	Total
ϵ_{coll}	8.58	32.98	36.62	—	95.72	87.19	86.64	—
ϵ_{ext}	17.76	19.56	43.59	—	38.25	37.68	43.04	—
T_e	1.52	6.45	15.96	0.02%	36.61	32.85	37.29	4.48%
G_{int}	—	—	—	994.57	—	—	—	884.46
G_{eff}	—	—	—	0.16	—	—	—	39.66

D.3.2 On Readout Side

Table D.8: ϵ_{coll}, ϵ_{ext}, T_e, G_{int} and G_{eff} for triple-GEM detector with detector configuration 3:1:2:1 mm having drift side single segmented foils at 0° orientation.

Parameters	Triple GEM Detector							
	Blank Segmentation				Random Segmentation			
Sample View								
	GEM1 [%]	GEM2 [%]	GEM3 [%]	Total	GEM1 [%]	GEM2 [%]	GEM3 [%]	Total
ϵ_{coll}	9.91	32.56	37.37	—	96.05	86.80	84.77	—
ϵ_{ext}	17.77	19.20	42.94	—	37.42	36.31	42.32	—
T_e	1.76	6.25	16.05	0.02%	35.94	31.52	35.87	4.06%
G_{int}	—	—	—	1363.18	—	—	—	1283.88
G_{eff}	—	—	—	0.24	—	—	—	52.17

Table D.9: ϵ_{coll}, ϵ_{ext}, T_e, G_{int} and G_{eff} for single-GEM detector with detector configuration 3:1 mm having readout side single segmented foils.

Parameters	Double Segmentation			
	Blank Segmentation		Random Segmentation	
Sample View				
ϵ_{coll}	83.74%	82.83%	98.98%	99.07%
ϵ_{ext}	35.75%	36.29%	28.40%	28.05%
T_e	29.94%	30.06%	28.11%	27.79%
G_{int}	21.77	19.99	27.09	25.46
G_{eff}	6.52	6.01	7.62	7.08

Table D.10: ϵ_{coll}, ϵ_{ext}, T_e, G_{int} and G_{eff} for triple-GEM detector with detector configuration 3:1:2:1 mm having drift side single segmented foils at 20° orientation.

Parameters	Triple GEM Detector							
	Blank Segmentation				Random Segmentation			
Sample View								
	GEM1 [%]	GEM2 [%]	GEM3 [%]	Total	GEM1 [%]	GEM2 [%]	GEM3 [%]	Total
ϵ_{coll}	82.86	50.16	56.95	—	98.93	35.13	58.22	—
ϵ_{ext}	26.87	32.21	40.98	—	19.82	32.39	40.93	—
T_e	22.26	16.15	23.34	0.84%	19.60	11.38	23.83	0.53%
G_{int}	—	—	—	4163.27	—	—	—	4170.84
G_{eff}	—	—	—	34.95	—	—	—	22.18

Table D.11: ϵ_{coll}, ϵ_{ext}, T_e, G_{int} and G_{eff} for triple-GEM detector with detector configuration 3:1:2:1 mm having drift side single segmented foils at 0° orientation.

Parameters	Triple GEM Detector							
	Blank Segmentation				Random Segmentation			
Sample View								
	GEM1 [%]	GEM2 [%]	GEM3 [%]	Total	GEM1 [%]	GEM2 [%]	GEM3 [%]	Total
ϵ_{coll}	84.16	48.67	57.89	—	98.77	55.22	55.42	—
ϵ_{ext}	25.50	31.15	40.31	—	30.27	32.13	40.59	—
T_e	21.46	15.16	23.33	0.76%	29.90	17.74	22.50	1.19%
G_{int}	—	—	—	4969.75	—	—	—	4931.38
G_{eff}	—	—	—	37.73	—	—	—	58.85

Publication and CMS Public Notes with Direct Contribution

[1] M. Abbas et al. Benchmarking LHC background particle simulation with the CMS triple-GEM detector. *JINST*, 16(12):P12026, 2021.

[2] J. Babbar et al. Fabrication and Characterization of Gaseous Detector for the identification of High Energy Particles. *IOP Conf. Ser. Mater. Sci. Eng.*, 1033(1):012055, 2021.

[3] M. Abbas et al. Quality control of mass-produced GEM detectors for the CMS GE1/1 muon upgrade. *Nucl. Instrum. Meth. A*, 1034:166716, 2022.

Papers Presented in Conferences, Workshops and Symposiums

[1] S. Kumar, V. Bhatnagar, S. S. Chauhan. Quantum Entanglement: A Novel Approach in PET Detector. *Chandigarh Science Congress (CHASCON-2019)*, March 14th -15th 2018, Punjab University, India.

[2] Sunil Kumar, Sushil Singh Chauhan, and Vipin Bhatnagar. Q-PET: PET with 3rd Eye Quantum Entanglement Based Positron Emission Tomography. *Springer Proc. Phys.*, 261:949–952, 2021.

[3] S. Kumar, O. Bouhali, V. Bhatnagar, A. Castaneda, S. S. Chauhan, T. Kamon, Y. Kang, and A. K. Virdi. Sensitivity of Triple-GEM Detectors for Background Radiation in CMS Experiment. *Springer Proc. Phys.*, 277:881–885, 2022.

[4] O. Bouhali, V. Bhatnagar, A. Castaneda, S. S. Chauhan, T. Kamon, Y. Kang, S. Kumar, and A. K. Virdi. Radiation background estimation for the GE11 Triple-GEM detectors in the CMS endcap. *J. Phys. Conf. Ser.*, 2374(1):012161, 2022.

Publications as Co-author with CMS Collaboration

[1] Georges Aad et al. Evidence for the Higgs Boson Decay to a Z Boson and a Photon at the LHC. *Phys. Rev. Lett.*, 132:021803, 2024.

[2] J. Babbar et al. Fabrication and Characterization of Gaseous Detector for the identification of High Energy Particles. *IOP Conf. Ser. Mater. Sci. Eng.*, 1033(1):012055, 2021.

[3] O. Bouhali, V. Bhatnagar, A. Castaneda, S. S. Chauhan, T. Kamon, Y. Kang, S. Kumar, and A. K. Virdi. Radiation background estimation for the GE11 Triple-GEM detectors in the CMS endcap. *J. Phys. Conf. Ser.*, 2374(1):012161, 2022.

[4] Aram Hayrapetyan et al. Combination of measurements of the top quark mass from data collected by the ATLAS and CMS experiments at $\sqrt{s} = 7$ and 8 TeV. 2023.

[5] Aram Hayrapetyan et al. Development of the CMS detector for the CERN LHC Run 3. 9 2023.

[6] Aram Hayrapetyan et al. Inclusive and differential cross section measurements of $t\bar{t}b\bar{b}$ production in the lepton+jets channel at $\sqrt{s}$ = 13 TeV. 9 2023.

[7] Aram Hayrapetyan et al. Measurement of multidifferential cross sections for dijet production in proton-proton collisions at $\sqrt{s}$ = 13 TeV. 12 2023.

[8] Aram Hayrapetyan et al. Observation of enhanced long-range elliptic anisotropies inside high-multiplicity jets in pp collisions at $\sqrt{s}$ = 13 TeV. 12 2023.

[9] Aram Hayrapetyan et al. Observation of four top quark production in proton-proton collisions at s=13TeV. *Phys. Lett. B*, 847:138290, 2023.

[10] Aram Hayrapetyan et al. Observation of the rare decay of the η meson to four muons. *Phys. Rev. Lett.*, 131(9):091903, 2023.

[11] Aram Hayrapetyan et al. Search for an exotic decay of the Higgs boson into a Z boson and a pseudoscalar particle in proton-proton collisions at $\sqrt{s}$ = 13 TeV. 10 2023.

[12] Aram Hayrapetyan et al. Search for charged-lepton flavor violation in the production and decay of top quarks using trilepton final states in proton-proton

collisions at $\sqrt{s}$ = 13 TeV. 12 2023.

[13] Aram Hayrapetyan et al. Search for dark matter particles in W^+W^- events with transverse momentum imbalance in proton-proton collisions at $\sqrt{s}$ = 13 TeV. 10 2023.

[14] Aram Hayrapetyan et al. Search for direct production of GeV-scale resonances decaying to a pair of muons in proton-proton collisions at $\sqrt{s}$ = 13 TeV. *JHEP*, 12:070, 2023.

[15] Aram Hayrapetyan et al. Search for flavor changing neutral current interactions of the top quark in final states with a photon and additional jets in proton-proton collisions at $\sqrt{s}$ = 13 TeV. 12 2023.

[16] Aram Hayrapetyan et al. Search for narrow trijet resonances in proton-proton collisions at $\sqrt{s}$ = 13 TeV. 10 2023.

[17] Aram Hayrapetyan et al. Search for new Higgs bosons via same-sign top quark pair production in association with a jet in proton-proton collisions at $\sqrt{s}$ = 13 TeV. 11 2023.

[18] Aram Hayrapetyan et al. Search for stealth supersymmetry in final states with two photons, jets, and low missing transverse momentum in proton-proton collisions at $\sqrt{s}$ = 13 TeV. 10 2023.

[19] Aram Hayrapetyan et al. Search for the lepton-flavor violating decay of the Higgs boson and additional Higgs bosons in the eμ final state in proton-proton collisions at $\sqrt{s}$ = 13 TeV. *Phys. Rev. D*, 108(7):072004, 2023.

[20] Aram Hayrapetyan et al. Search for the lepton flavor violating $\tau \to 3\mu$ decay in proton-proton collisions at $\sqrt{s}$ = 13 TeV. 12 2023.

[21] Aram Hayrapetyan et al. Search for W′ bosons decaying to a top and a bottom quark in leptonic final states in proton-proton collisions at $\sqrt{s}$ = 13 TeV. 10 2023.

[22] Aram Hayrapetyan et al. A search for bottom-type vector-like quark pair production in dileptonic and fully hadronic final states in proton-proton collisions at $\sqrt{s}$ = 13 TeV. 2 2024.

[23] Aram Hayrapetyan et al. Extracting the speed of sound in the strongly interacting matter created in ultrarelativistic lead-lead collisions at the LHC. 1 2024.

[24] Aram Hayrapetyan et al. Luminosity determination using Z boson production at the CMS experiment. *Eur. Phys. J. C*, 84(1):26, 2024.

[25] Aram Hayrapetyan et al. Measurement of energy correlators inside jets and determination of the strong coupling $\alpha_S(m_Z)$. 2 2024.

[26] Aram Hayrapetyan et al. Measurement of the double-differential inclusive jet cross section in proton-proton collisions at $\sqrt{s}$ = 5.02 TeV. 1 2024.

[27] Aram Hayrapetyan et al. Measurement of the τ lepton polarization in Z boson decays in proton-proton collisions at $\sqrt{s}$ = 13 TeV. *JHEP*, 01:101, 2024.

[28] Aram Hayrapetyan et al. Measurement of the Higgs boson production via vector boson fusion and its decay into bottom quarks in proton-proton collisions at $\sqrt{s}$ = 13 TeV. *JHEP*, 01:173, 2024.

[29] Aram Hayrapetyan et al. Observation of the $\Lambda_b^0 \to J/\psi \Xi^- K^+$ decay. 1 2024.

[30] Aram Hayrapetyan et al. Search for exotic decays of the Higgs boson to a pair of pseudoscalars in the $\mu\mu$bb and $\tau\tau$bb final states. 2 2024.

[31] Aram Hayrapetyan et al. Search for fractionally charged particles in proton-proton collisions at $\sqrt{s}$ = 13 TeV. 2 2024.

[32] Aram Hayrapetyan et al. Search for Inelastic Dark Matter in Events with Two Displaced Muons and Missing Transverse Momentum in Proton-Proton Collisions at s=13 TeV. *Phys. Rev. Lett.*, 132(4):041802, 2024.

[33] Aram Hayrapetyan et al. Search for long-lived particles decaying in the CMS muon detectors in proton-proton collisions at $\sqrt{s}$ = 13 TeV. 2 2024.

[34] Aram Hayrapetyan et al. Search for pair production of scalar and vector leptoquarks decaying to muons and bottom quarks in proton-proton collisions at $\sqrt{s}$ = 13 TeV. 2 2024.

[35] Aram Hayrapetyan et al. Search for Scalar Leptoquarks Produced via τ-Lepton–Quark Scattering in pp Collisions at s=13 TeV. *Phys. Rev. Lett.*, 132(6):061801, 2024.

[36] Aram Hayrapetyan et al. Test of lepton flavor universality in $B^\pm \to K^\pm \mu^+ \mu^-$ and $B^\pm \to K^\pm e^+ e^-$ decays in proton-proton collisions at $\sqrt{s}$ = 13 TeV. 1 2024.

[37] S. Kumar, O. Bouhali, V. Bhatnagar, A. Castaneda, S. S. Chauhan, T. Kamon, Y. Kang, and A. K. Virdi. Sensitivity of Triple-GEM Detectors for Background Radiation in CMS Experiment. *Springer Proc. Phys.*, 277:881–885, 2022.

[38] Armen Tumasyan et al. A portrait of the Higgs boson by the CMS experiment ten years after the discovery. *Nature*, 607(7917):60–68, 2022.

[39] Armen Tumasyan et al. A search for decays of the Higgs boson to invisible particles in events with a top-antitop quark pair or a vector boson in proton-proton collisions at $\sqrt{s} = 13$ TeV. *Eur. Phys. J. C*, 83(10):933, 2023.

[40] Armen Tumasyan et al. Evidence for four-top quark production in proton-proton collisions at s=13TeV. *Phys. Lett. B*, 844:138076, 2023.

[41] Armen Tumasyan et al. First measurement of the top quark pair production cross section in proton-proton collisions at $\sqrt{s}$ = 13.6 TeV. *JHEP*, 08:204, 2023.

[42] Armen Tumasyan et al. Measurement of simplified template cross sections of the

Higgs boson produced in association with W or Z bosons in the H $\rightarrow b\bar{b}$ decay channel in proton-proton collisions at $\sqrt{s}$ =13 TeV. 12 2023.

[43] Armen Tumasyan et al. Measurement of the $B_S^0 \rightarrow \mu^+\mu^-$ decay properties and search for the $B^0 \rightarrow \mu^+\mu^-$ decay in proton-proton collisions at $\sqrt{s}$ = 13 TeV. *Phys. Lett. B*, 842:137955, 2023.

[44] Armen Tumasyan et al. Measurement of the cross section of top quark-antiquark pair production in association with a W boson in proton-proton collisions at $\sqrt{s}$ = 13 TeV. *JHEP*, 07:219, 2023.

[45] Armen Tumasyan et al. Measurement of the dependence of the hadron production fraction ratio f_s/f_u and f_d/f_u on B meson kinematic variables in proton-proton collisions at $\sqrt{s}$ = 13 TeV. *Phys. Rev. Lett.*, 131:121901, 2023.

[46] Armen Tumasyan et al. Measurement of the differential $t\bar{t}$ production cross section as a function of the jet mass and extraction of the top quark mass in hadronic decays of boosted top quarks. *Eur. Phys. J. C*, 83(7):560, 2023.

[47] Armen Tumasyan et al. Measurement of the electroweak production of Wγ in association with two jets in proton-proton collisions at $\sqrt{s}$ = 13 TeV. *Phys. Rev. D*, 108(3):032017, 2023.

[48] Armen Tumasyan et al. Measurement of the top quark mass using a profile likelihood approach with the lepton + jets final states in proton–proton collisions at $\sqrt{s} = 13$ TeV. *Eur. Phys. J. C*, 83(10):963, 2023.

[49] Armen Tumasyan et al. Measurement of the tt^- charge asymmetry in events with highly Lorentz-boosted top quarks in pp collisions at s=13 TeV. *Phys. Lett. B*, 846:137703, 2023.

[50] Armen Tumasyan et al. Measurements of the azimuthal anisotropy of prompt and nonprompt charmonia in PbPb collisions at $\sqrt{s_{NN}}$ = 5.02 TeV. *JHEP*, 10:115, 2023.

[51] Armen Tumasyan et al. Measurements of the Higgs boson production cross section and couplings in the W boson pair decay channel in proton-proton collisions at $\sqrt{s} = 13$ TeV. *Eur. Phys. J. C*, 83(7):667, 2023.

[52] Armen Tumasyan et al. Multiplicity and transverse momentum dependence of charge-balance functions in pPb and PbPb collisions at LHC energies. 7 2023.

[53] Armen Tumasyan et al. Observation of same-sign WW production from double parton scattering in proton-proton collisions at $\sqrt{s}$ = 13 TeV. *Phys. Rev. Lett.*, 131:091803, 2023.

[54] Armen Tumasyan et al. Observation of τ lepton pair production in ultraperipheral lead-lead collisions at $\sqrt{s_{NN}}$ = 5.02 TeV. *Phys. Rev. Lett.*, 131:151803, 2023.

[55] Armen Tumasyan et al. Performance of the local reconstruction algorithms for

the CMS hadron calorimeter with Run 2 data. *JINST*, 18(11):P11017, 2023.

[56] Armen Tumasyan et al. Probing Small Bjorken-x Nuclear Gluonic Structure via Coherent J/ψ Photoproduction in Ultraperipheral Pb-Pb Collisions at sNN=5.02 TeV. *Phys. Rev. Lett.*, 131(26):262301, 2023.

[57] Armen Tumasyan et al. Proton reconstruction with the CMS-TOTEM Precision Proton Spectrometer. *JINST*, 18(09):P09009, 2023.

[58] Armen Tumasyan et al. Search for a heavy composite Majorana neutrino in events with dilepton signatures from proton-proton collisions at s=13 TeV. *Phys. Lett. B*, 843:137803, 2023.

[59] Armen Tumasyan et al. Search for a new resonance decaying into two spin-0 bosons in a final state with two photons and two bottom quarks in proton-proton collisions at $\sqrt{s}$ = 13 TeV. 10 2023.

[60] Armen Tumasyan et al. Search for central exclusive production of top quark pairs in proton-proton collisions at $\sqrt{s}$ = 13 TeV with tagged protons. 10 2023.

[61] Armen Tumasyan et al. Search for exotic Higgs boson decays $H \to \mathcal{A}\mathcal{A} \to 4\gamma$ with events containing two merged diphotons in proton-proton collisions at $\sqrt{s}$ = 13 TeV. *Phys. Rev. Lett.*, 131:101801, 2023.

[62] Armen Tumasyan et al. Search for high-mass exclusive diphoton production with tagged protons in proton-proton collisions at $\sqrt{s}$ = 13 TeV. 11 2023.

[63] Armen Tumasyan et al. Search for long-lived particles using out-of-time trackless jets in proton-proton collisions at $\sqrt{s}$ = 13 TeV. *JHEP*, 07:210, 2023.

[64] Armen Tumasyan et al. Search for medium effects using jets from bottom quarks in PbPb collisions at sNN=5.02TeV. *Phys. Lett. B*, 844:137849, 2023.

[65] Armen Tumasyan et al. Search for new heavy resonances decaying to WW, WZ, ZZ, WH, or ZH boson pairs in the all-jets final state in proton-proton collisions at s=13TeV. *Phys. Lett. B*, 844:137813, 2023.

[66] Armen Tumasyan et al. Search for new physics using effective field theory in 13 TeV pp collision events that contain a top quark pair and a boosted Z or Higgs boson. *Phys. Rev. D*, 108:032008, 2023.

[67] Armen Tumasyan et al. Search for pair-produced vector-like leptons in final states with third-generation leptons and at least three b quark jets in proton-proton collisions at s=13TeV. *Phys. Lett. B*, 846:137713, 2023.

[68] Armen Tumasyan et al. Search for resonances in events with photon and jet final states in proton-proton collisions at $\sqrt{s}$ = 13 TeV. *JHEP*, 12:189, 2023.

[69] Armen Tumasyan et al. Search for supersymmetry in final states with a single electron or muon using angular correlations and heavy-object identification in

proton-proton collisions at $\sqrt{s}$ = 13 TeV. *JHEP*, 09:149, 2023.

[70] Armen Tumasyan et al. Search for the Higgs boson decay to a pair of electrons in proton-proton collisions at s=13TeV. *Phys. Lett. B*, 846:137783, 2023.

[71] Armen Tumasyan et al. Search for top squark pair production in a final state with at least one hadronically decaying tau lepton in proton-proton collisions at $\sqrt{s}$ = 13 TeV. *JHEP*, 07:110, 2023.

[72] Armen Tumasyan et al. Two-particle Bose-Einstein correlations and their Lévy parameters in PbPb collisions at $\sqrt{s_{\mathrm{NN}}}$ = 5.02 TeV. 6 2023.

[73] Armen Tumasyan et al. Higher-order moments of the elliptic flow distribution in PbPb collisions at $\sqrt{s_{\mathrm{NN}}}$ = 5.02 TeV. *JHEP*, 2024(02):106, 2024.

[74] Armen Tumasyan et al. Measurement of the production cross section for a W boson in association with a charm quark in proton–proton collisions at $\sqrt{s} =$ 13 TeV. *Eur. Phys. J. C*, 84:27, 2024.

[75] Armen Tumasyan et al. Search for a scalar or pseudoscalar dilepton resonance produced in association with a massive vector boson or top quark-antiquark pair in multilepton events at $\sqrt{s}$ = 13 TeV. 2 2024.

[76] Armen Tumasyan et al. Study of charm hadronization with prompt Λ_c^+ baryons in proton-proton and lead-lead collisions at $\sqrt{s_{\mathrm{NN}}}$ = 5.02 TeV. *JHEP*, 01:128, 2024.

Selected Reprints

Journal of Instrumentation

PAPER • **OPEN ACCESS**

Benchmarking LHC background particle simulation with the CMS triple-GEM detector

To cite this article: M. Abbas *et al* 2021 *JINST* **16** P12026

Published by IOP Publishing for Sissa Medialab

Received: *June 16, 2021*
Revised: *August 21, 2021*
Accepted: *November 22, 2021*
Published: *December 16, 2021*

Benchmarking LHC background particle simulation with the CMS triple-GEM detector

M. Abbas,[n] **M. Abbrescia,**[t] **H. Abdalla,**[h,j] **A. Abdelalim,**[h,k] **S. AbuZeid,**[h,i] **A. Agapitos,**[d] **A. Ahmad,**[af] **A. Ahmed,**[q] **W. Ahmed,**[af] **C. Aimè,**[y] **C. Aruta,**[t] **I. Asghar,**[af] **P. Aspell,**[ak] **C. Avila,**[f] **I. Azhgirey,**[ag] **J. Babbar,**[p] **Y. Ban,**[d] **R. Band,**[am] **S. Bansal,**[p] **L. Benussi,**[v] **V. Bhatnagar,**[p] **M. Bianco,**[ak] **S. Bianco,**[v] **K. Black,**[ap] **L. Borgonovi,**[u] **O. Bouhali,**[al] **D. Bozzato,**[ak,1] **A. Braghieri,**[y] **S. Braibant,**[u] **S. Butalla,**[aq] **S. Calzaferri,**[y] **M. Caponero,**[v] **F. Cassese,**[x] **A. Castaneda,**[ae,*] **N. Cavallo,**[x] **S.S. Chauhan,**[p,*] **A. Colaleo,**[t] **A. Conde Garcia,**[ak] **M. Dalchenko,**[al] **A. De Iorio,**[x] **G. De Lentdecker,**[a] **D. Dell Olio,**[t] **G. De Robertis,**[t] **W. Dharmaratna,**[aj] **S. Dildick,**[al,2] **B. Dorney,**[a] **R. Erbacher,**[am] **F. Fabozzi,**[x] **F. Fallavollita,**[ak] **A. Ferraro,**[y] **D. Fiorina,**[y] **E. Fontanesi,**[u] **M. Franco,**[t] **C. Galloni,**[ap] **D. Gancarcik,**[ak,3] **P. Giacomelli,**[u] **S. Gigli,**[y] **J. Gilmore,**[al] **M. Gola,**[q] **M. Gruchala,**[ak] **A. Gutierrez,**[an] **R. Hadjiiska,**[c] **T. Hakkarainen,**[l] **J. Hauser,**[ao] **K. Hoepfner,**[m] **M. Hohlmann,**[aq] **H. Hoorani,**[af] **T. Huang,**[al] **P. Iaydjiev,**[c] **A. Irshad,**[a] **A. Iorio,**[x] **F. Ivone,**[m] **W. Jang,**[ab] **J. Jaramillo,**[g] **V. Jha,**[s] **A. Juodagalvis,**[ad] **E. Juska,**[al] **B. Kailasapathy,**[ah,ai] **T. Kamon,**[al] **Y. Kang,**[ab] **P. Karchin,**[an] **A. Kaur,**[p] **H. Kaur,**[p] **H. Keller,**[m] **H. Kim,**[al] **J. Kim,**[aa] **S. Kim,**[ab] **B. Ko,**[ab] **A. Kumar,**[q] **S. Kumar,**[p] **H. Kumawat,**[s] **I. Kurochkin,**[ag] **N. Lacalamita,**[t] **J.S.H. Lee,**[ab] **A. Levin,**[d] **Q. Li,**[d] **F. Licciulli,**[t] **L. Lista,**[x] **K. Liyanage,**[aj] **F. Loddo,**[t] **M. Luhach,**[p] **M. Maggi,**[t] **Y. Maghrbi,**[ac] **N. Majumdar,**[r] **K. Malagalage,**[ah] **S. Malhotra,**[al] **S. Mallows,**[n] **S. Martiradonna,**[t] **N. Mccoll,**[ao] **C. McLean,**[am] **J. Merlin,**[t] **M. Misheva,**[c] **D. Mishra,**[s] **G. Mocellin,**[m] **L. Moureaux,**[a] **A. Muhammad,**[af] **S. Muhammad,**[af] **S. Mukhopadhyay,**[r] **M. Naimuddin,**[q] **P. Netrakanti,**[s] **S. Nuzzo,**[t] **R. Oliveira,**[ak] **L. Pant,**[s] **P. Paolucci,**[x] **I.C. Park,**[ab] **L. Passamonti,**[v] **G. Passeggio,**[x] **A. Peck,**[ao] **A. Pellecchia,**[t] **N. Perera,**[aj] **L. Petre,**[a] **H. Petrow,**[l] **D. Piccolo,**[v] **D. Pierluigi,**[v] **G. Raffone,**[v] **M. Rahmani,**[aq] **F. Ramirez,**[g] **A. Ranieri,**[t] **G. Rashevski,**[c] **B. Regnery,**[am] **M. Ressegotti,**[y,4] **A. Riabchikova,**[ag] **C. Riccardi,**[y] **M. Rodozov,**[c] **E. Romano,**[y] **C. Roskas,**[b] **B. Rossi,**[x] **P. Rout,**[r] **D. Roy,**[aq] **J.D. Ruiz,**[g] **A. Russo,**[v] **A. Safonov,**[al] **A.K. Sahota,**[p] **D. Saltzberg,**[ao] **G. Saviano,**[v] **A. Shah,**[q] **A. Sharma,**[ak] **R. Sharma,**[q] **T. Sheokand,**[p] **M. Shopova,**[c] **F.M. Simone,**[t] **J. Singh,**[p] **U. Sonnadara,**[ah] **E. Starling,**[a] **B. Stone,**[ao] **J. Sturdy,**[an] **G. Sultanov,**[c] **Z. Szillasi,**[o] **D. Teague,**[ap] **D. Teyssier,**[o] **T. Tuuva,**[l] **M. Tytgat,**[b] **I. Vai,**[w]

[1]Also at Karlsruhe Institute of Technology, Karlsruhe, Germany.
[2]Now at Rice University, Houston, Texas, U.S.A.
[3]Also at Czech Technical University (CZ), Prague, Czech Republic.
[4]Now at INFN Sezione di Genova, Genova, Italy.

https://doi.org/10.1088/1748-0221/16/12/P12026

2021 JINST 16 P12026

N. Vanegas,[g] **R. Venditti,**[t] **P. Verwilligen,**[t] **W. Vetens,**[ap] **A.K. Virdi,**[p] **P. Vitulo,**[y] **A. Wajid,**[af] **D. Wang,**[d] **K. Wang,**[d] **I.J. Watson,**[ab] **N. Wickramage,**[aj] **D.D.C. Wickramarathna,**[ah] **S. Yang,**[ab] **Y. Yang,**[a] **U. Yang,**[aa] **J. Yongho,**[z] **I. Yoon,**[aa] **Z. You,**[e] **I. Yu**[z] **and S. Zaleski**[m]

[a] *Université Libre de Bruxelles, Bruxelles, Belgium*
[b] *Ghent University, Ghent, Belgium*
[c] *Institute for Nuclear Research and Nuclear Energy, Bulgarian Academy of Sciences, Sofia, Bulgaria*
[d] *Peking University, Beijing, China*
[e] *Sun Yat-Sen University, Guangzhou, China*
[f] *University de Los Andes, Bogota, Colombia*
[g] *Universidad de Antioquia, Medellin, Colombia*
[h] *Academy of Scientific Research and Technology — ENHEP, Cairo, Egypt*
[i] *Ain Shams University, Cairo, Egypt*
[j] *Cairo University, Cairo, Egypt*
[k] *Helwan University, also at Zewail City of Science and Technology, Cairo, Egypt*
[l] *Lappeenranta University of Technology, Lappeenranta, Finland*
[m] *RWTH Aachen University, III. Physikalisches Institut A, Aachen, Germany*
[n] *Karlsruhe Institute of Technology, Karlsruhe, Germany*
[o] *Institute for Nuclear Research ATOMKI, Debrecen, Hungary*
[p] *Panjab University, Chandigarh, India*
[q] *Delhi University, Delhi, India*
[r] *Saha Institute of Nuclear Physics, Kolkata, India*
[s] *Bhabha Atomic Research Centre, Mumbai, India*
[t] *Politecnico di Bari, Università di Bari and INFN Sezione di Bari, Bari, Italy*
[u] *Università di Bologna and INFN Sezione di Bologna, Bologna, Italy*
[v] *Laboratori Nazionali di Frascati INFN, Frascati, Italy*
[x] *Università di Napoli and INFN Sezione di Napoli, Napoli, Italy*
[y] *Università di Pavia and INFN Sezione di Pavia, Pavia, Italy*
[w] *Università di Bergamo and INFN Sezione di Pavia, Pavia, Italy*
[z] *Korea University, Seoul, Korea*
[aa] *Seoul National University, Seoul, Korea*
[ab] *University of Seoul, Seoul, Korea*
[ac] *College of Engineering and Technology, American University of the Middle East, Dasman, Kuwait*
[ad] *Vilnius University, Vilnius, Lithuania*
[ae] *Universidad de Sonora, Hermosillo, Mexico*
[af] *National Center for Physics, Islamabad, Pakistan*
[ag] *Institute for High Energy Physics of NRC Kurchatov Institute, Protvino, Russia*
[ah] *University of Colombo, Colombo, Sri Lanka*
[ai] *Trincomalee Campus, Eastern University, Sri Lanka, Nilaveli, Sri Lanka*
[aj] *University of Ruhuna, Matara, Sri Lanka*
[ak] *CERN, Geneva, Switzerland*
[al] *Texas A&M University, College Station, U.S.A.*
[am] *University of California, Davis, Davis, U.S.A.*

[*] Corresponding author.

2021 JINST 16 P12026

[an] Wayne State University, Detroit, U.S.A.
[ao] University of California, Los Angeles, U.S.A.
[ap] University of Wisconsin, Madison, U.S.A.
[aq] Florida Institute of Technology, Melbourne, U.S.A.

E-mail: castaned@cern.ch, schauhan@cern.ch

Abstract: In 2018, a system of large-size triple-GEM demonstrator chambers was installed in the CMS experiment at CERN's Large Hadron Collider (LHC). The demonstrator's design mimicks that of the final detector, installed for Run-3. A successful Monte Carlo (MC) simulation of the collision-induced background hit rate in this system in proton-proton collisions at 13 TeV is presented. The MC predictions are compared to CMS measurements recorded at an instantaneous luminosity of 1.5×10^{34} cm^{-2} s^{-1}. The simulation framework uses a combination of the FLUKA and GEANT4 packages. FLUKA simulates the radiation environment around the GE1/1 chambers. The particle flux by FLUKA covers energy spectra ranging from 10^{-11} to 10^{4} MeV for neutrons, 10^{-3} to 10^{4} MeV for γ's, 10^{-2} to 10^{4} MeV for $e^{\pm}$, and 10^{-1} to 10^{4} MeV for charged hadrons. GEANT4 provides an estimate of the detector response (sensitivity) based on an accurate description of the detector geometry, the material composition, and the interaction of particles with the detector layers. The detector hit rate, as obtained from the simulation using FLUKA and GEANT4, is estimated as a function of the perpendicular distance from the beam line and agrees with data within the assigned uncertainties in the range 13.7-14.5%. This simulation framework can be used to obtain a reliable estimate of the background rates expected at the High Luminosity LHC.

Keywords: Detector modelling and simulations I (interaction of radiation with matter, interaction of photons with matter, interaction of hadrons with matter, etc); Interaction of radiation with matter; Micropattern gaseous detectors (MSGC, GEM, THGEM, RETHGEM, MHSP, MICROPIC, MICROMEGAS, InGrid, etc); Detector modelling and simulations II (electric fields, charge transport, multiplication and induction, pulse formation, electron emission, etc)

ArXiv ePrint: 2107.03621

2021 JINST 16 P12026

Contents

1 Introduction

Most of the modern high energy particle physics experiments use colliding particle beams or a single beam impinging on a fixed target. Due to the high collision rate and the interaction of beam particles with matter, a hostile radiation environment is created. This radiation field is mainly composed of low energy neutrons, photons (γ), electrons/positrons ($e^{\pm}$) and charged hadrons, namely kaons ($K^{\pm}$), pions ($\pi^{\pm}$), and protons (p) [1]. These particles are commonly referred to as background particles. Due to the large interaction cross sections, background particles can cause damage to detector elements and front-end electronics [2]. Additionally, they can induce spurious signals that degrade the detector performance. A strategy for mitigating radiation effects is crucial to the design and upgrade of the LHC experimental facilities [3]. The strategy described in this paper uses estimates obtained with Monte Carlo (MC) simulation and measurements. Dedicated data taking campaigns are used to collect background data to understand the detector behaviour with respect to variations in the experimental parameters such as the instantaneous luminosity and the location of the detector element with respect to the interaction point. Additionally, new detector technologies are studied using high radiation doses in dedicated facilities such as the CERN High Energy AcceleRator Mixed Field (CHARM) [4] and the Gamma Irradiation Facility (GIF++) [5] at CERN. A set of detectors based

2021 JINST 16 P12026

on the triple-GEM technology [6] is being installed in Muon system of the Compact Muon Solenoid (CMS) detector [7] for Run-3 and the Phase-2 (High Luminosity LHC) muon upgrade program [8]. A similar technology has been adopted for the upgrade of the ALICE TPC [9]. Background studies are crucial to understand the impact of radiation on the detector performance. Detector simulations (GEANT4 [10] and FLUKA [11] in this study) that reproduce the measurements will allow us to evaluate the impact of radiation in muon detection performance. For instance, an overestimation of the neutron flux would lead to a larger probability of misreconstruction of muons. To study the radiation environment and its impact on the detector performance, dedicated simulation tools involving a description of complex physics processes and particle decay chains are used.

The present study for the CMS GE1/1 detector system extends our previous work [8, 12] and provides a foundation for future studies of the response to background particles by other detector systems in CMS and other experiments. This study includes a detailed simulation strategy and methodology, an accurate detector description, and the response of a triple-GEM detector as a function of the incident particle's kinematic properties. Variations of the detector configuration are considered to show the validity of the estimates and robustness of the simulation model. Furthermore, the simulation model is compared with experimental data collected in 2018 by the GE1/1 slice test at the CMS detector. Reliable modeling of the detector response will serve for future studies relevant to the preparation for the High Luminosity LHC [13] where the luminosity will increase by one order of magnitude and different detector technologies will be exposed to a harsher radiation environment. This work can be useful for simulation of the response of other muon systems to background particles [14, 15].

This article is organized as follows: section 2 gives an overview of the CMS GE1/1 GEM detector and the experimental setup of the detectors in the CMS experiment. Section 3 presents a simulation study of the response of a single triple-GEM detector to various particles and the simulation framework. The response and its variation as a function of energy and angle of incident particles are compared with previous simulation studies. In section 4, results for the response of superchambers for a given geometry and the actual readout conditions during the slice test are presented. A prediction of hit rates using the FLUKA simulation and its systematic uncertainties are given in sections 5 and 6. A comparison of these predictions with measurements taken during LHC running is presented in section 7, followed by a summary in section 8.

2 Overview of the CMS GE1/1 detector and slice test

2.1 CMS GE1/1 detector

The GE1/1 station in each muon endcap is upstream of the Muon Endcap Station-1 (ME1/1), as shown in figure 1 in the R-z plane. Here, R is the perpendicular distance from the beamline. The CMS coordinate system is a right-handed cartesian coordinate system with the origin at the collision point, the x-axis pointing towards the center of the LHC ring, the y-axis pointing upwards and the z-axis along the beam direction. The polar angle θ is measured from the positive z-axis to the x-y plane and the azimuthal angle ϕ is measured from the positive x-axis in the x-y plane. The pseudorapidity η is defined as $\eta = -\ln[\tan(\theta/2)]$ and gives the information about angle of particle relative to beam axis.

The GE1/1 detector system in each endcap consists of 36 superchambers where each superchamber is comprised of a pair of trapezoidal-shaped triple-GEM detectors, covering a ϕ slice of

2021 JINST 16 P12026

10.15°. The superchambers are arranged in a staggered configuration with an overlap of 0.075° to provide full 2π coverage in ϕ. The superchamber design maximizes the detection of muons. The superchambers alternate in ϕ between a long version covering a pseudorapidity region of $1.55 < |\eta| < 2.18$ and a short version covering $1.61 < |\eta| < 2.18$ (figure 2 right). The use of long and short superchambers provides maximal η coverage within the mechanical envelope of the existing endcap. The dimensions of the long and short chambers are summarized in table 1. The triple-GEM detector of a superchamber closer to the interaction point of the pp collision is called Layer-1 and the other detector of the pair is called Layer-2, as shown in figure 2 right. Moreover, each triple-GEM detector is segmented into eight η partitions, referred to as i_η (=1 to 8) and each partition has 384 radial readout strips.

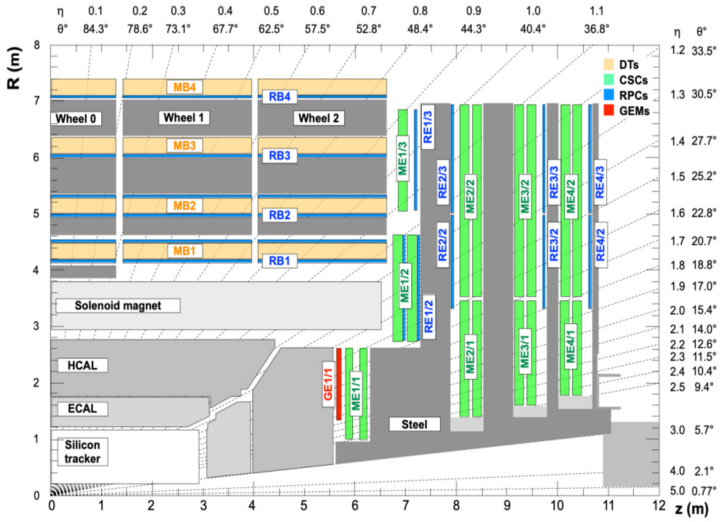

Figure 1. An *R*-*z* cross section of a quadrant of the upgraded CMS detector highlighting the location of the GE1/1 station (in red) with triple-GEM technology in the muon endcap region. Also shown are the previously existing muon stations, i.e., drift tubes (MB), cathode strip chambers (ME), and resistive plate chambers (RB, RE), and the flux-return steel yoke (dark areas).

Table 1. Dimensions of long and short trapezoidal-shaped triple-GEM detector.

Configuration	Long Chamber	Short Chamber
Height	1283.0 mm	1135.0 mm
Short Base Length	282.2 mm	282.2 mm
Long Base Length	510.0 mm	483.7 mm

2.2 GE1/1 slice test

Five triple-GEM pre-production superchambers were installed in the CMS experiment and exposed to pp collisions at 13 TeV in the period from 2017 to 2018 as shown in figure 3. This served as a demonstrator to obtain operational experience with the detector control system (DCS), the data

2021 JINST 16 P12026

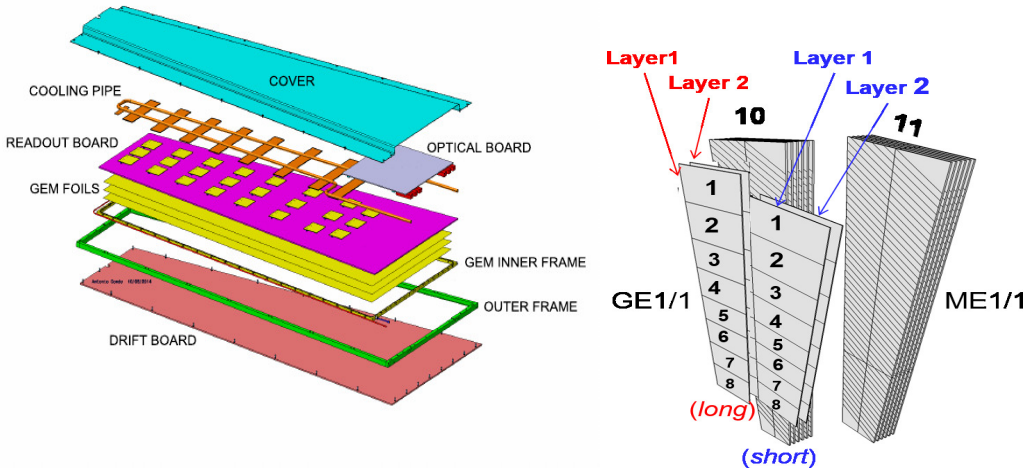

Figure 2. Single triple-GEM detector with various parts (left). Long (red) and short (blue) superchambers are mounted upstream of the ME1/1 station and cover the ranges in pseudorapidity $1.55 < |\eta| < 2.18$ and $1.61 < |\eta| < 2.18$, respectively, in a staggered configuration, with an overlap of 0.075°(right).

acquisition (DAQ) system, and the data quality monitoring (DQM) system, as well obtaining the first data to assess the performance of the detector with pp collisions. The design of these demonstrator superchambers is very similar to that of the final superchambers installed in the CMS endcap except for the use of an improved version of the front-end electronics mounted on the chamber. The improved version was realized by increasing the values of the protection resistor of each VFAT channel and the decoupling resistor for the chamber HV filter [16]. Figure 2 left shows a schematic drawing of the demonstrator chamber.

Superchambers 27, 28, 29, 30 ($\Delta\phi$ = 40°) in Slot-1 (shown in figure 3) were used to detect muons, while superchamber 1 ($\Delta\phi$ = 10°) in Slot-2 tested the upgraded electronics and a new GEM high voltage (HV) system [17] to be used in Run-3. The GE1/1 slice test chambers were operated at a gas gain amplification of ~1×10^4 with Ar/CO_2 gas mixture. Strip readout thresholds of 3 fC (i_η = 3-8), 4.0 fC (i_η = 2), and 8.8 fC (i_η = 1) were applied to the VFAT electronics based on electronic noise level. These thresholds are further discussed in detail in sections 3 and 4.

It should be noted that an irreversible channel loss was observed from April 2017 through December 2018 caused by discharges from one of the GEM foils nearest to the anode plane. As a result, only Layer-2 of superchamber 28 was operating with minimal channel loss (< 0.5%) throughout the slice test. The channel loss occurred both in the presence and the absence of particle beams in the LHC. Further details of the slice test setup and performance studies based on the data can be found in [18].

3 Response of a single triple-GEM detector to collision-induced background particles

In this section, the sensitivities (defined below) of a single triple-GEM detector of the CMS GE1/1 design, without electronics and aluminium frame, are evaluated and compared with results reported

2021 JINST 16 P12026

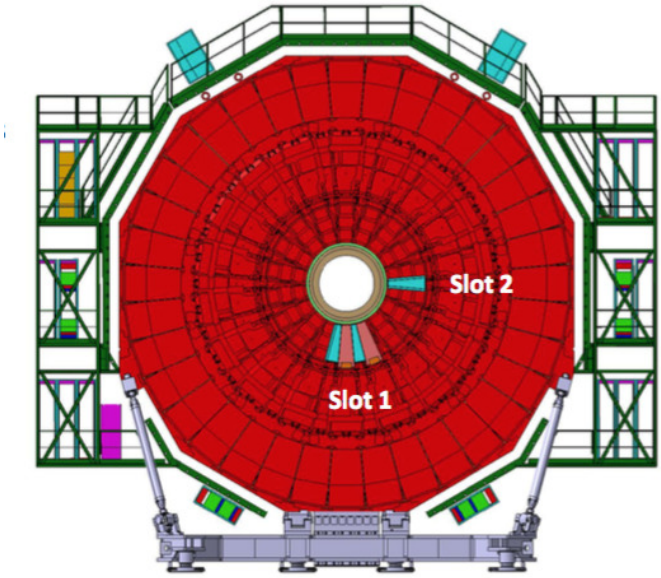

Figure 3. Schematic drawing of the negative muon endcap, showing the location of the five slice test superchambers.

in the GE1/1 Technical Design Report [8] and with studies done at the CHARM facility [12]. It should be noted that the response of the single triple-GEM detector is affected by material of other triple-GEM detectors within the superchamber.

3.1 Single triple-GEM detector geometry

The detector response is modeled using a GEANT4 [10] simulation with the geometry of a triple-GEM detector [8] and incident background particles with properties consistent with those generated in pp collisions at the LHC. A single triple-GEM detector is shown in figure 2. Chamber dimensions and material composition are presented in tables 1 and 2, respectively. Figure 4 shows a simplified schematic transverse view of a triple-GEM detector's gas gap configuration.

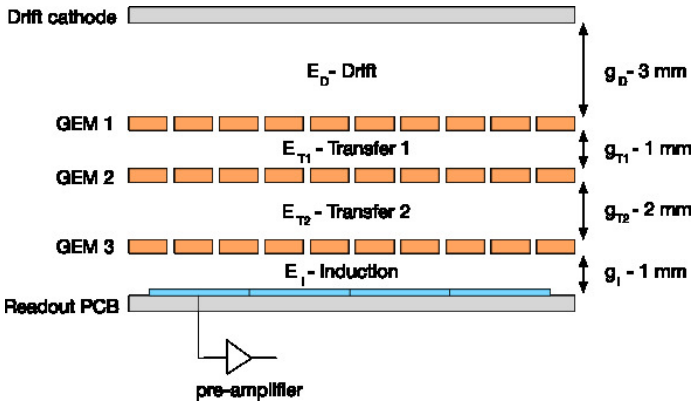

Figure 4. Representation of a transverse view of a triple-GEM detector.

2021 JINST 16 P12026

Table 2. Material and dimensions of the different layers in a single triple-GEM detector.

Layer	z-Dimensions	Material
Drift Board	35 µm / 3.2 mm / 35 µm	Copper / FR4 / Copper
Drift Gap	3 mm	Ar / CO_2
GEM1	5 µm / 50 µm / 5 µm	Copper / Kapton / Copper
Transfer-1 Gap	1 mm	Ar / CO_2
GEM2	5 µm / 50 µm / 5 µm	Copper / Kapton / Copper
Transfer-2 Gap	2 mm	Ar / CO_2
GEM3	5 µm / 50 µm / 5 µm	Copper / Kapton / Copper
Induction Gap	1 mm	Ar / CO_2
Readout Board	35 µm / 3.2 mm / 35 µm	Copper / FR4 / Copper

3.2 Simulation

The physics processes and decay chains are simulated using GEANT4 version 10.6 with the physics list recommended for standard HEP processes (FTFP_BERT_HP). The list includes all standard electromagnetic processes, the Bertini-style cascade for hadrons (<5 GeV), and the FTF (Fritiof) model for high energies (>4 GeV). It also includes a dedicated model for neutrons below 20 MeV [19].

The simulation setup has "source planes" that generate primary particles. The source planes are the same size as the drift board of the GEM detector and are located at a distance of 3 mm from the detector, on both sides. This configuration captures all possible incident angles and path lengths of the primary particles hitting the surface of the detector and traversing its sensitive volume. The response of the detector to the primary incident particles is estimated separately on each side for each source plane. The average is used to estimate the final response of the detector. Although the simulation considers the interaction of particles and the creation of secondaries in the different gaps of the triple-GEM detector, the detector response is extracted from the first two gas gaps, namely the drift and transfer-1 gaps (figure 4).

The signal induction is due to the production of a charged particle inside the detector originating from the interaction of neutral or charged background particles (e.g., neutrons, γ's, electrons, and charged hadrons). Other meaningful processes in signal evolution (such as electron drift, multiplication, charge transfer, and electronic response) are not covered in this study. Studies of the optimization of signal detection [20] using other simulation packages were used for the detailed design of the CMS GEM detectors.

The detector response is characterized using the *sensitivity* variable. *Sensitivity* is defined as the probability for a charged particle to deposit energy in the sensitive volume (e.g., Ar/CO_2 gas mixture), and to produce primary ionized electrons [8, 12]. Primary electrons go through a multiplication process, so that the charge is large enough to be detected by a readout system with charge thresholds. The charge threshold is related to the energy deposit required to separate signal

2021 JINST 16 P12026

from noise. Hence the sensitivity can be expressed as:

$$Sensitivity = \frac{N_{\text{hits}}}{N_{\text{total}}} \tag{3.1}$$

Here, N_{total} is the total number of incident particles entering the active surface of a GEM detector from any direction and N_{hits} is the number of total "hits" recorded above a certain energy threshold. The "hits" are counted for a given incident particle at a given incident energy and angle through the triple-GEM detector.

The simulated energy depositions in the first two gaps of a triple-GEM detector are converted to charge depositions using corresponding amplification factor, and required to be above the minimum threshold value of the VFAT chip. Although the readout electronics have a threshold of 3 fC, a value of 1.69 fC is used, corresponding to one electron in the drift gap, in order to study the effects of low levels of noise. Later in section 4.2, the energy thresholds are set to match the operational configuration of the GE1/1 chambers in CMS.

The minimum energy deposits required are estimated as follows:

- The gas gain amplification (G) was set to 1×10^4, corresponding to 24, 22, and 20 multiplications, respectively, in the transfer-1, transfer-2, and induction gaps.
- The readout thresholds for the strips were set to 1.69 fC for i_η = 1 to 8. Hence, to achieve this threshold a total of ~ 10547 (= 1.69 fC /1.6021$\times$ 10^{-19} C) electrons are required.
- The minimum average number of electrons required to be produced in the drift gap and the transfer-1 gap are 1 (= 10547/G) and 24 (= 10547/$G^{2/3}$), respectively.
- The effective average energy required to remove an electron due to ionization for an Ar/CO_2 gas mixture (in the ratio of 70/30) is $\langle W_i \rangle$ = 28.1 eV [21, 22]. Thus, energy losses of 28.1 eV and 674.4 eV (= 24$\times$ 28.1 eV) are needed to count as "hits" in drift and transfer-1 gaps, respectively. Those electrons produced in the drift and transfer-1 gaps are amplified by 10^4 and 440, respectively, at the readout strips. If the energy loss of a particle, simulated by GEANT4, is above the threshold, a "hit" is counted for (N_{hits}) in equation (3.1).

Due to the fact that GEANT4 does not report charged particles with a track length less than 0.7 mm [23], instead of counting secondary charged particles, we impose requirements on the amount of energy deposited in the gaps. This procedure is consistent with previously published results in ref. [12].

The detector response depends on the particle type, its kinematic properties, and the composition of the material in which the particle interacts. The dominant energy loss processes for neutrons are inelastic scattering at high energy (> 10 MeV), elastic scattering at intermediate energy (10^{-5} to 10 MeV), and neutron capture at low energy (< 10^{-5} MeV). The dominant processes for γ's are pair production at high energy (> 10 MeV), Compton scattering at intermediate energy (10^{-1} - 10 MeV), and the photoelectric effect at low energy (< 10^{-1} MeV). The dominant processes for $e^{\pm}$ are bremsstrahlung at high energy (> 1 MeV) and ionisation at low energy (< 1 MeV). Neutral particles (neutrons and γ's) interact before they produce a charged particle. The estimated sensitivity, as a function of kinetic energy and angle, is presented as a 2D map for neutrons (figure 5

2021 JINST 16 P12026

left) and γ's (figure 5 right). The one-dimensional projection of sensitivity as a function of incident energy for different particles at normal incidence to the detector is presented in figure 6 left. The sensitivity as a function of the incident angle for different particle types, at two energy values (1 and 100 MeV), is presented in figure 6 right.

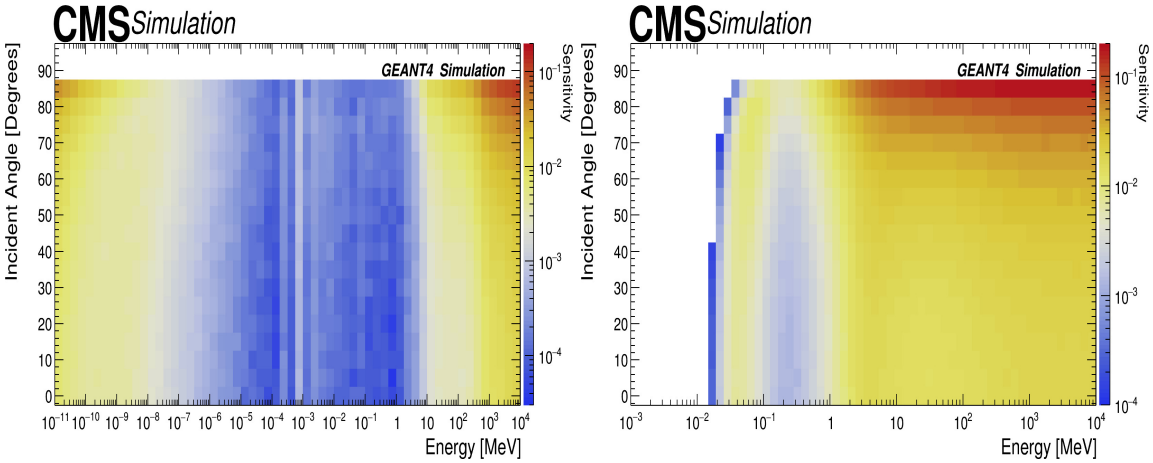

Figure 5. Sensitivity map for neutrons (left) and photons (right). The x-axis is kinetic energy and the y-axis is incident angle.

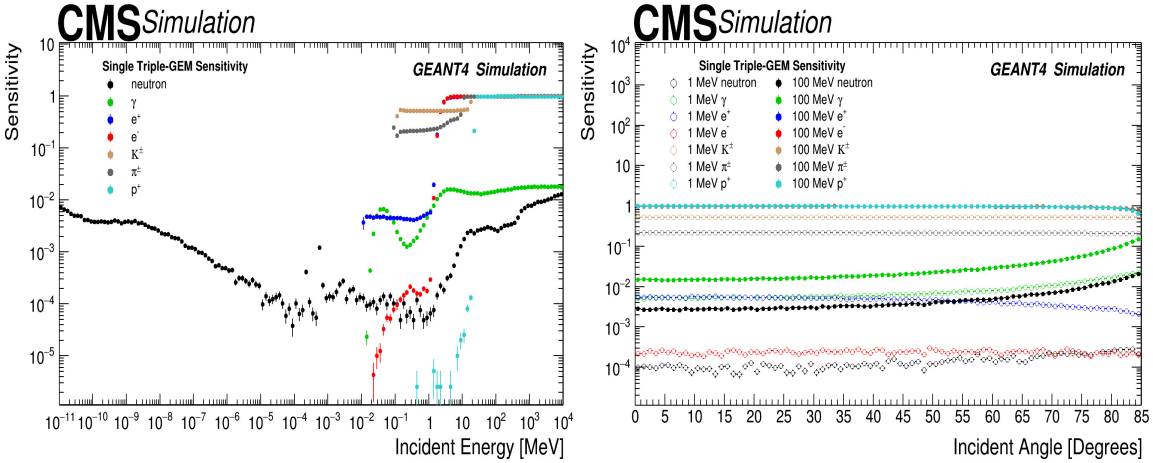

Figure 6. Sensitivity as a function of kinetic energy, for neutrons, photons and electrons, at normal incidence to the detector (left). Sensitivity as a function of incident angle for different types of particles for energy values of 1 MeV and 100 MeV (right).

The sensitivity is strongly dependent on the energy and incidence angle. The probability for an interaction is correlated to the detector width and the incidence angle. If the incidence angle increases the particle will traverse a larger distance inside the detector, so more material will be available as target for the interaction. The probability to interact is also process and energy dependent. To estimate the sensitivity, we take into account the energy spectrum of the incident particles, the energy dependent interaction probability, and the path length.

2021 JINST 16 P12026

Sensitivities are obtained using large simulated samples with $O(10^7)$ events. The statistical uncertainty depends on the type of particle under study and the region in the sensitivity map. Statistical uncertainties lie in the ranges 0-16% for neutrons, 0-2.1% for γ's, and 0-10.0% for $e^{\pm}$.

It is important to note that the sensitivities were obtained without constraints from a particular radiation environment. The only information considered was the energy ranges for the different types of particles. Thus, the results can be used for any facility in which similar triple-GEM detectors are installed [12].

The sensitivities for a single triple-GEM detector, shown in figure 6 left, are independent of the shape of the surface of the detector. These results are qualitatively similar and quantitatively compatible with those presented in ref. [12]. The main difference, for neutron sensitivity at low energies, is attributable to several reasons. The GEANT4 version used in this simulation has updated modeling for thermal neutrons. Energy thresholds for drift and transfer-1 gaps were applied in this study but not in the previous one. Lastly, the previous study simulated a detector with an additional layer of Kapton (50 µm) and FR4 (1.2 mm).

The sensitivity for photons found here is consistent with that found in the previous study. Note that a GEM detector that is part of a superchamber installed in the CMS experiment will have a response different from that of the single chamber considered here. In the following sections, the background modeling is adapted to the characteristic radiation environment of the CMS experiment and the specific detector geometry of the GE1/1 muon upgrade project.

4 Collision-induced background particles on the GE1/1 chambers

The prediction of background rate in the GE1/1 detectors requires two components: the simulation of the radiation environment and the detector response. The radiation environment is simulated with FLUKA for collision of the LHC proton beams with a center of mass energy of 13 TeV in the configuration of the CMS experiment. The simulation models particle interactions and transport through the different layers of the CMS detector. The estimation of detector response follows an approach that is similar to that described in section 3, but using the geometry of a superchamber. Both components are described in the following sections.

4.1 Radiation environment for GE1/1

The information for incoming particles reaching the GE1/1 system is extracted from a FLUKA simulation for the conditions during data-taking in Run-2, with instantaneous luminosity of 1.5×10^{34} cm^{-2} s^{-1}. The cross section of the CMS detector geometry used in the FLUKA simulation is shown in figure 7 top-left. A key property estimated with the FLUKA simulation is the flux of particles: the number of particles per unit area and per unit time weighted for their tracklength in a volume defined by the detector of interest. This distribution is presented in figure 7 top-right. Other important distributions that characterize the incoming particles are those for energy, shown in figure 7 bottom-left, and incident angle, shown in figure 7 bottom-right. These distributions are needed for the subsequent GEANT4 simulation.

The results in figure 7 are consistent with an earlier study using the FLUKA simulation [24]. The major contribution in the region where the GE1/1 detectors are located comes from low energy neutrons (10^{-11} to 10^4 MeV), γ's (10^{-3} to 10^4 MeV), $e^{\pm}$ (10^{-2} to 10^4 MeV) and charged hadrons

2021 JINST 16 P12026

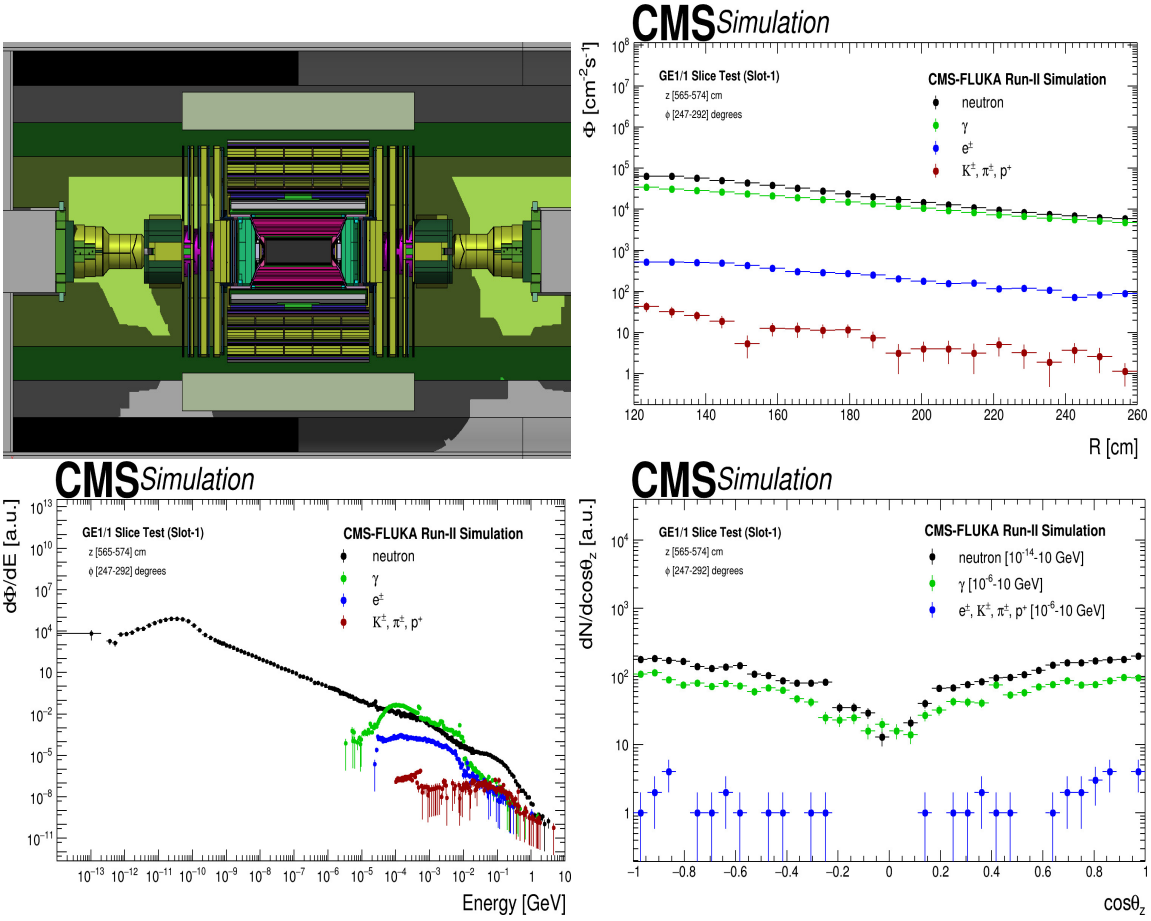

Figure 7. CMS geometry used in FLUKA simulation run v3.31.4.2 (top-left). Flux of particles, normalized to the instantaneous luminosity, arriving at the GE1/1 volume (top-right). Energy spectra of incoming particles (bottom-left) and distribution of direction cosine with respect to the normal to the detector surface for different particles (bottom-right).

(10^{-1} to 10^{4} MeV). Minor contributions to the radiation field, such as muons from gauge boson decays, are neglected as their production cross sections are an order of magnitude lower than those shown in figure 7.

4.2 Detector response for a superchamber

The detector response to background radiation depends on all the materials of the triple-GEM detector, including the electronics, cooling system, and mechanical support. The triple-GEM detectors used in the CMS experiment have additional components compared to the simple triple-GEM configuration described in section 3. Table 3 lists some of these important additional components and their details. For this study, a long chamber configuration is used, as shown in tables 1 and 2. The superchamber has a total thickness of 73.1 mm, including a space of 3.7 mm between the two detectors.

Each triple-GEM detector unit has a GEM Electronics Board (GEB) with the readout electronics and a cooling system that consists of cooling pads and cooling pipes. The cooling pipes contain

2021 JINST 16 P12026

circulating chilled water. Copper is used for the cooling pipes and pads because of its good thermal conductivity. A main component of the readout electronics for a superchamber are the VFAT-3 ASICs, based on the earlier Very Forward ATLAS and TOTEM (VFAT) ASICs [25, 26] and an Opto-Hybrid board. The VFAT-3s are used for reading, digitizing and processing the signals from the 384 strips of each η-sector of a superchamber layer. The Opto-Hybrid board is plugged into the GEB and contains Giga-Bit Transceiver (GBT) chip sets, optical receivers and transmitters, and a Field Programmable Gate Array (FPGA). Further details of the front-end electronics can be found in [8]. Figure 8 shows a GEANT4 based image of a superchamber, as used in this study.

Table 3. Additional material, layers and their dimensions used in the triple-GEM detector configuration in the CMS experiment.

Layer	z-Dimensions	Material
GEB	0.1 mm / 0.9 mm	Copper / FR4
VFAT and Opto-Hybrid	1.0 mm / 1.6 mm	FR4 / FR4
Cooling Pads	1.0 mm	Copper
Cooling Pipes	8.0 mm external, 6.0 mm internal	Copper (Filled with H_2O)
Spacers	3.0 mm / 1.0 mm / 2.0 mm / 1.0 mm	FR4
External Frame	7.2 mm	FR4
Aluminium Frame	11.5 mm	Aluminium
Cover	1.0 mm	Aluminium

The sensitivity is calculated by simulating the detailed detector configuration as described above, that is the same configuration used in the GE1/1 slice test [18]. Thresholds used in simulation are summarized in table 4 and estimated as discussed in section 3.2 but with an energy deposit threshold corresponding to 3 fC, as used in the slice test [18].

Table 4. The energy thresholds and related parameters used in the simulation of the drift and the transfer-1 gaps of the triple-GEM detector configuration. The effective gain is set to 1×10^4 and the charge threshold for readout is 3 fC.

Parameters	Drift Gap	Transfer-1 Gap
Minimum no. of electrons in the gap	2	43
Energy thresholds	56.2 eV	1.21 keV

5 Collision-induced background hit rates in GE1/1 superchambers

The hit rate is defined as the number of particles detected per unit of time in single chamber. In the slice test, the hit rate was measured for the GE1/1 superchambers as a function of instantaneous luminosity and detector area [18]. The hit rate is one of the most important quantities to measure for detector calibration and monitoring. It depends on the convolution of particle flux and sensitivities

2021 JINST 16 P12026

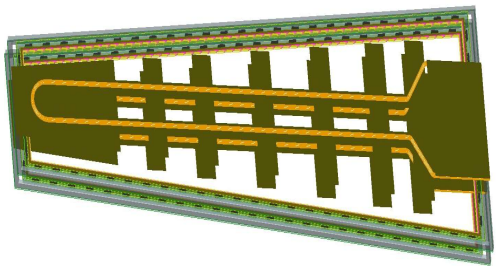

Figure 8. GEANT4 visualization of a superchamber containing two triple-GEM detectors.

for each particle type (neutrons, γ's, $e^{\pm}$, charged hadrons) as functions of energy and incident angle, as described in equation (5.1).

$$\text{Hit Rate} = \sum_{type} \text{Sensitivity}(type, E, \theta) \otimes \text{Flux}(type, E, \theta, R) \tag{5.1}$$

Here *type* is the kind of particle (*i.e.* neutrons, γ's, $e^{\pm}$ and charged hadrons), E is the energy of the incident particle and θ is the angle with respect to the normal to the detector surface. The perpendicular distance from the beamline is denoted by R. The particle flux is estimated using FLUKA as presented in figure 7 top-right and multiplied by an average sensitivity. The average sensitivity is obtained from the convolution of the sensitivity at a given energy and incident angle with the normalized abundance of particles at that energy and incident angle. The convolution over a given energy range gives the average sensitivity. The FLUKA simulation provides the information needed for all possible particle types arriving from different directions at a given position and time. The average sensitivity is used to convert the particle flux into total hits at that position.

The simulation technique used here for the sensitivity estimation is similar to that described in section 3. The main difference is that here we have a superchamber and additional material due to the presence of an extra triple-GEM detector. This affects the sensitivity of the other detector layers since sensitivity is measured for incident particles arriving at the superchamber surface from different directions. The sensitivities for Layer-2 of the superchamber, as a function of the energy of the primary incident particles arriving at the chamber surface, is shown in 9 for neutrons, photons, electrons/positrons and charged hadrons. It is convoluted over all possible incident angles and contribution from incident primary particles reaching the chamber surface from both sides are used.

The average sensitivity, estimated using the energy spectrum of the incident background particles, and the sensitivity for different energies are presented in table 5 for both Layer-1 and Layer-2. The method of using the average sensitivity is preferred over obtaining the sensitivity for different η-sectors because the detectors have a uniform response for each η-sector, as verified with X-rays during quality control tests [27].

The effect of detector material and configuration on the sensitivity can be seen by comparison of figure 6 left for the simplified geometry and figure 9 for the superchambers in the CMS experiment.

6 Systematic uncertainties

The accuracy of the sensitivity estimates relies on the correct description of the physics processes and on realistic detector modeling. The physics processes considered in this simulation are well

2021 JINST 16 P12026

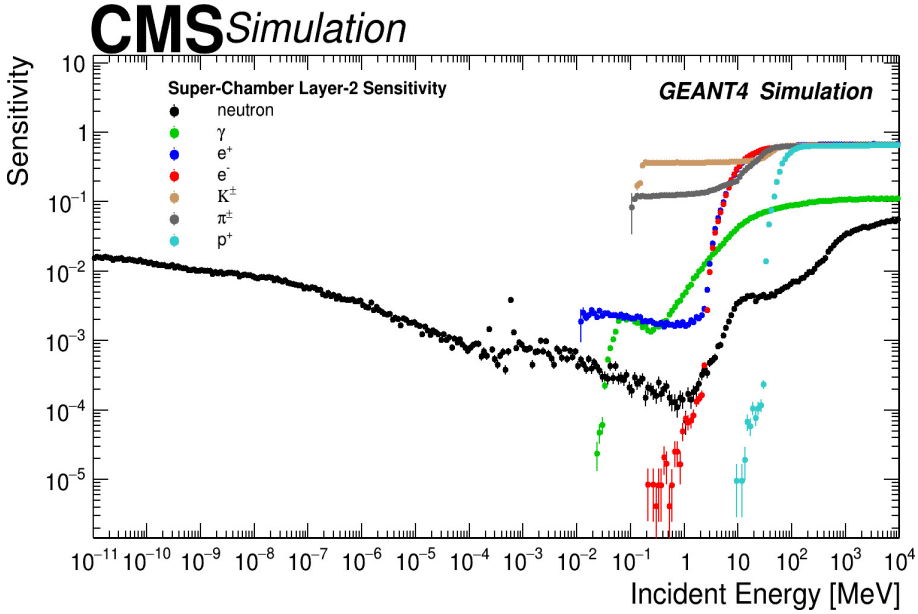

Figure 9. Sensitivity of Layer-2 as a function of incident energy for different particles. The sensitivity is convoluted over all possible incident angles.

Table 5. Average Sensitivity for each type of particle for Layer-1 and Layer-2 of the superchamber configuration used for data taking in 2018.

Particle	Average Sensitivity of Layer-1 (%)	Average Sensitivity of Layer-2 (%)
Neutron	0.64 ± 0.01 (stat.)	0.76 ± 0.01 (stat.)
γ	0.28 ± 0.01 (stat.)	0.22 ± 0.01 (stat.)
$e^{\pm}$	1.24 ± 0.04 (stat.)	0.31 ± 0.01 (stat.)
Charged Hadrons ($K^{\pm}$, $\pi^{\pm}$, p)	26.29 ± 1.24 (stat.)	24.29 ± 1.14 (stat.)

known and have been validated in the GEANT4 framework in several studies reporting comparisons with experimental data [28, 29]. To quantify the impact of the detector modeling on the sensitivity estimates the following parameters are varied.

- Drift Gap Width (DGW) variations could arise from mechanical deformations during detector assembly. Variations [8] of ±10% are used in the simulation for both layers of the superchamber. The impact on the average sensitivity of Layer-2 is shown in table 6.

- Gas Mixture Proportion (GMP) for the Ar/CO_2 (in the ratio 70/30) gas was monitored during detector operation and quality control testing and found to be negligible. However, conservative variations of (60/40) and (80/20) were considered in the simulation. The impact on the estimated average sensitivity of Layer-2 is shown in table 6.

2021 JINST 16 P12026

The impact of the parameter variations depends on the type of incident particle, kinetic energy and incident angle. We found that a single detector is less sensitive compared to the experimental configuration. The impact of parameter variations on the sensitivity for different energy ranges is also estimated. The energy ranges for neutrons are low energy (LE) from 10^{-11} to 10^{-2} MeV, intermediate energy (IE) from 10^{-2} to 1 MeV, and high energy (HE) from 1 to 10^{4} MeV. The energy ranges for γ's, $e^{\pm}$, and charged hadrons are LE from 10^{-2} to 1 MeV and HE from 1 to 10^{4} MeV. For neutrons, the maximum variation in sensitivity due to GMP variations is 1.0% for LE, 5.6% for IE, and 4.6% for HE. For γ's, $e^{\pm}$, and charged hadrons the variation in LE (HE) is estimated to be 0.8% (0.5%), 2.1% (0.3%), and 1.2% (0.1%), respectively. For DGW uncertainties, variations are similar to those for GMP, except for the neutron case in the IE region for which the statistics are low.

The systematic uncertainty is also evaluated arising from changes in the setup of the primary source near the surface of the detector. The distance of the source surface from the detector is varied by ±2 mm from the nominal value of 3 mm and the average sensitivity is re-calculated to measure the impact on the hit rate. A total variation of 0.5-0.8%, 0.0-1.0%, 0.2-0.4%, and 3.9-8.8% on the average sensitivity is estimated for neutrons, γs, $e^{\pm}$, and charged hadrons, respectively. These uncertainties are also summarized in table 6.

Table 6. Variations of simulation parameters and their impact on estimated average sensitivity. The change in sensitivity is relative to that obtained using the average sensitivity of Layer-2 shown in table 5.

Parameters	Values for Variations	Impact on average sensitivity of Layer-2 (in %)			
		Neutron	γ	$e^{\pm}$	Charged Hadrons
DGW	Drift Gap: 2.7 mm	0.6	1.4	1.0	0.5
	Drift Gap: 3.3 mm	0.3	0.4	0.0	0.6
GMP	Ar/CO_2 (60/40)	1.0	0.4	0.3	0.5
	Ar/CO_2 (80/20)	0.1	0.9	0.9	0.2
source z-position	1 mm	0.6	0.4	0.9	4.0
from superchamber	5 mm	1.0	1.4	0.9	9.9

Another systematic uncertainty comes from variation of the x-y dimensions of the source planes. The maximum variation for a 10% larger size of the source planes is about 1.3% or less for any type of incident particle. A 10% smaller size gives a maximum variation of 6.7% or less.

The uncertainties described in table 6 for different types of incident particles result in uncertainties on the hit rate. The overall uncertainty on the hit rate is dominated by neutron and photon contributions.

The systematic uncertainty associated with the particle flux is estimated by comparing the Run-2 scenario in FLUKA with an alternative scenario. In this alternative scenario, the material composition of the shielding in front of the Hadron Forward (HF) calorimeter is changed, replacing borated polyethylene by non-borated polyethylene; this change impacts the number of particles reaching the muon stations. The uncertainty is evaluated by comparing the particle flux between the two scenarios and a variation of 10 to 20% is found, depending on R, with a mean value of 15%. The latter value is considered as the associated uncertainty.

2021 JINST 16 P12026

The uncertainties in the hit rate from the FLUKA simulation and the GEANT4 detector simulation are added in quadrature. The total systematic uncertainty is about 14.5%.

7 Comparison of background modeling and experimental data

A comparison between simulation and measurement is used to validate the model presented in this study. Figure 10 compares the measured hit rate of Layer-2 of superchamber 28 with the prediction from simulation. The hit rate from simulation is obtained from the convolution of the average sensitivity shown in table 5 and the particle flux shown in figure 7 top-right. The data points in figure 10 correspond to different perpendicular distances R from the beamline to the centers of the η-sectors. As expected, the hit rate is higher at lower R (higher η) because the flux from the collision is higher in this region. The bottom panel of figure 10 shows the ratio of data to simulation and the estimated systematic uncertainty. The contributions from different types of particles to the total hit rate are shown in figure 11 for Layer-2. The largest contribution comes from neutrons while photons contribute about ~15%. Charged hadrons and $e^{\pm}$ contribute about 1% only.

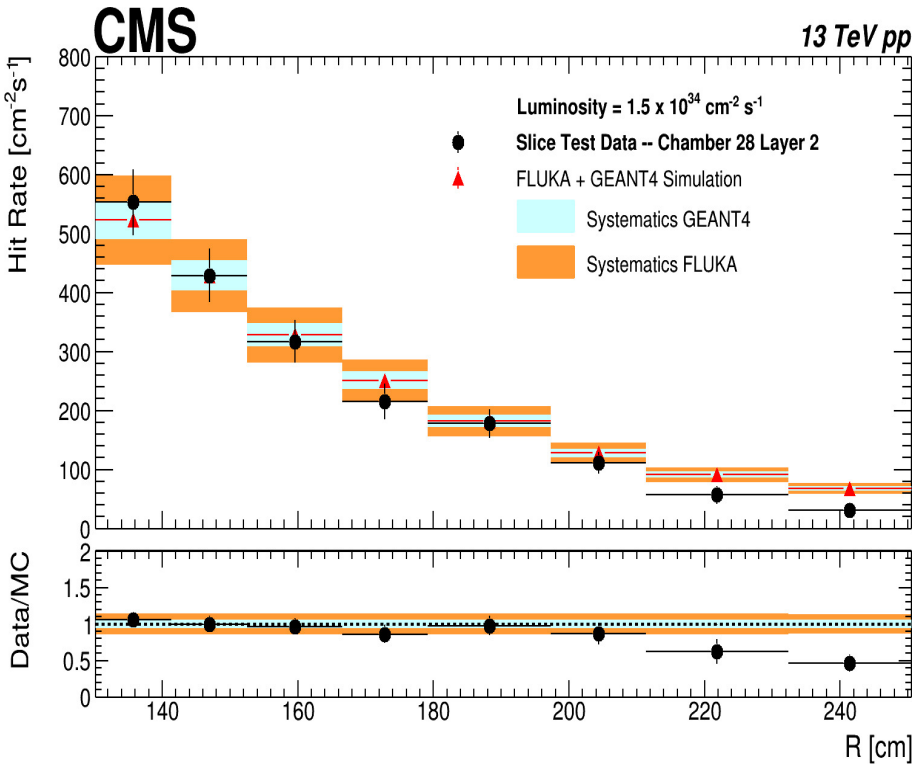

Figure 10. Comparison of the measured hit rates on Layer-2 of superchamber 28 in the slice test with the particle flux from the FLUKA simulation weighted by the sensitivity. The systematic uncertainties from the detector modelling (by the GEANT4 simulation) are shown as shaded blue bands around the prediction. The systematic uncertainties from the flux modelling for the CMS experimental configuration (by the FLUKA simulation) are shown as orange bands after adding them in quadrature with the systematic uncertainties shown in the blue band. The bottom panel shows the ratio of hit rates from data to those predicted from the simulation.

2021 JINST 16 P12026

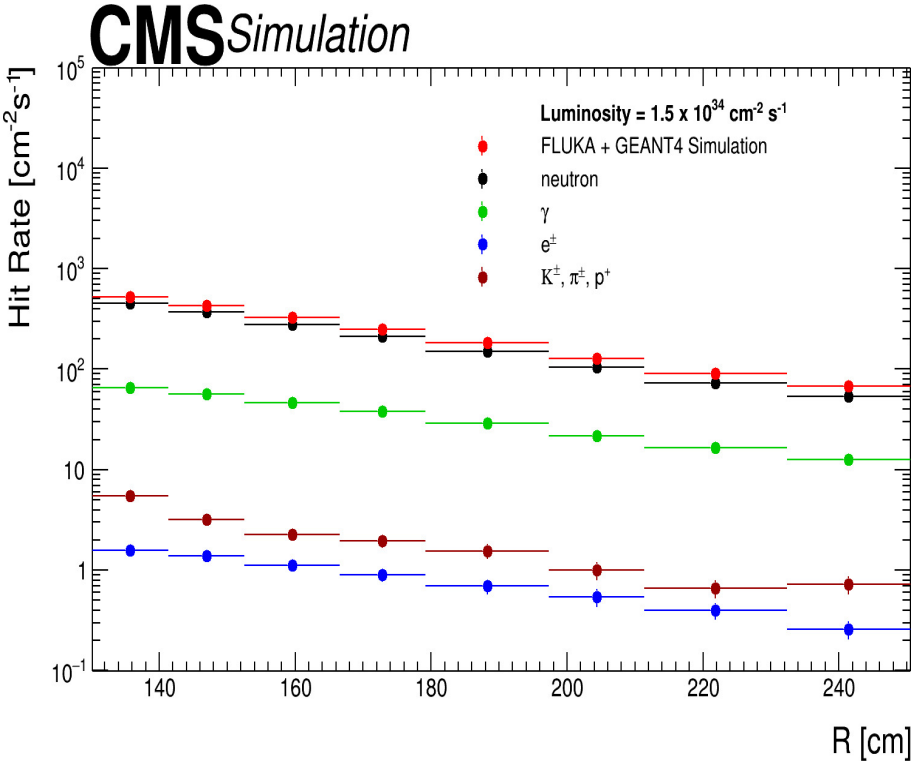

Figure 11. Prediction from simulation for hit rate contribution from different background particles at Layer-2 of superchamber 28.

The measured hit rates for the triple-GEM detector agree with those predicted from the simulation within the uncertainty except for η-sectors 1 and 2 for which data were taken with higher than nominal readout thresholds. The total uncertainty includes both the statistical uncertainty and the systematic uncertainties, described in the previous section, added in quadrature. The uncertainty of the hit rate in data includes the statistical uncertainty and uncertainties on the instantaneous luminosity measurement.

The hit rate data for $i_\eta = 1$ and 2 (sectors with $R > 210$ cm) in figure 10 are lower than the prediction. This can be explained by the higher than nominal thresholds for the VFAT-3 readout electronics during the data taking. The thresholds for $i_\eta = 1$ and 2 were 8.8 and 4.0 fC, respectively, corresponding to 6 and 3 electrons per strip in the drift gap. For $i_\eta = 1$, an energy loss of 168.6 eV ($= 6 \times 28.1$ eV) is needed to count as a "hit", resulting in a low sensitivity. In this way, the applied thresholds caused a distortion of the strip multiplicity distributions for $i_\eta = 1$ and 2. The detection efficiency for muons at $i_\eta = 1$ was most affected by the higher threshold at the strip level. While a threshold of 3 fC is low enough for our simulation model to reasonably reproduce the data, a threshold of 8.8 fC is not low enough, especially since the interaction of particles with Ar/CO_2 gas (energy loss rate) [30] and electron multiplication (gas gain) are non-linear phenomena. While it is difficult to reproduce the non-linear effects in the current simulation framework a future study could be improved with a detailed description of the electron multiplication (avalanche) e.g. using the GARFIELD [31] software package, as well as a simulation of the electronics.

2021 JINST 16 P12026

8 Summary

Collision-induced background hit rates in the CMS triple-GEM detector in pp collisions at the LHC were evaluated by modeling the radiation environment and detector response using a framework of the FLUKA and GEANT4 simulation packages. The FLUKA simulation provides kinetic energy and angular distributions of incident particles in the radiation environment. The GEANT4 simulation models particle interactions based on an accurate material description of each GEM detector. The simulated hit rates were obtained by combining the sensitivity and particle flux, and compared with measurements at a luminosity of 1.5×10^{34} cm^{-2} s^{-1} at 13 TeV. The predicted hit rates and experimental data are found to agree within their uncertainties for detector sectors with nominal operating parameters.

The framework presented in this article is generic, so it can be used for evaluation of hit rates on other detectors at High-Luminosity LHC, providing a better understanding of trigger rates and longevity of detectors.

Acknowledgments

We gratefully acknowledge support from FRS-FNRS (Belgium), FWO-Flanders (Belgium), MES and BNSF (Bulgaria), MOST and NSFC (China), BMBF (Germany), CSIR (India), DAE (India), DST (India), UGC (India), INFN (Italy), NRF (Korea), CONACYT (Mexico), MoSTR (Sri Lanka), DOE (U.S.A.), and NSF (U.S.A.).

References

[1] M. Huhtinen, *The radiation environment at the CMS experiment at the LHC*, master thesis, HU-SEFT-R-1996-14, Helsinki U. Tech., Helsinki, Finland (1996).

[2] Y. Musienko, A. Heering, R. Ruchti, M. Wayne, A. Karneyeu and V. Postoev, *Radiation damage studies of silicon photomultipliers for the CMS HCAL phase I upgrade*, *Nucl. Instrum. Meth. A* **787** (2015) 319.

[3] CMS collaboration, *The CMS muon project: technical design report*, Tech. Rep. CERN-LHCC-97-032, CERN, Geneva, Switzerland (1997) [CMS-TDR-3].

[4] R. Froeschl, M. Brugger and S. Roesler, *The CERN High Energy Accelerator Mixed Field (CHARM) facility in the CERN PS east experimental area*, in *Proceedings, 12th meeting of task-force on shielding aspects of accelerators, targets and irradiation facilities*, (SATIF-12), Batavia, IL, U.S.A., 28–30 April (2014).

[5] D. Pfeiffer et al., *The radiation field in the Gamma Irradiation Facility GIF++ at CERN*, *Nucl. Instrum. Meth. A* **866** (2017) 91 [arXiv:1611.00299].

[6] F. Sauli, *The Gas Electron Multiplier (GEM): operating principles and applications*, *Nucl. Instrum. Meth. A* **805** (2016) 2.

[7] CMS collaboration, *The CMS experiment at the CERN LHC*, 2008 *JINST* **3** S08004.

[8] A. Colaleo, A. Safonov, A. Sharma and M. Tytgat, *CMS technical design report for the muon endcap GEM upgrade*, Tech. Rep. CERN-LHCC-2015-012, CERN, Geneva, Switzerland (2015) [CMS-TDR-013].

[9] ALICE TPC collaboration, *Development of GEM-based read-out chambers for the upgrade of the ALICE TPC*, 2014 *JINST* **9** C04035.

2021 JINST 16 P12026

[10] GEANT4 collaboration, *GEANT4 — a simulation toolkit*, *Nucl. Instrum. Meth. A* **506** (2003) 250.

[11] A. Ferrari, P.R. Sala, A. Fassò and J. Ranft, *FLUKA: a multi-particle transport code (program version 2005)*, CERN yellow reports monographs CERN-2005-010, CERN, Geneva, Switzerland (2005),

[12] CMS Muon Group collaboration, *Triple-GEM discharge probability studies at CHARM: simulations and experimental results*, 2020 *JINST* **15** P10013.

[13] D. Contardo, M. Klute, J. Mans, L. Silvestris and J. Butler, *Technical proposal for the phase-II upgrade of the CMS detector*, Tech. Rep. CERN-LHCC-2015-010, CERN, Geneva, Switzerland (2015) [LHCC-P-008] [CMS-TDR-15-02].

[14] CMS collaboration, *Background rate study for the CMS improved-RPC at HL-LHC using GEANT4*, *Nucl. Instrum. Meth. A* **936** (2019) 430.

[15] C.U. Estrada et al., *RPC radiation background simulations for the high luminosity phase in the CMS experiment*, 2019 *JINST* **14** C09045.

[16] F. Ivone, *Discharge mitigation strategies for the CMS GE1/1 triple-GEM detectors*, 2020 *JINST* **15** C05009.

[17] M. Abbas et al., *Detector control system for the GE1/1 slice test*, 2020 *JINST* **15** P05023.

[18] M. Abbas et al., *Performance of a triple-GEM demonstrator in pp collisions at the CMS detector*, 2021 *JINST* **16** P11014 [arXiv:2107.09364].

[19] GEANT4 collaboration, *Physics reference manual*, in *GEANT4 — a simulation toolkit. Manual* **1** (2019) 1.

[20] M. Abi Akl, O. Bouhali, A. Castaneda, Y. Maghrbi and T. Mohamed, *Uniformity studies in large area triple-GEM based detectors*, *Nucl. Instrum. Meth. A* **832** (2016) 1.

[21] A. Sharma, *Properties of some gas mixtures used in tracking detectors*, SLAC-J-ICFA-16-3, (1998) [SLAC-JOURNAL-ICFA-16-3].

[22] F. Sauli, *Principles of operation of multiwire proportional and drift chambers*, CERN-77-09, (1977).

[23] Geant4 collaboration, *Recent developments in GEANT4*, *Annals Nucl. Energy* **82** (2015) 19.

[24] D. Abbaneo, *Impact of the radiation background on the CMS muon high-eta upgrade for the LHC high luminosity scenario*, *PoS* **TIPP2014** (2014) 086.

[25] P. Aspell et al., *VFAT2: a front-end "system on chip" providing fast trigger information and digitized data storage for the charge sensitive readout of multi-channel silicon and gas particle detectors.*, *IEEE Nucl. Sci. Symp. Conf. Rec.* (2008) 1489.

[26] P. Aspell et al., *VFAT3: a trigger and tracking front-end ASIC for the binary readout of gaseous and silicon sensors*, *IEEE Nucl. Sci. Symp. Med. Imag. Conf. Rec.* (2018) 1.

[27] M. Abbas et al., *Performance of prototype GE1/1 chambers for the CMS muon spectrometer upgrade*, *Nucl. Instrum. Meth. A* **972** (2020) 164104.

[28] A. Howard, G. Folger, J.M. Quesada and V. Ivanchenko, *Validation of neutrons in GEANT4 using TARC data — production, interaction and transportation*, *IEEE Nucl. Sci. Symp. Conf. Rec.* (2008) 2885.

[29] J. Apostolakis et al., *Validation and verification of GEANT4 standard electromagnetic physics*, *J. Phys. Conf. Ser.* **219** (2010) 032044.

[30] Particle Data Group collaboration, *Review of particle physics*, *PTEP* **2020** (2020) 083C01.

[31] R. Veenhof, *GARFIELD, recent developments*, *Nucl. Instrum. Meth. A* **419** (1998) 726.

2021 JINST 16 P12026

Chapter 136
Q-PET: PET with 3rd Eye Quantum Entanglement Based Positron Emission Tomography

Sunil Kumar, Sushil Singh Chauhan, and Vipin Bhatnagar

Abstract In the present ongoing study, we proposed a prototype model by the introduction of a new discriminatory window parameter, which can be a new-generation PET detection technique. Positron Emission Tomography (PET) detection technique involves a coincidence detection technique to correlate the two annihilation photons. We introduced polarization measurement of the annihilation photons as an additional parameter in our proposed prototype to correlate annihilation photons of particular annihilation event. The motivation behind this introduction is quantum entanglement relation between the two photons. Simulation studies for this research work are undergoing and some preliminary results were presented.

136.1 Introduction

Medical imaging is the field in which radiation is used for imaging the body of the diseased patient. For this purpose, many such systems have been developed to serve the mankind. X-ray radiography, Computed Tomography (CT), Ultrasonography, Magnetic Resonance Imaging, Nuclear Medicine Imaging and Positron Emission Tomography (PET) are some techniques generally used in medical imaging. Out of these, PET is widely used for the staging, restaging, drug and therapy response of patients diagnosed with cancer. PET enables us to get morphological imaging of biodistribution of positron-emitting radionuclide or radiopharmaceutical injected in the body of the patient/animal. Current PET detection technique involves coincidence detection technique to correlate the two annihilation photons emitted in the almost

S. Kumar (✉) · S. S. Chauhan · V. Bhatnagar
Department of Physics, Panjab University, Chandigarh 160014, India
e-mail: s.kumar@cern.ch

S. S. Chauhan
e-mail: schauhan@cern.ch

V. Bhatnagar
e-mail: Vipin.Bhatnagar@cern.ch

P. K. Behera et al. (eds.), *XXIII DAE High Energy Physics Symposium*,
Springer Proceedings in Physics 261,
https://doi.org/10.1007/978-981-33-4408-2_136

exactly opposite direction detected by a ring-type scintillation-based detection system [1].

To reconstruct the raw data in an informative PET image, one needs to investigate exactly the true events with paired photons from the random, scattered and multiple events [2].

False coincidences introduce noise and contrast lost in the reconstructed image and also enhance the chances of misinterpretation. PET systems involve the two windows for the selection of true events which are energy window and timing window. At present, time and energy windowing, which are applied over the primary coincidence data, discard all multiple events, as well as a considerable fraction of unscattered coincidence events due to the relatively poor energy resolution of current detectors [2].

Besides these parameters for the selection of true coincidence, there is another parameter which, possibly can accurately measure the true coincidence.

136.2 Motivation

The motivation towards this work comes from the fact that using Compton scattering, we can find the polarization of the photons and that can be used to identify the correlated true annihilation photons. Two photons emitted are linearly polarized such that the polarization vectors are orthogonal to each other, i.e. having a quantum entangled state in which both the photons have their planes of polarization perpendicular to each other [3]. This quantum entangled state can work as a discriminatory window for the identification of true annihilation events after clearing the first two windows. So if one can measure the polarization of each photon and can identify the orthogonal relation between them, this technique can work as a powerful tool to identify accurately the two annihilation photons.

136.3 Method

Compton cross section depends on the photon polarization and this dependence make us able to calculate polarization of the photons involved in the annihilation process [4]. It is also implied by Quantum Electrodynamics that the two photons emitted in an electron–positron annihilation process are polarized orthogonal(perpendicular) to each other [4]. In this study we have planned for using the angular correlation between Compton scattered photons. For this purpose, Klein–Nishina Model for Compton Scattering will be used as a theoretical basis. A GEANT4 Simulation will provide the requisite variables for the calculations of the angular correlation.

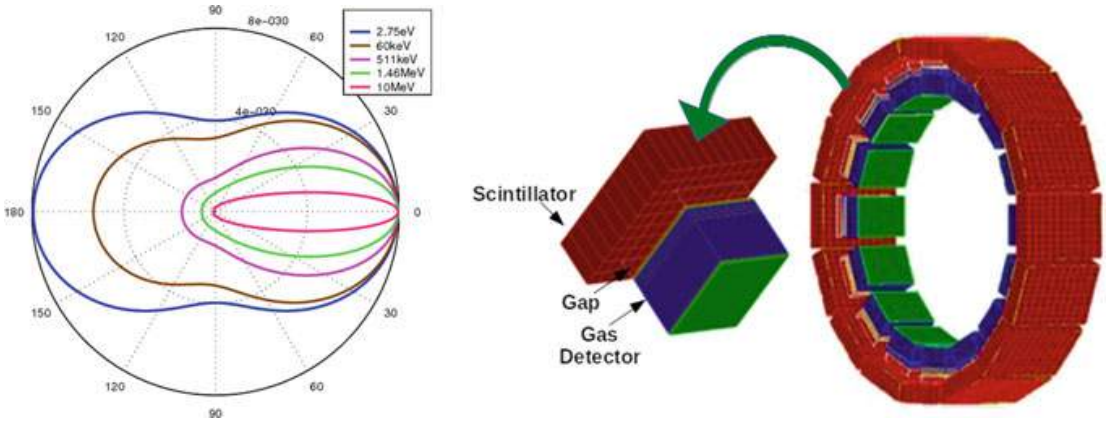

Fig. 136.1 Klein–Nishina Differential Cross Section for different energies (left) and a GEANT4 constructed geometry for the proposed prototype (right)

The differential cross section of Compton scattering [5] is expressed as

$$\frac{d\sigma}{d\Omega} = \frac{r_0^2}{2}\left(\frac{E'}{E}\right)^2\left(\frac{E}{E'} + \frac{E'}{E} - 2\sin^2\theta\cos^2\eta\right), \tag{136.1}$$

where

r_0 = classical electron radius, E = energy of incident γ ray, E' = energy of scattered γ ray, θ = angle of scattering, η = angle between plane of scattering & plane of polarization.

136.4 Prototype

136.4.1 Geometry

Q-PET consists of 16 units of detector arranged in a ring of inner radius 30.78 cm and outer radius 47.04 cm. Each unit consists of one gaseous detector (Scatterer/Tracker) and one scintillation block.

136.4.1.1 Tracker/Scatterer

In Tracker Section, Gas Chamber has been introduced for tracking purposes. Material used for the gas chamber is $Xe\mathrm{CO}_2C_4F_{10}$ in proportion $Xe(50\%)$, $\mathrm{CO}_2(15\%)$, $C_4F_{10}(35\%)$. The material ($Xe\mathrm{CO}_2C_4F_{10}$) so chosen for the gas detector contains Xenon, which is the highest density Noble gas can be used for the proportional chambers. To increase the probability of 511 keV photons interaction with gas molecule, density of the gas should be large. Besides this one has to consider some factor, i.e. interaction cross section for the desired process, density should be enough to have the interaction probability to get the Compton interaction.

Gas detector has dimension 10 cm × 10 cm × 8.96 cm. Gaseous detector will provide the position of very first interaction of annihilation photon in the gaseous medium. Signal generated by the gaseous detector also gives information on the track of recoil electron. Time Projection Chamber (TPC) configuration can be used to get the third coordinate (depth of interaction) point. Besides that, some other methods are there to get the depth of interaction point.

Tracking of recoil electron can provide the additional benefit of getting the real direction of gamma-ray entrance within some uncertainty. This feature is very important for large diameter scanners.

136.4.1.2 Scintillator

In Scintillator Section, $CdWO_4$ crystals are used to absorb the scattered gamma ray completely. Scintillation Block of each unit have 10 × 10 arrangement of crystals of dimension 1.58 cm × 1.58 cm × 5 cm each. This section will provide position and energy of the scattered gamma ray.

136.5 Summary and Future Work

The polarization measurement technique can work as a discriminatory window for the identification of annihilation photons. Presently, working to improve the interaction probability with the analysis of the simulation data and simulation for the differential cross-sectional data needed for the polarization calculation. We will update and publish the results soon.

Acknowledgements Sushil Singh Chauhan, Sunil Kumar and Vipin Bhatnagar offer sincere gratitude to UGC, CSIR & DST for the financial support.

References

1. M.E. Phelps, PET Physics, Instrumentation and Scanner (Springer) ISBN-13: 978-0387-32302-2
2. M. Toghyani, J.E. Gillam, A.L. McNamara, Z. Kuncic, Polarization-based coincidence event discrimination, an in silico study towards a feasible scheme for Compton-PET. Phys. Med. Biol. **61**, 5803–5817 (2016)
3. D. Robley, *Evans: the Atomic Nucleus* (TATA McGRAW-HILL Publishing Company LTD, Bombay, New Delhi, 1955)
4. N. Carlin, P. Woit, Theory of angular correlation of annihilation radiation. In: The Angular Correlation of Polarization of Annihilation Radiations. Available online http://www.math.columbia.edu/~woit/angular.pdf
5. W. Hajdas, Estela Suarez-Garcia: Polarimetry at High Energies. ISSI Scientific Reports Series, ESA/ISSI. (2010), pp. 559–571 ISBN 978-92-9221-938-8

Chapter 158
Sensitivity of Triple-GEM Detectors for Background Radiation in CMS Experiment

S. Kumar, O. Bouhali, V. Bhatnagar, A. Castaneda, S. S. Chauhan, T. Kamon, Y. Kang, and A. K. Virdi

Abstract The collider experiments of the modern era produce an extreme environment of radiation fields. It becomes quite challenging to operate the detectors in such an environment as the high-radiation background complicates the particle identification. Particles produced in proton–proton (pp) collisions interact with the beam pipe, shielding and the other detector supporting materials to produce charged hadrons and neutrons along with photons, electrons and positrons. These particles interact with the surrounding material acting as a common background radiation field for the CMS detector. CMS has installed new muon detectors based on Gas Electron Multiplier (GEM) technology at the endcap station 1 ($1.55 < |\eta| < 2.18$), called GE1/1. In this study, an estimation of the GE1/1 detector response to background radiation is presented using the FLUKA and GEANT4 frameworks.

S. Kumar, O. Bouhali, V. Bhatnagar, A. Castaneda, S. S. Chauhan, T. Kamon, Y. Kang, A. K. Virdi—for the CMS Collaboration.

O. Bouhali
Texas A&M University, Doha, Qatar

S. Kumar (✉) · V. Bhatnagar · S. S. Chauhan · A. K. Virdi
Panjab University, Chandigarh, India
e-mail: s.kumar@cern.ch

A. Castaneda
Universidad de Sonora, Hermosillo, Mexico

T. Kamon
Texas A&M University, College Station, TX, USA

Y. Kang
University of Seoul, Seoul, South Korea

B. Mohanty et al. (eds.), *Proceedings of the XXIV DAE-BRNS High Energy Physics Symposium, Jatni, India*, Springer Proceedings in Physics 277,
https://doi.org/10.1007/978-981-19-2354-8_158

158.1 Introduction

The sensitivity to new physics is expected to increase with a series of upgrades of the Large Hadron Collider (LHC) to the so-called High Luminosity-LHC (HL-LHC) [1]. The Compact Muon Solenoid (CMS) experiment [2] must follow the LHC evolution and perform detector upgrades to fully exploit the collisions at higher energy and higher luminosity. The goal of the CMS upgrade is to improve the physics performance of the detector subsystems and optimize the particle reconstruction for LHC luminosity up to $5 - 7 \times 10^{34}$ cm^{-2} s^{-1}. The rise in collision rate due to higher luminosity will increase the background rate in the forward region of the CMS muon endcaps. This background radiation field is mainly composed of low energy neutrons, photons (γ), electrons/positrons ($e^{\pm}$) and charged hadrons, namely, kaons ($K^{\pm}$), pions ($\pi^{\pm}$) and protons (p) [3]. These background particles can cause damage to detector elements and front-end electronics [4], additionally, they can induce spurious signals that degrade detector performance. This work is related to the first GE1/1 endcap station. The background rate is predicted using FLUKA [5] and GEANT4 [6] simulations.

158.2 Motivation

With the aim of gaining operation experience and demonstrating the integration of the GE1/1 system into the trigger, five superchambers (a combination of two single trapezoidal-shape triple-GEM detector) were installed as an exercise at the positions shown in Fig. 158.1. This exercise is known as GE1/1 Slice Test [7].

Superchambers 27, 28, 29, 30 ($\Delta\phi = 40°$) in Slot-1 are dedicated to muon rate, while superchamber 1 ($\Delta\phi = 10°$) in Slot-2 is to test electronics and a new high-voltage system. The triple-GEM [9] detector of a superchamber facing towards the interaction point of pp collisions is called "layer-1", while the one facing outwards is called "layer-2" and comes in two flavors; "Long" and "Short". The background

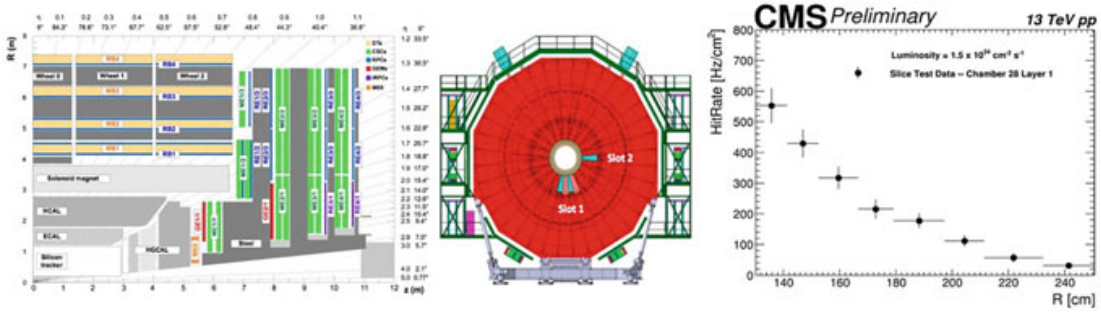

Fig. 158.1 GE1/1 (red) is the position of installation of Slice Test detetcors (left). Second from left in slot-1 of light pink colour is chamber 28 (middle). Background hit-rate data from GE1/1 Slice Test for chamber 28 layer 2 [8] (right)

rate for chamber 28 layer-2 is analyzed and a function of perpendicular distance R from beam-line using the zero-bias data is shown in Fig. 158.1. The motivation is to predict the experiential data within some uncertainty so that we can estimate the background rates in Run-3 and for future upgrades.

158.3 Method

For the calculation of the background rate in the GE1/1, the following method is used:

$$\text{Hit-Rate} = \sum_{part} \text{Flux}\,(part, E, \theta, \text{R}) \bigotimes \text{Sensitivity}\,(part, E, \theta),$$

where "$part$" is the type of particle (neutron, γ, $e^{\pm}$ and charged hadrons), E is the energy of the incident particle and θ is the angle with respect to the axis perpendicular to the detector surface. The GE1/1 response to background particles is termed "Sensitivity". Sensitivity is defined as the probability of a particle to deposit energies greater than a defined threshold in the sensitive volume, producing primary ionized electrons.

The flux is multiplied by an average sensitivity obtained convoluting the sensitivity at a given energy and incident angle with the normalized fraction of particles at that energy and incident angle. The integration of this convolution over a given energy range gives the average sensitivity shown in Fig. 158.2.

158.4 Simulation

As mentioned in the previous section, the flux entering the GE1/1 detector and the average sensitivity of the GE1/1 detector are required for the hit rate calculation. The flux and sensitivity are estimated using FLUKA and GEANT4, respectively.

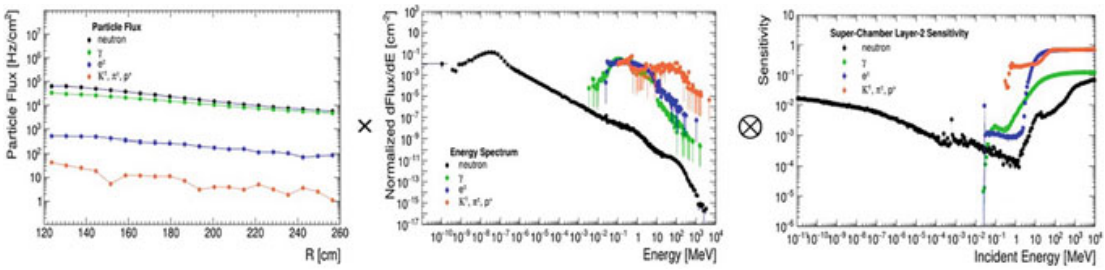

Fig. 158.2 Particle-flux (left) normalized energy distribution (middle) and sensitivity distribution (right) for different particles

158.4.1 FLUKA Simulation

FLUKA v2011-3.0 simulation including the effect of magnetic field in the CMS, Run-2 geometry version 3.31.4.2 is used to estimate the flux and differential energy spectrum of all the particles.

158.4.2 GEANT4 Simulation

The physics processes and decay chains are modeled using GEANT4 v10.6 and the recommended physics list for standard HEP processes (`FTFP_BERT_HP`). The simulation setup consists of a source plane, of the same size as the drift board of the GEM detector, for primary particle generation at a distance of 3 mm from the surface of the detector on both sides. Energy range used for different particles are 10^{-3}–10^{4} MeV for neutrons, 10^{-3}–10^{4} MeV for γ's, 10^{-2}–10^{4} MeV for $e^{\pm}$ and 10^{-1}–10^{4} MeV for charged hadrons ($K^{\pm}$, $\pi^{\pm}$, p).

158.4.3 A Single Triple-GEM Detector

A simplified single triple-GEM detector geometry is simulated for the general response. The sensitivity of the GEM detector is studied as a function of the energy and the angular distribution of each particle.

158.4.4 Superchamber

To compare the prediction with experimental data, a superchamber geometry has been simulated to obtain the right plot in Fig. 158.2 for chamber 28 layer-2. This geometry includes all the components, i.e. pull-outs, readout electronics and cooling system as explained in [10].

Table 158.1 shows the average sensitivity of background particles is not same for Layer-1 and Layer-2. It depends on the particle and the interacting material, i.e. for neutron, the average sensitivity for Layer-1 is less as compared to Layer-2 because of the combined effect of the cooling material (Cu) of both the layers.

Table 158.1 Average Sensitivity for each type of particle for the layer-1 and layer-2 of the super-chamber configuration used in CMS data taking in 2018

Particle	Average sensitivity of layer-1 (%)	Average sensitivity of layer-2 (%)
Neutron	0.63 ± 0.01 (stat.)	0.75 ± 0.01 (stat.)
γ	0.29 ± 0.01 (stat.)	0.20 ± 0.01 (stat.)
$e^{\pm}$	1.18 ± 0.03 (stat.)	0.31 ± 0.01 (stat.)
Charged Hadrons	27.0 ± 1.3 (stat.)	25.1 ± 1.2 (stat.)
($K^{\pm}$, $\pi^{\pm}$, p)		

158.5 Conclusion

A comparison of data and simulation was used to validate the FLUKA+GEANT4 model presented in this study. For example, the simulation agrees with the hit rate 600 Hz/cm^2 at 1.5×10^{34} cm^{-2} s^{-1} for $i_\eta = 8$ [10] from the GE1/1 Slice Test within its uncertainties. This model helps us to improve the background hit rate estimation in Run-3 and at HL-LHC.

References

1. C.M.S. Collaboration, The phase-2 upgrade of the CMS muon detectors. CERN-LHCC-2017-012 (2017) CMS-TDR-016 (2017)
2. C.M.S. Collaboration, The CMS experiment at the CERN LHC. JINST **3**, S08004 (2008)
3. M. Huhtinen, The radiation environment at the CMS experiment at the LHC. Master Thesis, (1996)
4. Y. Musienko et al., Radiation damage studies of silicon photomultipliers for the CMS HCAL phase I upgrade. Nucl. Instrum. Methods A **787**, 319–322 (2015)
5. A. Ferrari, R.P. Sala, A. Fasso, J. Ranft, FLUKA: a multi-particle transport code (Program version 2005), CERN-2005-010; INFN-TC-2005-11; SLAC-R-773
6. GEANT4 Collaboration, GEANT4 a simulation toolkit. Nucl. Instrum. Methods A **506**, 250–303 (2003)
7. M. Abbas et al., Detector control system for the GE1/1 slice test. JINST **15**, P05023 (2020)
8. CMS Collaboration, Environmental background hit rate on GE1/1 in the 2018 slice test. CERN-CMS-DP-2020-053, http://cds.cern.ch/record/2749429 (2020)
9. F. Sauli, Principles of operation of multiwire proportional and drift chambers. 5CERN-77-09 (1977)
10. CMS Technical design report for the muon endcap GEM upgrade. CERN-LHCC-2015-012 (2015), [CMS-TDR-013]

Radiation background estimation for the GE11 Triple-GEM detectors in the CMS endcap

Journal of Physics: Conference Series **2374** (2022) 012161 doi:10.1088/1742-6596/2374/1/012161

Radiation background estimation for the GE11 Triple-GEM detectors in the CMS endcap

O Bouhali[1], V Bhatnagar[2], A Castaneda[3], S S Chauhan[2], T Kamon[4], Y Kang[5], S Kumar[2] and A K Virdi[2] on behalf of the CMS collaboration

[1] Texas A&M University, Qatar
[2] Panjab University, Chandigarh, India
[3] Universidad de Sonora, Mexico
[4] Texas A&M University, USA
[5] University of Seoul, South Korea

E-mail: s.kumar@cern.ch

Abstract. The Compact Muon Solenoid (CMS) is a general-purpose particle detector at the Large Hadron Collider (LHC) designed to study a wide range of particles produced in high energy collisions. The interaction of the beams with the pipe, shielding and detector supporting materials can produce neutrons, photons, electrons and positrons, forming a common background radiation field for CMS detector. A Monte-Carlo simulation is used to predict the background rate for a newly installed detector. In the forward region, the upgrade includes Gas Electron Multiplier (GEM) detectors called GE1/1. In this study, an estimate of the GE1/1 detector response to the background radiation is presented. The flux of background radiation is predicted using the FLUKA framework and the response of the detector is predicted using the GEANT4 framework. A comparison with actual GEM slice data is used as validation.

1. Introduction

The sensitivity to new physics of the Large Hadron Collider (LHC) is expected to increase with a series of upgrades to the so-called High Luminosity-LHC (HL-LHC) [1]. The Compact Muon Solenoid (CMS) experiment [2] must follow the LHC evolution and perform detector upgrades to fully seize the increased energy and luminosity. The goal of the CMS upgrade is to improve physics performance of detector subsystems and optimize the particle reconstruction for LHC luminosity up to 5 - 7 $\times$ 10^{34} cm^{-2} s^{-1}. The rise in collision rate with higher luminosity will increase the background rate in the forward region of the CMS muon endcaps. This background radiation field is mainly composed of neutrons, photons (γ), electrons/positrons ($e^{\pm}$) and charged hadrons, namely kaons ($K^{\pm}$) , pions ($\pi^{\pm}$), protons (p) [3]. These background particles can cause damage to detector elements and front-end electronics [4], additionally they can induce spurious signals that degrade detector performance. The GE1/1 background rate is predicted using FLUKA [5] and GEANT4 [6] simulations.

With the aim of gaining operational experience and demonstrating the integration of the GE1/1 system into the trigger, five superchambers (a combination of two single trapezoidal shape triple-GEM detector) were installed as an exercise known as GE1/1 Slice Test [7]. The background data for one of the superchambers (chamber 28 layer-2) was analyzed and hit rate

as a function of perpendicular distance R from beam-line was obtained using the zero-bias data [8]. The motivation is to predict the expected hit rate from data within some uncertainty, so that we can estimate the background rates in Run-3 and for future upgrades.

2. Method

For the calculation of the background rate in the GE1/1, the following method is used:

$$\text{Hit-Rate} = \sum_{particle\text{-}type} \text{Flux}\ (particle\text{-}type,\ E,\ \theta,\ \text{R}) \otimes \text{Sensitivity}\ (particle\text{-}type,\ E,\ \theta)$$

where "*particle-type*" is the type of particle (neutron, γ, $e^{\pm}$ and charged hadrons), E is the energy of the incident particle and θ is the angle with respect to the axis perpendicular to the detector surface. The GE1/1 response to background particles is termed as "Sensitivity". Sensitivity is defined as the probability for a charged particle to deposit energy in the sensitive volume (e.g., Ar/CO_2 gas), producing primary ionized electrons [9] which go through a multiplication process, so that the charge is large enough to be detected by a readout system with charge thresholds. Flux is multiplied by the average sensitivity obtained by integrating the convolution of sensitivity at a given energy and incident angle with the normalized fraction of particles at that energy and incident angle.

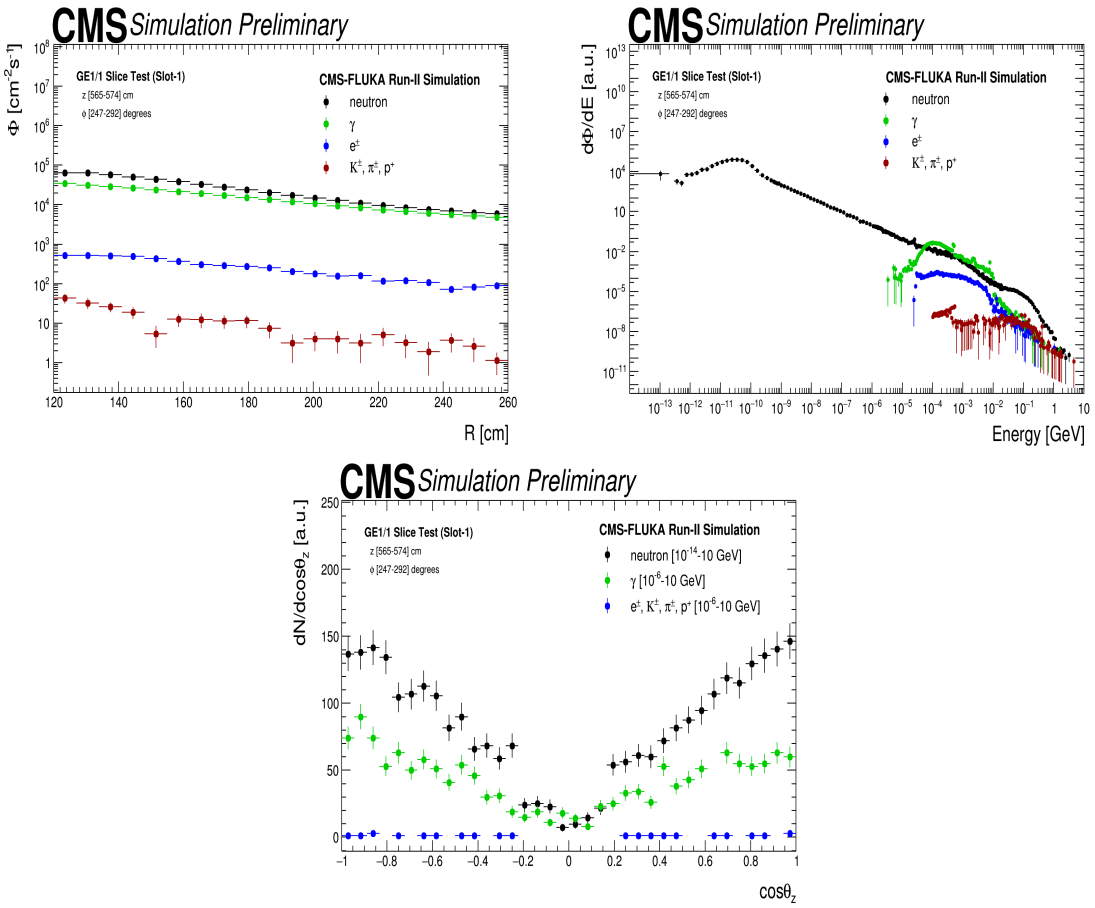

Figure 1. Particle flux arriving to GE1/1 volume, normalized to luminosity (top-left). Energy spectra of incoming particles (top-right), direction cosine of different particles with respect to axis perpendicular to detector surface (bottom)

3. Simulation

The flux and sensitivity are estimated using FLUKA and GEANT4 respectively.

3.1. FLUKA Simulation

The particle flux, differential energy spectrum and direction cosines at the CMS in the region 120 cm $<$ R $<$ 260 cm, 565 cm $<$ |Z| $<$ 574 cm for all particles is estimated using FLUKA v2011-3.0 shown in figure 1.

The primary *pp* collisions with an energy of 6.5 TeV per beam including the effect of magnetic field are simulated for Run-2 geometry. An inelastic cross section of 80 mb is used for normalization of flux to luminosity 1.5×10^{34} cm^{-2} s^{-1}.

3.2. GEANT4 Simulation

The response of a GE1/1 detector is estimated using he GEANT4 v10.6. The primary particle are uniformly generated at a distance of 3 mm from a surface of same size and shape as of the drift board of the GE1/1 detector. Energy range used for different particles are 10^{-3}-10^{4} MeV for neutrons, 10^{-3}-10^{4} MeV for γ's, 10^{-2}-10^{4} MeV for $e^{\pm}$ and 10^{-1}-10^{4} MeV for charged hadrons ($K^{\pm}, \pi^{\pm}, p$). The dimensions of CMS specific trapezoidal shape GE1/1 detectors are used for the GEANT4 simulation [9].

3.2.1. A single Triple-GEM Detector. A simplified single triple-GEM detector geometry (without service volume i.e. cooling system, cover and GEB) is simulated to study the effect of energy and angle of the incident particle on sensitivity. The sensitivity of GE1/1 detector is studied as a function of the energy and the angular distribution of each particle shown in figure 2 using threshold of 28.1 eV and 674.4 eV per incident particle for drift and transfer-1 gap respectively.

3.2.2. Superchamber. To compare the prediction with experimental data, a superchamber geometry (including service volume for both detectors) has been simulated to obtain the average sensitivity for superchamber 28 layer-2. This geometry includes all the components i.e. pull-outs, readout electronics and cooling system as explained in [9] along-with single Triple-GEM detector. The Triple-GEM detector [10] of a superchamber facing towards the interaction point of *pp* collisions is called "Layer-1" while the one facing outwards is called "Layer-2". A threshold of 56.2 eV and 1.21 keV per incident particle are used for drift and transfer-1 gap respectively, assuming gain of approximately $\approx 10^{4}$.

Particle	Average Sensitivity of Layer-1 (%)	Average Sensitivity of Layer-2 (%)
Neutron	0.63 ± 0.01 (stat.)	0.75 ± 0.01 (stat.)
γ	0.29 ± 0.01 (stat.)	0.20 ± 0.01 (stat.)
$e^{\pm}$	1.18 ± 0.03 (stat.)	0.31 ± 0.01 (stat.)
Charged Hadrons ($K^{\pm}$, $\pi^{\pm}$, p)	27.0 ± 1.3 (stat.)	25.1 ± 1.2 (stat.)

Table 1. Average Sensitivity for each type of particle for the layer-1 and layer-2 of the superchamber configuration.

4. Systematics

The accuracy on the sensitivity estimations depends on a correct description of the physics processes and on a realistic detector modeling. To quantify the collective impact on hit-rate,

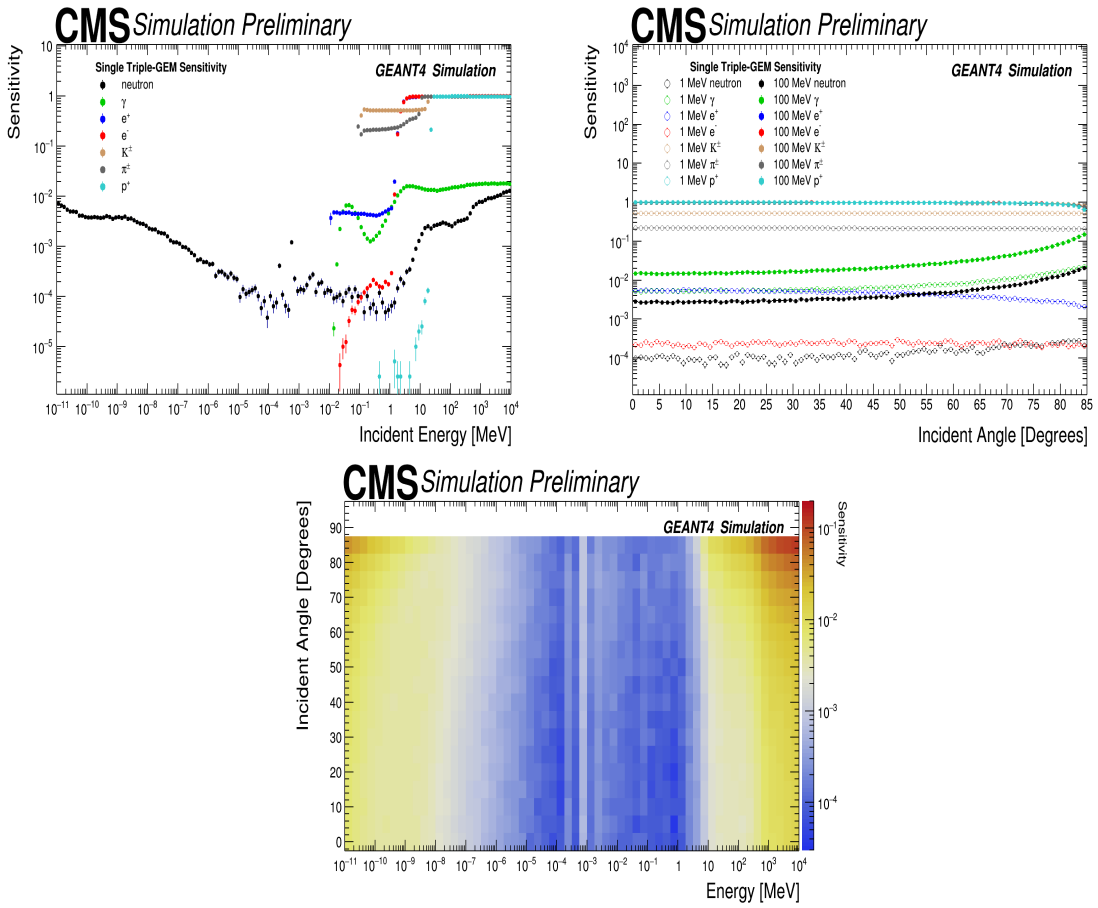

Figure 2. Sensitivity as a function of kinetic energy, for different particles, at incident angle of zero degrees with respect to normal to the detector surface (top-left). Sensitivity as a function of incident angle for different types of particles for 1 MeV and 100 MeV (top-right). Sensitivity 2D map for neutrons (bottom)

systematics on flux and sensitivity are considered for different parameters. Below are the paramters considered for GEANT4 systematics:

- Drift Gap Width (DGW) - variations of ±10% of nominal value (3 mm)
- Gas Mixture Proportion (GMP) - a variation of ±10% in Ar and CO_2 proportion of nominal (70:30)
- Source Generation Point (SGP) - a variation of ±2 mm from nominal (3 mm)
- Source Plane Area (SAR) - variations of ±10% of nominal (area of drift board)

Maximum systematics for DGW, GMP, SGP and SAR are found to be 1.4 %, 1.0 %, 9.9 % and 6.7 % respectively for each type of particle. FLUKA systematics is evaluated comparing the particle flux between the two CMS-FLUKA geometry, both consistent with Run-2 data taking scenario. The average uncertainty evaluated is 15.0%. The total combined uncertainty from FLUKA simulation and GEANT4 detector simulation is estimated to be about ≈ 14.5 % on hit rate, after adding them in quadrature for the whole range of R considered in this study.

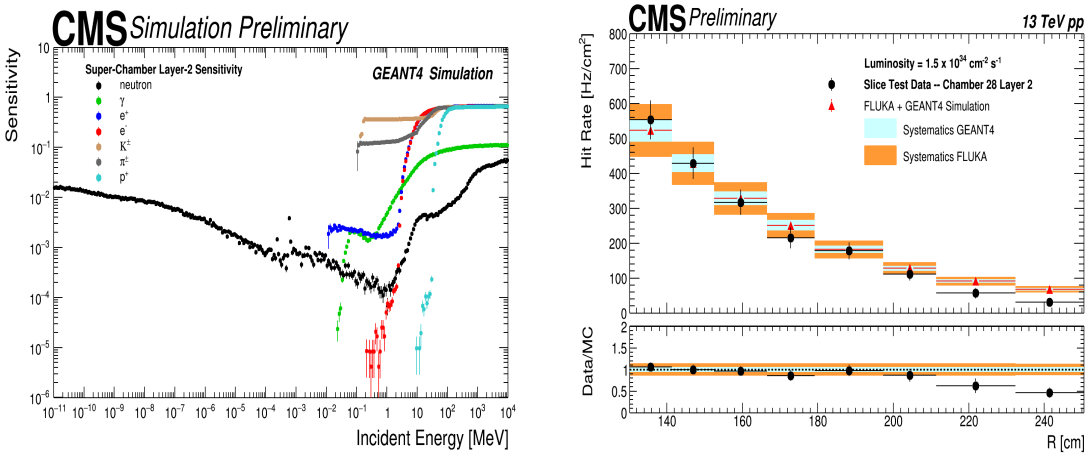

Figure 3. Sensitivity of "layer-2" as a function of incident energy for different particles (left). Comparison of slice test data with FLUKA+GEANT4 Simulation of Chamber 28 Layer-2 (right).

5. Comparison of Background Modeling and Experimental Data

A comparison between simulation and experimental measurements can be used to validate the model presented in this study. Figure 3 (right) compares the simulation with measured hit rate from data of layer-2 of superchamber 28 from the CMS experiment. The simulation results are obtained by taking the multiplication of average sensitivity shown in table 1 and values shown in Figure 1 (top-left). The FLUKA+GEANT4 simulation model discussed here describes the data hit rate well within the total uncertainties (including both statistical and systematics uncertainty added in quadrature) for the different data points correspond. The simulation prediction for first two η sectors show a larger discrepancy from data most likely due to relatively higher threshold set for these two sectors as compared to other sectors during data taking operations. Such effects can be studied in detail using GARFIELD software and a simulation of the electronics.

6. References

[1] CMS Collaboration, 2017 The Phase-2 Upgrade of the CMS Muon Detectors *CERN* **CERN-LHCC-2017-012, CMS-TDR-016**
[2] CMS Collaboration 2008 The CMS experiment at the CERN LHC *JINST* **S08004** 3
[3] M. Huhtinen 1996 The Radiation environment at the CMS experiment at the LHC *CERN* **HU-SEFT-R-1996-14**
[4] Y. Musienko et al. 2015 Radiation damage studies of silicon photomultipliers for the CMS HCAL phase I upgrade *Nucl. Instrum. Meth.* A **787** 319-322
[5] A. Ferrari, R. P. Sala, A. Fasso and J. Ranft 2005 FLUKA: A Multi-Particle transport code (Program version 2005) *CERN-2005-010* **INFN-TC-2005-11, SLAC-R-773**
[6] GEANT4 Collaboration 2003 GEANT4 a simulation toolkit *Nucl. Instrum. Meth.* A **506** 250-303
[7] M. Abbas et al. 2020 Detector Control System for the GE1/1 slice test *JINST* **P05023** 15
[8] CMS Collaboration 2020 Environmental Background Hit Rate on GE1/1 in the 2018 Slice Test *http://cds.cern.ch/record/2749429* **CERN-CMS-DP-2020-053**
[9] CMS Collaboration 2015 CMS Technical Design Report for the Muon Endcap GEM Upgrade *CERN* **CERN-LHCC-2015-012, CMS-TDR-013**
[10] F. Sauli, 1977 Principles of Operation of Multiwire Proportional and Drift Chambers *CERN* **CERN-77-09**

CERTIFICATE

OF PARTICIPATION

THIS IS TO CERTIFY THAT

Mr. Sunil Kumar

FROM

Panjab University, Chandigarh

HAS SUCCESSFULLY PARTICIPATED AND PRESENTED A POSTER IN THE

XXIII DAE-BRNS HIGH ENERGY PHYSICS SYMPOSIUM

(DECEMBER 10-14, 2018)

Held at the

Indian Institute of Technology Madras

P.K. Behera

Dr. Pramod Kumar Behera
Associate Professor
Department of Physics
Indian Institute of Technology Madras
Chennai - 600 036, India

Convener

Certificate

Sunil Kumar

has successfully participated and presented a talk titled

Sensitivity of Triple-GEM Detector for background radiation in CMS Experiment

XXIV DAE-BRNS Symposium on High Energy Physics

held **ONLINE** by the

National Institute of Science Education and Research

Jatni 752050 Odisha India

during

December 14-18, 2020

Prof. Bedangadas Mohanty
(Chair)

Prof. Sanjay Swain
(Co-Chair)

Sponsors & Organizers